

**COMSAT**  
Technical Review

Volume 12 Number 1 Spring 1982

*Advisory Board* Joseph V. Charyk  
William W. Hagerty  
John V. Harrington  
John L. McLucas

*Editorial Board* Pier L. Bargellini, Chairman  
Ali E. Atia  
S. J. Campanella  
William L. Cook  
C. Dorian  
H. W. Flieger  
Jorge C. Fuenzalida  
William J. Getsinger  
R. W. Kreutel  
Robert K. Kwan  
Akos G. Revesz  
George R. Welti

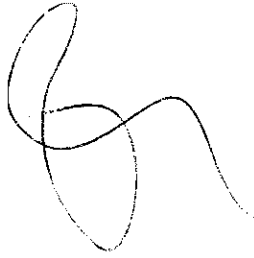
*Editorial Staff* Daniel N. Crampton  
MANAGING EDITOR  
Margaret B. Jacocks  
Elizabeth Christie  
Pearl Coleman  
TECHNICAL EDITORS  
Edgar Bolen  
PRODUCTION  
Shirley T. Cofield  
CIRCULATION

COMSAT TECHNICAL REVIEW is published twice a year by Communications Satellite Corporation (COMSAT). Subscriptions, which include the two issues published within a calendar year, are: one year, \$7 U.S.; two years, \$12; three years, \$15; single copies, \$5; article reprints, \$1. Make checks payable to COMSAT and address to Treasurer's Office, Communications Satellite Corporation, 950 L'Enfant Plaza, S.W., Washington, D.C. 20024 U.S.A.

## COMSAT TECHNICAL REVIEW

Volume 12 Number 1, Spring 1982

- 1 PRECIPITATION FADE STATISTICS FOR 19/29-GHZ COMSTAR BEACON SIGNALS AND 12-GHZ RADIOMETRIC MEASUREMENTS **Prabha N. Kumar**
- 29 SATELLITE SWITCHING CENTER FOR SS-TDMA COMMUNICATIONS **F. Assal, R. Gupta, J. Apple, and A. Lopatin**
- 69 RF TESTS ON THE ETAM STANDARD C ANTENNA **R. Price**
- 93 60-MBITS/QPSK-TDMA/DSI FIELD TEST VIA PACIFIC BASIN INTELSAT IV **T. Dobyns, D. Chakraborty, H. Suyderhoud, and C. J. Wolejsza**
- 121 AN APPROXIMATION TECHNIQUE FOR REALIZING THE RECIPROCAL SIN (X)/(X) FREQUENCY RESPONSE **J. Poklemba**
- 157 A DEMAND-ASSIGNED MIXED TDMA AND FDMA/TDMA SYSTEM **R. J. F. Fang**
- 181 SATNET PACKET DATA TRANSMISSION **L. Palmer, J. Kaiser, S. Rothschild, and D. Mills**
- 213 DIGITAL SIMULATIONS OF SBS SPACECRAFT DESPIN OPERATION **J. Hsing**
- 231 TRANSLATIONS OF ABSTRACTS  
FRENCH 231 SPANISH 235
- 241 1981 CTR AUTHOR INDEX
- 243 1981 INDEX OF PRESENTATIONS AND PUBLICATIONS BY COMSAT AUTHORS



## ***Precipitation fade statistics for 19/29-GHz COMSTAR beacon signals and 12-GHz radiometric measurements***

PRABHA N. KUMAR

(Manuscript received October 14, 1981)

### ***Abstract***

Long-term measured propagation data at frequencies greater than 10 GHz, especially at 19/29 GHz, are not commonly found in the literature. This paper discusses studies of the effects of rain on the 19/29-GHz COMSTAR beacon signals and 12-GHz radiometrically measured atmospheric noise temperature. Data covering four years of continuous measurement are presented, which consist of measurements of beacon signals from three COMSTAR satellites (COMSTAR D-1, D-2, and D-3), 11.6-GHz radiometrically measured atmospheric noise temperature, and surface point rain rate. Analysis of these data includes cumulative fade distributions at 19.04 and 28.56 GHz; diurnal fade distributions and fade duration histograms at 19.04 and 28.56 GHz; cumulative distribution of measured surface point rain rate; excess rain attenuation derived from radiometrically measured atmospheric noise temperature; and diurnal and fade duration histograms of these 11.6-GHz fades. Elevation angle dependence is briefly discussed.

### ***Introduction***

Satellite communications systems at 4 and 6 GHz are now common. As these bands will eventually be saturated, studies of the higher frequency bands have become important [1]-[12]. Unfortunately, at frequencies above 10 GHz attenuation by rain constitutes a serious obstacle in the design of communications systems [4], [13]. Several years of

measured data analyses are required in order to establish the attenuation [14], depolarization and fade duration statistics [15], and year-to-year variations of these statistics [16].

This paper presents precipitation attenuation statistics derived from monitoring 28.56- and 19.04-GHz beacons from COMSTAR geostationary satellites (COMSTAR D-1, D-2, and D-3), and 11.6-GHz excess rain attenuation derived from radiometric measurements along the same slant path over a period of approximately four years. For convenience, the data base is divided into three categories. Table 1 shows the satellite locations; elevation angles from the measurement facility at COMSAT Laboratories, Clarksburg, Maryland; and the time periods of the analyzed data along with other important parameters. The measurement facility at Clarksburg is briefly described and the cumulative statistics of rain rate and attenuation for each of the three measurement periods are presented. Finally, fade duration statistics and their diurnal variations are discussed.

TABLE 1. CHARACTERISTICS OF COMSTAR SATELLITES

	COMSTAR D-1	COMSTAR D-2	COMSTAR D-3
Location (W. Long.)	128°	95°	87°
Elevation Angle	21°	41°	43.5°
Data Period	7/14/76-8/17/77	8/17/77-8/18/78	8/18/78-9/1/80
Polarization	Linear	Linear	Linear
Tilt Angle (from local vertical)	4°	21°	1.7°
Frequencies (GHz)	19 and 29	19 and 29	19 and 29

**Experimental setup**

Figure 1 is a simplified block diagram of the measurement facility at Clarksburg, Maryland; a detailed description can be found elsewhere [2], [3]. The facility consists of a 5-m Cassegrain antenna with RF down-converter, IF beacon receiver, and chart recorder. A tipping bucket rain gauge and an 11.6-GHz radiometric receiver operating independently through a 2-m antenna are provided to measure the rain accumulation and fades at 11.6-GHz. Figure 2 is a block diagram of the front end of the RF receiver, and Figure 3 is a block diagram of the receiver baseband section.

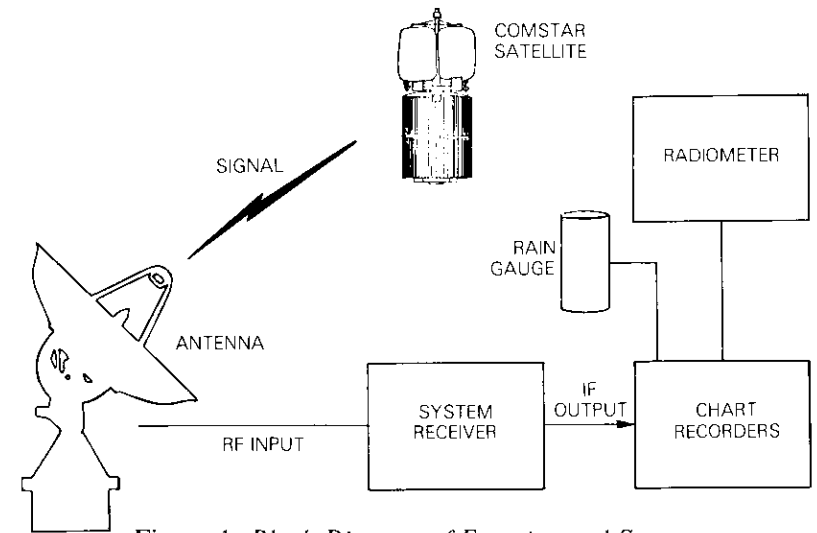


Figure 1. Block Diagram of Experimental Setup

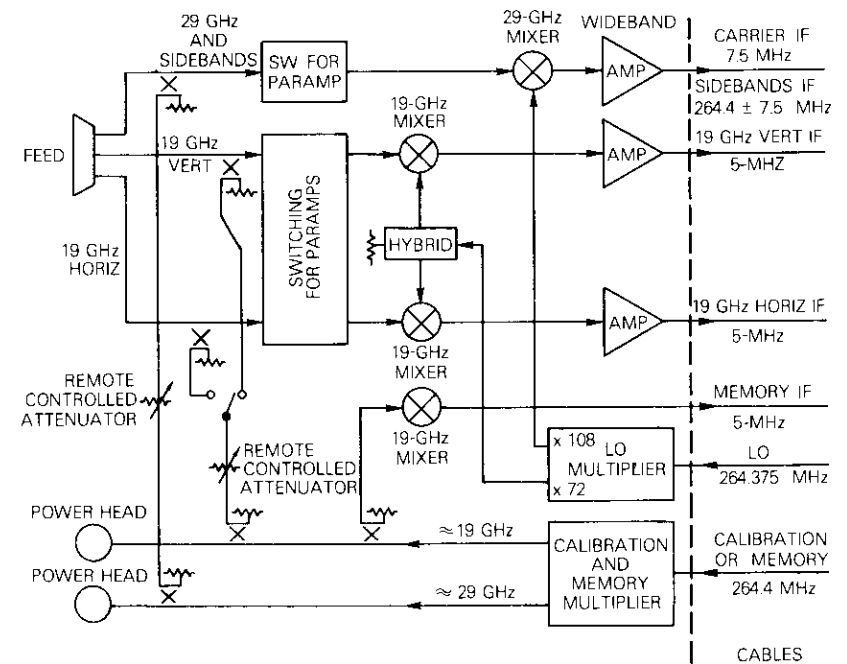


Figure 2. Block Diagram of the RF-Front End

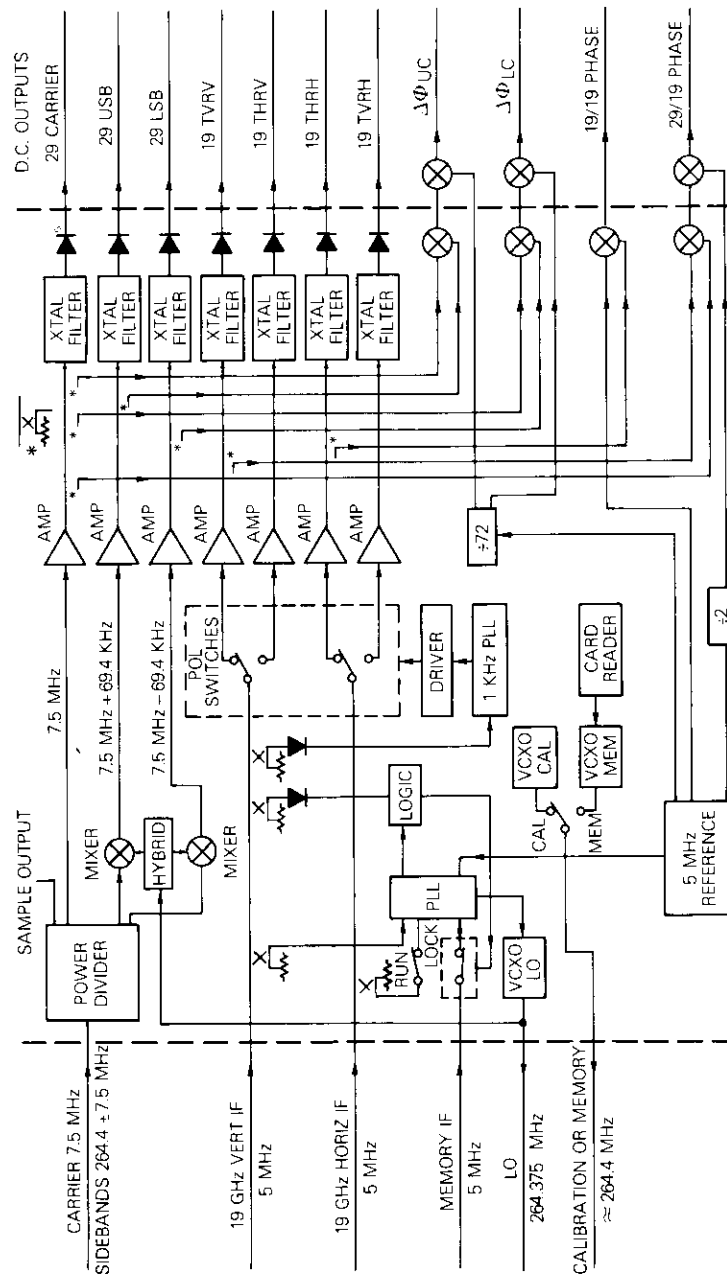


Figure 3. Receiver Baseband Block Diagram

### Description

COMSTAR beacon signal characteristics have been previously described [2], [17], [18], as have beacon receiver design, operations, and data collection procedures [2], [18]. It is noted here that the 5-m Cassegrain antenna receives signals at both 19 and 29 GHz. The vertically polarized signals at 29 GHz (carrier), 28.29 GHz (lower sideband), and 28.82 GHz (upper sideband) arrive at the receiving antenna ports with phases coherent to the 19-GHz vertically polarized signal. The phase-locked loop (PLL) technique is used to lock onto the 19-GHz vertically polarized signal, which is expected to sustain shallower fades than the other signals. The coherence of 29-GHz signals and of the 19-GHz vertically polarized signal assures the reception of 29-GHz signals as long as the 19-GHz vertically polarized signal receiver remains locked.

### Results of measurements

Measured rain rate and attenuation will be discussed for the three measurement periods defined in Table 1.

#### Rain rate statistics

During the COMSTAR D-1 measurement period, from July 14, 1976, to August 17, 1977, the measured total rain accumulation was 814 mm. Figure 4a shows the comparison of measured rain rate with Rice-Holmberg model [19] distributions for a mean annual rainfall ( $M$ ) of 745 mm and values of the thunderstorm ratio  $\beta$  (ratio of thunderstorm rain to total rain) equal to 0.2 and 0.3. From Figure 4a, it is clear that the measured rain rate appears to be in excellent agreement with the Rice-Holmberg model distribution for  $\beta$  equal to 0.3, which happens to be the mean value of  $\beta$  for Clarksburg, Maryland, derived from the available propagation data base.

During the second year, from August 17, 1977, to August 18, 1978, the measured rain accumulation was 799 mm. Figure 4b shows the variation of rain rate with percentage of time. The distributions obtained from the Rice-Holmberg model for  $M$  equal to 797 mm, and  $\beta$  of 0.2 and 0.3 are also plotted in Figure 4b. For this measurement period, the measured rain rate is in good agreement with model distributions for  $\beta$  equal to 0.2 and 0.3 for percentages of time greater than 0.5. However, for percentages of time less than 0.5 but greater than 0.01, which constitute the range of greatest interest, the Rice-Holmberg distribution for  $\beta$  equal to 0.2 is in better agreement with the measured data.

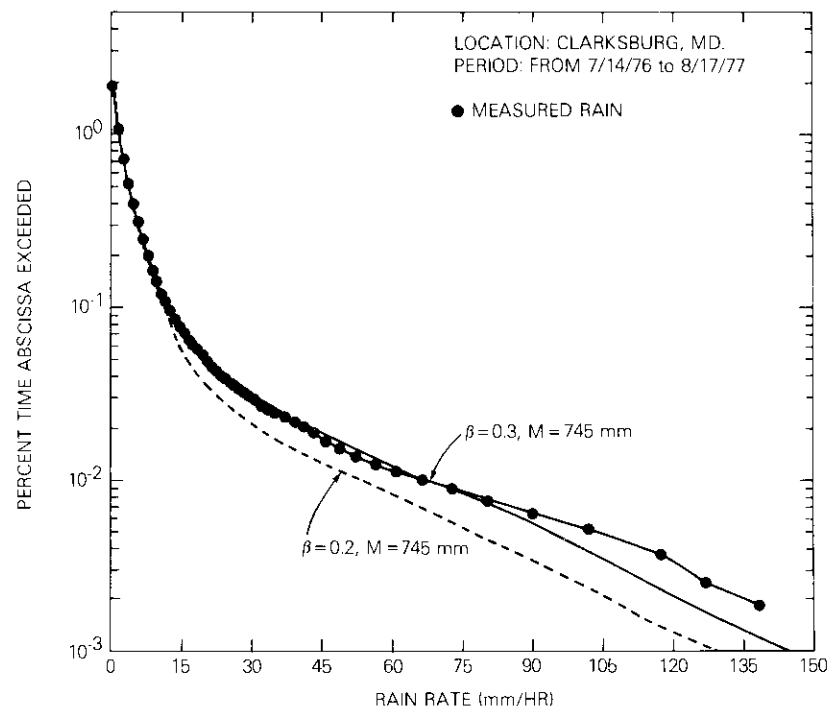


Figure 4a. Comparisons of Measured Surface Point Rain Rate with Theoretical Model Distributions

In Figure 4c, the measured rain rate for the third measurement period, from August 18, 1978, to September 1, 1980 (see Table 1), is plotted with the Rice-Holmberg distributions for mean annual rainfall of 748 mm and  $\beta$  equal to 0.3 and 0.4. During this period, the total accumulation of rain was 1,526 mm. As is evident from Figure 4c, the measured rain rate is in good agreement with the model for  $\beta$  equal to 0.4 for percentages of time greater than 0.1. For time percentages less than 0.1 but greater than 0.03, the measured rain rate agrees better with the model distribution for  $\beta$  equal to 0.45 (see Figure 4c). For time percentages less than 0.03 and greater than 0.01, the measured data have a tendency to agree better with the model distribution for  $\beta$  between 0.3 and 0.4 (see Figure 4c).

In Figure 4d, the measured rain rates for all three above-mentioned periods are plotted (individually and combined) versus percentage of time. Notice that the rain rate distribution curve for the combined years is smoother than the distribution curve for individual periods for high rain

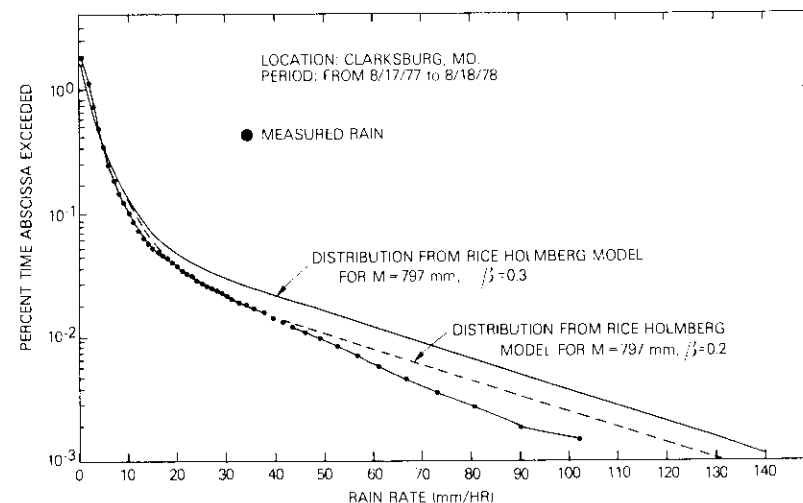


Figure 4b. Comparisons of Measured Surface Point Rain Rate with Theoretical Model Distributions

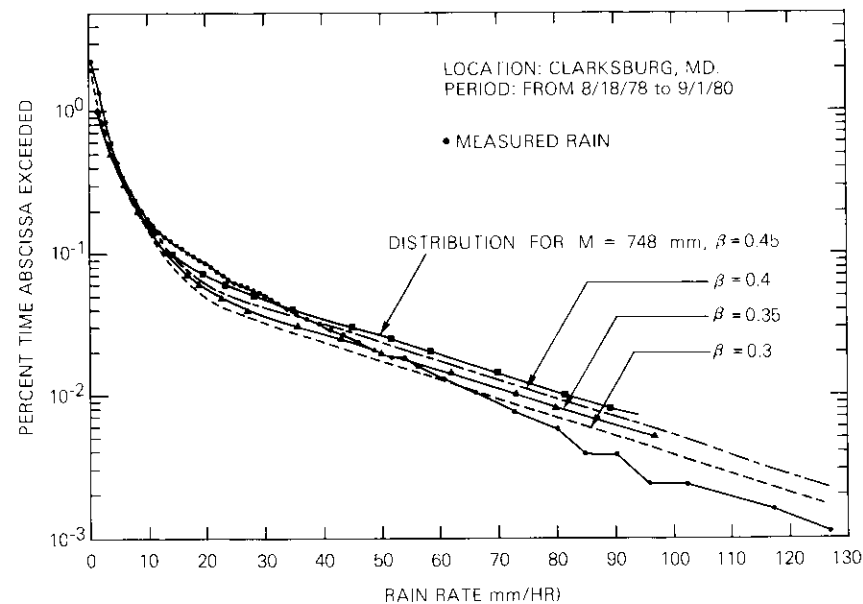


Figure 4c. Comparisons of Measured Surface Point Rain Rate with Theoretical Model Distributions

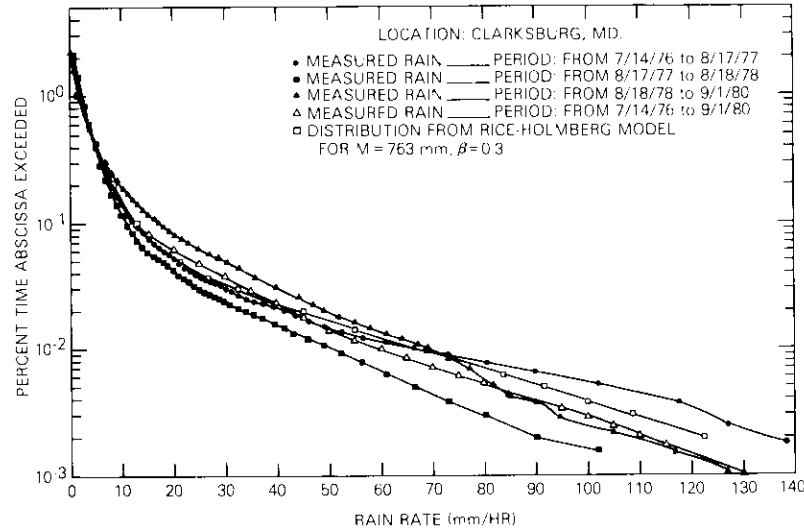


Figure 4d. Comparisons of Measured Surface Point Rain Rate for the Entire Measurement Period with Theoretical Distributions

rates. The theoretical distribution based on the Rice-Holmberg model for a mean annual rainfall of 763 mm (M) and  $\beta$  equal to 0.3 is also plotted in Figure 4d. As is evident from Figure 4d, the measured distribution for the entire measurement period is in excellent agreement with Rice-Holmberg model distribution for mean annual rainfall of 763 mm and  $\beta$  equal to 0.3 for all percentages of time above 0.01 percent. The curves in Figure 4d represent year-to-year variability in rainfall [15], [16] over a period of four years. Although the factor  $\beta$  varied from 0.2 to 0.4, the average  $\beta$  for the entire measurement period agrees with the mean value of  $\beta$  equal to 0.3 for Clarksburg, Maryland. There was no significant difference in the total accumulation of rain for each year. The difference in total accumulation varied less than 40 mm for an average year for the entire measurement period. During these observations the average experiment up time was 93 percent.

**Attenuation statistics**

Some results of precipitation attenuation studies based on the measured data for frequencies greater than 10 GHz have been reported [1]-[3], [6]-[14], [20]. COMSTAR D-1 and D-2 beacon data have been examined from the point of view of frequency scaling, and results have been re-

ported in Reference 3. In this section, the measured attenuation for 19- and 29-GHz beacon signals and for 12-GHz radiometric measurements are discussed. Table 2 gives the measured and nominal e.i.r.p. values for the three COMSTAR beacon signals. Figure 5a represents cumulative attenuation distributions derived from measured 12-GHz radiometric noise temperature, for 19-GHz vertically and horizontally polarized beacon signals, and for the 29-GHz carrier. In Figure 5b, cumulative distributions of measured attenuation for 12, 19, and 29 GHz are compared with model distributions based on the Rice-Holmberg model of rain rate for a mean annual rainfall of 745 mm and  $\beta$  equal to 0.3.

TABLE 2. COMSTAR BEACON e.i.r.p.'s

SIGNAL	NOMINAL e.i.r.p. (dBW)	MEASURED e.i.r.p. (dBW)*		
		D-1	D-2	D-3
19TV	23	22.1	24.0	26.5
19TH	23	23.8	26.3	26.2
29C	24	28.9	31.8	31.5
28LSB	17	20.7	22.1	19.5
28USB	17	20.2	20.9	26.1

\*Post-launch measurements by K. Betaharon, I. Atohoum, and R. Johnson; D-1 on 8/21/78; D-2 on 8/21/78; D-3 on 9/5/78.

The model distributions of excess rain attenuation were calculated using software developed at COMSAT Laboratories. In this model, for a given percentage time,  $P$ , the rain rate,  $R$  (mm/hr), is determined and the effective path length,  $L$ , is computed. This calculation of effective path length ( $L$  as a function of percent time and path elevation angle) is based on more recent information [21] and a much improved curve fit for a rain-rate-dependent effective path length [22]. The specific attenuation  $\alpha$  (dB/km) is calculated using the expression [21]

$$\alpha = aR^b \text{ (dB/km)} \quad (1)$$

where  $R$  is the point rain rate (mm/hr) and  $a$  and  $b$  are constants dependent on frequency, temperature, and drop size distribution.

The path attenuation  $A$  for a particular percentage time is computed using the expression

$$A = \alpha L \text{ (dB)} \quad (2)$$

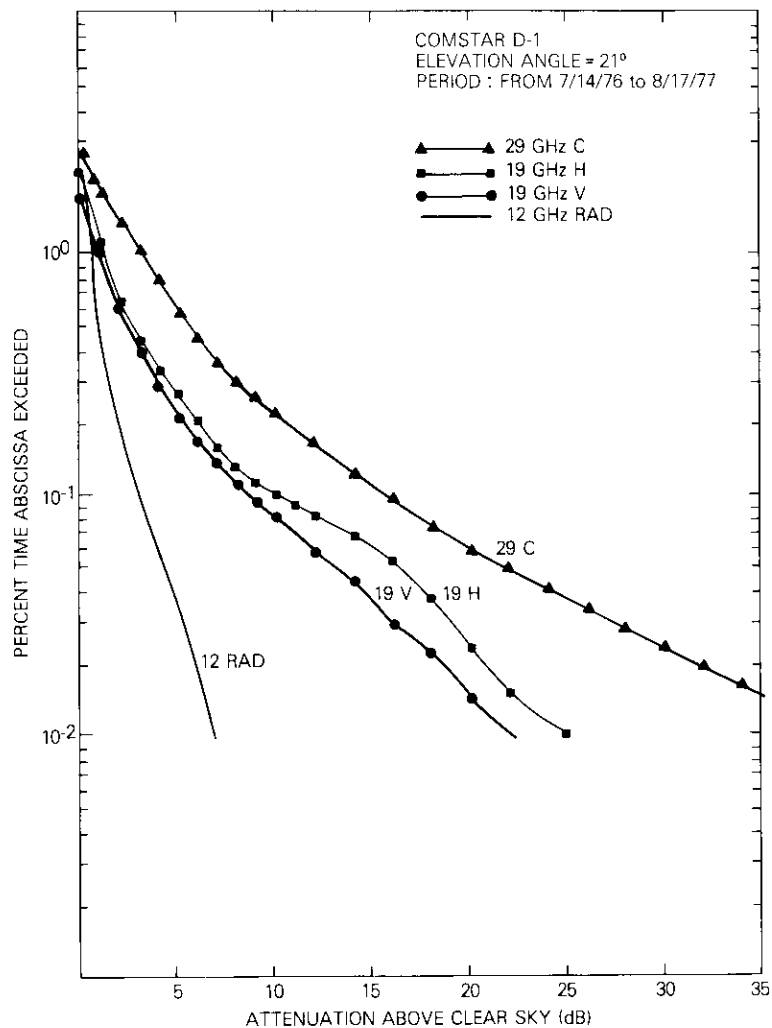


Figure 5a. Cumulative Distributions of Fading at 12, 19, and 29 GHz Along the Earth-Satellite Path

For 12 and 19 GHz, the model is in very good agreement for the percentages of time greater than 0.03 percent, whereas for 29-GHz signals, the model predicts higher attenuation than the measured data for all percentages of time less than 0.5.

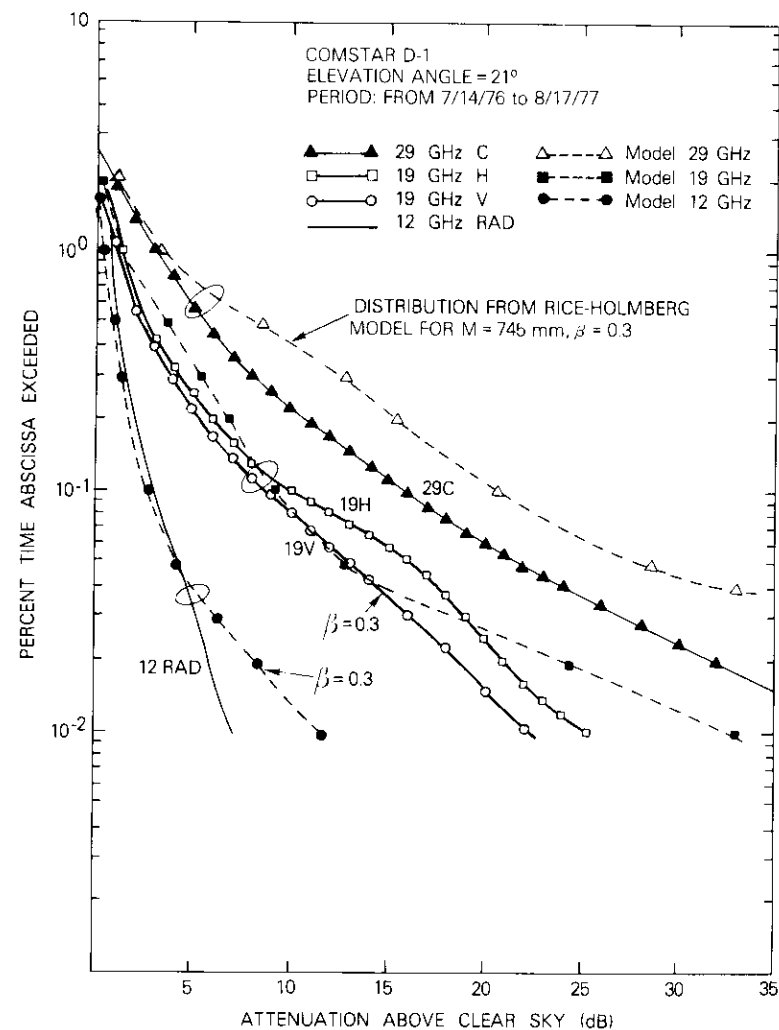


Figure 5b. Comparisons of Measured Attenuation with Theoretical Distributions Based on Measured Surface Point Rain Rates

Figure 6a shows the measured attenuation distributions for the second year of measurement for 12, 19, and 29 GHz. Figure 6b compares measured distributions with model distributions based on Rice-Holmberg rain parameters [19],  $M$  equal to 797 mm, and  $\beta$  equal to 0.3.

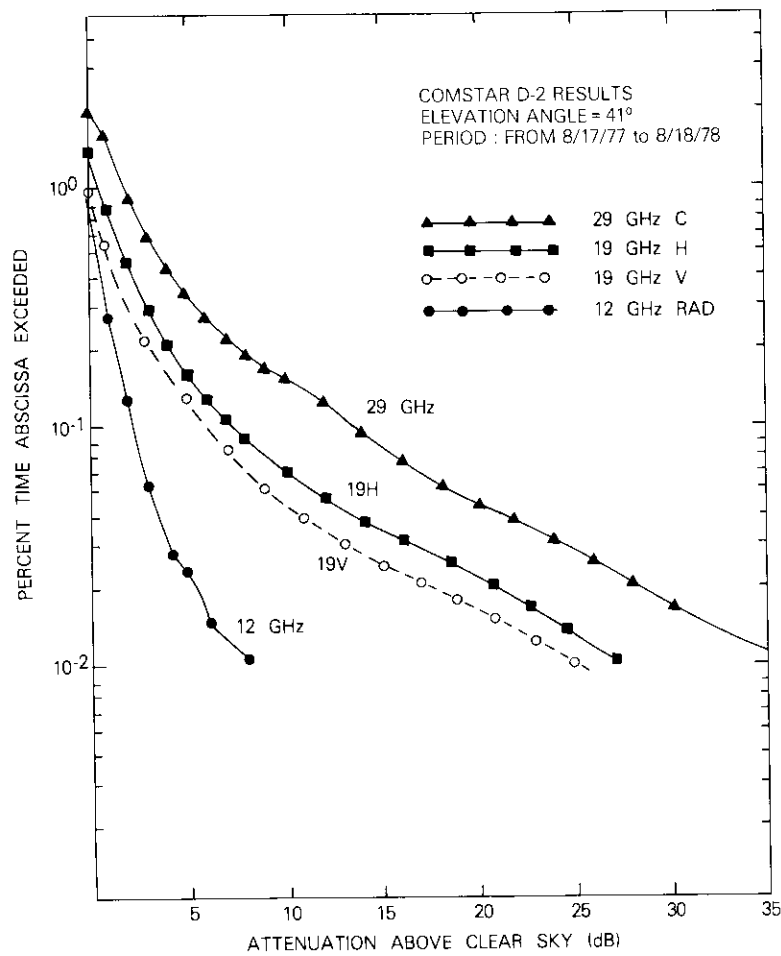


Figure 6a. Cumulative Distributions of Fading at 12, 19, and 29 GHz Along the Earth-Satellite Path

For this measurement period, the model distributions are in good agreement for  $\beta$  equal to 0.3 for the three frequencies 12, 19, and 29 GHz, and for percentages of time greater than 0.01.

Figure 7a shows measured attenuation distribution for the third phase of the measurement period. The 19-GHz horizontally polarized signals consistently show more attenuation than the 19-GHz vertically polarized signals for all percentages of time greater than 0.018, where the

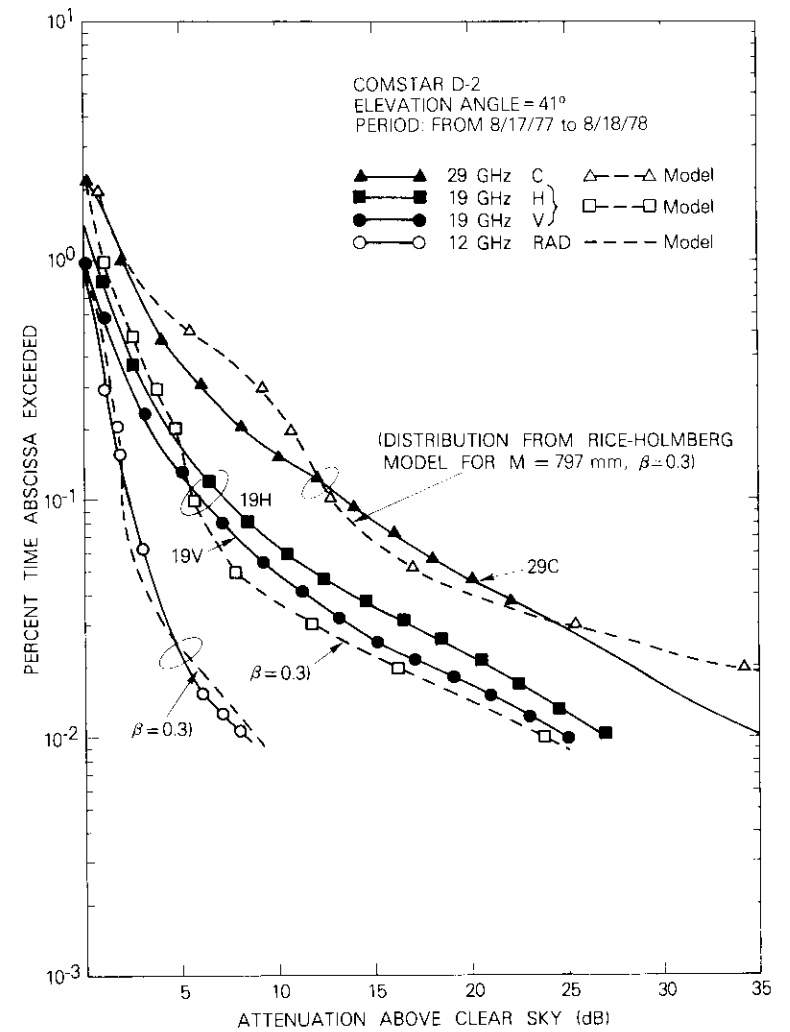


Figure 6b. Comparisons of Measured Attenuation with Theoretical Distributions Based on Measured Surface Point Rain Rates

two curves cross each other. This discrepancy may be attributed to uncertainty in the data due to the PLL losing lock for high rain rates. The attenuation distributions for 12 and 29 GHz behave normally as observed during previous years.

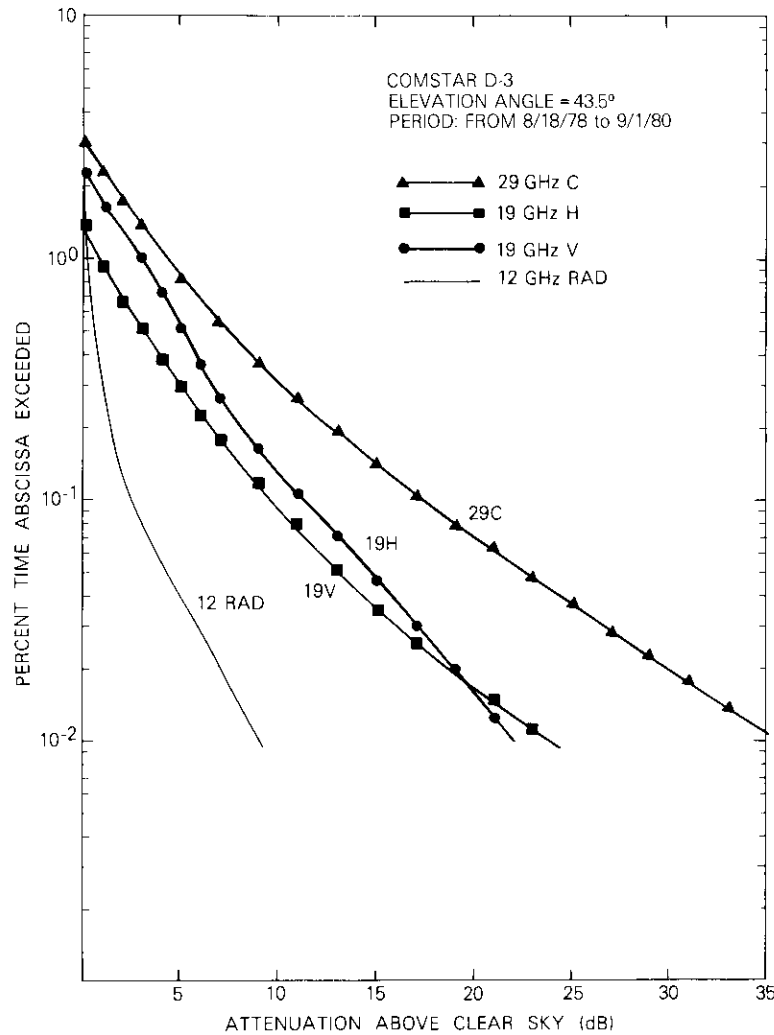


Figure 7a. Cumulative Distributions of Fading at 12, 19, and 29 GHz Along the Earth-Satellite Path

Figure 7b compares measured attenuation distributions with the model predictions based on the Rice-Holmberg rain parameters  $M$  equal to 748 mm and  $\beta$  equal to 0.3 and 0.4. The maximum deviation from measured and theoretical distribution occurs at 0.1 percentage of time for

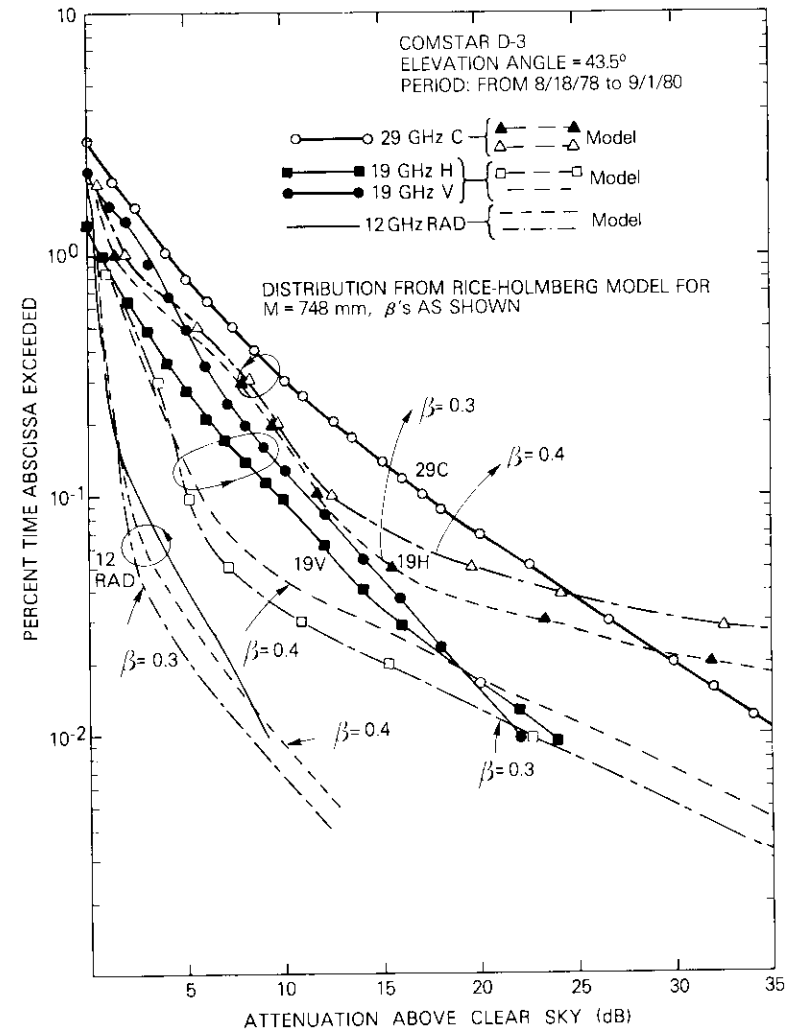


Figure 7b. Comparisons of Measured Attenuation with Theoretical Distributions Based on Measured Surface Point Rain Rate

19 and 29 GHz. Table 3 compares attenuation for 12, 19, and 29 GHz for the entire measurement period. This table shows that measured attenuation is not only a function of frequency and path elevation angle [13], but also depends on the nature of the rain for that particular year.

TABLE 3. ATTENUATION (DB) STATISTICS FOR ENTIRE MEASUREMENT PERIOD

PERCENT TIME OF THE YEAR ATTENUATION EXCEEDED	FREQUENCY (GHz)								
	12			19			29		
	ELEVATION ANGLE (DEG.)								
	21	41	43.5	21	41	43.5	21	41	43.5
1.0	0.5	0.25	0.25	1.0	—	0.75	3.0	1.8	4.2
0.5	1.0	0.6	0.6	2.4	1.3	3.0	5.5	3.8	7.4
0.3	1.5	1.0	0.9	3.75	2.5	5.0	7.9	6.0	10.2
0.2	1.8	1.4	1.35	5.0	3.6	6.5	10.5	8.0	12.5
0.1	3.0	2.25	2.25	8.6	6.0	9.75	15.6	13.4	17.25
0.05	4.25	3.25	4.25	13.0	9.8	13.0	22.0	19.0	22.6
0.03	5.1	4.1	5.75	16.0	14.0	16.0	27.0	24.5	26.6
0.02	5.75	5.5	7.0	18.5	17.5	18.75	31.6	28.4	30.0
0.01	6.8	8.5	8.9	22.2	—	23.75	—	—	—

Figure 8 compares slant path attenuation with equiprobable values of rain intensity for elevation angles of 21° and 43.5° and for frequencies of 12, 19, and 29 GHz. Basically, these curves are in agreement with the idea [23] that attenuation increases as the elevation angle decreases for a particular frequency. In Figure 8, however, the curves for elevation angles 21° and 43.5° intersect each other for frequencies 12 and 19 GHz. It is important to note that such variations were also observed by others [24], [25] with the attenuation statistics and rain rate statistics measured concurrently at the same site. It should also be noted that although the curves in Figure 8 represent variations of attenuation with rain rates for the same percentage of time, the measured data for different elevation angles belong to entirely different time periods. In other words, there is no overlapping period where the measured data are available for two elevation angles concurrently. Therefore, a long-term measurement which includes frequency, elevation angle, and year-to-year variability of rain at a particular site of interest would be extremely useful in establishing a propagation model for predicting attenuation.

**Diurnal and fade duration statistics**

The diurnal distribution of excess attenuation represents the cumulative fade duration (min) of a given fade level that was equalled or exceeded during a particular hour of the day, and its variations for the entire measurement year. In Figures 9a through 9d, the diurnal distribution of excess rain attenuation for frequencies of 12 GHz, 19 GHz-V

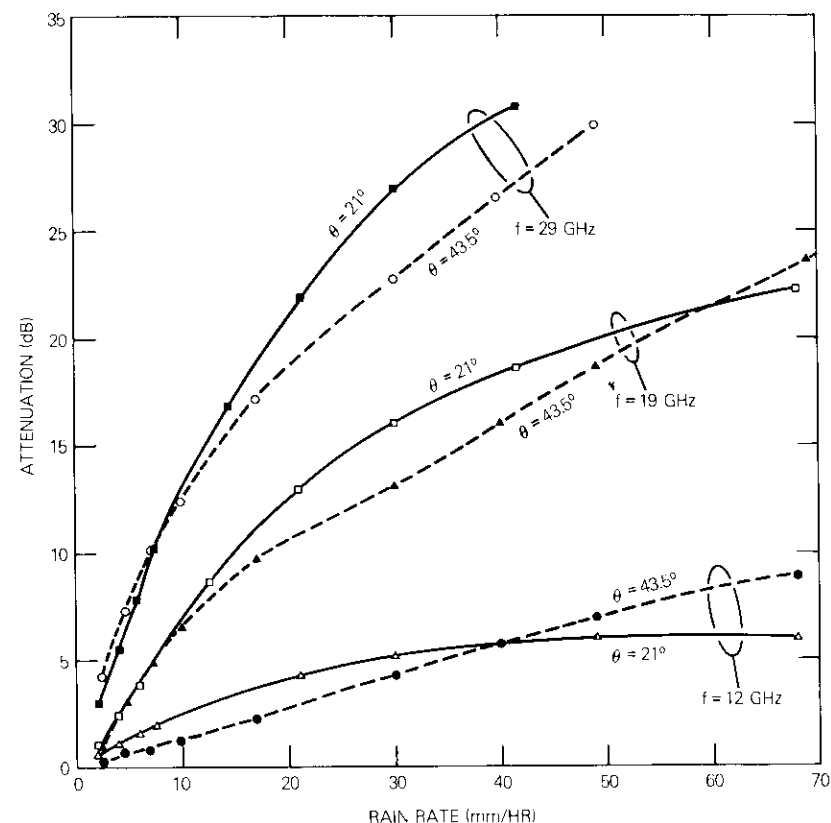


Figure 8. Comparisons of Slant-Path Attenuation with Equiprobable Values of Rain Intensity as a Function of Frequency and Elevation Angle

(vertical polarization), 19 GHz-H (horizontal polarization) and 29 GHz are presented for the COMSTAR D-1 beacon measurement period. From Figure 9a it is clear that attenuation values of greater than 4 dB were observed for 12 GHz during 0400 to 0500, 1300 to 1700, and 2300 to 0400 hours local time. No fades greater than 4 dB were observed in the morning and late evening hours. As the frequency increased to 19 and 29 GHz, attenuation exceeding 4 dB was observed throughout the day (Figures 9b through 9d).

Fade duration histograms of excess rain attenuation give information about how many fades of a certain attenuation level occurred during a

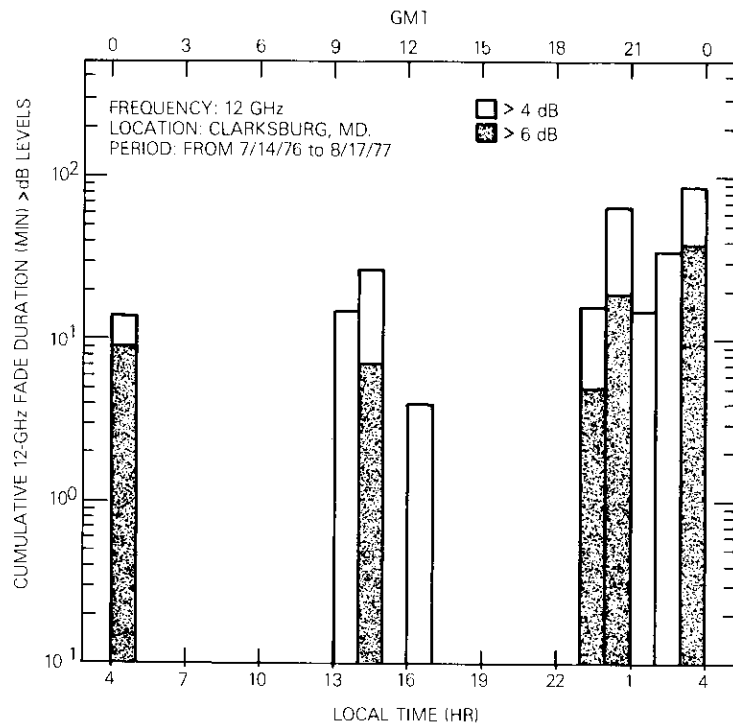


Figure 9a. Diurnal Distribution of Rain Fades at 12 GHz

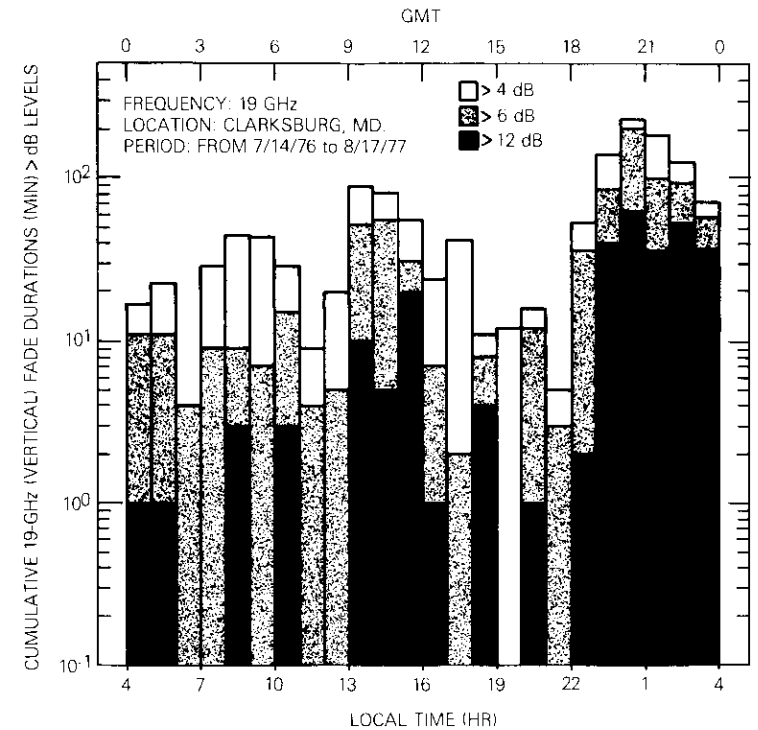


Figure 9b. Diurnal Distribution of Rain Fades at 19 GHz (Vertical Polarization)

given time period and how long the fades lasted. For instance, Figures 10a through 10d represent fade duration histograms for 12-GHz, 19-GHz-V, 19-GHz-H, and 29-GHz signals, respectively, during the period 1976 to 1977. Figure 10b shows that there were about 132 fades for which attenuation exceeded 4 dB, 97 fades for which attenuation exceeded 6 dB, and 42 fades for which attenuation exceeded 12 dB. The longest fade of 4-dB attenuation level lasted 70 minutes, that of 6-dB lasted 54 minutes, and that of 12-dB lasted about 49 minutes.

At higher frequencies, there are more fades of all levels of attenuation with durations greater than those of the 12-GHz fades. Quantitative analyses at the duration and diurnal variations of higher attenuation levels are expected to appear in future papers on COMSTAR beacon measurements.

### Conclusions

Rain and radiometer data, 19-GHz vertically and horizontally polarized signal attenuation, and 28-GHz attenuation data have been reduced and analyzed for a period of approximately four years.

The observed rainfall for an average year at Clarksburg, Maryland, was less than the mean annual rainfall (945 mm). The average  $\beta$  for the entire measurement period, however, was the same as the expected mean value (0.3) for Clarksburg.

The observed precipitation attenuation for 12, 19, and 29 GHz has patterns similar to those observed previously [2], [3]. The 29-GHz signal attenuated the most and the 12-GHz signal, the least. In general, observed attenuation is a function of path elevation angle. A long-term

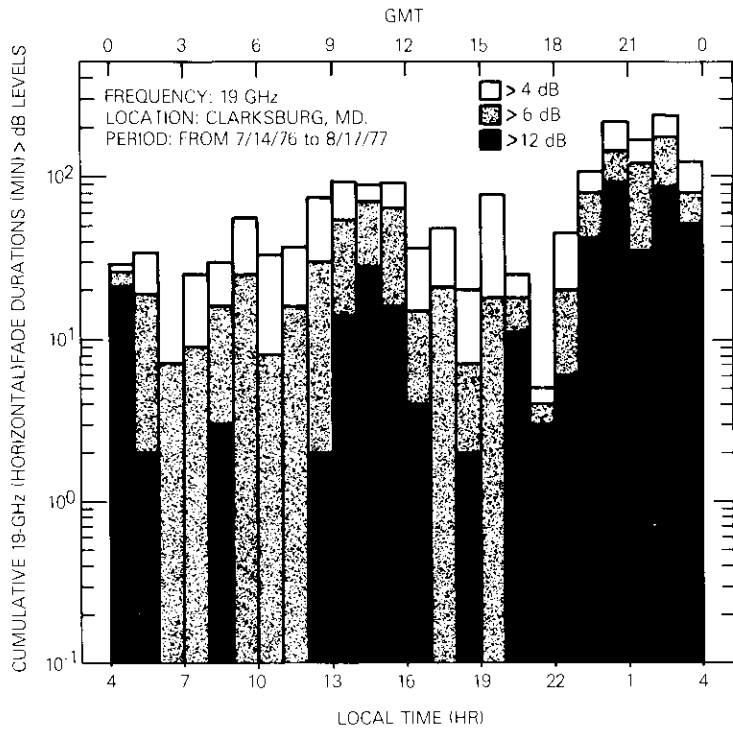


Figure 9c. Diurnal Distribution of Rain Fades at 19 GHz (Horizontal Polarization)

data base [4], [20], [23] is required to deduce any functional relationship between the elevation angles and attenuation at different frequencies. The attenuation data have consistently shown more attenuation for 19-GHz horizontally polarized signals than for 19-GHz vertically polarized signals, except in the third and fourth years, where the two curves cross each other at 0.018 percent of the time. This discrepancy, as mentioned before, is due to uncertainty in the measured data for high rain rates.

The measured attenuation for all three frequencies is in fairly good agreement with theoretical prediction based on equations (1) and (2). The discrepancy in the measured and theoretical distributions for 12, 19, and 29 GHz can be mainly attributed to weakness in the model used in finding

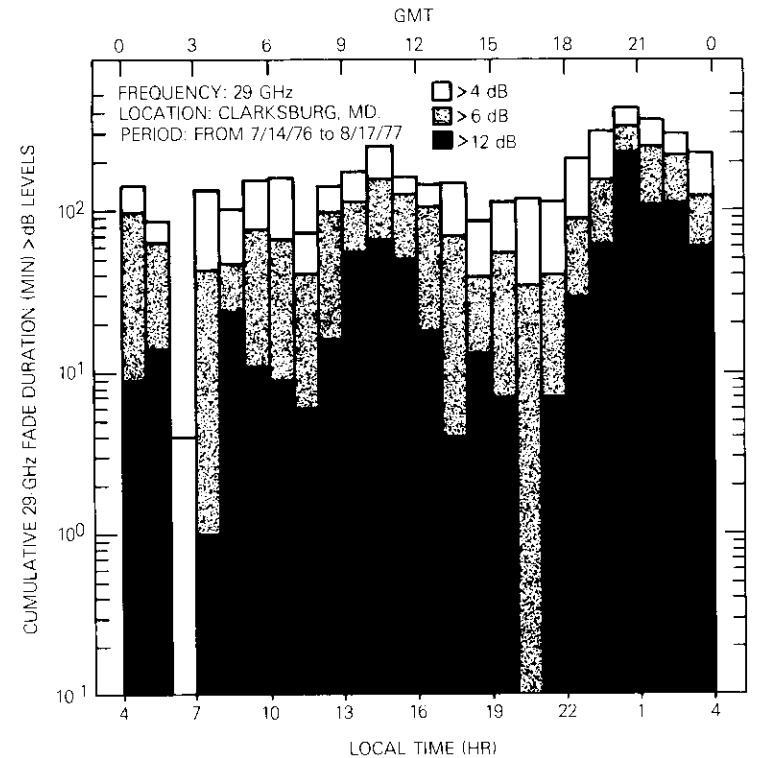


Figure 9d. Diurnal Distribution of Rain Fades at 29 GHz

the effective path length [2], [23]. The method of finding the effective path lengths has not been well established. Further work in this area should provide data for a more accurate theoretical prediction model.

The diurnal distribution of excess rain attenuation for 12 GHz, 19 GHz-V, 19 GHz-H, and 29 GHz indicate that for 19- and 29-GHz frequencies, fades greater than 12 dB have been observed during afternoon, evening, and nighttime.

Fade duration histograms for the COMSTAR D-1 measurement period indicate that the total number of fades of attenuation levels increases significantly for 19 and 29 GHz. These observations, along with those of another three years, indicate that precipitation attenuation plays a significant role in future communications system design for frequencies greater than 10 GHz.

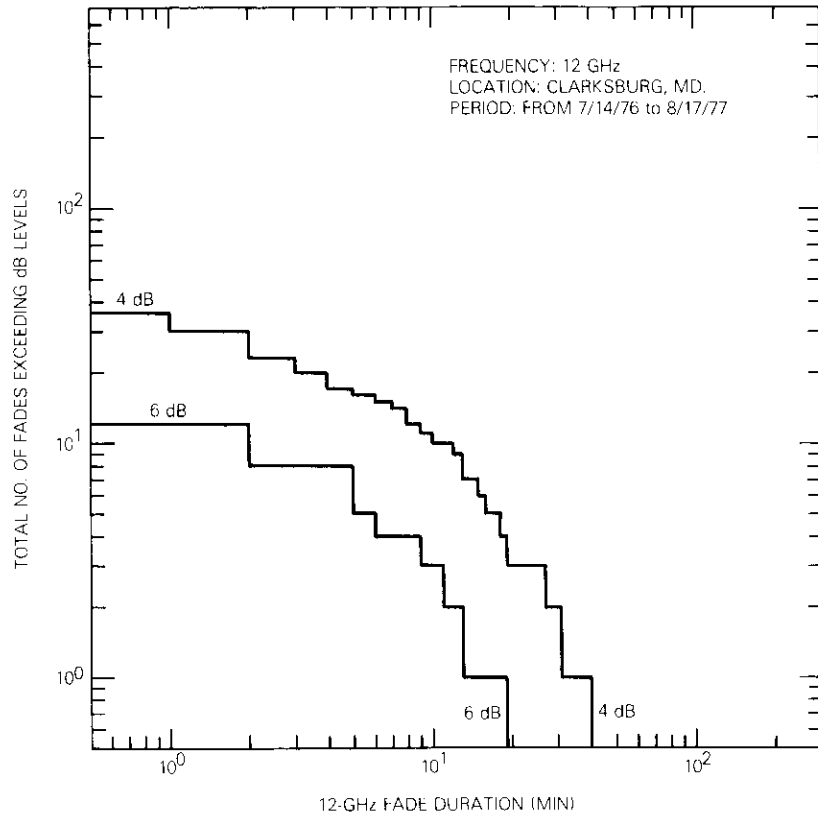


Figure 10a. Fade Duration of Excess Rain Attenuation at 12 GHz

**Acknowledgments**

The work reported is the result of the efforts of many people. The Microwave Laboratory provided much of the hardware used in the measurements and provided support when needed, which is gratefully acknowledged. Thanks are due to D. V. Rogers and M. Pontes for many hours of their time and useful discussions about the data analyses. S. Struharik was very helpful in review-

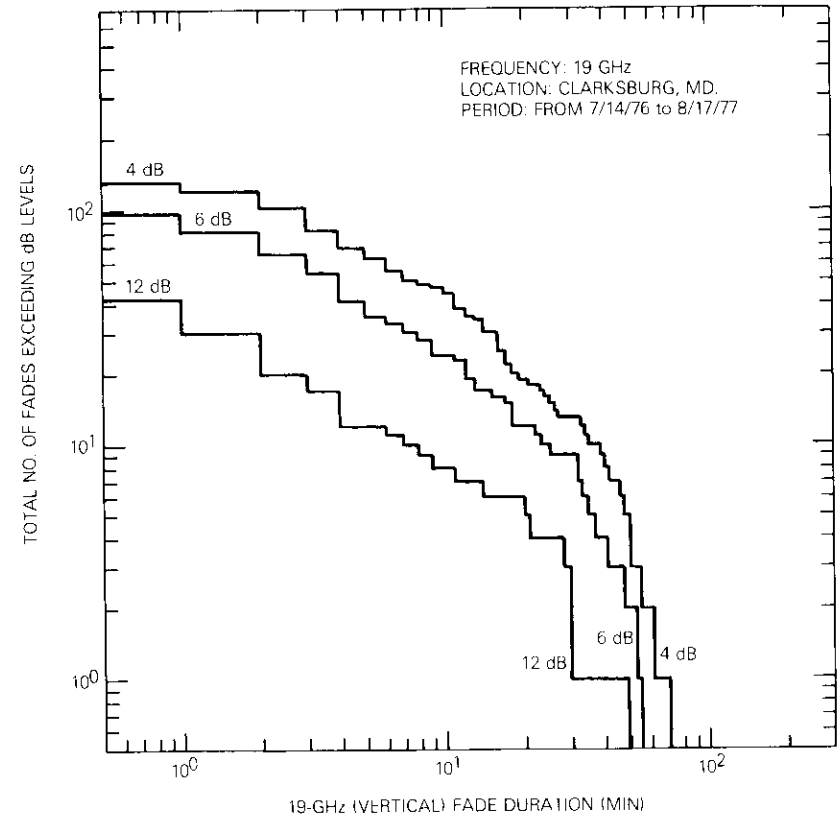


Figure 10b. Fade Duration of Excess Rain Attenuation at 19 GHz (Vertical Polarization)

ing the receiver operations and hardware problems, and in providing much information about the receiver that was not easily accessible. D. Fang and D. V. Rogers provided useful reference material. G. Hyde showed considerable interest in this work and offered useful comments. K. Yeh and her colleagues reduced, rechecked, and made computer runs for most of the data. Thanks are also due to L. Pollack for his uninterrupted support of this work.

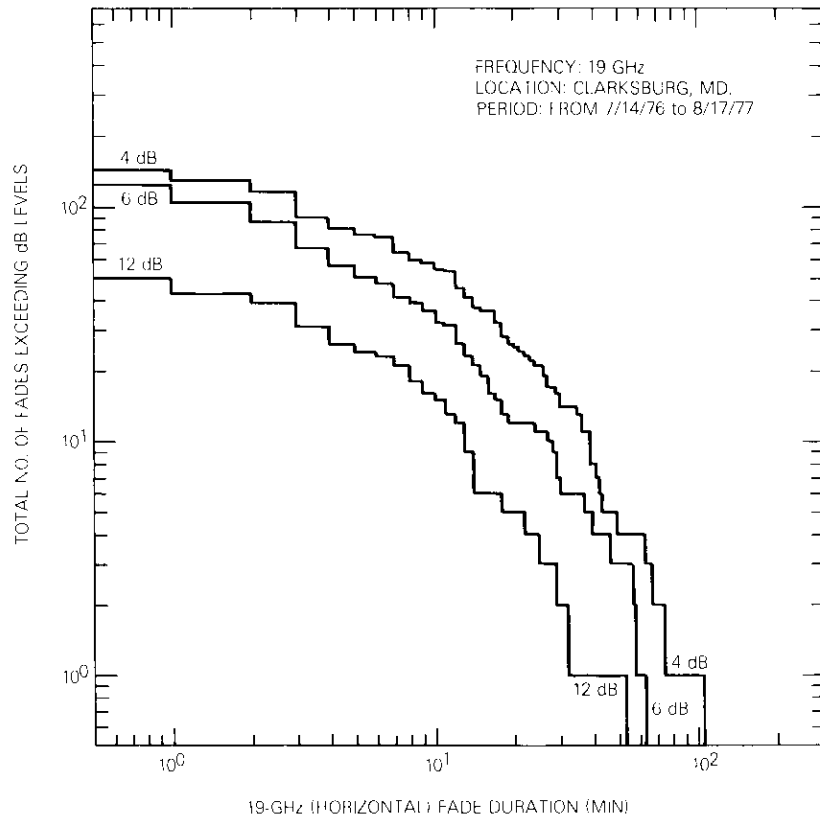


Figure 10c. *Fade Duration of Excess Rain Attenuation at 19 GHz (Horizontal Polarization)*

## References

- [1] H. W. Arnold et al., "Rain Attenuation Statistics from a 19- and 28-GHz COMSTAR Beacon Propagation Experiment: One-Year Cumulative Distributions and Relationships Between the Two Frequencies," *IEEE Transactions on Communications*, Vol. COM-27, No. 11, November 1979, pp. 1725-1728.
- [2] J. M. Harris and G. Hyde, "Preliminary Results of COMSTAR 19/29-GHz Beacon Measurement at Clarksburg, Maryland," *COMSAT Technical Review*, Vol. 7, No. 2, Fall 1977, pp. 599-624.

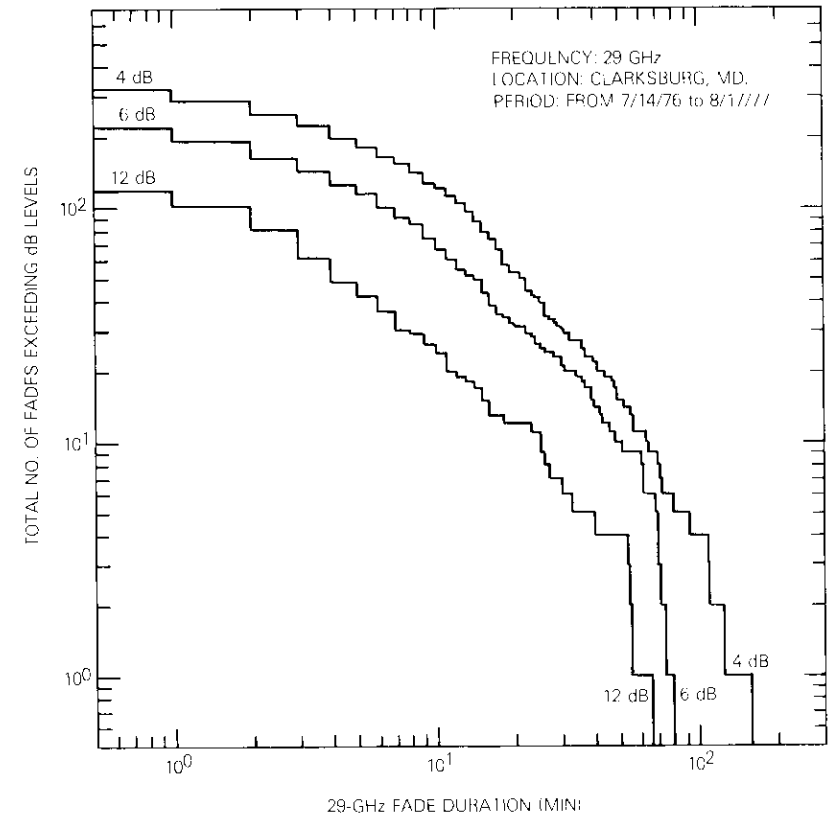


Figure 10d. *Fade Duration of Excess Rain Attenuation at 29 GHz*

- [3] F. Tseng and G. Hyde, "Frequency Scaling of Attenuation Above 10 GHz," *EASCON '78 Record*, September 1978, pp. 396-403.
- [4] D. C. Hogg and T. Chu, "The Role of Rain in Satellite Communications," *Proceedings of the IEEE*, Vol. 63, September 1975, pp. 1308-1331.
- [5] T. Oguchi, "Attenuation and Phase Rotation of Radio Waves Due to Rain; Calculations at 19.3 and 34.8 GHz," *Radio Science*, Vol. 8, No. 1, 1973, pp. 31-38.
- [6] L. J. Ippolito, "Effects of Precipitation on 15.3- and 31.65-GHz Earth-Satellite Transmissions with ATS-5 Satellite," *Proceedings of the IEEE*, Vol. 59, 1971, pp. 189-205.

- [7] L. J. Ippolito, "ATS-6 Millimeter Wave Propagation and Communications Experiments at 20 and 30 GHz," *IEEE Transactions on Aerospace and Electronic Systems*, Vol. AES-11, November 1975, pp. 1067-1082.
- [8] J. Goldhirsh and I. Katz, "Useful Experimental Results for Earth-Satellite Rain Attenuation Modeling," *IEEE Transactions on Antennas and Propagation*. Vol. AP-27, 1979, pp. 413-415.
- [9] D. D. Tang, D. Davidson, and S. Bloch, "Tampa Triad, 19-GHz Rainy Season Diversity Results and Implications for Satellite Communications System Design," International Conference on Communications, June 8-12, 1980, Seattle, WA, *Conference Record*, Vol. 1, pp. 40.4.1-40.4.5.
- [10] D. D. Tang, D. Davidson, and S. Bloch, "Diversity Reception of a 19-GHz Satellite Beacon Signal During Intense Rainy Periods in Florida," IEE Second International Conference on Antennas and Propagation, University of York, York, U.K., April 1981, pp. 124-128.
- [11] O. G. Nackoney, "CTS 11.7 GHz Propagation Measurements—Third Year's Data and Final Report," TR 79-471.3, October 1979, GTE Labs, Waltham, Mass.
- [12] L. J. Ippolito, "Radio Propagation for Space Communications Systems," *Proceedings of the IEEE*, Vol. 69, No. 6, June 1981, pp. 697-727.
- [13] R. K. Cranc, "Prediction of Effects of Rain on Satellite Communications Systems," *Proceedings of the IEEE*, Vol. 65, March 1977, pp. 456-474.
- [14] D. J. Fang and J. M. Harris, "Precipitation Attenuation Studies Based on Measurements of ATS-6 20/30 GHz Beacon Signals at Clarksburg, Maryland," *IEEE Transactions on Antennas and Propagation*, Vol. AP-27, No. 1, January 1979, pp. 1-11.
- [15] J. Goldhirsh, "Multiyear Slant-Path Fade Statistics at 28.56 GHz for Wallops Island, Virginia," *IEEE Transactions on Antennas and Propagation*, Vol. AP-28, No. 6, November 1980, pp. 934-941.
- [16] E. J. Dutton and H. T. Dougherty, "Year-to-Year Variability of Rainfall for Microwave Applications in the U.S.A.," *IEEE Transactions on Communications*, Vol. COM-27, No. 5, May 1979, pp. 829-832.
- [17] L. Pollack, "Centimeter Wave Beacons for the COMSTAR Satellites," *COMSAT Technical Review*, Vol. 7, No. 1, Spring 1977, pp. 103-108.
- [18] A. F. Standing, "The COMSTAR Beacon Receiver," *COMSAT Technical Review*, Vol. 8, No. 1, Spring 1978, pp. 187-203.
- [19] P. L. Rice and N. R. Holmberg, "Cumulative Time Statistics of Surface-Point Rainfall Rates," *IEEE Transactions on Communications*, Vol. COM-21, October 1973, pp. 1131-1136.
- [20] H. W. Arnold, D. C. Cox, and A. T. Rustako, "Rain Attenuation at 10-30 GHz Along Earth Space Paths: Elevation Angle, Frequency, Seasonal, and Diurnal Effects," *IEEE Transactions on Communications*, Vol. COM-29, No. 5, May 1981, pp. 716-721.
- [21] R. L. Olsen, D. V. Rogers, and D. B. Hodge, "The  $aR^b$  Relation in the Calculation of Rain Attenuation," *IEEE Transactions on Antennas and Propagation*, Vol. AP-26, No. 2, March 1978, pp. 318-329.
- [22] International Radio Consultative Committee (CCIR), "Propagation Data Required for Space Telecommunications Systems," Report 564-1, *Documents of the XIVth Plenary Assembly*, Kyoto, 1978, Vol. V.
- [23] J. Goldhirsh, "Prediction Methods for Rain Attenuation Statistics at Variable Path Angles and Carrier Frequencies Between 13 and 100 GHz," *IEEE Transactions on Antennas and Propagation*, Vol. AP-23, No. 6, November 1975, pp. 786-791.
- [24] G. Brussaard, "Prediction of Attenuation Due to Rainfall on Earth-Space Links," *Radio Science*, Vol. 16, No. 5, September-October 1981, pp. 745-760.
- [25] G. Brussaard, "Attenuation Due to Rain on a Slant Path," *Alta Frequenza*, Vol. XVI, No. 4, April 1979, pp. 104E-108E.

Prabha N. Kumar received a B.S. and an M.S. from Bangalore University, India, in 1968 and 1970, and a Ph.D. in Applied Physics from Southern Illinois University in 1973. From 1970 to 1972 she was a Senior Research Fellow in Modulated Surface Wave Structures at the Microwave Laboratory of the Indian Institute of Science, Bangalore. She was with Computer Sciences Corporation between 1977 and 1979, where she worked on laser reflector arrays. Dr. Kumar joined COMSAT Laboratories in 1979. Her present research centers on the effects of precipitation on satellite signals for frequencies greater than 10 GHz, and on a laser optical rain gauge. Dr. Kumar received the NASA recognition award for her work on laser reflectors in 1981. She is a member of IEEE.



## ***Satellite switching center for SS-TDMA communications***

F. ASSAL, R. GUPTA, J. APPLE, AND A. LOPATIN

(Manuscript received August 10, 1981)

### ***Abstract***

This paper describes the design and development of an  $8 \times 8$  satellite switching center (SSC) for satellite switched time-division multiple-access (SS-TDMA) operation at 6 GHz (up-link) and/or 4 GHz (down-link). The SSC consists of a light-weight broadband crossbar microwave switch matrix (MSM) and a distribution control unit (DCU). Wideband Wilkinson power dividers/combiners and low-power-consuming resistively matched PIN diode switches have been developed to provide highly flexible interconnect possibilities that are nearly communications transparent in the 3.5- to 6.5-GHz frequency range. The DCU consists of a micro-processor-based design for the telemetry and command interface subsystem, and custom-designed LSI chips to control and drive the microwave switches. Broadband push-pull connectors are used to simplify assembly and disassembly of the modular SSC. Each switching module, which contains 8-PIN diode switches, has been provided with a separate switch control electronics circuit and dual memory. Design considerations and performance characteristics of the SSC are presented.

### ***Introduction***

SS-TDMA [1] involves the rapid and cyclic interconnection of up-link beams of a multiple beam satellite to the respective down-link beams. The resulting SS-TDMA frequency reuses within the existing spectrum

allocations increase satellite utilization efficiency significantly in comparison to conventional multiplexing, modulation, and multiple-access schemes. To increase the communications capacity of the INTELSAT-VI satellites, for instance, six frequency-reuse beams will be included for the SS-TDMA transmission of two 120-Mbps QPSK channels per beam.

In addition to the multibeam antenna, the principal on-board element of an SS-TDMA system is the SSC, which consists of an MSM, a DCU, and a time-base generator (TBG) [2], [3]. The MSM routes communications traffic by cyclically connecting the required microwave input-to-output ports. The DCU controls the states of the microwave switches, and receives and stores the control data from a reference earth station via the telemetry, tracking, and command (TT&C) subsystem. The TBG provides accurate frame and frame unit reference timing information to the DCU and the MSM. The SSC achieves the desired rapid and cyclic interconnectivity among the beams, thus allowing TDMA bursts transmitted in one up-link beam to be routed to all other down-link beams, as dictated by traffic requirements.

This paper presents the design of a broadband SSC developed at COMSAT Laboratories. The 3.5- to 6.5-GHz bandwidth characteristics of the SSC provide a single design for all the channelized bands in the 6-GHz up-link and/or 4-GHz down-link bands. This SSC may be used as a broadband IF on-board switching center for 6/4-, 14/11-, and/or 30/20-GHz SS-TDMA satellites. A photograph of the MSM and control electronics assembly of the SSC is shown in Figure 1.

### SSC operation

This section provides a brief introduction to the SSC, as well as a cursory description of SS-TDMA operation [1]-[4].

Figure 2 illustrates the operation of an on-board switch matrix. The system [5] includes only three stations redrawn for illustrative purposes on either side of the satellite to separate the up- and down-link transmission paths. In this representation, the primary reference station (E/S #1) synchronizes the transmission of its reference bursts with respect to SSC switch states. These bursts may also contain communications data. Each terminal, including the standby reference station, organizes its burst transmission so that bursts to each destination occupy discrete time positions with respect to the designated reference burst; each earth station adjusts the timing of its transmissions by viewing its own loopback burst in the TDMA frame. The bursts must be properly timed to avoid overlapping at the satellite and to permit the SSC to route up-link bursts to

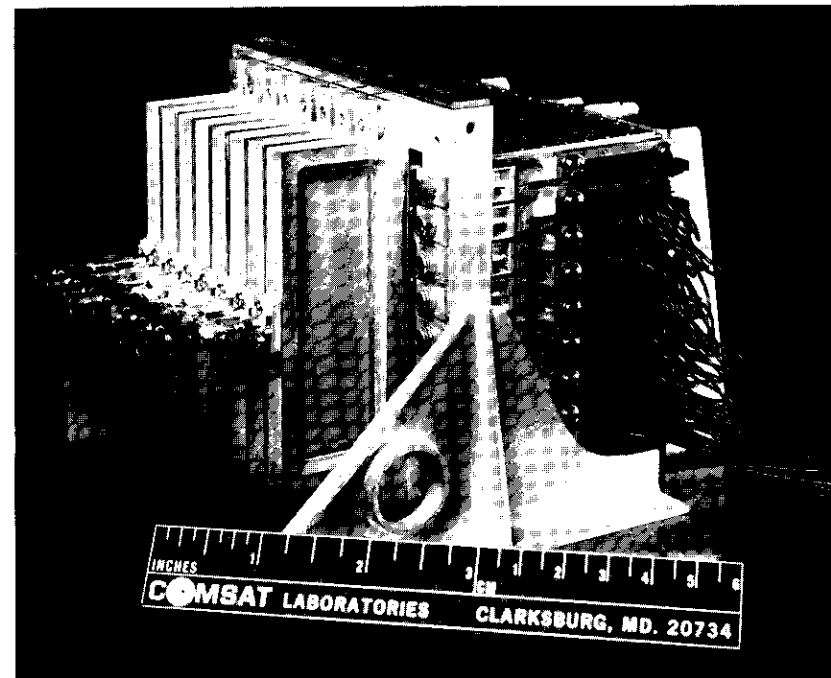


Figure 1. Microwave Switch Matrix and Control Electronics Assembly

appropriate down-link destinations by using a sequence of programmed switching states. In Figure 2, each of the bursts to each destination is designated by a different pattern. For example, black bursts are destined to E/S #1, whereas those designated by cross-hatch or dot patterns are destined to E/S #2 and #3, respectively. Inserts at the bottom of the figure show how the SSC routes the traffic bursts.

To accommodate several stations located within the same beam, a number of bursts of varying durations may be transmitted to the satellite within each switching state. Furthermore, to maximize overall satellite capacity, it may be necessary to repeat, in each frame period, some of the same interconnections (or switching states) among the up- and down-links. Sinha [6], Ito et al. [7], and Inukai [8] have formulated algorithms for selecting and scheduling these states, and have estimated the number of switching states necessary to accommodate traffic requirements. Inukai has shown that the upper bound for the number of switching states among  $N$  beams is  $N^2 - 2N + 2$ . The duration of the switching states, in particular the shortest frame interval, depends on the transmission rates

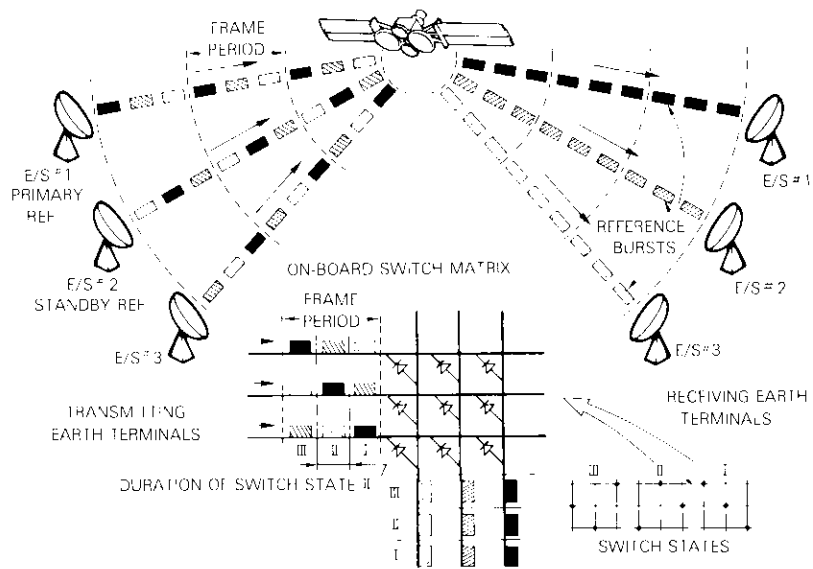


Figure 2. Operation of the Satellite Switching Center (SSC)

to the satellite, the duration of the periodic frame, and the overhead loss due to TDMA guard spaces and satellite switching times. To ensure maximum switch pattern flexibility, a number of selectable frame unit increments per frame period should be included in DCU design.

Figure 3 is a simplified block diagram of an SS-TDMA satellite for six frequency reuse beams. The data controlling the programmable cyclic switching states are transmitted for storage in the off-line memory of the DCU via the TT&C subsystem. The off-line memory is always available for switch state information update for SSC control, while a DCU on-line memory actively controls the MSM. The new switch-state information is implemented by exchanging the roles of on-line and off-line memories. Data transfer, data verification commands, and other telemetered information are routed via the TT&C subsystem. Time base control, if necessary, can be derived from an on-board regenerator or from periodic ground command via the TT&C subsystem [9]. Figure 4 is a more generalized block diagram of a frequency reuse satellite. In this representation, the available bandwidth in each spot beam is channelized, and a number of switching planes may be used in various channels to carry the SS-TDMA communications traffic.

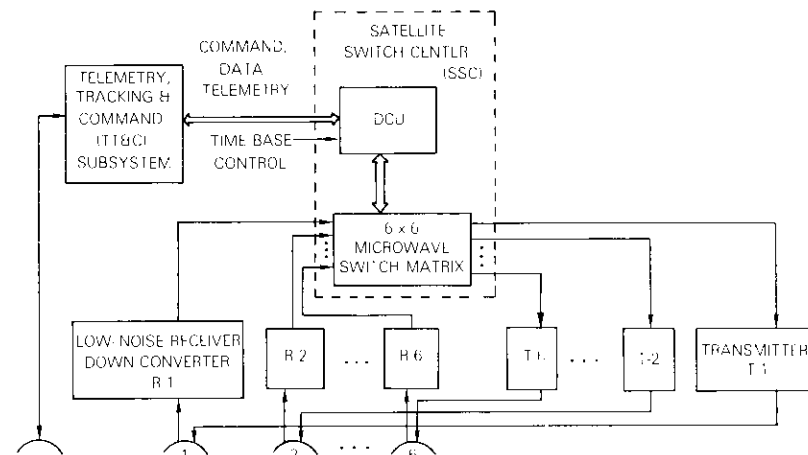


Figure 3. Simplified Block Diagram of an SS-TDMA Satellite

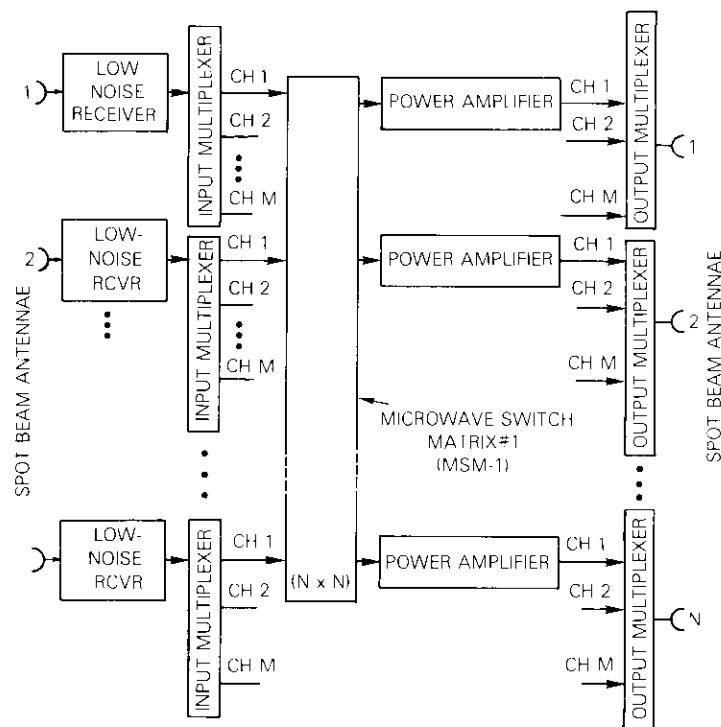


Figure 4. Block Diagram of a Frequency Reuse Satellite

### SSC description

A crossbar configuration of a fully redundant  $6 \times 6$  SSC is shown in Figure 5. It consists of an MSM, a DCU, and MSM redundancy networks. The MSM consists of eight input and eight output distribution networks interconnected via a set of  $8 \times 8$  microwave switching elements. Redundant paths are provided via an array of 64 switching elements to serve a set of six frequency reuse beams.

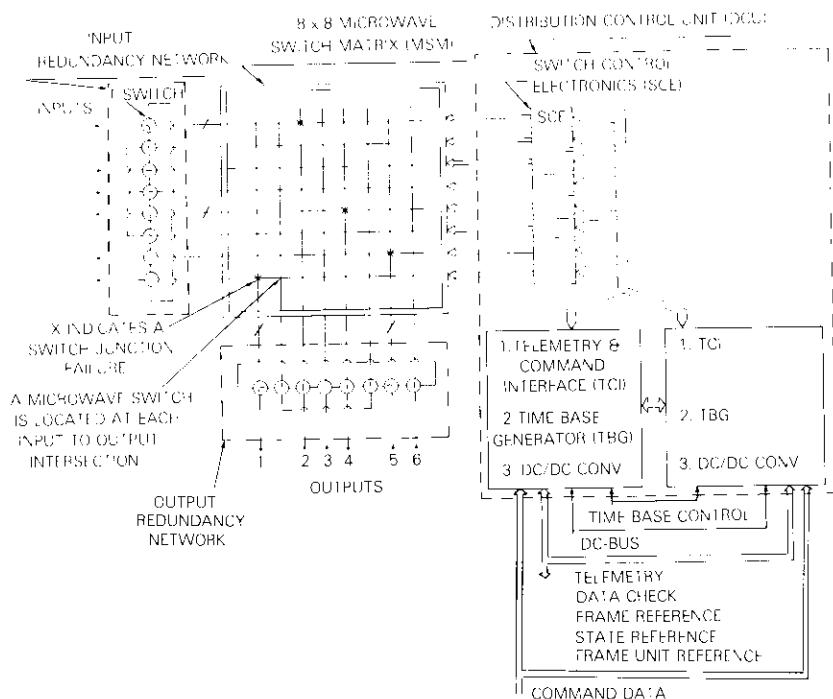


Figure 5.  $6 \times 6$  SSC for SS-TDMA Satellite

The DCU may be a single unit or may be partitioned as indicated in Figure 5. In this design, the switch control electronics (SCE) of the DCU are integrated within each microwave input distribution (horizontal line) network to control and drive all the eight microwave switches associated with a particular input. The telemetry and command interface (TCI) section of the DCU contains all functions common to the SCE and interfaces with the TT&C subsystem. For the design of the TBG, a long term

clock drift no greater than one part in  $10^{11}$  is required for plesiochronous operation with the terrestrial system. Since the on-board clock may drift as much as one part in  $10^6$  over satellite lifetime, clock correction schemes will be required [10]. Redundant TCI/TBG sections and DC/DC converter subsystems with cross-strapped interconnections may be provided to enhance the overall reliability of this interface. The performance objectives listed in Table 1 were established for the SSC design.

TABLE 1. SSC PERFORMANCE CHARACTERISTICS

Array Size	$8 \times 8$
Bandwidth (instantaneous)	3.5 to 6.5 GHz
Insertion Loss of Any On-Path	$\leq 23$ dB
Insertion Loss Variation (any 500 MHz)	$\leq 1$ dB
Path-to-Path Insertion Loss Variation (500 MHz)	$\leq 1.7$ dB
On-to-Off Isolation	$\geq 50$ dB
Group-Delay Variation (any 500 MHz)	$\leq 0.5$ ns
Phase Linearity ( $P_{out} \leq -15$ dBm)	$< 3^\circ$
Amplitude Linearity (C/I) for Two Equal-Amplitude Tones ( $P_{out} \leq -15$ dBm)	$\geq 45$ dB
Frame Units per Frame	250 or 500 (selectable)
Length of Frame Unit	15, 30, 60, or 120 $\mu$ s (selectable)
Frame Period	3.25 to 60 ms (selectable)
Rise or Fall Time	$\leq 60$ ns
Differential Delay	$\pm 2.5$ ns (max)
Timing Jitter	$\pm 5$ ns (max)
Connectivity	Any $N$ to any $M$
MSM Mass	2.95 kg
MSM Volume	$15 \times 16 \times 11$ cm <sup>3</sup>
Power Consumption	$< 7.5$ W

The MSM redundancy network consists of two sets of eight electro-mechanical T-switches that are connected to form two redundancy rings [11], [12]. In Figure 5, redundancy rerouting via the T-switches is indicated for four assumed switch junction failures. This network topology significantly enhances overall SSC reliability by providing a maximum of rerouting alternatives.

### MSM design

The MSM may be implemented in cellular [13], rearrangeable [14], [15], or crossbar configurations. An analysis of these architectures (see Ap-

pendix A) indicates that the crossbar switch matrix configuration is the most desirable for SS-TDMA applications, and, therefore, it was adopted for this design. Crossbar MSMs [16], [17] have been designed to operate at 4 GHz with a 500-MHz instantaneous bandwidth. The design features of a 3.5- to 6.5-GHz bandwidth, 8 × 8 crossbar MSM will now be presented.

The major building blocks of the 8 × 8 MSM are the eight input and eight output frame modules. Each input frame module consists of an 8-way divider, eight PIN diode switches, and an SCE assembly. Each output frame module consists of an 8-way divider/combiner network. These input and output frame modules are assembled on a central frame via wideband, push-pull, microwave connectors to form a 3-dimensional structure. The orientation of these modules is arranged so that all eight connectors at the output of each divider/switch module are interconnected with one input of each output combiner module. The on states of the PIN diode switches establish the interconnections between an input port and various output ports of the MSM. The switch states of each input shelf are dynamically controlled from the SCE, which provides the proper current bias to the eight PIN diode switches via eight feedthrough connectors in each input frame module. These modules are designed to provide mechanical rigidity to the MSM structure and heat sink capability to the SCE. The modular configuration of the MSM has proved to be particularly convenient during testing, troubleshooting, and replacement of components before and after assembly of the matrix.

The 3.5- to 6.5-GHz broadband performance of the 8-way divider is obtained by designing a 2-way, and two 4-way Wilkinson dividers [18] with multistep cascaded line lengths and interconnecting resistors [19]. To satisfy the physical layout requirement, the 2- and 4-way Wilkinson dividers were designed with four and six sections, respectively. In addition, a 50Ω transmission line is included between each arm of the 2-way divider and the input to each 4-way divider to adjust the physical separations of the output ports.

The physical layout of an 8-way divider/combiner and the element values for transmission lines and resistors are included in Figure 6. Some of the resistors were specifically designed to be open circuits to simplify physical layout and yet achieve the desired bandwidth response. Figure 7 is a photograph of an 8-way divider corresponding to the output assembly of the MSM; its transmission loss, return loss, and output port-to-port isolation characteristics over the 3.5- to 6.5-GHz band are presented in Figure 8. All dividers in the MSM had path-to-path insertion loss variations less than 0.4 dB, path-to-path isolation greater than 18 dB, and input return loss better than 13 dB over the 3.5- to 6.5-GHz band.

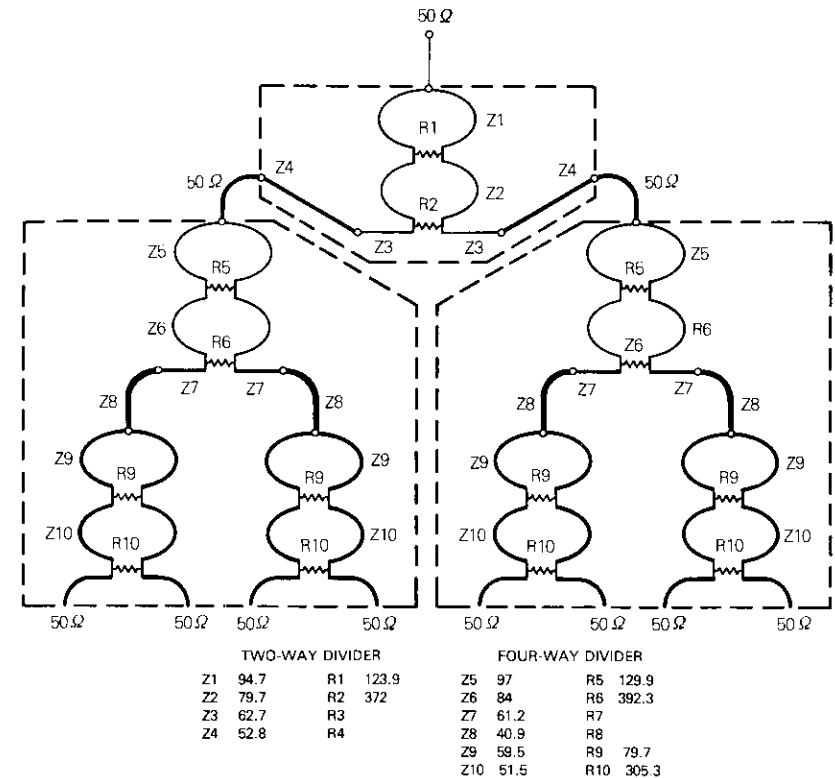


Figure 6. Broadband 8-Way Wilkinson Divider

To improve MSM electrical performance, a resistively matched PIN diode switch [20] was designed to provide good impedance matching across the desired frequency band for both of its switching states. To meet the desired isolation requirements, previously designed PIN diode switches [16], [17] used only two PIN diodes and reflected most of the incident RF power when the diodes were forward biased (RF off state). In this case, the MSM isolation and path-to-path insertion loss variations suffer considerable degradation, particularly when broadband operation is required. To overcome this mismatch, the switch configuration shown in Figure 9, which required four PIN diodes separated by quarter wavelength transformers in the circuit, was designed.

In the RF off state (forward bias), all four diodes are in low impedance (effective short circuit) states and only the 50Ω resistors in the end net-

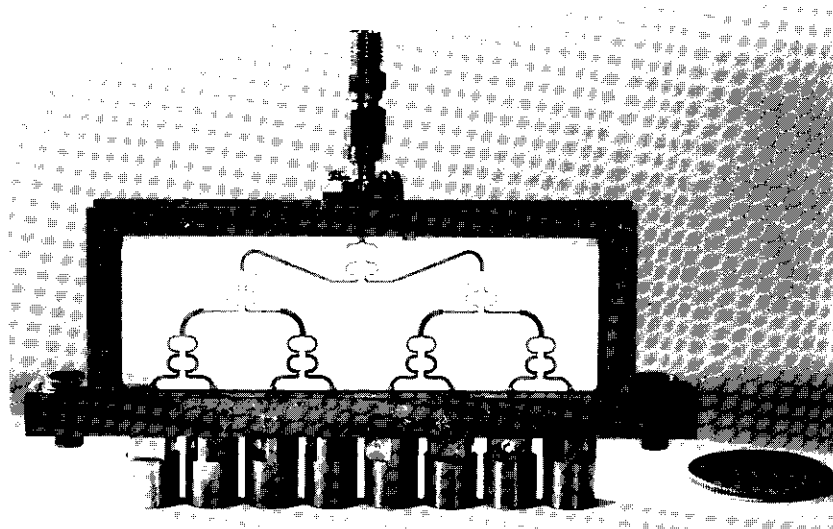


Figure 7. 8-Way Divider in Output Frame

works are seen as the input and output ports of the switch. The short circuit resulting from biasing the central diodes is transformed through quarter wavelength transformers into open circuits across the 50Ω impedances at the input and output ports. Short-circuited quarter-wave high impedance transmission lines are added across 50Ω resistors to bypass the DC current of the switch and hence reduce the power dissipation. In the RF on state, all the PIN diodes are open circuited; therefore, only 50Ω transmission paths are seen at the input and output of the switch element. The transmission, isolation, and return loss performance characteristics over 3.5- to 6.5-GHz frequency bands for a typical switch are shown in Figure 10. The insertion loss increases gradually from 1.4 dB at 3.5 GHz to 2.6 dB at 6.5 GHz, the return loss is better than 15 dB in the RF on state, and an off-state isolation greater than 50 dB is achieved across the 3-GHz bandwidth.

All the PIN diodes were carefully selected so that they had similar DC and RF characteristics. All 64 switches integrated in the input shelves of the MSM display less than 0.2-dB peak-to-peak scatter of their insertion loss characteristics at any frequency in the 3.5- to 6.5-GHz range. A typical input shelf assembly is shown in Figure 11 and its measured RF performance characteristics are shown in Figure 12. Each input shelf assembly has path-to-path insertion loss scatter less than 0.5 dB at any

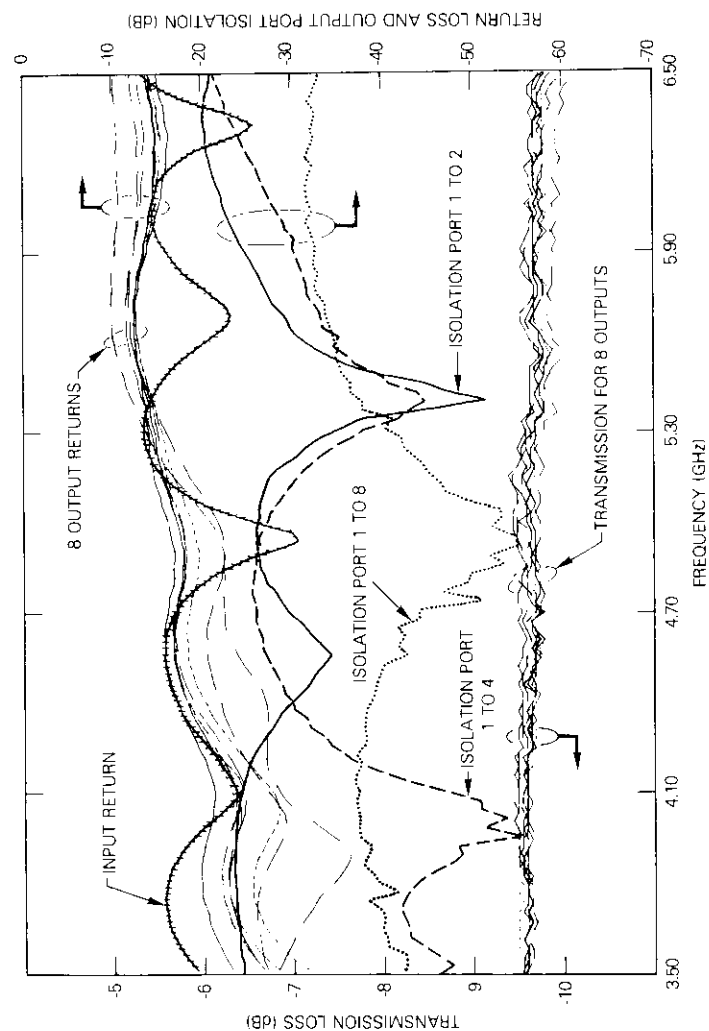


Figure 8. Performance of a Typical 8-Way Divider in Output Frame

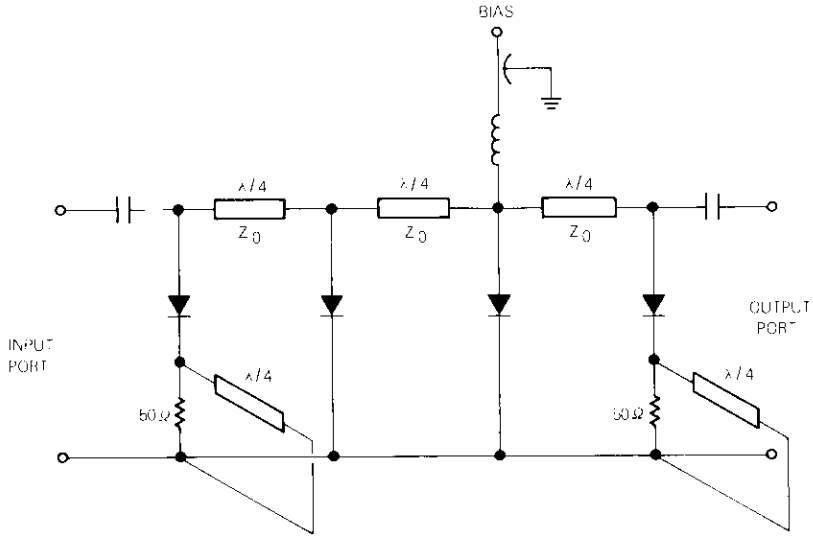


Figure 9. Broadband Resistively Matched Microwave PIN-Diode Switch

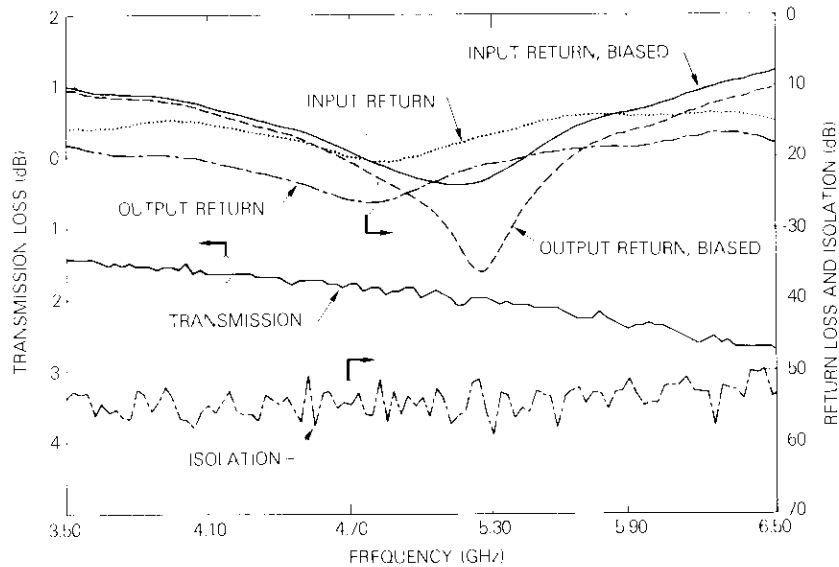


Figure 10. Performance of a Typical PIN-Diode Switch

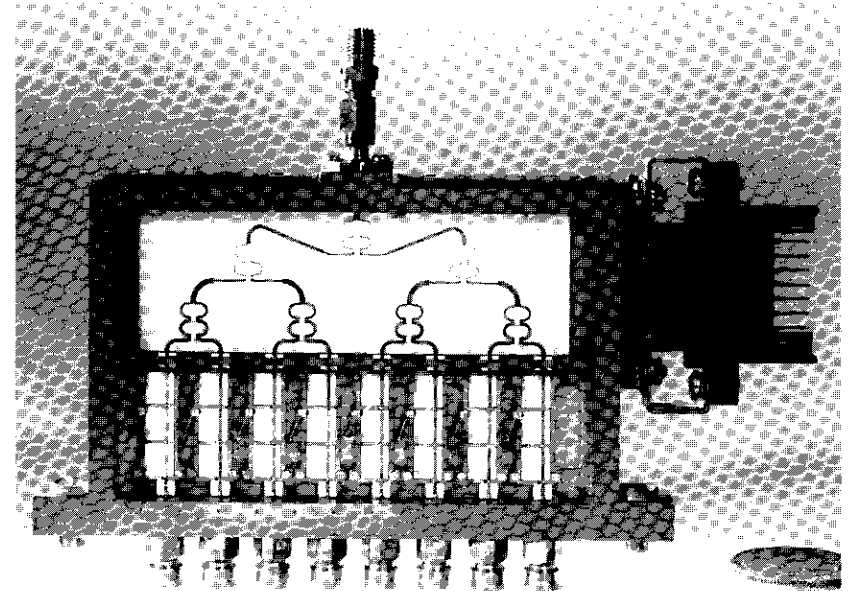


Figure 11. PIN-Diode Switches and 8-Way Divider in Input Frame

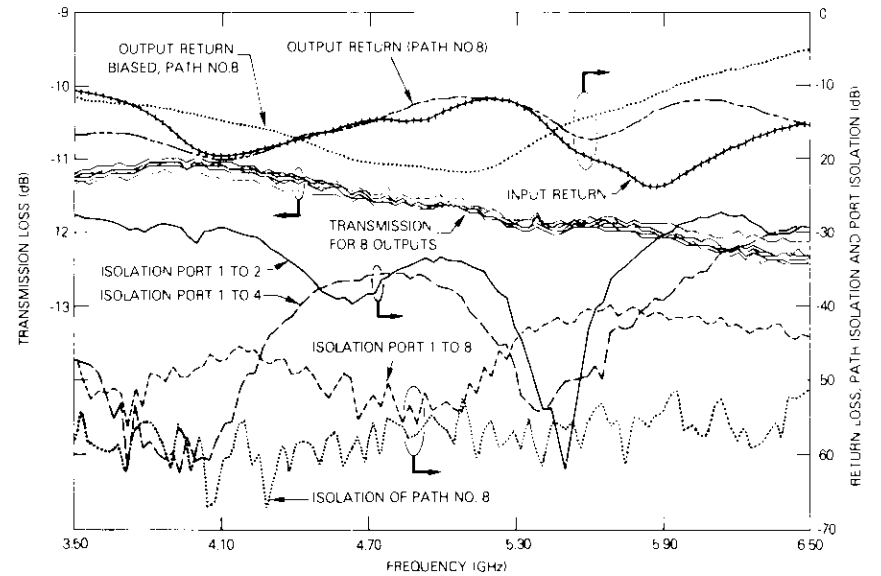


Figure 12. Performance of a Typical Input Shelf

frequency in the 3.5- to 6.5-GHz frequency band, and an insertion loss slope less than 1.5 dB over the 3-GHz MSM bandwidth.

The MSM has been designed to meet all electrical and environmental requirements. Its mechanical configuration can withstand vibration levels normally encountered in spacecraft. Stress relief has been provided at all critical interconnections susceptible to failure during vibration tests [21]. The input and output frame modules of the MSM have been designed so that all of their longitudinal natural resonance frequency modes are in excess of 200 Hz. Kovar has been used for the support frames because its coefficient of thermal expansion is nearly the same as that of alumina substrates used for microwave integration. Since Kovar is a relatively poor conductor, it has been gold plated for MIC work. Aluminum heat sinks, provided for the SCE circuits in each input shelf, also provide a ground return for the SCE. MSM mass has been reduced considerably by fabricating hollow channels for the MSM support structure without sacrificing mechanical rigidity.

### DCU functions and design

The primary function of the DCU is to provide the MSM with control signals corresponding to the sequence of switch states. Each state represents a particular interconnection configuration of the MSM, and the total sequence of states defines an SS-TDMA frame. While states may be variable in duration, each state duration must contain an integral number of frame units where a frame unit is the smallest period for which a particular switch configuration is allowed to exist.

DCUs have been developed from hybrid combinations of commercially available logic circuits and MOS/LSI devices [22], and PMOS/LSI technology [23]. The DCU in the SSC described in this paper consists of a micro-processor-based design for the telemetry and command interface (TCI), and custom-designed LSI chips to control and drive the microwave switches. Figure 13 is a block diagram of the complete DCU. The memory circuits of the DCU are sufficiently large to store the switch states of the MSM for cyclic implementation, and to allow any input to be connected to any one or a number of outputs (point-to-point or point-to-multipoint interconnections). On-line and off-line memories are provided to change the MSM control switching patterns without affecting the dynamic operation of the SSC. New control data may be written to the off-line memory and after ground verification via TT&C subsystem; off-line and on-line memories can be interchanged on command so that the new switch

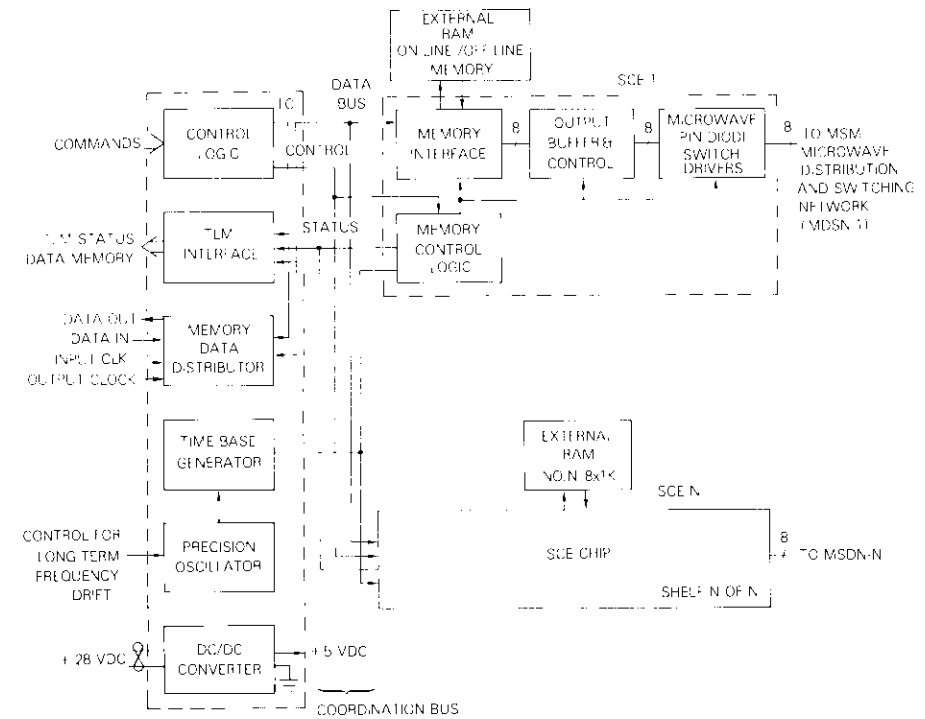


Figure 13. Simplified Block Diagram of the DCU

patterns may take control of the MSM. A maximum of 500 frame units per frame with a minimum frame unit duration of  $15 \mu\text{s}$  are available. Since all eight switches in each input shelf of the MSM are independently controlled, a memory size of 8 kbits per shelf is required. The memory is accessed serially with an access time of at most 900 ns.

The DCU is of the partitioned type, consisting of a TCI and SCE for eight individual MSM shelves (Figure 13). The TCI provides DCU reference control timing, collects shelf status signals for the spacecraft telemetry, and performs all interfacing functions between the SCE of the DCU and the TT&C subsystem of the spacecraft (Figure 14). Each SCE contains all timing regeneration, memory control and bus interface functions, memory circuits and PIN-diode switch drivers necessary for control and operation of the shelf. All MSM shelves have been identified by unique addresses and connected by an 8-line system coordination bus. Thus, the bulky cables in previously developed DCUs have been eliminated with the

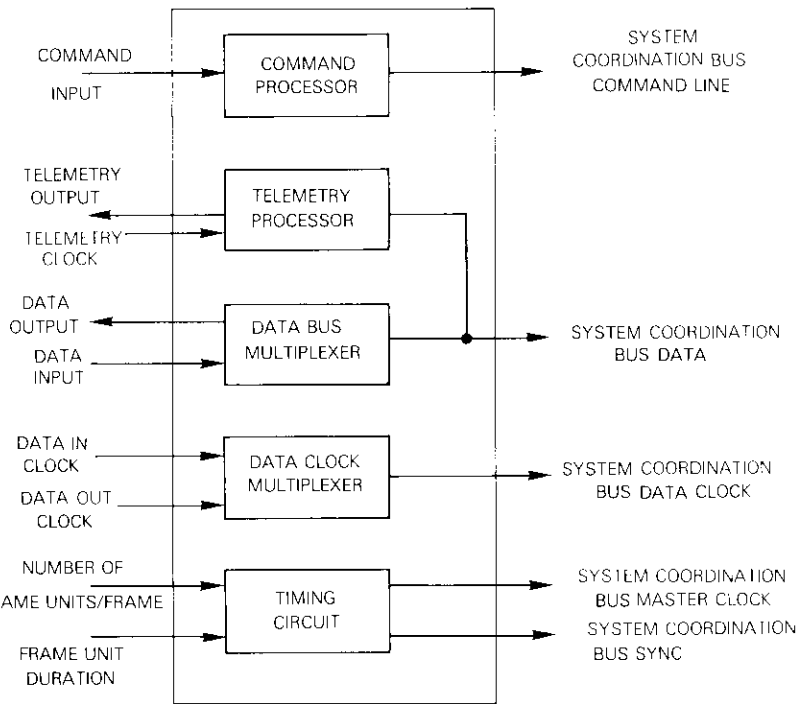


Figure 14. TCI Block Diagram

advantages of reduced mass and simplified assembly, and/or replacement of faulty modules.

**Telemetry and command interface**

The TCI controls DCU timing and synchronization and provides access to the DCU from the spacecraft's TT&C subsystem through four ports: command, telemetry, data input, and data output. The TCI interfaces with the shelves via five of the system coordination bus lines listed in Table 2. The remaining system coordination bus wires carry DC power and ground connections for the shelves. All TCI timing functions are derived from a reference 5.33-MHz oscillator.

The TCI is implemented with an RCA 1802 microprocessor using 2 kbytes of random access memory (RAM), and 1 kbyte of programmable read only memory (PROM). Status data and program variables are stored in the RAM while the TCI operating firmware is implemented in the

TABLE 2. COORDINATION BUS TCI SIGNALS

Command Bus	Carries serial command data to shelves for execution.
Master Clock Bus	A system timing signal having a frequency 16 times the frame unit rate.
Synchronization Bus	A timing signal having a period of one frame. It synchronizes shelf counters and establishes clock phases within the shelves.
Data Bus	A bidirectional data bus that carries memory addresses, data, and status information between the TCI and shelves.
Read/Write Clock	A clock derived from the TT&C subsystem, data read, and data write clocks that sequences data transfers on the data bus.

PROM. All timing and synchronization functions are carried out by complementary metal oxide semiconductor (CMOS) and low-power transistor transistor logic (LPTTL). A hardware block diagram is shown in Figure 15.

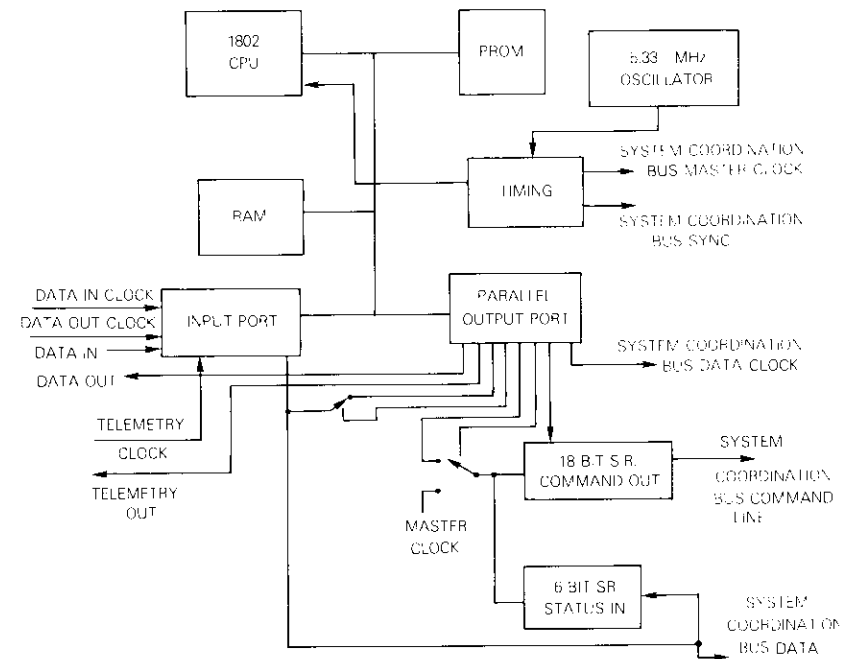


Figure 15. TCI Hardware Block Diagram

The logical functions implemented in the 1802 microprocessor transfer command, status, and memory data within the DCU, and between the DCU and TT&C subsystems. These functions are command receiving and distribution, status collection and transmission, and data transfers for MSM state control. Each of these functions will be described in the following subsections.

#### **Command processing**

The command processing function of the TCI consists of accepting serial commands from the TT&C interface, decoding them for possible data transfer operations, and forwarding them to the command bus line of the system coordination bus. For data transfer commands, the command processing function of the TCI configures its data bus multiplexer and read/write clock multiplexer to the appropriate state for the type of transfer that is about to occur. In the case of commands not involving data transfer, the command processing function requires only that the command received be forwarded to the SCE for execution.

In the absence of TT&C subsystem generated commands, the TCI autonomously generates no operation (NOP) commands to each of the SCE circuits for collecting status information.

#### **Status collection and transmission**

Collection of SCE and TCI telemetry data is accomplished by the telemetry processor function in cooperation with the command processor function. SCE status bits are generated by each MSM shelf each time a valid command is received. These six bits express pertinent conditions of the SCE, and are important for operation and for detection of failures. Further details on status bit definitions can be found in the SCE description. Because of the small number of lines available on the system coordination bus, a system of polling has been used whereby the TCI sequentially requests from each shelf its status bits of information. These status bits are stored in RAM of the TCI from which the TT&C subsystems can access them. The status bits are transmitted from each SCE to the TCI along the data bus line of the system coordination bus during the interval immediately following command transmission. The TCI command processing function automatically issues NOP commands for status collection whenever TT&C subsystem command actions are not occurring. This permits regular status updates to the RAM in the TCI. The TCI prefixes the shelf status bits sent to the telemetry encoder by 24 status bits of its own, expressing the contents of its command register, and other condition signals.

#### **Data transfer function**

The data transfer function of the TCI involves control of both data and read/write clock multiplexers, and block counters in the TCI. Depending on the command action required, the data multiplexer is configured to pass data and clock signals either to or from the SCEs on the data and read/write bus lines, respectively. Status data from the commanded SCE are received on the data bus before the same is configured for data transfer, and during the interval of data transfer no status polling is performed by the TCI. Reception of another command terminates any data transfer sequence in progress.

#### **Switch control electronics**

The SCE controls each shelf by cyclically applying 8-bit codes to the shelf's control inputs, which directly drive the microwave PIN diodes. A synchronization pattern (sync word code) is implemented during each cycle to ensure that each node of the communications network is synchronized to the beginning of the SS-TDMA frame.

The SCE microcircuit (Figure 16) interfaces the TCI circuit via the system coordination bus, which consists of the command bus, data bus, the data clock, the master clock, the sync signal, and three power supply voltages.

The SCE interfaces the MSM PIN diode switches through PIN diode drivers. Six hardwired inputs form a particular shelf address, which is used by the SCE's command processor to identify the commands addressed to it. A single input line is provided to determine the length of the sync word. Depending upon the state of this input, the sync word will be output for 5/8 of a frame unit or an entire frame unit. Two external memories store the duplicate cyclic patterns which control the configuration of the PIN diode switches.

The SCE microcircuit provides four modes of operation: normal, data transfer, memory select, and shelf off.

#### **Normal mode**

The timing circuits, which control the operational sequence of the SCE, generate the three clock signals (see Figure 17). The clocks throughout the DCU are synchronized by the sync signal from the system coordination bus, which ensures that the clock phases and counters of all the SCEs are aligned. The period of the sync signal is a function of frame length and frame unit rate. The memory bit clock increments the on-line and off-line memory counters located in the memory control and timing unit. The

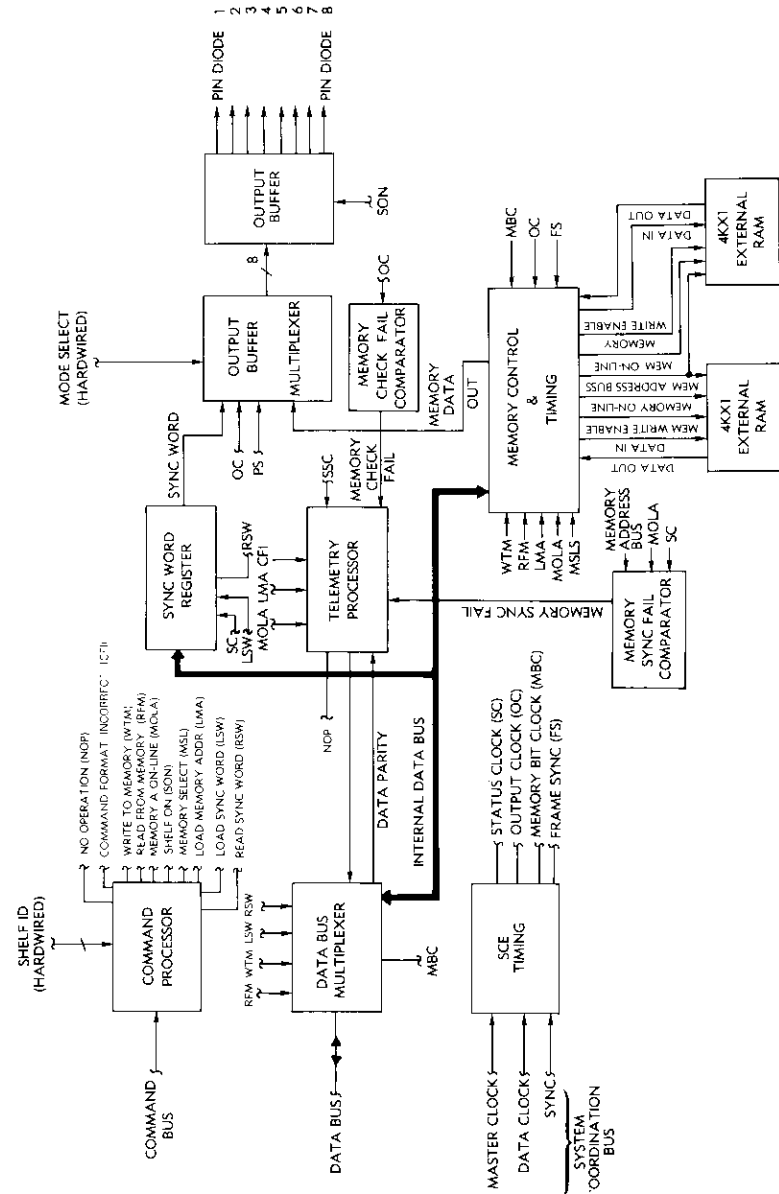


Figure 16. Shelf Control Electronics Block Diagram

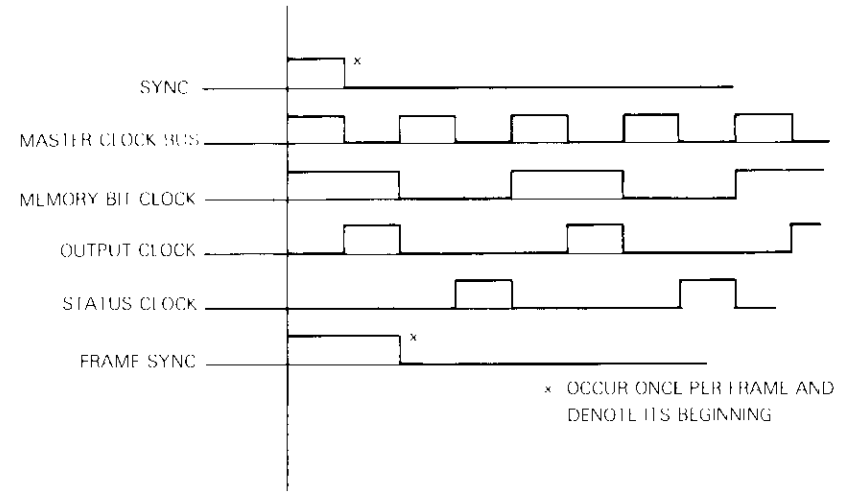


Figure 17. SCE Circuit Clock Timing Relationships

status clock transfers the status bits into the telemetry processor. The output clock transfers the memory data from the on-line memory into the output buffer multiplexer.

After both on-line and off-line memories have been loaded with the desired data pattern, they are synchronized with each other by the frame sync signal. During the one state of the memory bit clock, the on-line memory data bit at the memory address designated by the on-line memory counter is output from the memory and transferred into the input stage of the output data shift register by the output clock. The output of the first stage of this register is applied to one input of the memory check-fail comparator.

During the zero state of the memory bit clock, the data bit stored in the equivalent memory address in the off-line memory is output to the memory check-fail comparator. Since the data bits applied to the memory check-fail comparator represent the same bit in identical memory locations, the memory check-fail comparator should indicate an equality. The status clock transfers the condition of the memory check-fail comparator to the SCE's telemetry processor.

This process is repeated until a complete serial data word has been converted to a parallel word by the output buffer multiplexer. The data word is then parallel transferred to the PIN diode drivers, where it is signal con-

ditioned by the output buffer and is directly applied to the PIN diodes of the MSM input shelf.

Since the command processor receives no operation commands in the normal mode of operation, the telemetry processor collects the internal status bits of the SCE and transmits them to the TCI circuit via the data line of the system coordination bus for storage and eventual transmission to the ground command center. The following status bits are transmitted to the TCI:

- a. *Parity*: indicates the parity of the data (if any) transferred on the data bus during the last command.
- b. *Memory Sync Fail*: indicates that the counters for the off-line and on-line memory are not synchronized, preventing valid switch pattern comparison.
- c. *Memory Check Fail*: indicates that the on-line and off-line memory contents differ by at least one bit.
- d. *AOL*: indicates that memory A is currently assigned as the on-line memory, and memory B is the off-line memory.
- e. *LMA*: indicates that the SCE has just executed a load memory address command, and is expecting a read or write command.
- f. *Command Format "Incorrect"*: indicates that the command was not properly received.

When both memories are synchronized, both memory counters output the identical address data. Should the synchronism between the two counters be lost, the counters will be resynchronized by the frame sync signal. This approach limits the loss of synchronism to one frame.

The on-line and off-line counter outputs are compared during each memory clock cycle by the memory sync fail comparator. The status clock transmits the status of this comparison to the telemetry processor for transmission to the TCI circuit.

The output is updated continuously per frame unit except for the state which occurs during frame sync period. During the sync word period initiated by the frame sync signal, a predetermined code is output from the sync word register to the PIN diode driver via the output buffer multiplexer. This code identifies the starting point within the frame and uniquely identifies each matrix within the system. When the sync word period elapses, the data stored in the on-line memory are output to the PIN diode driver via the output buffer multiplexer.

#### **Data transfer mode**

The data transfer mode of operation consists of transferring data, either

from the off-line memory (read) or to the off-line memory (write), in single 8-bit bytes or blocks of bytes. The only difference between a read command and a write command is the direction of the bidirectional data bus and the memory control logic. While the memory control section is responding to a read or write command, the remainder of the SCE microcircuit operates in its normal mode of operation.

When either a write or read command is decoded by the command processor, status information is no longer transmitted by the telemetry processor, the off-line memory counter is reset, and its clock input is transferred from the internal memory bit clock to the external data clock input. When the data clock is received from the TCI circuit, the off-line memory counter begins incrementing at the data clock rate.

Because it is necessary to continue to drive the microwave switch matrix from the on-line memory during each memory address increment, the off-line memory must be synchronized with the operation of the on-line memory. After the off-line data bit is transferred, no further data are transferred until the next data clock. The process continues until the command is terminated by the command processor.

If the read command is active, the internal data bus is transferred to its output state, which connects the output of the off-line memory to the external data bus. Memory data are transferred from the off-line memory to the data interface during the first zero state of the memory bit clock, which occurs during the one state of the data clock. No further data are transferred until the leading edge of the next data clock is detected.

If the write command is active, the internal data bus is transferred to its input state, which connects the input of the off-line memory to the external data bus. Memory data are written into the off-line memory by the logical combination of the output clock and the write enable strobe from the command processor.

There is a secondary form of data transfer between the SCE microcircuit and the TCI circuit known as the block move, which transfers single bytes of memory or a number of bytes of memory data. When the block move mode of data transfer is implemented, the off-line memory counter is preset to the desired memory address by loading the address into the counter from the external data bus via the load memory address command from the command processor. Data are then transferred between the SCE microcircuit and the TCI circuit, as determined by the next data transfer command received by the command processor. Data will continue to be transferred during the occurrence of each successive data clock until the active data transfer command is terminated by a new command. Any command can be terminated by another valid command.

### Memory select mode

The design of the DCU provides for instantaneous transition from one switching pattern to another. Selection of memory A or B as on-line or off-line memory is achieved by the use of either the A or B on-line commands followed by the memory select command. The memory select command synchronizes the memory interchange so that all shelves respond simultaneously.

### Shelf off mode

In the case of internal failures within the RAMs or some other section of the SCE or an external failure, it may be necessary to turn off each individual shelf. This is achieved by issuing a shelf off command which turns off the microwave PIN diode driver. The shelf can be turned on again by issuing a shelf on command.

### DCU implementation

The DCU was implemented as two different assemblies: the first assembly, which contains all of the functions common to the MSM and is located externally to it, consists of the TCI unit, the reference oscillator, and the power supply unit. The second assembly, which consists of the SCE MOS/LSI microcircuit and two 4 kbit  $\times$  1 RAMs, is located within each input shelf of the MSM. Each SCE MOS/LSI microcircuit contains all of the control functions for the 8-PIN diode switches located within each input shelf (Figure 18).

The TCI unit, which controls the operation of each SCE MOS/LSI microcircuit, is connected to each input shelf of the MSM via an 8-conductor cable which connects each input in parallel from shelf 1 through shelf N (in this system  $N = 8$ ). The 8-conductor cable carries all command and data transfer lines, clock lines, and power supply voltages required by the SCE MOS/LSI microcircuit, its output driver circuit, and the two 4 kbit  $\times$  1 RAMs.

One of the concerns for flight qualification of the developed SSC is the radiation tolerance of SCE microcircuits, the 4 kbit RAMs, and the 1802 microprocessor [21]. Radiation testing of NMOS circuits, which is the technology employed in the fabrication of the SCE and RAM microcircuits, indicates a wide variation in radiation resistance between different manufacturers of identical circuits, and even between lots of the same manufacturer. Tests performed on 1802 microprocessors produced with a modified process showed failure at  $5 \times 10^5$  rads (Si) [24]. The DCU LSI

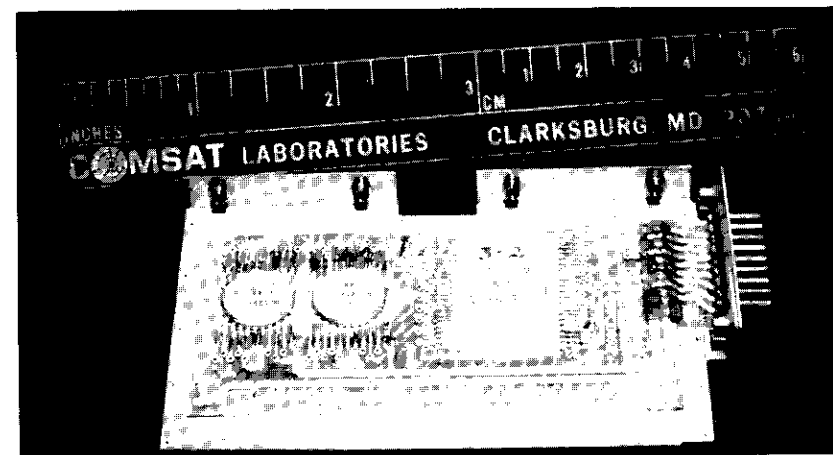


Figure 18. Switch Control Electronics Circuit Assembly

chips must have a radiation tolerance exceeding  $4 \times 10^3$  rads (Si) for survival in a 7-year spacecraft mission with aluminum shield thickness greater than 10 mm. Radiation hardness of the LSI chips will be determined by radiation tests.

### Test results

The MSM and DCU were extensively tested before final integration into the SSC. The measured insertion loss characteristics of all 64 paths of the MSM are shown in Figure 19. These are grouped as eight sets of curves, each corresponding to one input port and all eight outputs. The SCE microcircuits were successfully tested for logic functions over a temperature range from  $0^\circ$  to  $55^\circ\text{C}$  and for different frequencies of the system clock. The measured rise and fall times of the RF envelope at the output of PIN diode switches under the control of SCE are shown in Figure 20. These transition times are less than 60 ns. The measured electrical performance characteristics of the SSC indicate that the performance objectives listed in Table 1 are being met.

### Reliability considerations

The most critical requirement in the design of an SSC for SS-TDMA applications is the reliability of the interconnections that must be pro-

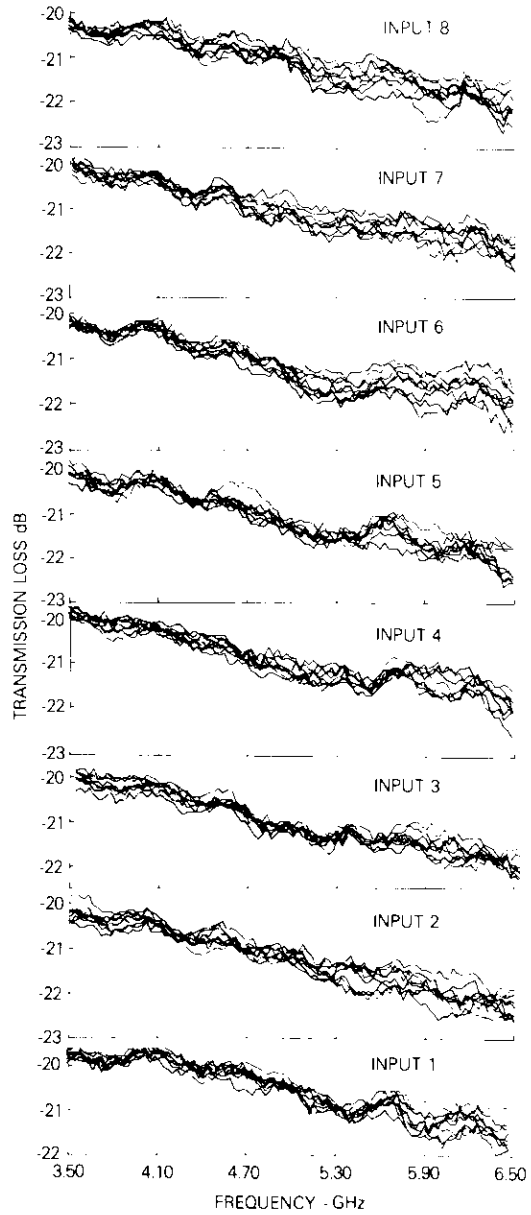


Figure 19. Measured MSM Insertion Loss for all 64 Transmission Paths (all 8 paths are measured for each input connection)

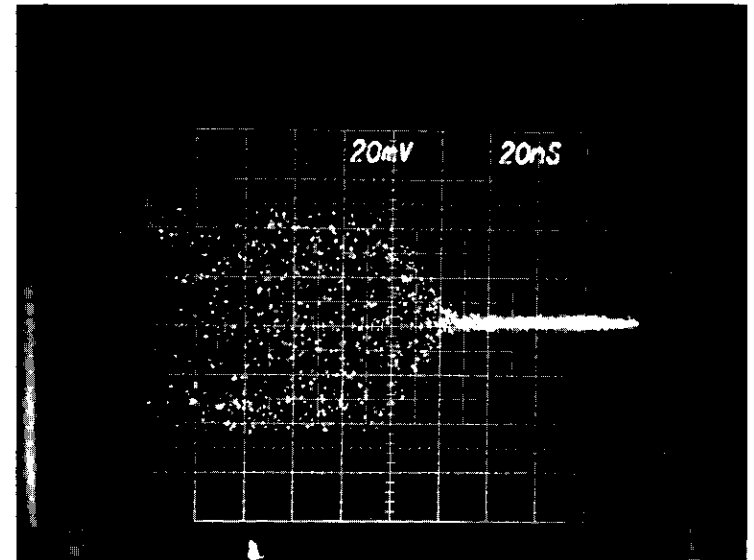
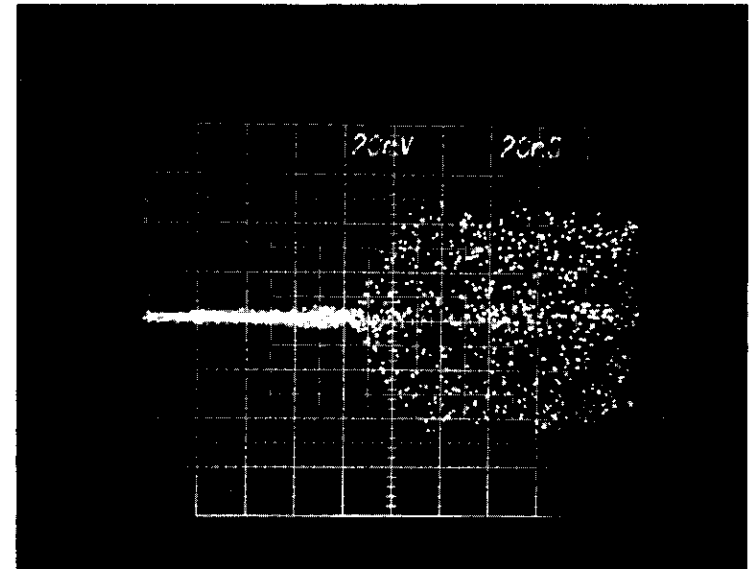


Figure 20. Rise and Fall Times of RF Envelope of the Microwave Switch Matrix

vided during the specified satellite lifetime (7 to 10 years). Extra switch junctions in the MSM configuration and redundancy networks to accommodate any switch junction failures may be required. Failures may occur due to vibrations during deployment of the spacecraft or random failures of the active devices within the switches. Various redundancy configurations for a representative  $6 \times 6$  switch matrix, which include functionally redundant paths, were investigated for reliability (see Appendix B). An examination of computed reliability characteristics for these configurations indicates that a ring-redundancy configuration offers superior reliability. At least three types of switches may be used with this highly flexible configuration: double-pole double-throw (DPDT), R-, and T-switches. Electromechanical latching type DPDT- and R-switches are commercially available and T-switches have been developed. Since T-switches maximize the number of alternate redundant paths that may be selected to correct for switch junction failures, they are preferred. In general, functional path redundancy may be provided at the MSM inputs and outputs to permit  $(M - N)$  and  $(K - N)$  failures in an  $M \times K$  matrix. Therefore, the  $8 \times 8$  MSM developed at COMSAT Laboratories may be configured to produce a fully redundant  $6 \times 6$  SSC as shown in Figure 5, with enhanced reliability.

### Conclusions

The design, development, and fabrication of a broadband  $8 \times 8$  satellite switching center has been presented. This SSC is physically compact, rugged, and easily reproducible. To simplify testing, troubleshooting, and component replacement, a modular approach easily assembled and disassembled via broadband push-pull connectors was chosen. MOS/LSI implementation of the SCE microcircuits, flatpack packaging of the LSI chips and RAMS, and their mounting on a multilayer printed circuit board further reduced SSC size. The microprocessor implementation of the TCI provides additional flexibility and compatibility with future spacecraft requiring only simple software modifications.

The input-to-output beam interconnections are easily and rapidly (less than 60 ns) achieved in a highly flexible manner. Any of the inputs could be connected to any or all of the outputs. Identification and location of a fault or failure are very simple in this crossbar configuration, and rerouting is easily achieved via a ring redundancy network.

### Acknowledgments

The authors wish to acknowledge the efforts of K. Betaharon and A. Zaghoul in the development of the MSM, H. Gerson for its mechanical design, J. Kasser, A. Ramos and J. Dunnington in the development of the DCU, and J. Popper and K. Shah of Standard Micro Systems Corp. (SMC) for fabrication of the custom SCE microcircuits. They wish to thank Peggy Cline and M. Urcuyo for fabrication and testing of the MSM and E. Hare for testing of the DCU. Encouragement provided by L. Pollack, A. Berman, and S. J. Campanella is gratefully acknowledged.

### References

- [1] W. G. Schmidt, "An On-Board Switched Multiple-Access System for Millimeter Wave Satellites," *Proc. of the INTELSAT/IEE International Conference on Digital Satellite Communications*, November 1969, London, pp. 399-467.
- [2] F. Assal et al., "Wideband Microwave Switch Matrix for SS-TDMA Systems," *Proc. of the 5th International Conference on Digital Satellite Communications*, Genoa, Italy, March 1981.
- [3] F. Assal, A. Berman, R. Gupta, "Satellite Switching Center for SS-TDMA Systems," *International Conference on Communications*, Denver, June 1981, pp. 5.1.1-5.1.8.
- [4] S. J. Campanella and R. Colby, "Network Control for TDMA and SS-TDMA in Multiple Beam Satellite Systems," *Fifth International Conference on Digital Satellite Communications*, Genoa, Italy, March 23-26, 1981.
- [5] S. J. Campanella, F. Assal, and A. Berman, "Onboard Communications Processing Technology," *XXVII Convegno Internazionale delle Comunicazioni*, Genoa, Italy, October 7-10, 1980, *Proc.*, pp. 243-251.
- [6] A. K. Sinha, "A Model for TDMA Burst Assignment and Scheduling," *COMSAT Technical Review*, Vol. 6, No. 2, Fall 1976, pp. 219-251.
- [7] Y. Ito, Y. Urano, and T. Muratani, "Analysis of a Switch Matrix for an SS/TDMA System," *IEEE Proceedings*, Vol. 65, March 1977, pp. 411-419.
- [8] T. Inukai, "An Efficient SS/TDMA Time Slot Assignment Algorithm," *IEEE Transactions on Communications*, COM-27, No. 10, October 1979, pp. 1449-1455.
- [9] S. J. Campanella and T. Inukai, "SS-TDMA Frame Synchronization," *International Conference on Communications*, Denver, June 1981, pp. 5.5.1-5.5.7.
- [10] T. Inukai and S. J. Campanella, "Onboard Clock Correction for SS/TDMA and Baseband Processing Satellites," *COMSAT Technical Review*, Vol. 11, No. 1, Spring 1981, pp. 77-102.

- [11] F. Assal, C. Mahle and A. Berman, "Network Topologies to Enhance the Reliability of Communications Satellites," *COMSAT Technical Review*, Vol. 6, No. 2, Fall 1976, pp. 309-322.
- [12] F. Assal, C. Mahle, and A. Berman, U.S. Patent No. 4,070,637, January 24, 1978.
- [13] W. H. Kautz, K. N. Levitt, and A. Waksman, "Cellular Interconnection Arrays," *IEEE Transactions on Computers*, C-17, No. 5, May 1968.
- [14] Y. Ito and M. Kyogoku, "SDMA On-Board Switching System Using Rearrangeable Multi-Stage Network," International Conference on Satellite Communications Systems Technology, April 1975, London, pp. 227-232.
- [15] A. Waksman, "A Permutation Network," *Journal of the Association for Computing Machinery*, Vol. 15, No. 1, January 1968.
- [16] X. Rozec and F. Assal, "Microwave Switch Matrix for Communications Satellites," *Proc. of the International Conference on Communications*, Vol. 3, June 1976, pp. 35.13-35.17.
- [17] F. Assal and X. Rozec, "Fast Fully-Redundant, 4 GHz,  $8 \times 8$  Microwave Switch Matrix for Communications Satellites," *Proc. of the 9th European Microwave Conference*, September 1979, pp. 216-222.
- [18] E. J. Wilkinson, "An N-Way Hybrid Power Divider," *IRE Transactions on Microwave Theory and Techniques*, January 1960, pp. 116-119.
- [19] S. B. Cohn, "A Class of Broadband Three-Port TEM Mode Hybrids," *IEEE Transactions on Microwave Theory and Techniques*, MTT-16, No. 2, February 1968, pp. 110-116.
- [20] F. Assal, A. Berman, and K. Betaharon, Resistively Matched Microwave PIN Diode Switch, U.S. Patent No. 4,267,538, May 12, 1981.
- [21] R. Gupta and F. Assal, "Integration, Environmental and Radiation Testing of a Microwave Switch Matrix System," International Conference on Communications, Denver, June 1981, pp. 5.4.1-5.4.6.
- [22] D. Boroin and R. Cooperman, "A Distribution Control Unit for Satellite Signal Routing," IEEE Electronics and Aerospace Systems Convention, Washington, D.C., September 29-October 1, 1975, *EASCON '75 Record*, pp. 203A-203E.
- [23] D. P. Dobson and A. E. Ring, "An LSI Controller for Satellite Switches TDMA," International Telemetry Conference, 1976.
- [24] E. King and R. Martin, "Effects of Total Dose Ionizing Radiation on the 1802 Microprocessor," *IEEE Transactions on Nuclear Sciences*, NS-24, No. 6, December 1977, pp. 2171-2176.

### Appendix A. Microwave switch matrix architecture

A number of generic switch matrix configurations were considered for the MSM design:

*a. Cellular configuration.* The configuration of a  $4 \times 4$  cellular switch matrix [13] is shown in Figure A-1. The basic building blocks of this configuration are the six transfer switches, also known as  $\beta$ -elements. The  $\beta$ -

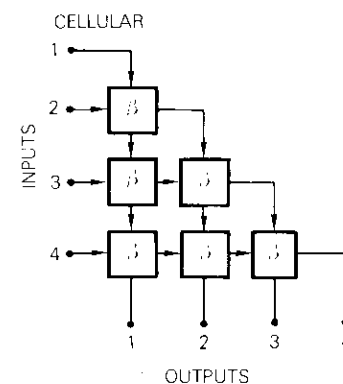


Figure A-1a. Cellular Configuration of a  $4 \times 4$  Switch Matrix

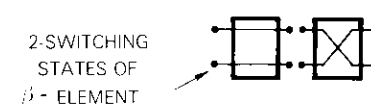


Figure A-1b. Switching States of a  $\beta$ -Element (known also as a C-switch)

elements assume the two states shown in Figure A-1b and can be obtained from four single-pole single-throw (SPST) switches. This basic configuration can be extended to larger arrays by adding the appropriate number of transfer switches to the grid of a right triangle. The algorithm to provide one-to-one path connectivity is relatively easy to program, but broadcast modes are not possible.

*b. Rearrangeable configuration.* The  $4 \times 4$  rearrangeable switch matrix, shown in Figure A-2, consists of five  $\beta$ -elements which are interconnected to provide all of the one-to-one interconnect possibilities between inputs and outputs. Extension to larger matrices may be achieved by using  $4 \times 4$

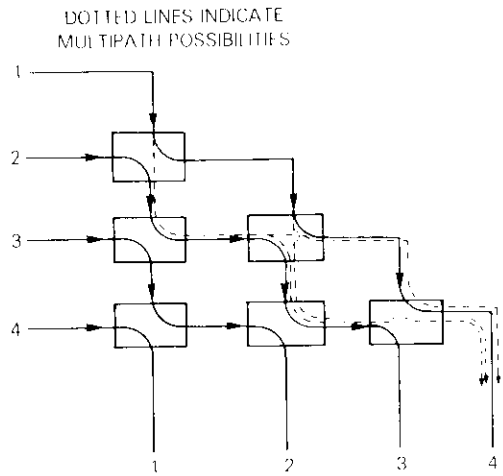


Figure A-1c. Possible Multipath Effects Through the Cellular Matrix

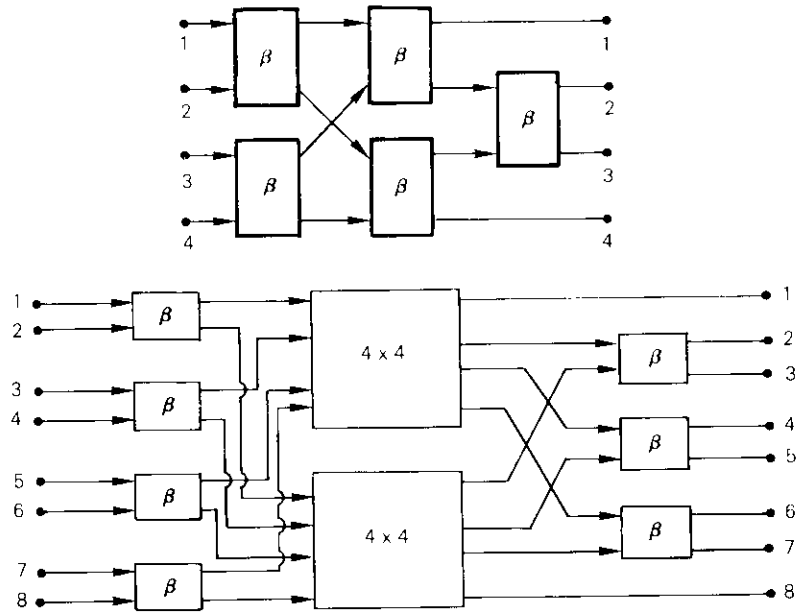


Figure A-2. Rearrangeable Configurations of  $4 \times 4$  and  $8 \times 8$  Matrices Using  $\beta$ -Elements

submatrices and a number of  $\beta$ -elements as building blocks. The  $\beta$ -elements must be connected to each  $4 \times 4$  matrix such that the number of  $\beta$ -elements for each signal path may be equalized. Therefore, the path-to-path insertion loss and transmission delay variations could be made relatively small. In the canonical (minimum elements) form, rearrangeable matrices are of interrupting type; *i.e.*, some interconnections may require rerouting whenever other interconnections in the matrix are altered.

*c. Crossbar configurations.* The configuration of a  $4 \times 4$  crossbar switch matrix is shown in Figure A-3. Crossbar matrices may be designed as lossy or minimum loss networks. In the lossy configuration, each signal input is equally distributed among the  $N$  transmission paths, where  $N$  is the dimen-

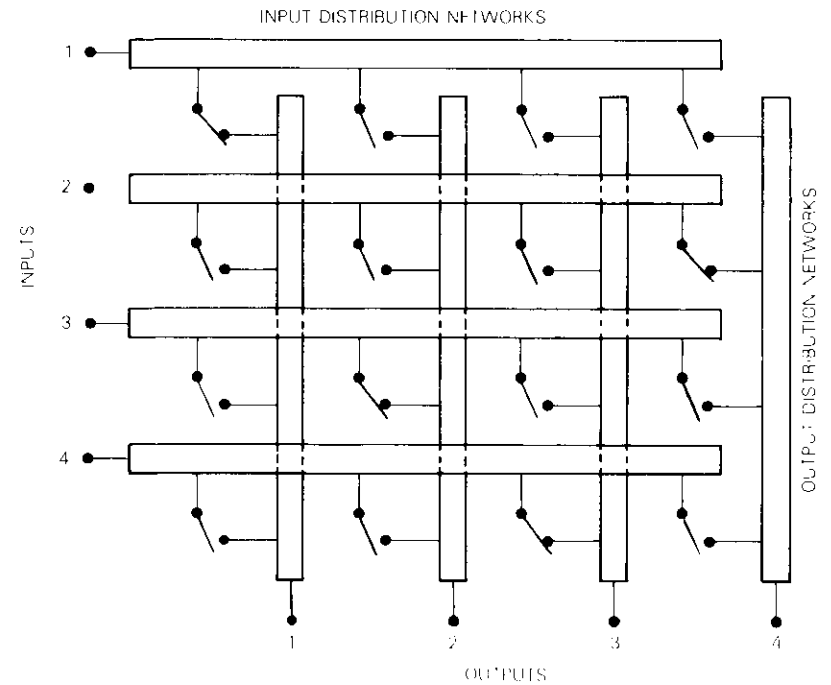


Figure A-3. Crossbar Configuration of a  $4 \times 4$  Microwave Switch Matrix

sion of the square switch matrix array. In the minimum loss configuration, RF power is reflected from all the SPST switches except the one transmitting the RF signal to the designated output port. Because of inherent mismatch reflections, the electrical characteristics such as bandwidth, VSWR, transmission loss, and group delay ripples are expected to be poorer in the minimum-loss crossbar switch matrix. Minimum loss configuration requires double the number of switches required in lossy configuration. Although lossy crossbar matrices have power division and recombination losses, they are preferred because of superior electrical performance characteristics among the two crossbar configurations.

The number of SPST switches required to realize an  $N \times N$  matrix in any of these three configurations is shown in Table A-1. Even though the rearrangeable matrix contains the smallest number of switching elements for  $N \geq 16$ , it is the least desirable MSM configuration. Because the matrix is interruptive, some bursts may have to be unnecessarily and temporarily interrupted to accommodate rerouting through a set of disjoint transmission paths. The input-to-output interconnection algorithm is relatively complicated and the switch junction failure identification necessary to reroute signals through a redundant path of the MSM is difficult and may result in a temporary transmission outage of the SS-TDMA system.

TABLE A-1. MINIMUM NUMBER OF SPST SWITCHES  
REQUIRED BY THE THREE GENERIC SWITCH  
MATRIX CONFIGURATIONS

ARRAY SIZE	(A) CELLULAR	(B) REARRANGEABLE	(C) CROSSBAR
$4 \times 4$	24	20	16
$8 \times 8$	112	68	64
$16 \times 16$	480	196	256
$32 \times 32$	1984	516	1024
$64 \times 64$	8064	1284	4096
$128 \times 128$	32,512	3076	16,384
$N \times N$	$2N(N-1)$	$4(n-1)2^n + 4$ where $N = 2^n$	$N^2$

An  $N \times N$  cellular matrix contains the maximum number of switching elements as compared to either the rearrangeable or the crossbar matrix. Since the signals must pass through a number of  $\beta$ -elements, multipath effects shown in Figure A-1c would be observed in a number of input-to-output connections. Since the  $\beta$ -elements are cascaded in any particular input-to-output path in both the rearrangeable and cellular matrices, the path-to-path insertion loss variations would be critically dependent on the transmission gain or loss of  $\beta$ -elements and their VSWRs. Both of these configurations display relatively narrow bandwidth, impedance mismatches, and larger transmission loss or gain ripple caused by the

reflective type cascaded  $\beta$ -element switches. Only one-to-one interconnections can be provided in these configurations; hence, the use of broadcast mode for possible simultaneous time synchronization and SS-TDMA network control are not possible.

Crossbar matrices are significantly more desirable than either rearrangeable or cellular matrices for SS-TDMA applications, since they are noninterruptive and only one switching junction is used for each connection. Path-to-path interconnection programming is very simple, requiring only drive control to the desired switch junction. A failed switch is easily identified from the ground, and the signal may be rerouted to an alternate redundant path without difficulty. Since more than 50 dB of path-to-path isolation may be obtained in a microwave crossbar matrix, the multipath effect is virtually nonexistent. The problem associated with amplitude/phase nonlinearities is alleviated because all the signal power levels into the switching devices are equal. The lossy crossbar matrix is preferred for SS-TDMA satellite switching centers because one-to-one, broadcast mode, and any  $n$  to any  $m$  connection patterns are possible.

### Appendix B. Redundancy and reliability considerations

Several representative examples of  $6 \times 6$  switch matrix redundancy configurations, shown in Figure B-1, were investigated for reliability. These configurations provide functional path redundancy, which is the most effective method of enhancing the reliability of crossbar switch matrices. In these examples, each redundant configuration consists of a number of redundancy switches and an  $M \times 6$  matrix so that six input paths may be connected to  $M$  input ports of the MSM. For the  $12 \times 6$  MSM configuration with two-for-one, four-for-two, and three-for-two redundancy, the redundancy switches can be reconfigured to select alternate paths in case of failure of a switch junction in any row. If, however, switch junction failures are such that the number of available MSM ports at the output of redundancy switches is less than the number of its inputs, the MSM would be permanently disabled. In comparison, the ring redundancy provides the capability of enhancing the reliability of an  $N \times N$  matrix by allowing switch junction failures in up to any  $(M - N)$  redundant paths.

The computational technique of Assal et al. [9] was used to derive the following equations for computing the reliability characteristics of the redundancy configurations included in Figure B-1:

$$p(6 \times 6) = p_R^6$$

$$p(12 \times 6, 2 \text{ for } 1) = [p_S p_R (1 + q_R)]^6$$

$$p(12 \times 6, 4 \text{ for } 2) = [p_S^2 \{p_R^4 + p_R^3 q_R (2 + 2p_S) + p_R^2 q_R^2 (1 + 4p_S + p_S^2)\}]^3$$

$$p(9 \times 6, 3 \text{ for } 2) = [p_S^2 \{p_R^3 + p_R^2 q_R (1 + 2p_S)\}]^3$$

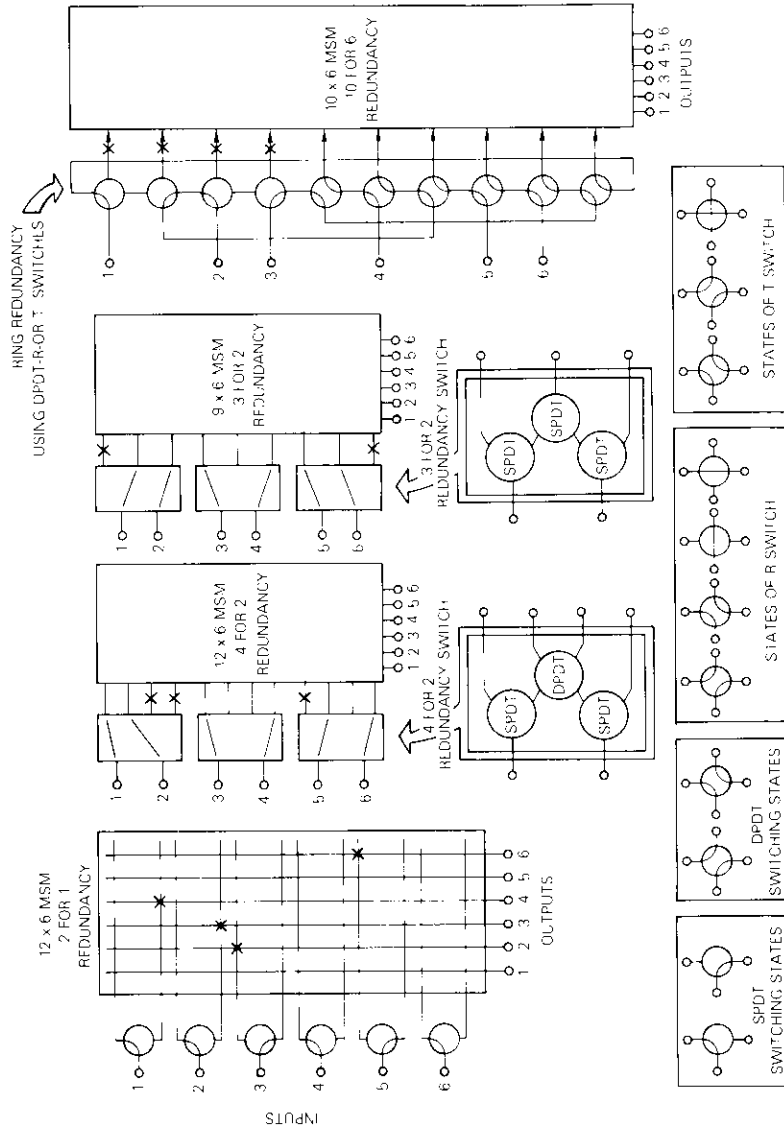


Figure B-1. Representative Redundancy Configurations for a 6 x 6 Microwave Switch Matrix

$$\begin{aligned}
 p(8 \times 6, 8 \text{ for } 6) &= p_S^6 p_R^6 [p_R^2 + p_R q_R (2 + 4p_S + 2p_S^2) \\
 &\quad + q_R^2 (1 + 4p_S + 12p_S^2 + 10p_S^3 + p_S^4)] \\
 p(10 \times 6, 10 \text{ for } 6) &= p_S^6 p_R^6 [p_R^4 + p_R^3 q_R (4 + 6p_S) \\
 &\quad + p_R^2 q_R^2 (6 + 20p_S + 19p_S^2) \\
 &\quad + p_R q_R^3 (4 + 11p_S + 50p_S^2 + 42p_S^3 + 2p_S^4) \\
 &\quad + q_R^4 (1 + 8p_S + 34p_S^2 + 74p_S^3 + 67p_S^4 + 26p_S^5)]
 \end{aligned}$$

where  $p_R = p_j^6 = \exp(-6\lambda_j t)$   
 $q_R = 1 - p_R$   
 $p_S = \exp(-\lambda_S t)$   
 $\lambda_j$  = electronic switch junction failure rate  
 $\lambda_S$  = failure rate per microwave connecting path of the electrochemical switch  
 $t$  = time in hours.

In these computations, it is assumed that the useful life of components exceeds the satellite mission time of 10 years and only random failures with constant failure rate (failures per  $10^9$  hrs, FITS) occur. A switch junction is defined as failed whenever it remains in on or off conditions and its state can no longer be altered. These failures may occur because of failures in active devices, switch driver and control electronics, and/or in any of the interconnections. The T-switch has been assigned a path failure rate rather than a switch failure rate since, if the T-switch is stuck in one position, full interconnectivity can still be provided.

The preceding equations were used to compute reliability for various switch junction failure rate assignments and fixed failure rate per microwave connecting path of the electromechanical switches (10 FITS). The resulting reliability characteristics plotted in Figure B-2 show that the plot for  $10 \times 6$  MSM with ten-for-six ring redundancy remains relatively flat as the switch junction failure rate is increased. The ten-for-six ring redundancy configuration is considered to be superior to all other configurations, and contains fewer electronic switches (60) than the  $12 \times 6$  MSM that displays the closest reliability characteristics.

These results are illustrated for rectangular MSM configurations, but may be generalized to square ( $M \times M$ ) configurations by using double redundancy rings in the input and output ports of the MSM.

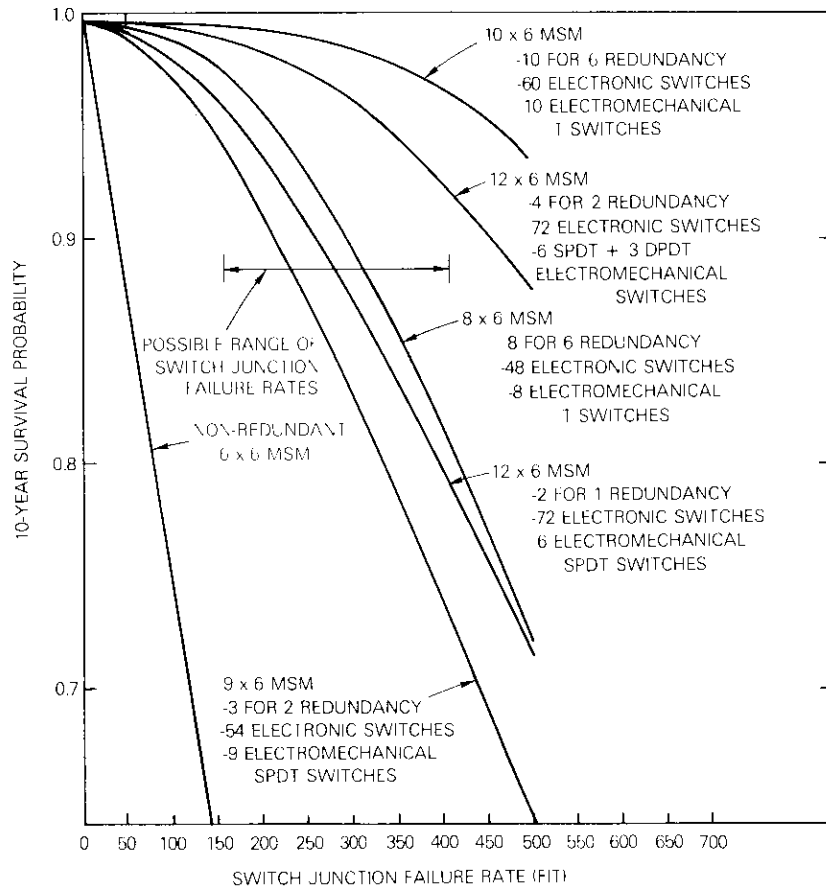


Figure B-2. Ten-Year Probability of Survival of Redundant 6 x 6 Microwave Switch Matrix

Francois T. Assal received a B.E.E. and an M.E.E. from the City College of New York (C.C.N.Y.). Prior to joining COMSAT in 1969, he held a National Science Foundation Traineeship and was a lecturer at C.C.N.Y. Since joining COMSAT, where he is currently Manager of the Microwave Systems Department of the Microwave Technology Division, he has participated in and contributed to earth station and transponder design and utilization to maximize analog and/or digital communications capacity in bandwidth-restricted and power-limited satellite environments. Presently, he is directing COMSAT Laboratories' development of microwave monolithic integrated circuits (MMIC). He is a member of Tau Beta Pi and Eta Kappa Nu.



Ramesh K. Gupta received a B.Sc. (Honors) in electronics and communications engineering from Punjab University, India, in 1974, and an M.Sc and a Ph.D. in electrical engineering from the University of Alberta, Canada, in 1976 and 1980, respectively. Prior to joining COMSAT Laboratories in 1980, Dr. Gupta held an Alberta Government Telephones Centennial Fellowship for research in telecommunications. From 1974 to 1979, he was involved with computer-aided design and modeling of solid-state microwave devices and circuits. Since joining COMSAT as a Member of the Technical Staff, he has been responsible for developing satellite switching technology for SS-TDMA systems, and for designing microwave circuits and subsystems for advanced satellite applications. Dr. Gupta is a member of IEEE.

Joseph H. Apple received a B.S.E.E. from West Virginia University. Currently, he is a Member of the Technical Staff in the Network Control Techniques Department, Communications Technology Division. He is presently engaged in research and development activities for future SS-TDMA satellite communications networks, employing baseband switch matrices, on-board processing, and other communications processing techniques. Prior to joining COMSAT Laboratories in 1976, he was a project engineer responsible for digital controllers for materials handling systems and fare collection systems.





*Andrew J. Lopatin received a combined M.S.E.E./B.S.E.E. with highest honors from Northeastern University in 1975. Since that time he has been a Member of the Technical Staff at COMSAT Laboratories in the Spacecraft Technology Division. His work involves the design, simulation, analysis, and testing of spacecraft electronics. Mr. Lopatin is a member of AIAA.*

Index: antennas

## **RF tests on the Etam Standard C antenna**

R. PRICE

(Manuscript received October 16, 1981)

### **Abstract**

Radiometric measurements on the Etam Standard C antenna are described in this paper. Gain-to-noise temperature ratio (G/T), receive and transmit gain, noise temperature, return loss, and port-to-port isolation were measured, and communication and tracking patterns taken.

Because of the very low spectral flux densities in the 14/11-GHz bands, it was necessary to use radiometric methods for measuring G/T, gain, and temperature. Although in Standard A antennas  $Y$ -factors range between 3 and 6 dB, in Standard C antennas they are only 0.4–0.5dB. Thus, errors and uncertainties, which are negligible in a 6/4-GHz test, become major at 14/11 GHz. This difficulty was overcome at Etam by applying a refinement in switched radiometry, which resulted in the collection of a large amount of useful data.

### **Introduction**

RF characteristics of the new Etam Standard C antenna were measured by the radio star  $Y$ -factor method. This method, generally used with Standard A antennas, presents difficulties at 14 and 11 GHz because of the much lower levels of spectral flux densities available. These difficulties were overcome at Etam by means of a self-balancing gain modulation radiometer.

G/T, receive and transmit gains, low noise amplifier (LNA), system, and

antenna noise temperatures were measured with the radiometer. Voltage standing-wave ratio (VSWR) and port-to-port isolation were measured by standard swept frequency methods; and, finally, receive and transmit patterns were taken, first with the aid of SIRIO, the Italian experimental satellite, and later with an orbiting INTELSAT V and a cooperating ground station.

### **The Etam-3 antenna**

Etam-3 (Figure 1), the first U.S. INTELSAT antenna to operate in the 14/11-GHz frequency bands, is an 18-m linearly polarized, shaped Cassegrain with a corrugated horn beam wave-guide feed, mounted on an elevation-over-azimuth, wheel-and-track pedestal. Autotracking is by monopulse. An identical antenna to provide spatial diversity is under construction at Lenox, West Virginia, some 34 km from Etam.

### **G/T and receive gain**

In the radio star method for measuring G/T, the antenna is pointed at a noise-emitting celestial source having a known flux density, and then moved off the source in azimuth towards the cold sky. The ratio of noise power received under the two conditions is called the Y-factor, from which G/T may be computed directly using the expression [1]:

$$G/T = \frac{8\pi K}{SA^2} (Y - 1) k_1 k_2 k_3 \quad (1)$$

where  $Y$  = ratio of noise power received when the antenna is directed towards the radio star to the noise power received when the antenna is directed towards the cold sky

$K$  = Boltzmann's constant =  $1.38 \times 10^{-23}$  J/K  
= -228.6 dBW/K

$S$  = the star flux density in W/m<sup>2</sup>/Hz

$k_1$  = a correction for atmospheric attenuation, and a function of elevation angle

$k_2$  = a correction for the angular extent of the star. This correction accounts for the fact that radio stars are not point sources. It is a rather complicated function of antenna beamwidth and star brightness distribution, and is significant for narrow antenna beamwidths

$k_3$  = the correction for radio star polarized flux (not needed for Cassiopeia A).

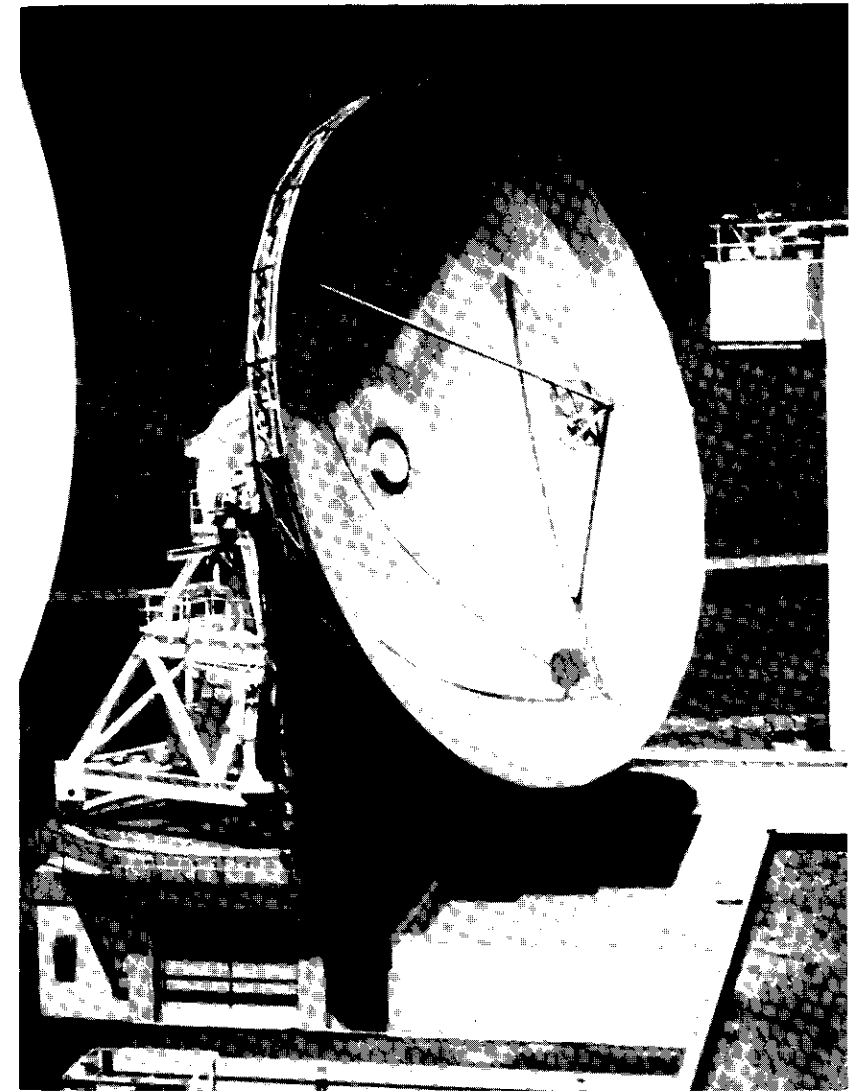


Figure 1. *The Etam-3 Antenna*

At 4 GHz, the Y-factor method has proved convenient for measuring G/T, and is almost universally used with Standard A antennas. The method can also be applied at 11 GHz, but satisfactory accuracy becomes

more difficult to achieve, primarily because of the low spectral flux densities.

In May 1981, Cassiopeia A had a flux density at 3.95 GHz of  $-230.1$  dB W/m<sup>2</sup>/Hz.\* This level yields  $Y$ -factors for Standard A antennas ranging from 3 to 6 dB. In this range, a measurement uncertainty of  $\pm 0.1$  dB translates to an uncertainty in  $G/T$  and gain of  $\pm 0.1$  dB, an amount that is seldom critical.

At 11 GHz in May 1981 the flux density of Cassiopeia A was  $-233.4$  dBW/m<sup>2</sup>/Hz, yielding  $Y$ -factors for Standard C antennas of the order of 0.4-0.5 dB. Measured  $G/T$  and gain now become highly sensitive to short-term atmospheric and LNA gain fluctuations, and measurement uncertainties of  $\pm 0.1$  dB in  $Y$ -factor translate to uncertainties in  $G/T$  and gain of  $\pm 1.0$  dB.

### The Etam radiometer

#### Theory of operation

Etam's requirement for high sensitivity in an environment of random gain fluctuations was met by a switched self-balancing gain modulation radiometer.

In the standard Dicke-type radiometer, the receiver input is switched between a reference termination and the unknown under test. The output of the receiving system is a DC level related to the difference in temperatures under the two switching conditions:

$$V_{\text{out}} = G(T_{\text{reference}} + T_{\text{LNA}}) - G(T_{\text{unknown}} + T_{\text{LNA}}) \quad (2)$$

In the gain modulation mode, the input to a receiving system is also switched between a reference termination and the unknown under test, but the output is a DC level proportional not to the difference but to the ratio of temperatures under the two switching states:

$$V_{\text{out}} = \frac{G(T_{\text{unknown}} + T_{\text{LNA}})}{G(T_{\text{reference}} + T_{\text{LNA}})} = \frac{T_{\text{unknown}} + T_{\text{LNA}}}{T_{\text{reference}} + T_{\text{LNA}}} = Y \quad (3)$$

\*Based on a spectral index of  $-0.79$  and a secular decrease per annum of  $1.1$  percent applied to a base flux of  $1072 \times 10^{-26}$  W/m<sup>2</sup>/Hz at 3.95 GHz on January 1, 1968 (Interim Communications Satellite Consortium [ICSC] T-23-16E, Appendix B).

As can be seen, system gain  $G$ , which can fluctuate, is eliminated as a variable, thereby improving sensitivity. This concept has been described in the literature and used in various applications since the early 1960's [2], but the measurements at Etam were, to the author's knowledge, the first applications of the method to an INTELSAT ground station. Equation (3) also defines a measurable  $Y$ -factor from which the unknown temperature (for Etam, the antenna noise temperature) can be calculated:

$$T_{\text{antenna}} = Y T_{\text{reference}} + T_{\text{LNA}}(Y - 1) \quad (4)$$

Radiometer circuitry in the gain modulation mode balances a voltage derived from a known reference temperature,  $V_R$ , with a voltage,  $V_A$ , derived from the temperature source under test (see Figure 2). This null balancing function was accomplished at Etam at IF and audio by the AIL Model 800 Universal Radiometer. The two voltages enter a comparator, whose output is an error signal that drives a  $2^{10}$  step binary attenuator operating on the reference voltage. Control circuitry continually adjusts the binary attenuator for zero error signal at the output of the comparator, in which condition the reference- and antenna-derived voltages are equal. From the attenuator readout, front panel settings, and certain internal calibrations, it is then possible to calculate the temperature (or  $Y$ -factor) of the device under test.

Measurement resolution is the range of measurement divided by the  $2^{10} - 1$  (1023) steps of the binary attenuator. The narrower the measurement range, which is adjustable from  $T_{\text{high}} - T_{\text{low}}$ , the greater the resolution (see Figure 3). The initial setting is based on an *a priori* estimate of the temperatures to be measured. The ultimate sensitivity of the radiometer, regardless of the range, can never exceed the limitation set by the overall system noise temperature, and the pre- and post-detection bandwidths [3]:

$$\Delta T_{\text{min}} = \frac{\sqrt{2} T_{\text{sys}}}{\sqrt{BT}} \quad (5)$$

where  $\Delta T_{\text{min}}$  = smallest detectable temperature differential

$T_{\text{sys}}$  = system noise temperature

$B$  = IF noise bandwidth

$T$  = radiometer integration time constant.

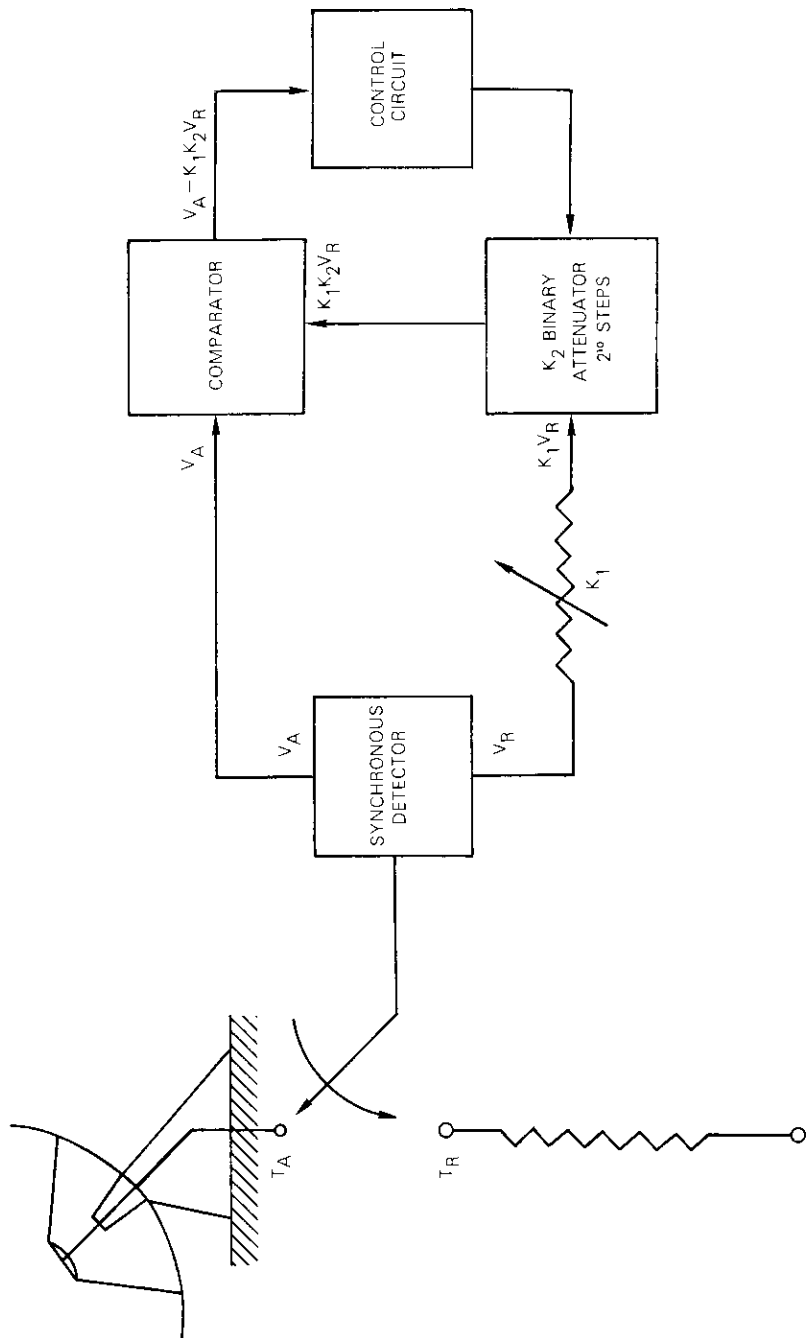


Figure 2. Radiometer Block Diagram

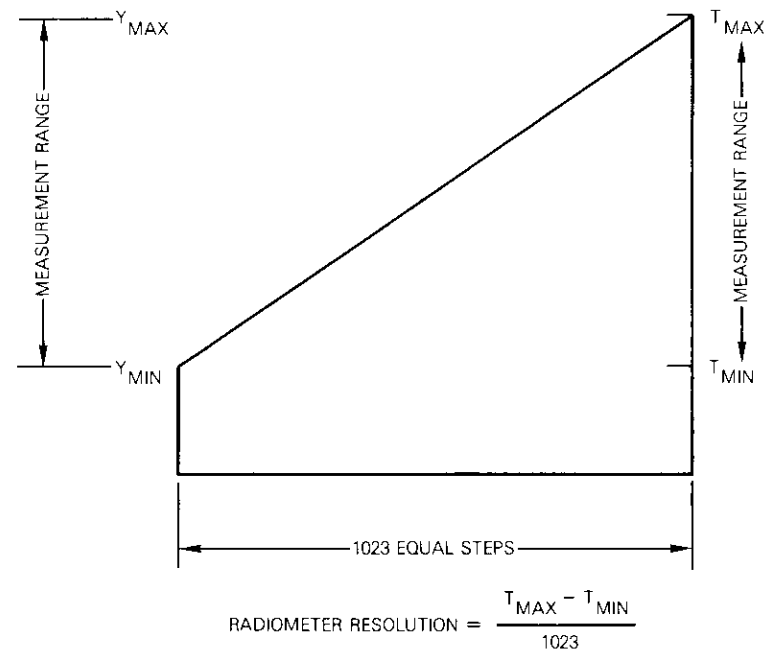


Figure 3. Gain Modulation Radiometer Range and Resolution

**Radiometer configuration**

The Etam radiometer consists of two major subsystems: the IF subsystem, which performs the null balancing function, and the RF/down-converter subsystem. The IF subsystem consists of the AIL Model 800 radiometer, which accepts and processes the down-converted signals derived from RF sources of any frequency, and provides the driving waveform for the Dicke switch.

The RF/down-converter subsystem translates the received RF noise power from the antenna under test to the IF range for further processing by the AIL unit. The subsystem is made up of the following components:

- a. separate latching circulator (Dicke) switches for the 11- and 14-GHz bands that switch the LNA between the antenna and the reference load at an audio rate;
- b. a 14-GHz parametric amplifier with a 3-dB noise figure and a 13.6-dB nominal gain;
- c. a SpaceKom down-converter with a 55-dB conversion gain and a 4.5-dB noise figure;

d. power supplies and interconnections; and

e. a GASFET amplifier with 60-dB gain over both the transmit and receive bands, and a 4-dB noise figure.

To obtain valid measurement data with this system, careful attention must be paid to all power and voltage levels. Meeting the interface requirements of the Model 800 is critical. The input IF power level must be maintained within a range of -65 to -50 dBm because an excessively high level causes unstable readouts, and a level that is too low results in loss of sensitivity. The optimum level is the minimum IF input that yields adequate sensitivity.

The automatic gain control regulates the voltage level observed by the square law detector, which monitors the switched power from the reference termination and the antenna. This level must be maintained between 1.4-1.6 V. At the same time the gain of the DC amplifier that follows the detector must be appropriately set, and both levels must be readjusted whenever there is any change in local oscillator (LO) power input to the down-converter. Best results at 14 GHz were obtained with an LO input power of 1.5 mW.

### Receive band measurements

The test setup for these measurements is shown in Figure 4. The station's rather than the radiometer's down-converter was used for the receive band tests. Two measurements are required to obtain a G/T Y-factor: first, a measurement of the sky + LNA temperature vs the reference + LNA temperature, and second a sky + star + LNA temperature vs the reference + LNA temperature. Each yields a Y-factor, and the two are combined as shown in equations (6), (7), and (8), to obtain the resulting  $Y_{G/T}$ . G/T is then calculated from equation (1).

$$Y_{\text{star}} = \frac{T_{\text{system}}^{\text{star}} + T_{\text{star}}}{T_{\text{reference}} + T_{\text{LNA}}} \quad \text{with antenna pointed at star} \quad (6)$$

$$Y_{\text{sky}} = \frac{T_{\text{system}}}{T_{\text{reference}} + T_{\text{LNA}}} \quad \text{with antenna pointed off star} \quad (7)$$

$$Y_{G/T} = \frac{Y_{\text{star}}}{Y_{\text{sky}}} = 1 + \frac{T_{\text{star}}}{T_{\text{system}}} \quad (8)$$

where  $T_{\text{system}} = T_{\text{antenna}} + T_{\text{LNA}}$

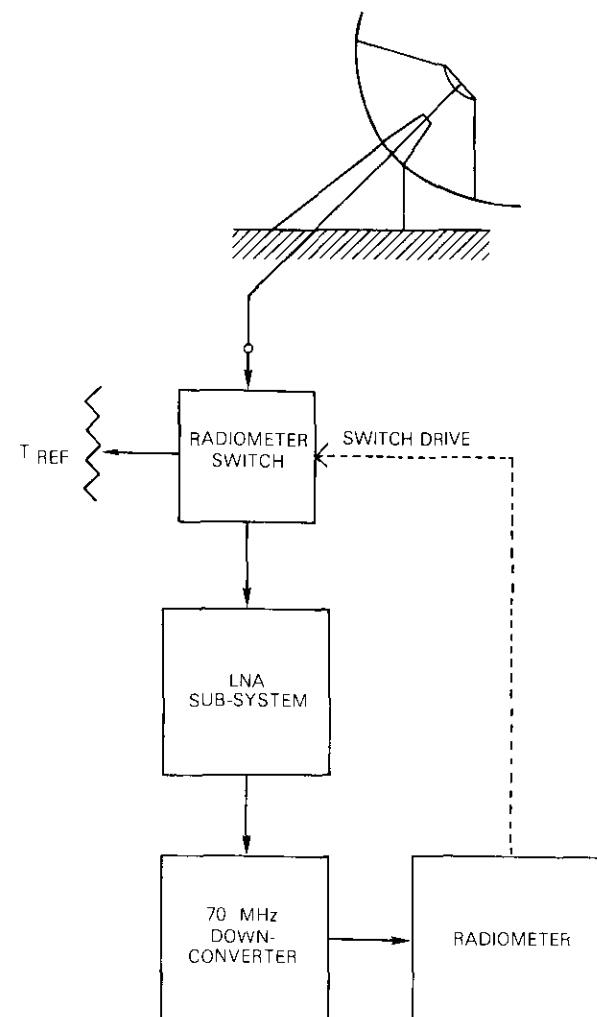


Figure 4. Test Setup for G/T and System Noise Temperature

Figure 5 plots G/T as measured with Cassiopeia A and Taurus A. Taurus A measurements were made at 0° and 90° polarization angles and averaged to account for the polarized component of star flux. Over the measured band, the G/T as measured with the two stars differed on average by less than 0.5 dB and was within 0.25 dB of a mean value. This difference was largely due to uncertainty regarding the precise values of

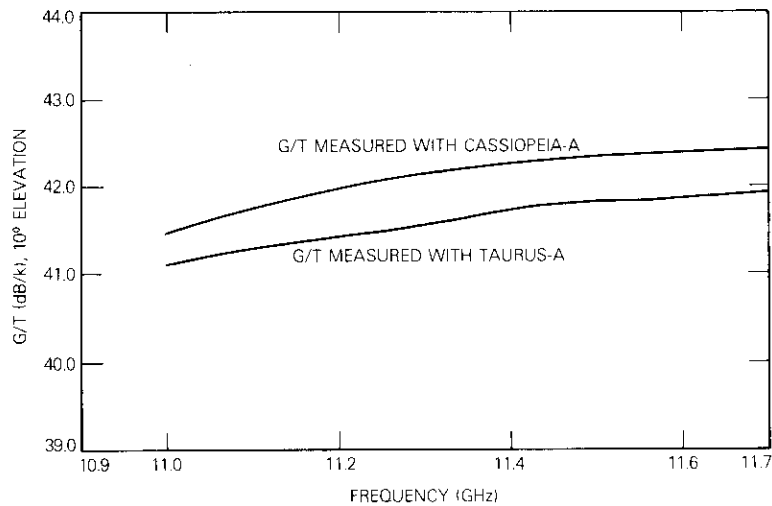


Figure 5. Etam-3 Measured G/T

the spectral flux densities of the two stars. It was possible to reduce slightly the spread between the two results by using a modified spectral index for Taurus A provided by Sato and Ogawa.\*

Antenna gain is obtained by adding to the G/T the system noise temperature in dB measured at the same elevation angle. Gain is plotted in Figure 6.

### Receive gain measured with SIRIO

An additional measurement of antenna receive gain was made at 11.597 GHz using a calibrated beacon from SIRIO. This permitted comparison of a radio star result with that obtained by an alternative method.

The main beam axis of the spacecraft antenna was repointed from Fucino towards Etam, and an absolute receive power measurement was then made by injecting a calibrated signal into a coupler located between

\*Based on work at KDD, Messrs. Sato and Ogawa suggested using a spectral index of  $-0.287$  rather than  $-0.263$  for Taurus A. The lower value given by Kreutel and Pacholder (Reference 1 and ICSC/T-23-16E) has been generally used.

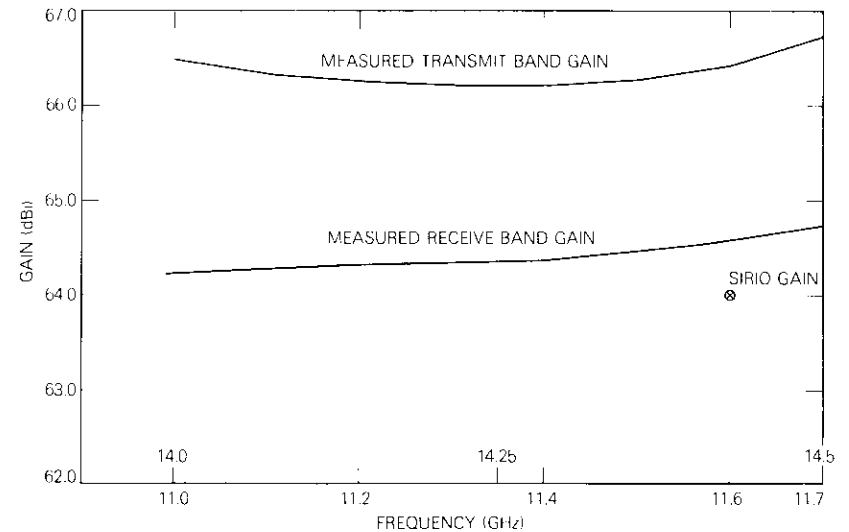


Figure 6. Etam-3 Antenna Receive and Transmit Gain

the output feed orthomode transducer (OMT) and the LNA as shown in Figure 7.

TELESPAZIO then provided a calibrated down-link e.i.r.p. From the transmitted e.i.r.p., space loss, and receive power, the antenna gain was calculated using

$$G = P_r - P_t + L + k_t + P \quad (9)$$

where  $G$  = antenna gain

$P_r$  = power received at antenna output OMT flange

$P_t$  = spacecraft transmit e.i.r.p. in the direction of the earth station

$L$  = path loss

$k_t$  = correction for atmospheric attenuation ( $\theta$  is the elevation look angle to the satellite)

$p$  = polarization loss, taken as 3 dB between circularly polarized spacecraft and linearly polarized earth station.

The gain obtained by this method was 64.25 dB as compared with 64.5 dB with the radio star method. This close match promoted confidence in the radiometric results.

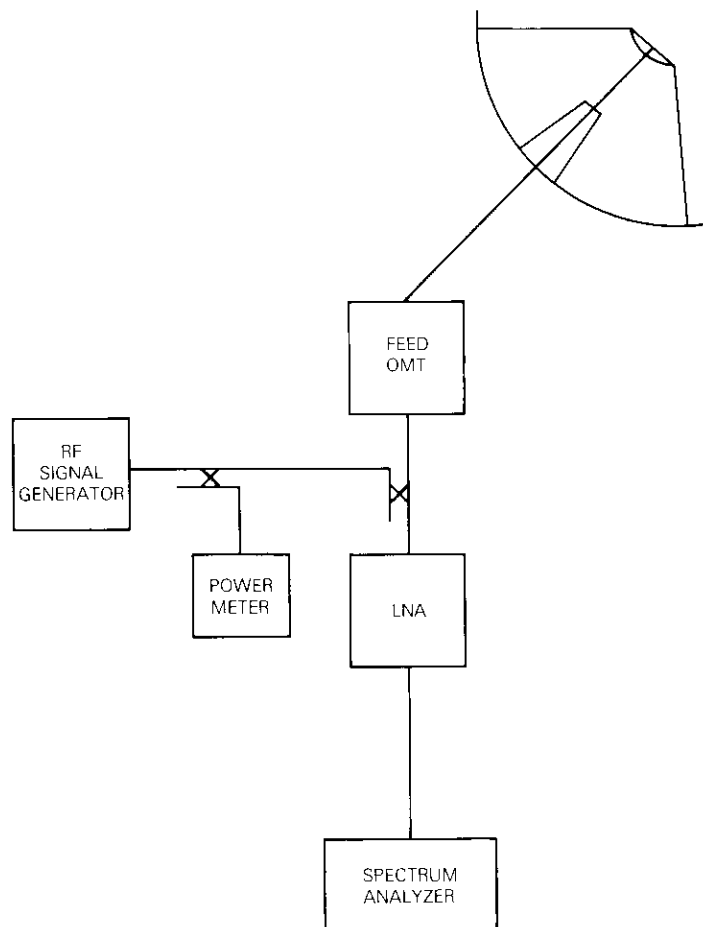


Figure 7. Setup for Receive Gain Measurement with SIRIO Satellite

### Antenna noise temperature

Antenna noise profiles, plotted in Figure 8, were obtained by subtracting the LNA temperature from the system temperatures measured at a set of elevation angles. System temperatures were calculated from the radiometric data using equations (10) and (12). LNA temperatures were measured with the well-known hot and cold load Y-factor method [2] using the radiometer and a Maury microwave liquid nitrogen termina-

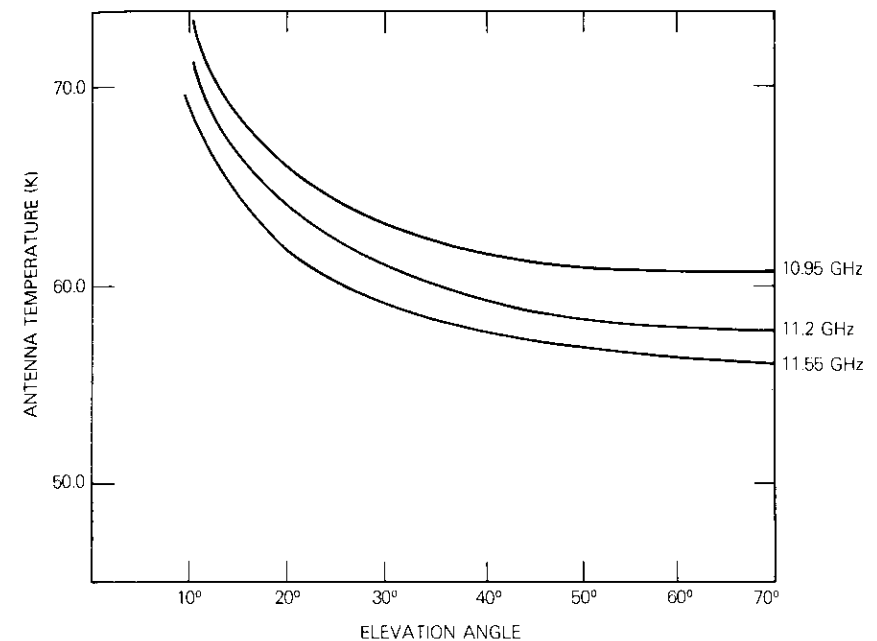


Figure 8. Etam-3 Antenna Noise Temperature

tion. The cold load temperature was corrected with equations (11) and (12) for the difference between ambient temperatures and barometric pressures obtained at Etam during the tests and those obtained at the site and time of initial calibration.

$$T_{\text{system}} = T_{\text{antenna (off star)}} + T_{\text{LNA}} = Y_{\text{sky}}(T_{\text{ref}} + T_{\text{LNA}}) \quad (10)$$

$$T_{\text{cold}} = T'_c + 0.01078 P + 0.0187 T_p + 0.00122 T_{\text{amb}} \quad (11)$$

where  $T'_c$  = factory calibration temperature

$P$  = difference between barometric pressure at test site and at site of original calibration = 8.604 mm

$T_p$  = temperature of mounting plate = 31.4°C

$T_{\text{amb}}$  = ambient temperature = 18.5°C

The LNA temperature can be computed from

$$T_{\text{LNA}} = \frac{YT_{\text{hot}} - T_{\text{cold}}}{1 - Y} \quad (12)$$

The temperature contribution, calculated by equation (13), of an 11-in. WR 75 waveguide, which included a bend between the Maury load and the switch, had to be added to the load temperature.

$$T_{\text{cold out}} = \frac{T_{\text{cold in}}}{L} + (1 + 1/L) T_{\text{ambient}} \quad (13)$$

where  $L$  = loss factor.

The temperature measurements of the LNA subsystem uncovered an instability in one of the amplifiers, and all measurements were thereafter performed with the more stable amplifier.

### **Transmit gain**

The usual method of measuring the transmit gain of earth station antennas has been by e.i.r.p. matching with a TTC&M antenna; but this method was not available at Etam because INTELSAT V had not yet been launched nor was there a calibrated standard. Instead, transmit gain was measured as in the receive band by radio star. This procedure required a 14-GHz LNA, a device not normally in the complement of earth station equipment. Fortunately, a developmental model parametric amplifier for spacecraft use having a gain of 13.5 dB and a noise figure of 3 dB was made available by INTELSAT.

The procedure for measuring transmit gain was identical to that used in the receive band. G/T and system noise temperature were measured separately using the radiometer RF down-converter subsystem, and their product was calculated. The test setup is shown in Figure 4. The relatively low gain of the 14-GHz parametric amplifier required referring the down-converter noise temperature to the amplifier input when calculating system temperature and gain, a step not necessary in the receive band calculation because of the high (greater than 50 dB) gain of the station LNA. Transmit band gain results are plotted in Figure 6.

### **The angular extent correction**

The correction for the angular extent of the star is a nonlinear function of antenna beamwidth, becoming very large as the beamwidth narrows.

On Standard A antennas with receive beamwidths of the order of  $0.16^\circ$ , the correction is approximately 0.25 dB. On Etam-3 with a beamwidth of about  $0.08^\circ$  the correction, based on the formulation of Baars, Mezger, and Wendker [4], is upwards of 2.0 dB. This correction, based on a disc spectral distribution for Cassiopeia A, and a Gaussian distribution with elliptical symmetry for Taurus, was adopted in ICSC/T-23-16E, issued in 1968, and has not been changed since. The Etam data reduction utilized the more recent results of Sato and Ogawa [5], based on high resolution contour plots of star brightness distributions. In general, these yielded smaller corrections than those of Baars, Mezger, and Wendker.

### **VSWR considerations**

The effect of vswr's on temperature measurement accuracy has been the subject of numerous papers, some of which are cited in References 6, 7, and 8. In general, a mismatch changes the amount of noise power delivered to the radiometer from a source, which may be the antenna under test or a calibrated termination. The amount of change is a function of the amplitude and phase of the source and load reflection coefficients. In most cases, including those considered in this paper, the end effect of mismatches is to reduce the measured  $Y$ -factors, resulting in higher apparent LNA noise temperatures and lower system G/T ratios. Therefore, from a vswr standpoint, the results reported in this paper are conservative. Since the star rise at 11 GHz is only about 18 K above a 170-K background and the relevant vswr's are moderately low (in the 1.2–1.3 range), the errors should be quite small. Less than 0.02-dB error in G/T is estimated.

### **Radiation patterns**

When the initial series of RF tests was performed in November 1980, the first INTELSAT V spacecraft had not been launched and therefore was unavailable for RF focusing of the subreflector. Fortunately, SIRIO with a beacon at 11.597 GHz was visible from Etam and could be used for this purpose. Figure 9 shows the communication patterns taken with the aid of SIRIO, and Figure 10 shows the tracking patterns.

By April 1981, when a second series of measurements was performed, INTELSAT V was available, and a set of wide angle patterns was taken at 10,962.5, 11,690.5, and 14,065 MHz. These are shown in Figures 11 through 16 with the FCC and INTELSAT recommended 32–25 log  $\theta$  envelope indicated. The antenna complies with INTELSAT requirements.

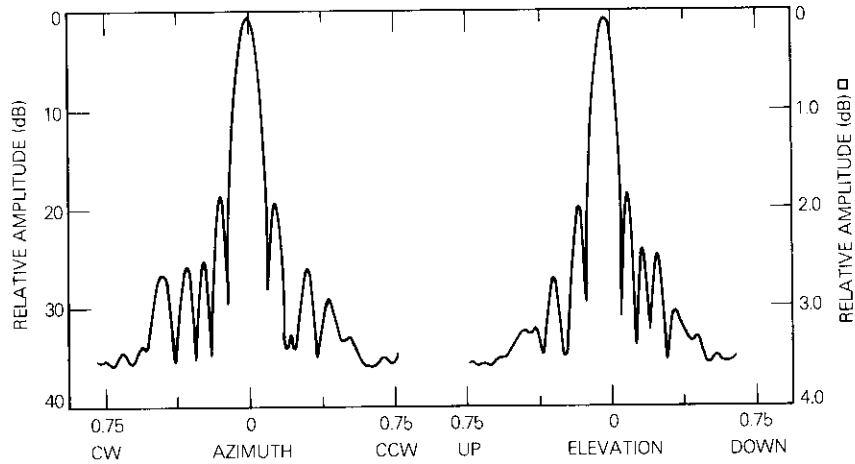


Figure 9. *Etam-3 Sum Patterns 11.597 GHz (SIRIO Beacon)*

**Summary and conclusions**

The G/T, gain, and temperature characteristics of the new Etam Standard C antenna were measured by radio star using gain modulation radiometry. This method proved successful in overcoming the difficulties

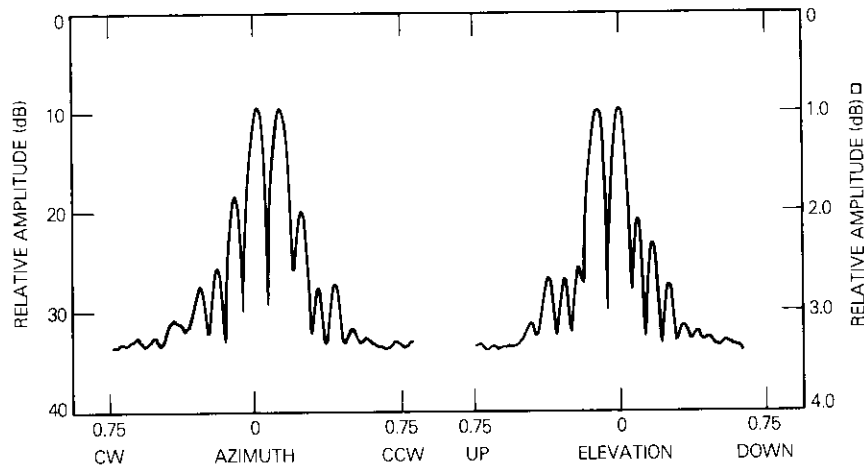


Figure 10. *Etam-3 Difference Patterns 11.597 GHz (SIRIO Beacon)*

posed by the low spectral flux densities available at 14/11 GHz. A supplementary receive gain measurement with SIRIO verified the radiometric method. It is concluded that antennas with low Y-factors (due to low gain or low spectral flux density) can be measured by radio star techniques described in this paper, but great care is needed in the implementation and execution of measurements.

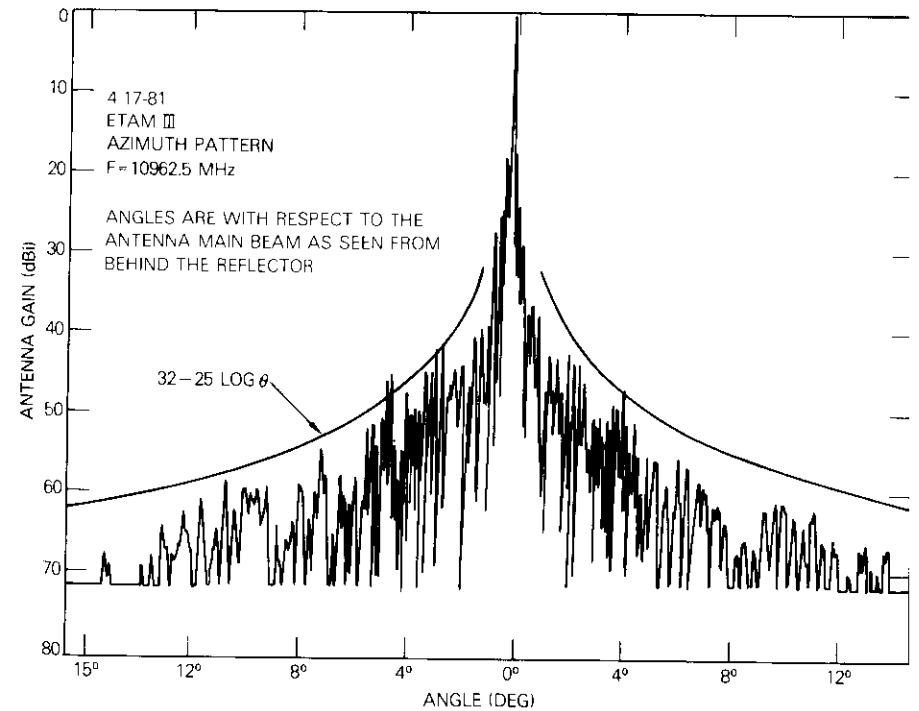


Figure 11. *Azimuth Pattern—10,962.5 MHz*

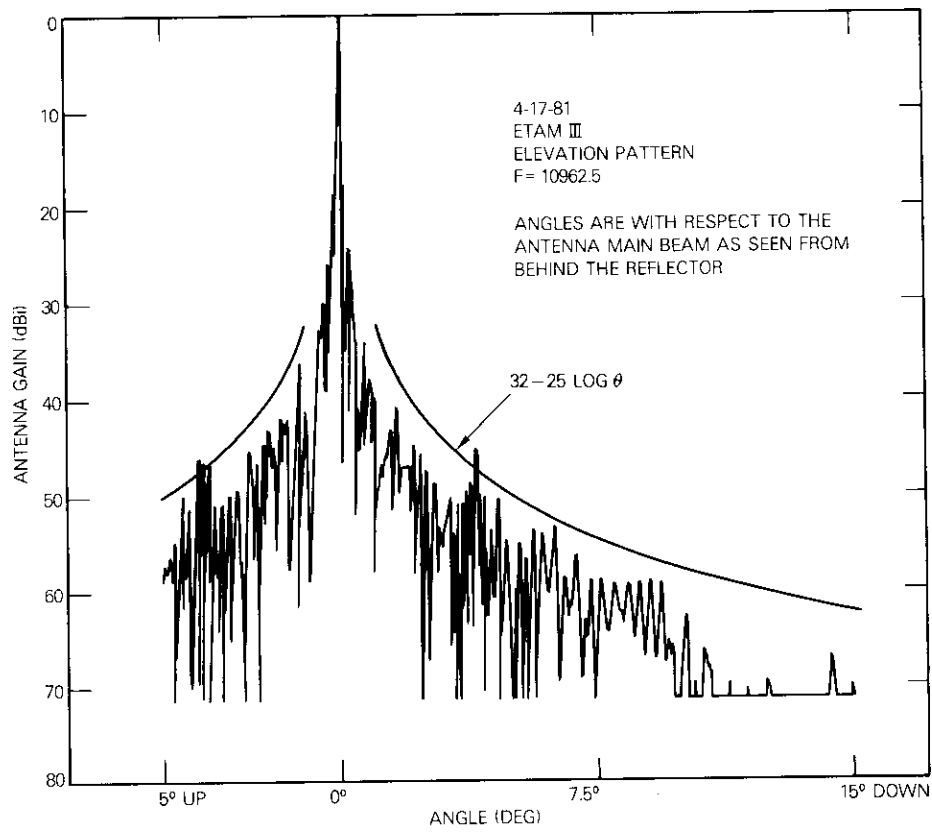


Figure 12. Elevation Pattern—10,962.5 MHz

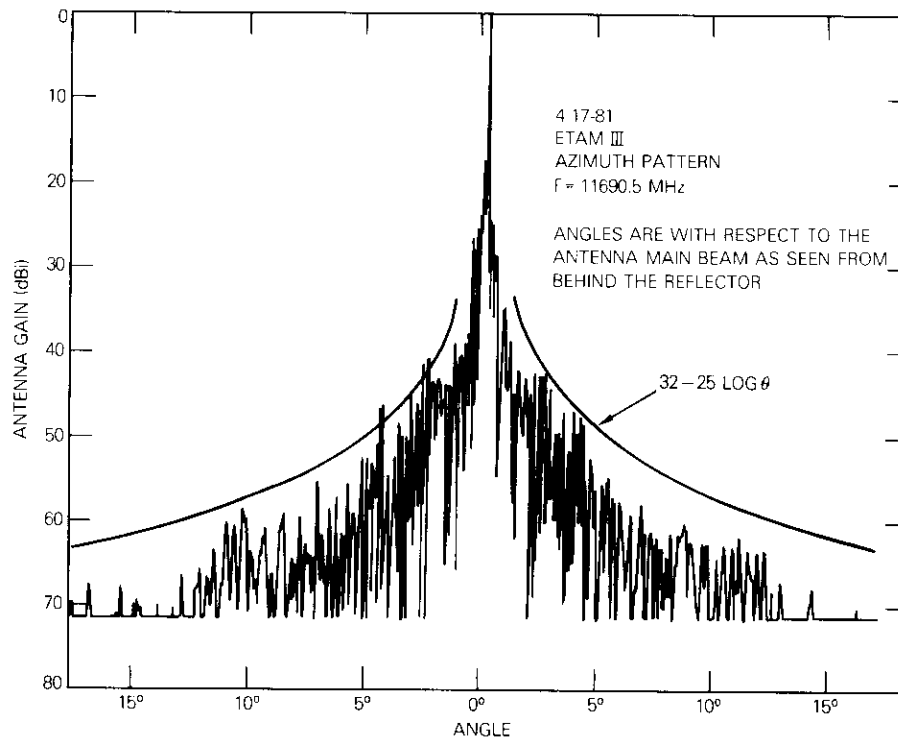


Figure 13. Azimuth Pattern—11,690.5 MHz

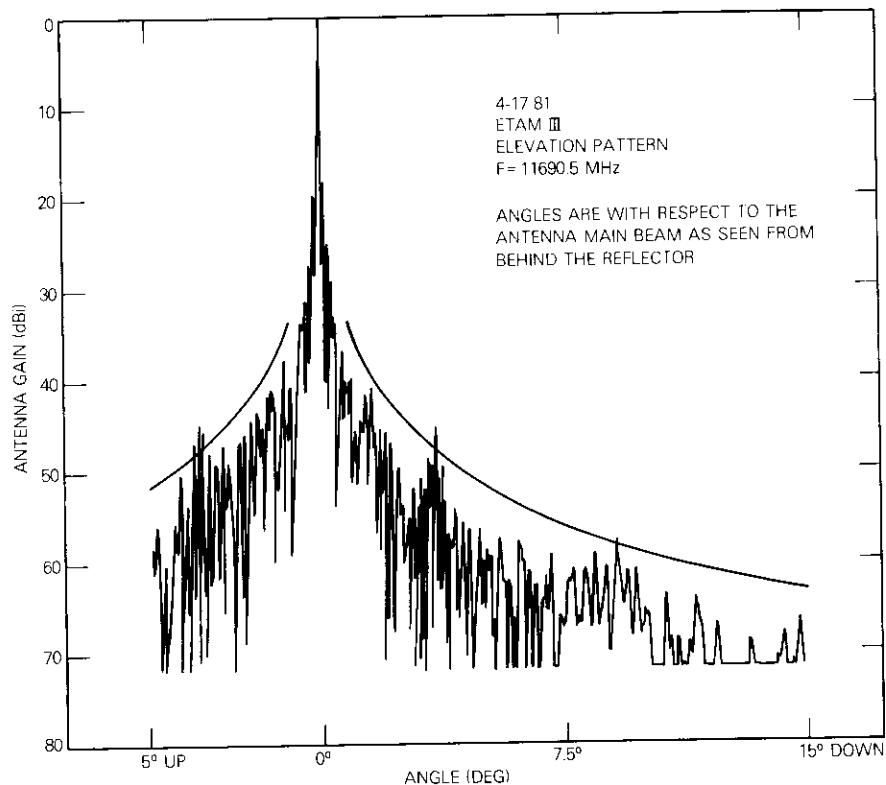


Figure 14. Elevation Pattern—11,690.5 MHz

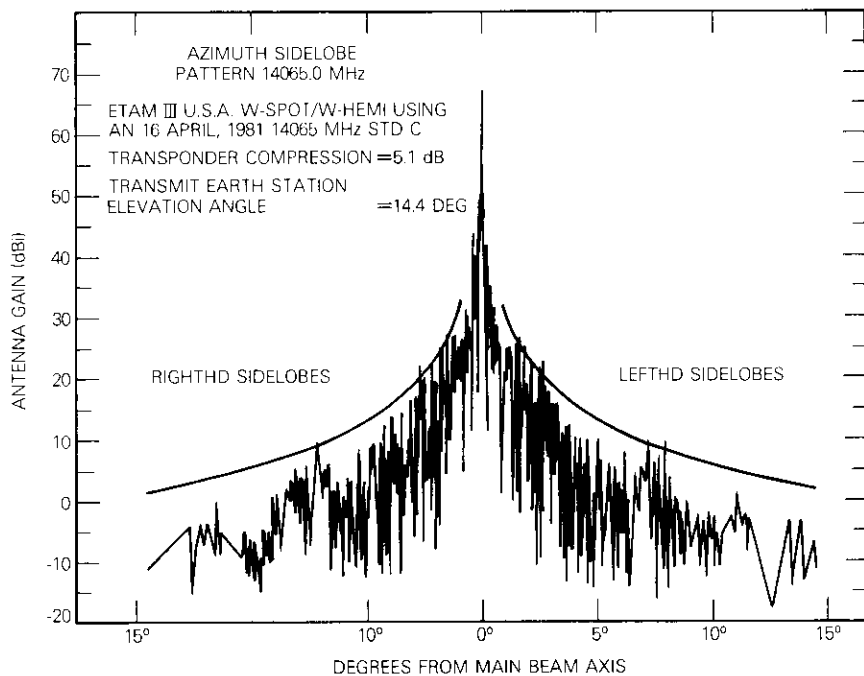


Figure 15. Azimuth Sidelobe Pattern—14,065 MHz

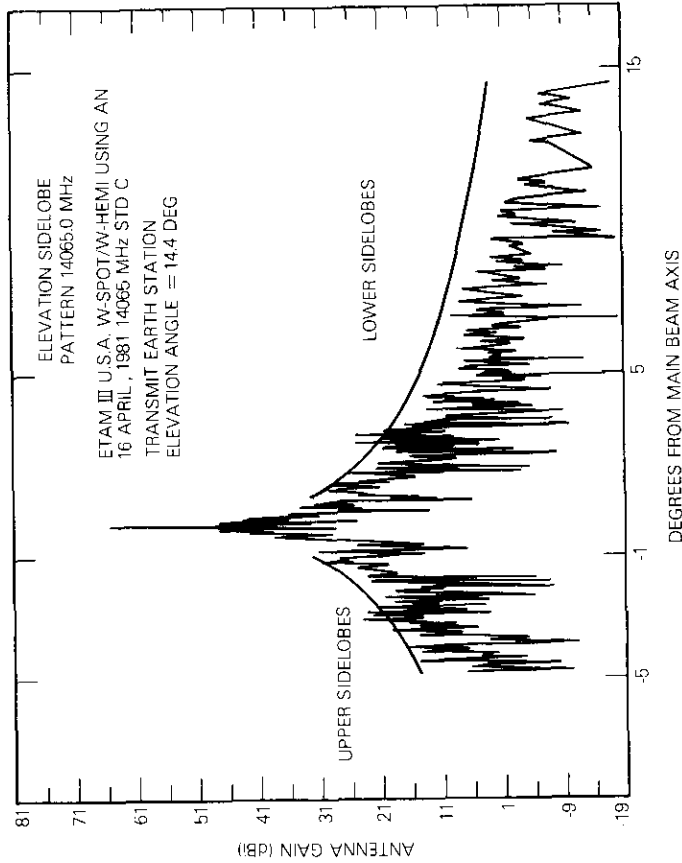


Figure 16. Elevation Sidelobe Pattern—14,065 MHz

### Acknowledgments

It is a pleasure to acknowledge the contributions of several individuals: Steve Struharik provided much guidance in the assembly and operation of the Etam radiometer; Peter Ackerman assembled the front end of the radiometer and effectively accomplished the troubleshooting that was all too often required; T. Flateau of AIL gave invaluable guidance in use of the Model 800 radiometer; and W. Nickerson of TIW who in executing measurements showed an uncanny knack for staying ahead of fast moving stars.

### References

- [1] R. Kreutel and A. Pacholder, "The Measurement of Gain and Noise Temperature of a Satellite Communication Earth Station," *Microwave Journal*, October 1969, pp. 61-66.
- [2] T. Orhaug and W. Waltman, "A Switched Load Radiometer," Publications of the National Radio Observatory, Vol. 12.
- [3] G. Evans and C. W. McLeish, *RF Radiometer Handbook*, Equation 1.1, p. 2.
- [4] J. W. M. Baars, P. G. Mezger, and H. Wendker, "The Spectra of the Strongest Non-Thermal Radio Sources in the Centimeter Wavelength Range," *The Astrophysical Journal*, Vol. 142, No. 1, July 1965, pp. 122-134.
- [5] T. Sato and A. Ogawa, "Exact Gain Measurement of Large Aperture Antennas Using Celestial Radio Sources," *IEEE Transactions on Antennas and Propagation*, Vol. AP-30, No. 1, January 1982, pp. 157-161.
- [6] T. Y. Otoshi, "The Effect of Mismatched Components on Microwave Noise Temperature Calibrations," *IEEE Transactions on Microwave Theory and Techniques*, Vol. MTT-16, No. 9, September 1968, pp. 675-686.
- [7] M. M. Brady, "The Influence of Mismatch Error on Noise Performance Measurements," *Proceedings of the IEEE*, Vol. 52, September 1964, pp. 1075-1076.
- [8] D. F. Wait, "Considerations for the Precise Measurements of Amplifier Noise," Technical Note 640, National Bureau of Standards.



York; and subsequently with the General Electric Company, Space and Re-Entry Systems Division, in Valley Forge, Pennsylvania.

*Ronald Price received a B.E.E. in 1960 from the Polytechnic Institute of Brooklyn where he also did graduate work. He joined COMSAT in 1968 as a Member of the Technical Staff of the RF Transmissions Laboratory, where he worked on antennas and associated RF devices. Later, he was with the Systems Engineering and Earth Station Engineering Divisions, and is currently Senior Staff Engineer with the Project Management and Engineering Division. Before joining COMSAT, Mr. Price was with the Sperry Gyroscope Company, Radiation Division, in Great Neck, New*

**Index: modems, speech processing, synchronization, transmission systems, TDMA**

## **60-Mbit/s QPSK-TDMA/DSI field test via Pacific Basin INTELSAT IV**

T. DOBYNS, D. CHAKRABORTY, H. SUYDERHOUD, AND C. J. WOLEJSZA

(Manuscript received August 6, 1981)

### **Abstract**

This paper presents the results of a COMSAT field test of TDMA terminals equipped for digital speech interpolation (DSI). The test was conducted in the Pacific Ocean region in 1980 with participation of KDD, Japan, and Cable and Wireless, Ltd., United Kingdom. Its main purpose was to obtain operational experience and to evaluate simplified time-division multiple-access (TDMA) network protocols. Constraints encountered in a typical band-limited nonlinear satellite channel are also discussed.

Testing was conducted among earth stations in Paumalu, Hawaii; Ibaraki, Japan; and Hong Kong via INTELSAT IV F8, transponder 12. The test program included link calibration, optimization of the channel bit error rate (BER), TDMA equipment test, and baseband performance (objective and subjective).

### **Introduction**

A TDMA terminal was developed during 1978 and 1979 as part of COMSAT Laboratories' TDMA research and development program; it consisted of a burst modem [1], [2], TDMA controller [3], and terrestrial interface units. Figure 1 shows the field test configuration for the three terminals, which interfaced with D-3 pulse code modulation (PCM)

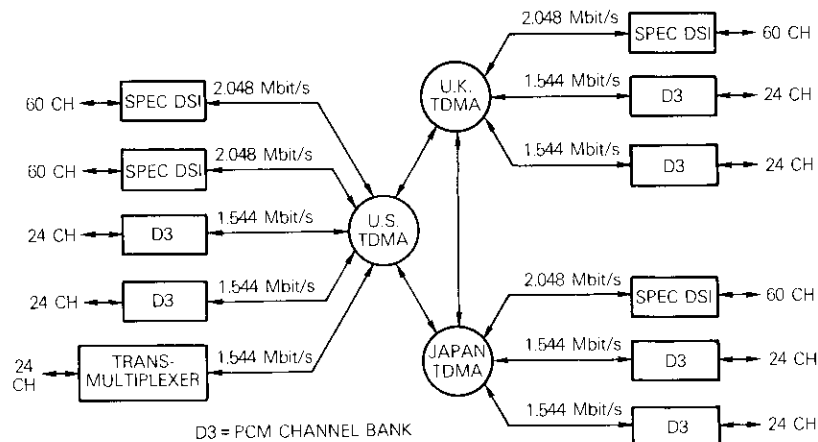


Figure 1. Field Test Configuration

channel banks (T-carrier format), DSI/SPEC\* [4] with CEPT channel banks, and a 24-channel transmultiplexer. The program included both subjective and objective testing, and a significant part was devoted to the establishment of a high-quality link for 60-Mbit/s TDMA in a 36-MHz transponder.

This paper summarizes the results of the test program by successive discussion of TDMA modem performance, TDMA equipment tests, and baseband-to-baseband tests.

The TDMA terminals were operated with a 750- $\mu$ s frame at a clock rate of 30.016 MHz using quaternary phase-shift keying (QPSK) modulation. The network protocols are a simplified version of the INTELSAT BG-1-18 specification. The burst preamble consists of 96 symbols for carrier and bit timing, 15 for unique word, 3 for the station identification code, and 13 (maximum available) for order wire channels [5].

A traffic burst is designated as a reference burst for network frame synchronization. An alternate traffic burst serves as the frame reference if the primary fails. Burst position and burst length are assignable anywhere in the frame with one-symbol resolution. An open-loop procedure was used for initial acquisition, and closed-loop for steady-state synchronization.

Terrestrial interface units were developed for the T-1 carrier (1.544 Mbit/s) and for the SPEC/DSI operating at 2.048 Mbit/s. The SPEC/DSI interconnected with CEPT channel banks. The terminal multi-

\*The speech predictive encoding communications equipment had been previously developed by COMSAT Laboratories.

destinational mapping capability allows any group of four channels from the 24 generated by a D-3 channel bank (T-1 carrier) to be assigned to any other system D-3 channel bank. Thus, each channel bank can be interconnected with up to six other network channel banks [3].

The DSI equipment for this experiment consisted of the SPEC design previously developed at COMSAT Laboratories. It incorporated the latest DSI concepts, including a floating threshold voice switch and dynamic aperture zero-order predictor which virtually eliminates speech clipping [4].

The commercially procured transmultiplexer equipment consisted of an all-digital implementation employing discrete cosine transform processing with transversal tap weighting. Two channel banks interfacing at 60-108 kHz were converted to the standard T-carrier digital format ( $\mu$ -law) at 1.544 Mbit/s, and vice versa.

### Satellite channel model

The satellite channel model is depicted in Figure 2.\* Signals are corrupted by additive thermal noise on both the up- and down-links. Interference can also arise from signals in adjacent satellite transponders (out-of-band emissions).

Additional signal distortion is produced by earth station transmitters and the satellite amplifiers operating in their nonlinear regions. These nonlinearities together with the channel filters cause distortion which leads to intersymbol interference.

The up-path noise is principally contributed by the satellite receiver noise and the earth noise as seen by the global coverage receive antenna. A typical up-path noise temperature is around 1,000 K. The down-path noise is contributed by the earth station receiver low-noise amplifier (LNA), loss in the feeder line connecting the feed with the LNA, earth station antenna sidelobe and backlobe pickup, and galactic radiation. A typical down-path noise temperature is around 50 K at elevation angles above 10°.

The effects of broadband thermal noise are minimized by filtering the up-link signal at the satellite and the down-link signal in the earth station demodulator. Since interference from adjacent channels cannot be removed by filtering, the system must be engineered to control these sources of interference. Out-of-band emissions, which cause adjacent channel interference, are controlled by operating the earth station transmitter in a quasi-linear region, that is, backed off from saturation. Maximizing satellite transponder usage in terms of carrier power requires

\*Courtesy of L. C. Palmer, COMSAT Labs.

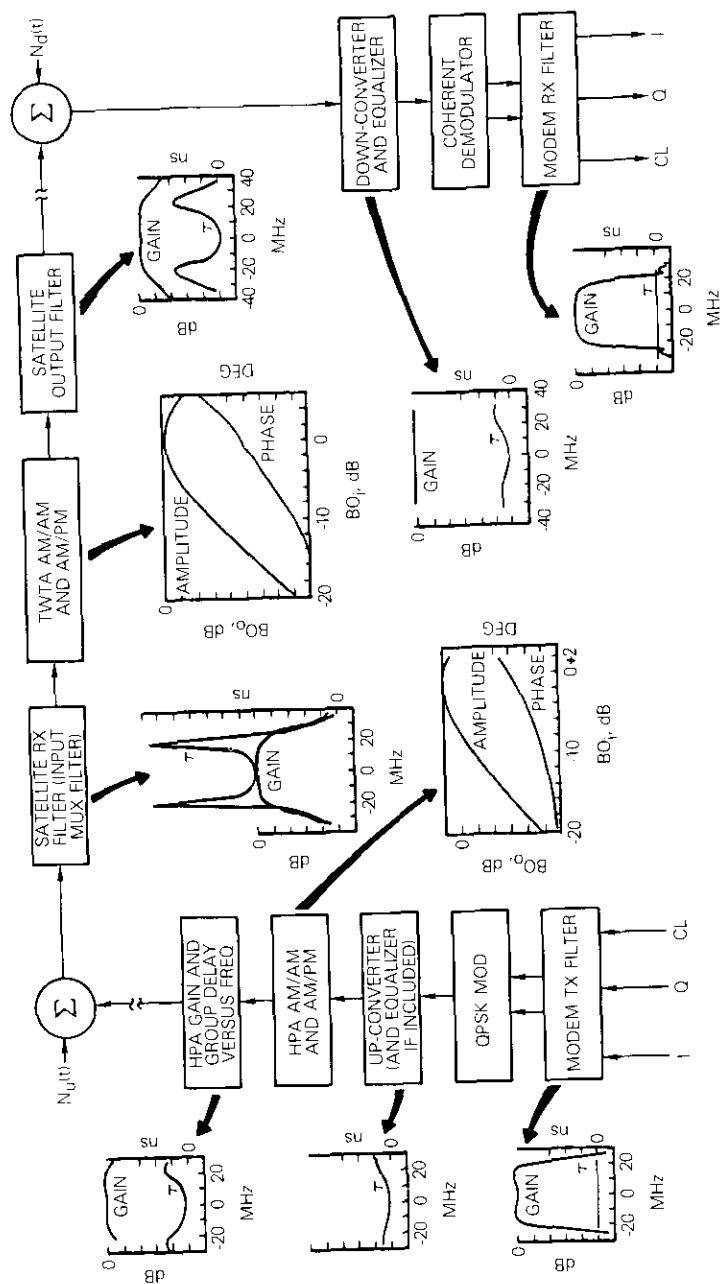


Figure 2. General Channel Model

operation near saturation. Signal dispersion can be controlled by overall link equalization, as discussed later. The principal elements which affect channel performance are channel filters, the high-power amplifier (HPA), transponder filters, and the transponder traveling wave tube amplifier (TWTA).

### Channel filters

The channel filter configuration adapted in the present modem is shown in Figure 3, where the critical items are the transmit and receive low-pass filters. The wideband transmit and receive bandpass filters are spectrally transparent to the data; their major functions are the suppression of spurious emission from the modulator and the reduction of the wideband noise in the demodulator, respectively.

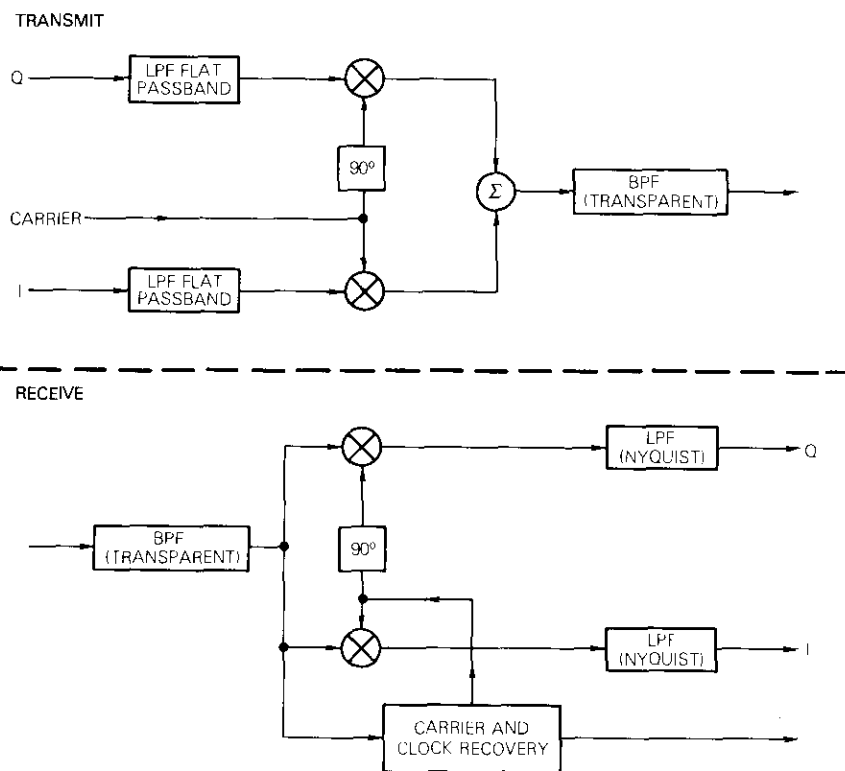


Figure 3. Channel Filter Configuration

The transmit low-pass filter is a dual low-pass, flat passband type with a bandwidth symbol duration product ( $BT \cong 1.1$ ), and the corresponding receive low-pass filter is a dual low-pass Nyquist type with 40-percent cosine roll-off, including aperture equalization ( $x/\sin x$  compensation) [2].

**Channel equalization**

Two types of equalizers are available for either amplitude or group-delay equalization. The first is a fixed type which has either flat group delay and a particular amplitude characteristic, or a flat amplitude response and a known group-delay characteristic. Fixed equalizers can be designed to compensate for amplitude or group-delay distortion with complex shapes; the only disadvantage is that these equalizers are made as cascaded all-pass sections as shown in Figure 4 and are not generally

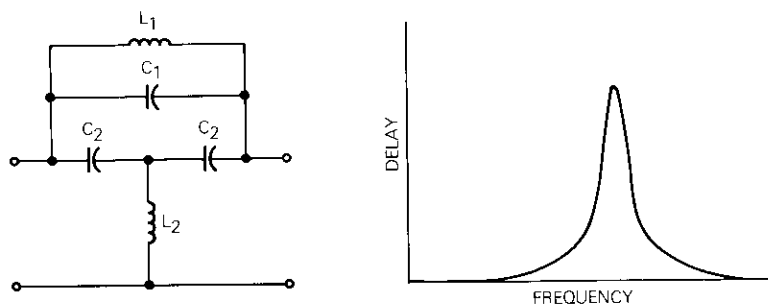


Figure 4. Bridged-T Equalizer

adjustable over a wide range [6]. The second type, a transversal equalizer, shown in Figure 5, can be adjusted to yield many combinations of amplitude and group-delay characteristics with more regular behavior in terms of gain or delay slopes [7],[8].

For nonlinear operation of the satellite TWT, amplitude or delay distortion existing in the up-link cannot be compensated in the down-link. Appropriate compensation must be introduced in the up-link chain. Therefore, transversal equalizer placement was planned at the modulator output for the up-link compensation and at the demodulator input for the down-link compensation. In addition, a fixed equalizer was planned for the down-link side to compensate the transponder delay distortion principally due to the transponder output multiplexer.

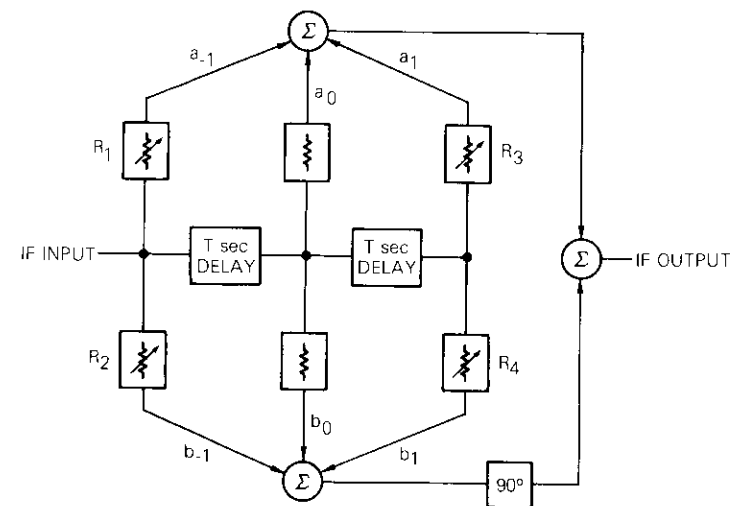


Figure 5. Transversal Equalizer Block Diagram

**Link calculations**

The link parameters were as follows:

*Up-Link*

Satellite (G/T) at beam peak	-13.1 dB/K
Saturation flux density at beam peak (full gain transponder)	-75 dBW/m <sup>2</sup>
Gain of 1 m <sup>2</sup> at 6 GHz	37 dB
Transponder usable bandwidth	36 MHz
Transponder input backoff (assumed for optimum BER performance)	2 dB

*Down-Link*

Transponder e.i.r.p. at saturation at beam peak	25.8 dBW
Transponder output backoff (assumed for optimum BER)	0.3 dB

These parameters result in the carrier-to-noise ratio (C/N) calculations given in Table 1 for the links involved.

The TDMA system was initially installed at the U.S. earth stations in

TABLE 1. C/N CALCULATIONS

EARTH STATION	UP-PATH LOSS (dB)	UP-PATH ASPECT CORRECTION (dB)	DOWN-PATH LOSS (dB)	DOWN-PATH ASPECT CORRECTION (dB)	RECEIVE G/T (dB/K)	RECEIVE C/N OVER 36 MHz (dB)
Jamesburg	200.4	3.2	196.8	3.0	41.3	19
Paumalu #2	199.5	1.5	195.9	1.5	41.9	20.5
Ibaraki #3	199.7	2.0	196.2	2.1	41.7	20.4
Hong Kong	200.1	2.5	196.6	2.5	41.2	19.8

Jamesburg, California, and Paumalu, Hawaii, where verification testing was performed prior to shipping the terminals to Ibaraki and Hong Kong. During these tests, the phase-shift keying (PSK) spectrum regeneration characteristics of the satellite transponder and the effect of regeneration on the adjacent transponder were examined. The resulting excess out-of-band noise (OBN) falling on the transponder 11 carrier (976 ch FDM/FM from Jamesburg) was measured by the Ibaraki earth station; the resulting data are shown in Figure 6. Although the PSK spectrum regeneration in transponder 12 caused about 2-dB signal-to-noise (S/N) degradation on the Jamesburg FDM/FM carrier when received by Ibaraki, the overall S/N met INTELSAT specifications.

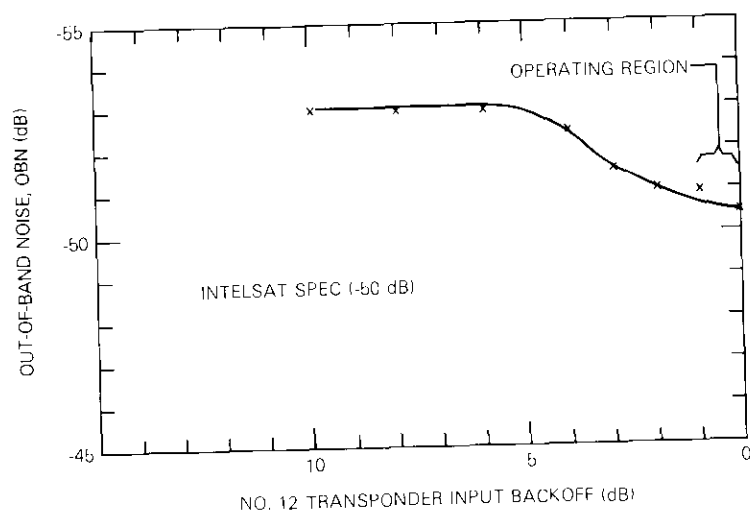


Figure 6. Out-of-Band Emission vs Transponder Input Backoff for Transponder 11 Carrier due to Transponder 12 Spectrum Regeneration

After verification testing, the TDMA equipment was installed at earth station facilities in Paumalu, Hawaii, Ibaraki, Japan, and Hong Kong. Each station was calibrated individually, including the following tests:

- amplitude and delay equalization of the up-chain, the down-chain, the combined up- and down-chain using a 6/4 GHz station translator, and the entire satellite loop;
- examination of the HPA nonlinearity (calibrated attenuator settings vs HPA output or earth station e.i.r.p.), to generate a satellite power transfer curve and the link carrier-to-noise ratio;
- optimization of the satellite loop BER as a function of transponder input backoff by finer adjustment of the transversal equalizer in addition to the fixed equalizers used for amplitude and group-delay equalization;
- station-to-station tests between Ibaraki and Hong Kong;
- TDMA equipment tests;
- baseband-to-baseband performance evaluation.

The above tests were performed at each of the accessing earth stations.

#### TDMA modem performance

The performance of the TDMA modem over the actual links had to be assessed indirectly for two reasons. *First*, it was not possible to isolate the effects of the noise distribution of the up- and down-path. *Second*, the up-path noise was compressed by the nonlinearity of the satellite TWT, so that field measurement of the actual  $E_b/N_o$  was subject to error.

The satellite power transfer curve, which can be determined with reasonable accuracy by measuring received power vs e.i.r.p., was used to establish the system operating point. The BER was then measured as a function of input backoff, as shown for the three loopback conditions in Figure 7. Note that there is approximately a 1.5-dB spread in performance from one station to another. However, if the prelaunch data and the link budget for each station are used to calculate  $E_b/N_o$  vs operating point, the modem BER performance vs calculated  $E_b/N_o$  can be obtained and is shown in Figure 8. In this case, the spread from one station to another is a few tenths of a dB. These differences most likely result from variations in overall amplitude and group delay from one station to another, while those shown in Figure 7 result from the different link budgets. Also, the modem BER performance vs  $E_b/N_o$  relative to back-to-back is degraded by about 1 dB because of link effects.

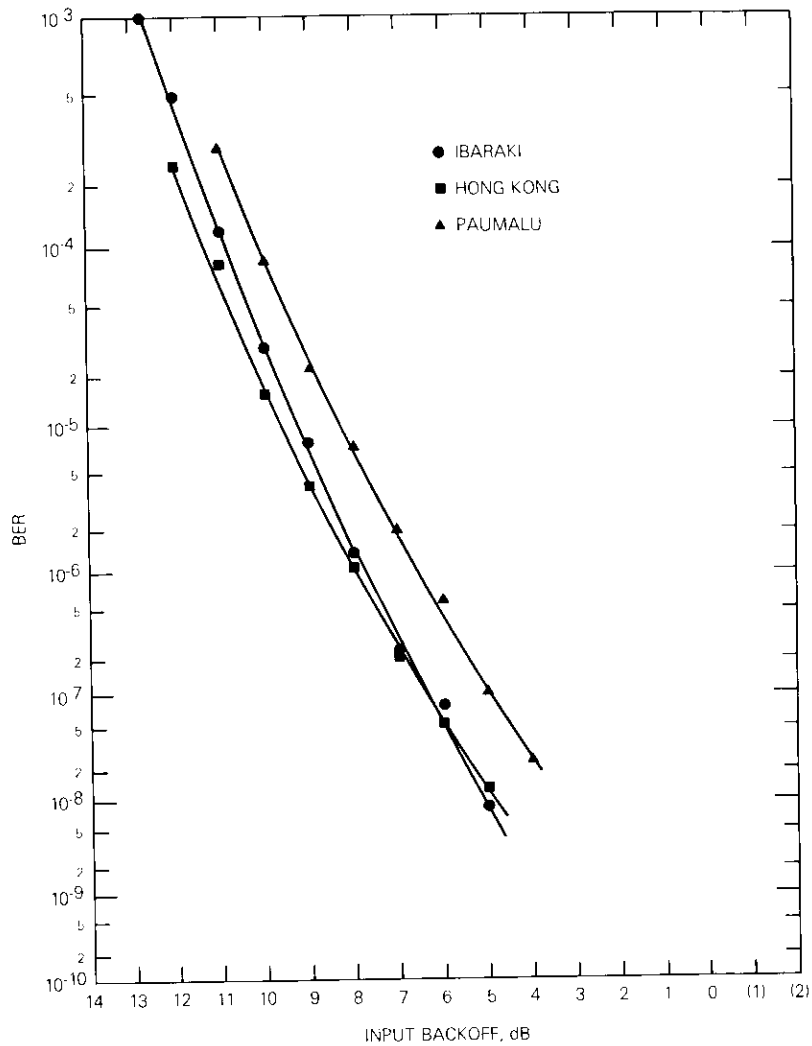


Figure 7. BERs vs Input Backoff at Paumalu, Ibaraki, and Hong Kong Earth Stations in Loopback Configuration

Figure 9 shows the modem performance vs operating point for station-to-station tests between Ibaraki and Hong Kong after loopback tests had been completed. In both cases, performance was considerably worse than loopback, even though up-path noise should have been constant, and loopback results were similar in each case. Further, the performance

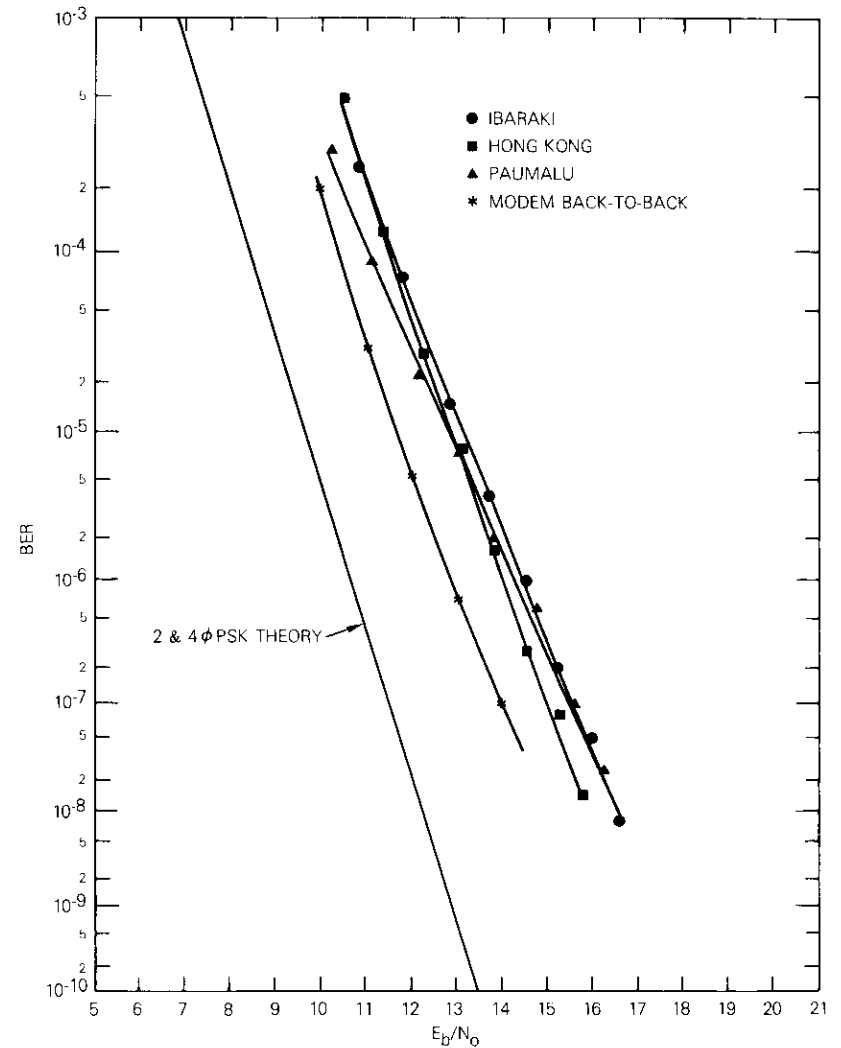


Figure 8. BER vs Calculated  $E_b/N_0$  for Paumalu, Ibaraki, and Hong Kong (Loopback Mode)

varied considerably for different directions of transmission. It is very likely that a part of this performance loss is caused by a mismatch in equalization between each up-link and the corresponding down-link in the other station. This is illustrated in Figure 10, which compares link transmission characteristics for several different transmitting/receiving

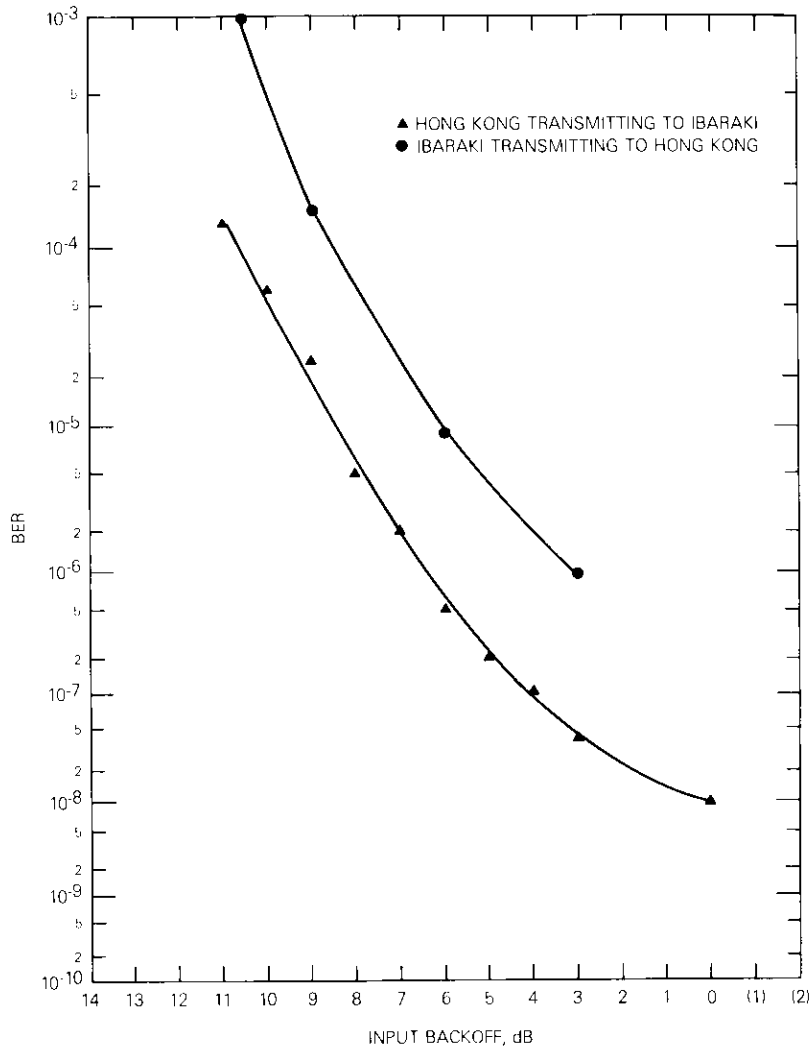


Figure 9. Burst Mode BER vs Backoff, Ibaraki Transmitting and Hong Kong Receiving

station combinations. Other effects contributing to this difference include day to day changes in link budget, due to weather, earth station tracking, and satellite motion.

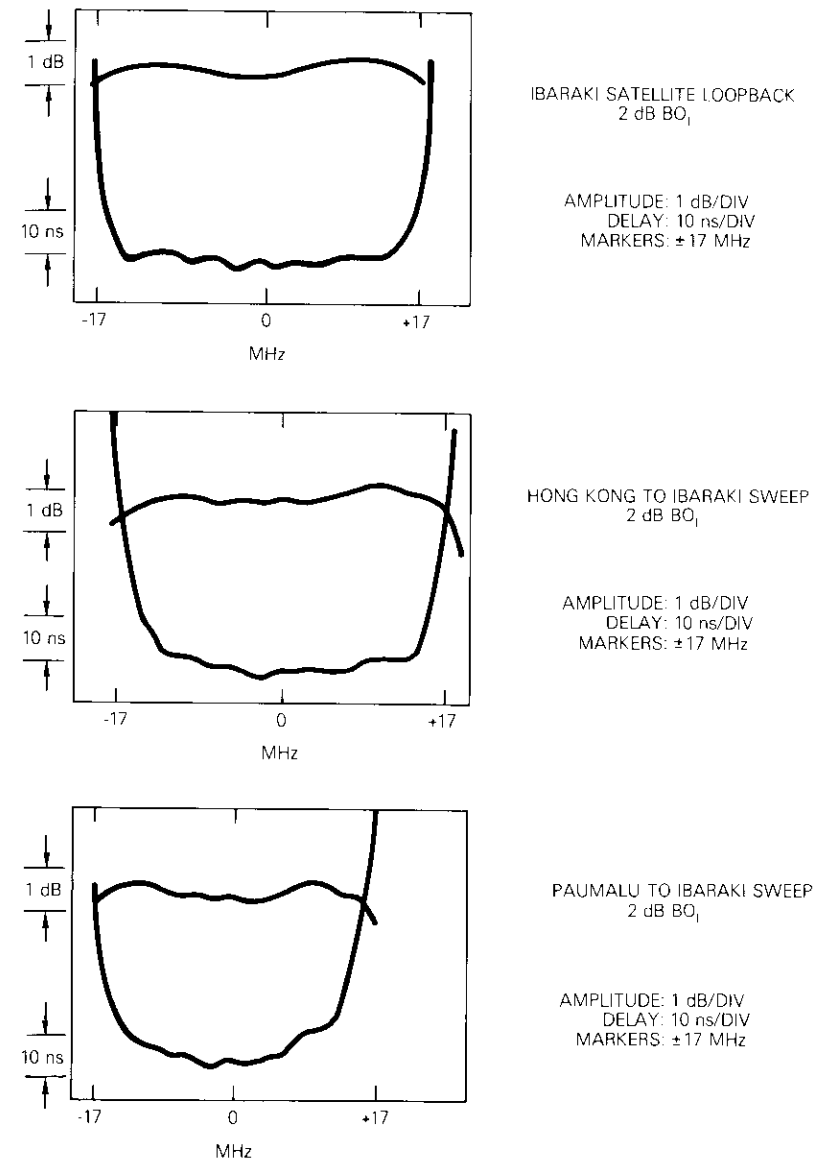


Figure 10. Comparison of Multiple Link Equalization

**TDMA equipment tests**

The TDMA common equipment [3] is an all-digital unit placed between compression/expansion memories and the burst modem (PSK). This unit controls transmit start time, preamble generation, data scrambling, and modem transmission. It also generates apertures for detecting unique words, descrambling data, and processing order wire channels. The common equipment is thus a control unit whose performance is measured in terms of ease of operation, ability to achieve and maintain synchronization, and interfacing to terrestrial modules. Figure 11 is a block diagram of the TDMA terminal.

Timing for the terrestrial network is provided by digital frequency synthesizers. These units generate T-1 and CEPT carrier timing that is synchronous with the transmit and receive TDMA frame rates, respectively. Since all bursts are synchronized to a reference, terrestrial network timing is also synchronized to the TDMA reference station oscillator. Thus, the overall network is synchronous.

Synchronization performance was first tested during an early equipment verification test. The link error rate was increased progressively until the terminal was unable to maintain synchronization. It was found that synchronization was maintained up to a BER of approximately  $10^{-1}$ . This testing also included offsetting the local station oscillator from the specified system symbol rate. The limit of this offset under which the terminal maintained synchronization was also tested. The terminal could maintain synchronization up to  $\pm 9$ -Hz offset in local symbol clock vs reference station symbol clock. This limit, which is based on a software algorithm, provided a range greater than that which will be needed in future TDMA operation.

The reference and alternate stations were identified during the terminal initialization procedure by entering their identification codes from the CRT keyboard. The control procedure continually monitored the reference station reception. When the reference was not detected for several frames, the terminal automatically synchronized to a backup or alternate reference. When the reference reappeared, the terminal again synchronized to it. The aperture used was 12 symbols; thus, the reference had to reappear within this window or switchover could not take place.

To test the automatic switchover procedure, the reference station was taken off the air. The link between the alternate reference and standard traffic terminal was monitored to detect disturbance to the terrestrial network. This included continuous BER measurements on the voice band link, a continuous distortion measurement of a sine wave, and a third-

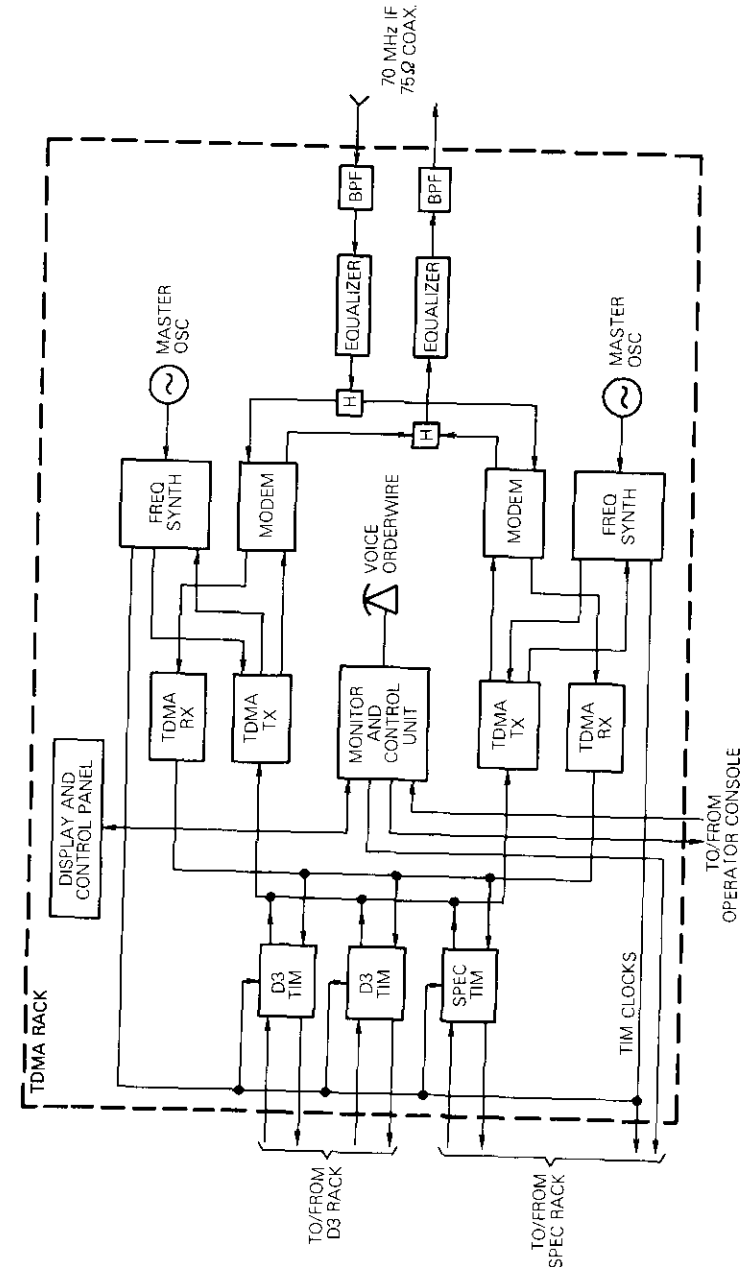


Figure 11. Simplified Block Diagram of the TDMA Terminal

party observed conversation to detect glitches or disturbances. There were no recorded errors or noticeable disturbances under reference station switchover.

The simplified TDMA system operated as a synchronous network. All terrestrial timing was derived from the reference station oscillator. Digital frequency synthesizers generated a 1.544-Mbit/s and 2.048-Mbit/s clock for the D-3 channel bank and SPEC/DSI system, respectively.

Synchronous network operation was achieved by locking the receive terrestrial synthesizer to the received reference burst. Transmit terrestrial timing was generated by frequency synthesizers locked to the transmit frame. Because of satellite motion, the transmit and receive frames slipped relative to each other as a result of Doppler effects.

The synchronous network was tested by making end-to-end BER tests and recording block errors. The operation of the frequency synthesizer was verified in the laboratory and again in the field. However, because satellite time was never available for more than a few hours at a time, long-term testing could not be conducted.

The TDMA terminal is controlled from an operator station with a CRT/keyboard terminal. The interconnection between the TDMA terminal and its operator station is an RS232 serial interface. During the field trials, the operator station was located adjacent to the terminal rack. However, the RS232 interface allows it to be remotely located.

#### Baseband-to-baseband performance

A series of measurements was performed to quantify transmission at analog telephone baseband frequencies. The measurements consisted of test tone to total noise ratio ( $TT/N_t$ )\* and 9.6-kbit/s data modem BER over PCM, DSI, and T-Mux, under a variety of system and terminal conditions. In addition, the prediction aperture of the SPEC [9] transmitter and the attendant  $TT/N_t$  of the distant receiver were monitored at 30-ms intervals. The test results were obtained by specially designed equipment referred to as the data acquisition system (DAS). Each earth station was equipped with a DAS unit, with the Paumalu, Hawaii, installation operating as a master unit for centralized data collection. Measurements made at Hong Kong and Ibaraki were coded and formatted for transmission (via a 4.8-kbit/s modem) to Paumalu where they were recorded.

Table 2 shows typical  $TT/N_t$  measurements recorded at Paumalu upon receipt of a 0-dBm0 1004-Hz test tone transmitted from either Hong Kong

\*This includes noise due to quantizing and bit errors.

or Ibaraki. The TDMA link BERs were  $10^{-6}$  and  $10^{-5}$ . Similarly, Tables 3 and 4 show baseband-to-baseband  $TT/N_t$  performance measured at Ibaraki and Hong Kong.

TABLE 2. BASEBAND-TO-BASEBAND PERFORMANCE  $TT/N_t$  (dB) MEASURED AT PAUMALU (TT IS SINUSOID)

INTERFACING TDMA VIA TIM	DSI GAIN	$TT/N_t$ (dB) BER = $10^{-6}$	$TT/N_t$ (dB) BER = $10^{-5}$	DSI TERRESTRIAL PORT LOADING (%)
PCM (T-Carrier)	—	36.5	34	—
DSI/SPEC	2.4	41.25*	39.25*	84
DSI/SPEC	2	41.25*	39.5*	84
T-Mux	—	36.8	35.2	—

\*C-message weighted.

TABLE 3. BASEBAND-TO-BASEBAND PERFORMANCE  $TT/N_t$  (dB) MEASURED AT IBARAKI (TT IS SINUSOID)

INTERFACING TDMA VIA TIM	DSI GAIN	$TT/N_t$ (dB) BER < $10^{-7}$	$TT/N_t$ (dB) BER = $10^{-6}$	$TT/N_t$ (dB) BER $\approx 10^{-5}$
PCM (T-Carrier)	—	36	—	—
DSI/SPEC	2.0	43 <sup>a</sup>	42 <sup>a,b</sup>	33 $\pm$ 2
DSI/SPEC	2.4	43 <sup>a</sup>	41.5 <sup>a</sup>	—
T-Mux	—	36.4 <sup>c</sup>	—	—

<sup>a</sup>C-message weighted.

<sup>b</sup>Occasionally degraded to 37 dB because of link conditions.

<sup>c</sup>Obtained with 0-dBm0 test tone;  $TT/N_t$  = 26 dB for test tone of -29 dBm0.

TABLE 4. BASEBAND-TO-BASEBAND PERFORMANCE  $TT/N_t$  (dB) MEASURED AT HONG KONG (TT IS SINUSOID)

INTERFACING TDMA VIA TIM	DSI GAIN	$TT/N_t$ (dB) BER $\approx 10^{-7}$	$TT/N_t$ (dB) BER $\approx 10^{-6}$	$TT/N_t$ (dB) BER = $10^{-5}$
PCM (T-carrier)	—	36.5	36.3	—
DSI/SPEC	2.0	43 <sup>a</sup>	42 <sup>a,b</sup>	—
DSI/SPEC	2.4	43 <sup>a</sup>	41.5 <sup>a,c</sup>	43
T-Mux	—	37.2 <sup>d</sup>	—	—

<sup>a</sup>C-message weighted.

<sup>b</sup>Occasionally decreased to 37 dB because of link conditions.

<sup>c</sup>Actively varying to as low as 30 dB because of link conditions.

<sup>d</sup>Measured at -5 dBm0 test tone level; dropped to 32.5 dB for TT = -15 dBm0, and to 27.3 dB for TT = -26 dBm0.

T-Mux equipment was located only in Paumalu; however, the 1.544-Mbit/s bit stream which resulted after digital conversion of two 12-channel FDM groups was of T-carrier format. Therefore, transmission from Paumalu could be received by D-3 channel equipment at both Ibaraki and Hong Kong.

Typical performance of the SPEC/DSI system is shown in Figure 12. The lower trace shows the test tone to noise ratio, whereas the upper trace indicates ensemble speech activity. A negative correlation arises between these two quantities because higher speech activity forces a larger predictor aperture, which in turn causes a decrease in TT/N ratio [9].

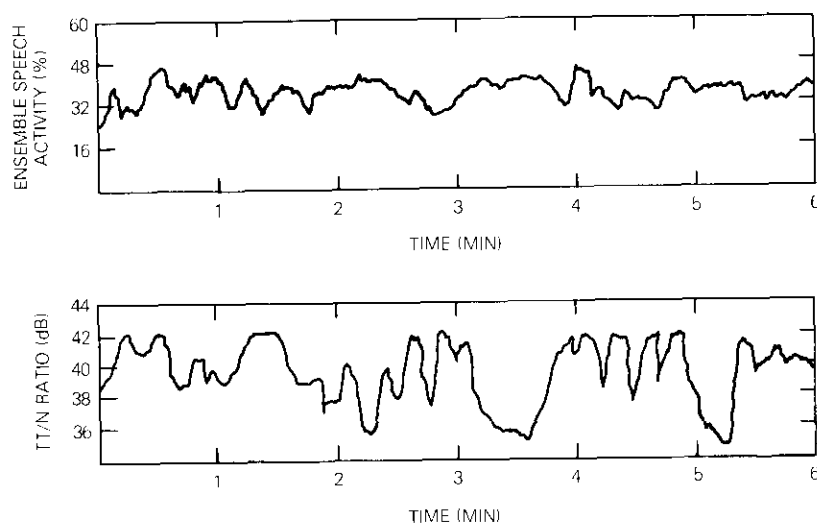


Figure 12. SPEC/DSI Performance

The 9.6-kbit/s modem tests were performed with CCITT V.29 compatible equipment. Modems were located at each earth station and connected to the terminals via simulated terrestrial access circuits with injected noise at typical levels. The BERs of the 9.6-kbit/s data were measured for various TDMA link (BER) conditions.

In general, satisfactory modem performance was not obtained unless the TDMA link operated at a BER of about  $10^{-7}$  or less. The general performance trend is shown by the curve in Figure 13, which is fitted through scattered points that resulted from measurements. Actual BER values

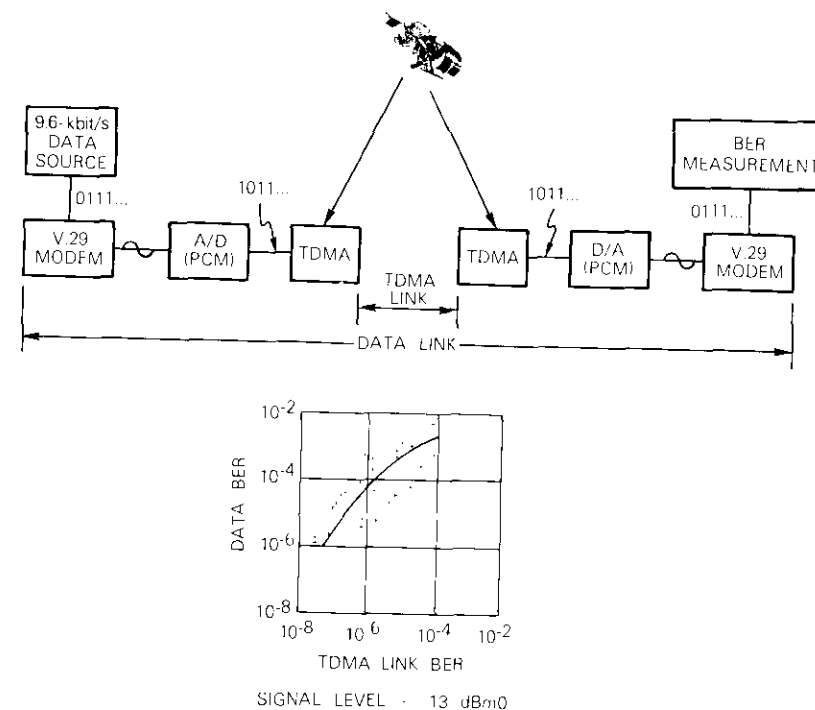


Figure 13. 9.6-kbit/s Data BER vs TDMA Link BER

could deviate by a factor of as much as 4 from the curve.

The 9.6-kbit/s error rate was almost two orders of magnitude worse than the TDMA link error rate. Errors in the modem usually occurred in spurts of as many as 100 bits. This situation perhaps can be partially explained by realizing that when a large PCM sample is significantly in error, a ripple in the reconstructed data modem waveform of several milliseconds could result. This, in turn, could cause many consecutive symbols, each representing four bits, to be in error.

#### Subjective test results for U.S. end

The subjective test consisted of conversations between pairs of talkers (one member at Paumalu and the other in Hong Kong), under a variety of connections and conditions. Each pair conducted 12 conversations brought about by a task that involved mutual agreement on rank ordering

a set of pictures. After each conversation, the circuit quality was rated by the subjects as excellent (E = 4), good (G = 3), fair (F = 2), poor (P = 1), or unacceptable (U = 0). The circuit conditions under test were as shown in Table 5.

TABLE 5. CIRCUIT CONDITIONS FOR SUBJECTIVE TEST

CIRCUIT CONDITION VIA TDMA	BIT ERROR RATE	ACCESS LINE CONDITION
PCM	$10^{-6}$	Nominal
SPEC/DSI		Nominal
PCM		3-dB high loss at each end
SPEC/DSI	$10^{-4}$	3-dB high loss at each end
PCM		Nominal
SPEC/DSI		3-dB high loss at each end
PCM	$10^{-6}$	Nominal
SPEC/DSI		3-dB high loss at each end
PCM		3-dB high loss at each end
SPEC/DSI	$10^{-4}$	Nominal
SPEC/DSI		3-dB high loss at each end
PCM		3-dB high loss at each end
T-Mux at Paumalu	$10^{-6}$	Nominal
T-Mux at Paumalu		3-dB high loss at each end
FDM/FM*	$10^{-4}$	Nominal
FDM/FM*		3-dB high loss at each end

\*-51 dBm0p

The 12 circuit conditions were suitably arranged in a Latin Square [10] experimental design so the effects of the test subject and conversation stimulus could be separated from that of the circuit condition. Note that the experiment was "anchored" by including a regular FDM/FM satellite circuit as one of the test conditions.

The experiment was also designed to estimate contributions to overall variability from three other possible sources independently: test subject variability (S), picture set variability (P), and inherent human perception variability (E). The latter is also termed experimental or residual error.

The results of the analysis for U.S. subjects are shown in the usual format of an Analysis of Variance Table in Table 6.

TABLE 6. ANALYSIS OF VARIANCE RESULTS FOR SUBJECTIVE TEST

SOURCE OF VARIATION	SUM OF SQUARES	DEGREES OF FREEDOM	MEAN SQUARE	F-RATIO
Circuit Condition (C)	21.38	11	1.94	3.80 <sup>a</sup>
Subjects (S)	41.42	11	3.77	7.39 <sup>b</sup>
Picture Sets (P)	2.86	11	0.26	0.51 <sup>c</sup>
Residual Error (E)	50.87	99	0.51	

<sup>a</sup>Very significant; circuit conditions differed more than by chance alone.

<sup>b</sup>Highly significant; test subjects showed very different reactions to circuit quality.

<sup>c</sup>Not significant; picture sets had no influence on test subject response to circuit quality.

A similar analysis was performed on the responses obtained in Hong Kong, with results similar to those given in Table 6. The mean opinion scores of U.S. and Hong Kong subjects are provided in Table 7. The effect of high access circuit loss was a noticeable factor for the Hong Kong subjects, who generally rated the quality lower because of it.

TABLE 7. MEAN OPINION SCORES (MAX = 4, MIN = 0) OBTAINED FROM SUBJECTIVE TEST

EARTH STATION	PCM AT BER $10^{-6}$	DSI AT BER $10^{-6}$	PCM AT BER $10^{-4}$	DSI AT BER $10^{-4}$	T-MUX AT BER $10^{-6}$	FDM/FM
Nominal Circuit Loss						
U.S.	3.42	3.67	2.75	3.17	3.33	3.42
H.K.	3.40	3.17	2.92	3.08	2.92	2.75
6-dB High Circuit Loss						
U.S.	3.67	3.58	2.83	3.17	3.42	3.42
H.K.	2.67	2.75	3.00	2.83	2.92	2.58

### System summary

#### Link calibration tests

Link equalization and maintenance of bit error stability were considered the most difficult items in the overall link calibration test program. Table 8 gives the best BER results and the maximum system C/N measured (over 36-MHz bandwidth) during the test programs.

#### TDMA test summary

The architectural concepts incorporated into the TDMA terminal design were the use of a computer-type bus structure for interconnecting

TABLE 8. BEST BER RESULTS AND MAXIMUM C/N

EARTH STATION (RECEIVING)	TEST CONFIGURATION	BEST BER (CONTINUOUS MODE)	MAXIMUM SYSTEM C/N (dB)	
			MEASURED	COMPUTED
Paumalu	Satellite Loopback	Better than $1 \times 10^{-8}$	20.5	20.5
Ibaraki	Satellite Loopback	Better than $1.5 \times 10^{-9}$	22.8*	20.4
Ibaraki	Hong Kong Transmitting	Better than $1.5 \times 10^{-8}$	—	—
Hong Kong	Satellite Loopback	Better than $1.2 \times 10^{-8}$	20.2	19.8
Hong Kong	Ibaraki Transmitting	Better than $9 \times 10^{-7}$	—	—

\*Suspect up-path noise compression or difference in saturation flux density as used in computations and the actual flux density required.

terrestrial interface module (TIM) units with the common equipment, a microprocessor for terminal operation and network control, and a multiplexing/demultiplexing network that could be reconfigured by updating control memory patterns, and which also allowed independent routing of PCM multiplexed channels.

The compression/expansion memories located in the TIM units are viewed from the common equipment as a single random access memory. The multiplexing network which contains control memories is located in the common equipment. This network controls the transfer of data from the compression memory to the modem for transmission, and loads burst data into the assigned expansion memory. It can be quickly and easily altered to provide new network interconnections via keyboard entries from an operator station.

The TDMA terminal mapping procedure which formats and loads the multiplexer/demultiplexer control memories is used each time the terminal is powered on. During the field test, this procedure was used each day for several weeks. The mapping capability operated as expected and was found to be easily understood. The ability to rearrange traffic by simple operator commands demonstrated the flexibility of TDMA. The burst time plan can be prepared off-line well in advance of frame format and traffic changes; or via the addition of software and signaling channels, burst-time plans can be dynamically implemented. The single-carrier-per-

transponder advantage of TDMA allows this rapid traffic rearrangement.

During laboratory and field testing, these concepts in terminal architecture were continually tested. They allowed extreme ease in network operation, and earth station personnel had no difficulty in grasping the TDMA concept or in operating the terminals.

#### Observation on baseband-to-baseband tests

The analysis of the results from the subjective test was complicated by malfunctioning T-Mux equipment toward the end of the experiment. This resulted in 11 conversations which either were not conducted via the T-Mux, or occurred under dubious conditions. The resultant 11 data points (*i.e.*, ratings) were omitted and treated as "missing observations" in the analysis; that is, ratings were estimated by minimizing the mean square experimental error variance. However, the following general observations can be made:

- a. At the TDMA BER of  $10^{-6}$ , PCM, DSI, T-Mux, and FDM/FM circuits performed very well and equally well statistically for U.S. subjects; Hong Kong subjects rated conventional FM/FDM circuits significantly lower.
- b. At the TDMA BER of  $10^{-4}$ , a marked drop in quality was experienced in both PCM and DSI (T-Mux was not tested at that BER). However, DSI performed significantly better than PCM, most likely due to the action of the voice switch of DSI which prevents the listener from hearing distortion caused by bit errors during the silent intervals of speech.
- c. Access circuit loss did not influence the opinion of the test subjects in the United States, but Hong Kong subjects rated the calls lower when high access circuit loss existed.

#### Conclusions

The field test reported in this paper demonstrated the feasibility of TDMA in an operational satellite network. In particular, the TDMA equipment featured architectural concepts incorporating a computer-type bus structure for interconnecting terrestrial interface units with common equipment; microprocessors for terminal operation and network control; and a multiplexing/demultiplexing network that could be reconfigured by updating control memory patterns and allowing independent routing of PCM multiplexed channels.

The TDMA terminal design was based on the INTELSAT BG-1-18

Specification. It operated with a 750- $\mu$ s frame period at a rate of 60.032 Mbit/s. The network protocols were simplified to reduce terminal expenses. Operation of the equipment by earth station technicians was easily understood and mapping procedures for rerouting traffic were executed by simple entry on a keyboard terminal, demonstrating the flexibility of TDMA.

Link equalization for achieving best BER performance and maintenance of this BER over a prolonged period was given special attention. The overall technical performance was excellent. In subjective terms, PCM/TDMA transmission provided equal or better quality than that of FDM/FM/EDMA transmissions of current satellite systems.

#### Acknowledgments

The TDMA field test emerged through the initiative of S. J. Campanella, who also had led the R&D program related to the development of TDMA equipment. A. Ghais and S. Skjei of COMSAT's International Communications Division conducted negotiations with foreign partners and provided valuable assistance during the test program development.

The TDMA terminal implementation was directed by R. P. Ridings. R. Lindstrom and S. Gupta developed the hardware design; P. Hoover was responsible for the software implementation; and R. Jones managed the fabrication and hardware assembly and assisted with equipment testing.

The 60-Mbit/s modem was the responsibility of D. Collins, under the guidance of C. Wolejsza and V. Uzunoglu. Considerable support during the field test was provided by D. Chakraborty in link lineup procedures, and by J. Poklemba and M. Kappes for modem operation.

J. H. Rieser had overall responsibility for DSI terminal implementation and operation, while W. M. Hoblit and P. Lea Clark were responsible for instrumentation to measure baseband performance characteristics. J. G. Phipps, Jr., with assistance from local Paumalu personnel, was responsible for executing the subjective test.

The authors would also like to thank the earth station managers, engineers, technicians, and support personnel at Paumalu, Ibaraki, and Hong Kong. Their cooperation was indispensable to the success of the field test.

#### References

- [1] C. J. Wolejsza, D. Chakraborty, and V. Uzunoglu, "A Universal Modem Design for Digital Satellite Communications," *ICC 1976 Conference Record*, Vol. 1, pp. 3-12-3-18.

- [2] D. Chakraborty, T. Noguchi, S. J. Campanella, and C. J. Wolejsza, "Digital Modem Design for Nonlinear Satellite Channels," Fourth International Conference on Digital Satellite Communications, Montreal, Canada, October 23-25, 1978.
- [3] T. Dobyns, V. Gupta, R. Ridings, R. Lindstrom, and P. Hoover, "Simplified TDMA Terminal," Fifth International Conference on Digital Satellite Communications, Genoa, Italy, March 23-26, 1981.
- [4] S. J. Campanella and J. A. Sciulli, "Speech Predictive Encoding Communications System for Multichannel Telephony," *IEEE Transactions on Communications*, COM-21, No. 7, 1973, pp. 827-835.
- [5] W. G. Schmidt, "The Application of TDMA to the INTELSAT IV Satellite Series," *COMSAT Technical Review*, Vol. 3, No. 2, Fall 1973, pp. 257-275.
- [6] G. P. Vergelli and D. Chakraborty, "Computer-Aided Group Equalization for Broad-Band Satellite Transponder Applications," *IEEE Transactions on Communications*, COM-21, October 1973, pp. 1152-1156.
- [7] R. W. Lucky, "Automatic Equalization for Digital Communication," *Bell System Technical Journal*, Vol. 44, pp. 547-588.
- [8] M. A. Rappaport, "Automatic Equalization of Data Transmission Facility Distortion Using Transversal Equalizers," *IEEE Transactions on Communications Technology*, COM-12, 1964, pp. 65-73.
- [9] H. Suyderhoud, J. Jankowski, and R. Ridings, "Results and Analysis of the Speech Predictive Encoded Communications System Field Trial," *COMSAT Technical Review*, Vol. 4, No. 2, Fall 1974, pp. 371-392.
- [10] O. L. Davies, *Design and Analysis of Industrial Experiments*, Longman, London, 2nd Edition, 1978, pp. 151-198.

Thomas R. Dobyns received a B.S.E.E. from the University of Florida in 1963, and an M.S.E.E. from George Washington University in 1968. He is presently Director of the Digital Communications Laboratory at COMSAT Laboratories. In this capacity, he is responsible for supervising activities in advanced modem development, TDMA development, on-board baseband processing, and network control techniques. His experience includes ARQ error control techniques, earth station monitoring, monopulse tracking, and TDMA terminal design. Mr. Dobyns is a member of IEEE.





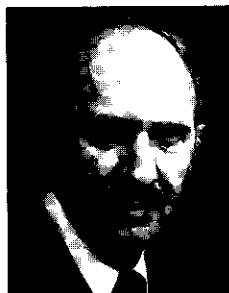
*Dayamoy Chakraborty received a Ph.D. in microwave physics from the University of Surrey, England, in 1967. Since 1968, he has been employed by COMSAT. From 1968 to 1971, he was involved with the satellite system optimization study and the analysis of transmission deviations. Dr. Chakraborty transferred to COMSAT Laboratories in 1971 and has been involved in developing high-speed digital satellite communications systems. Currently, as a Senior Staff Scientist in the Digital Communications Laboratory, he directs research in nonlinear satellite channel model design,*

*maximum likelihood sequence estimation, and digital link technology. Prior to joining COMSAT, he was employed by the British Post Office, Research Department, Dollis Hill, London. Dr. Chakraborty is the author of numerous publications on microwave techniques and communications technology, and is a senior member of IEEE and a corporate member of IEE.*

*H. G. Suyderhoud received the Ingenieur degree in electrical engineering from Delft Technological University in the Netherlands in 1955, and the M.S. degree in applied mathematical statistics from Rutgers, New Brunswick, in 1966.*

*After joining COMSAT laboratories in 1968, he became involved in research on echo suppression and echo cancellation, and the development of subjective evaluation techniques. He became Section Head in 1969 and Department Manager in 1974. In 1981 he assumed the position of Senior Scientist and Assistant to the Executive Director of the Communications Technology Division, where his responsibilities encompass various special projects including speech research and security for television transmission via satellite.*

*Prior to joining COMSAT Laboratories, Mr. Suyderhoud was employed for more than 11 years at Bell Laboratories, where he worked on exchange area and high-density broadband carrier transmission engineering, conducted the first laboratory experiments with echo cancellation, and helped develop standards for picture-phone transmission. He is a senior member of IEEE and a member of the American Statistical Association and the AAAS.*



*Chester J. Wolejsza, Jr., received a B.S.E.E. from Cooper Union in 1966, and an M.S. and E.E. from M.I.T. in 1967, and immediately joined COMSAT Laboratories, where he is currently Manager of the Modulation Techniques Department of the Digital Communications Laboratory, Communications Technology Division. In 1980, he received a Ph.D. in electrical engineering from the Catholic University of America. His current responsibilities include supervision of the design and development of PSK modulation and coding systems, which perform optimally in the band- and power-limited environment of a satellite communications channel. This includes work on single-channel-per-carrier techniques, advanced TDMA modulation systems, and specialized modulation and coding equipment for small terminals. Dr. Wolejsza has authored papers on modulation systems for professional journals and numerous international conferences. He has been a member of Tau Beta Pi and Eta Kappa Nu, and an associate of Sigma Xi. He is currently a member of IEEE.*



# ***An approximation technique for realizing the reciprocal $\sin(x)/x$ frequency response***

J. POKLEMBA

(Manuscript received August 6, 1981)

## ***Abstract***

This study is intended to develop and evaluate network approximations for the reciprocal  $\sin(x)/x$  frequency response utilized in digital data transmission. Two simple transfer functions emerge from the analysis, one with complex poles and the other with both complex poles and zeros. Their performance is evaluated in terms of a computer simulated bit error rate (BER) with raised cosine data filtering for roll-off rates of 10, 50, and 100 percent. The effects of group delay equalization are included. Results indicate that both an improvement in error performance and operation at the Nyquist rate are feasible with reciprocal sinc compensation. The tradeoff between the amount of enhancement and degree of complexity varies depending on the sharpness of the data filtering. If compensation is built into the data filtering, it is possible to obtain near optimum performance with little or no increase in network complexity.

## ***Introduction***

The objective of this investigation is to present a technique for realizing filters that approximate a reciprocal  $\sin(x)/x$  or  $\text{sinc}^{-1}$  frequency response. In digital communications systems, this response is widely used in conjunction with Nyquist filtering so that data may be transmitted with minimal intersymbol interference [1], [2].

The background section of this paper presents a simple model of a data communications link which demonstrates the need to match the source, whose output is an arbitrary digital data sequence, to a band-limiting Nyquist channel filter, whose characteristics are defined for an impulsive input. The basic properties of the Nyquist transfer function, which give rise to data transmission without intersymbol interference, are outlined. The reciprocal sinc matching characteristic is then defined in terms of its magnitude and group delay responses.

The solution is carried out by expansion of the sinc function as a power series in frequency. A hierarchy of network transfer functions is similarly expanded, and their coefficients equated; a pole-zero approximation for the  $\text{sinc}^{-1}$  function ensues. In particular, a generalized second-order transfer function in numerator and denominator was selected as the highest-order solution to be evaluated. From a network point of view, this corresponds to two poles and two zeros. As the results unfolded, other degenerate cases appeared to be of interest, namely, the complex-pole and the single pole-zero solutions.

The relative merit of this technique was evaluated by means of BER performance. Degradation due to the sinc approximation was isolated using ideal computer-simulated square-root Nyquist data filters and detection processing. The effect of varying the roll-off rate of the filtering was examined by employing 10-, 50-, and 100-percent raised cosine responses. To be equitable, BER comparisons were made with respect to an unmatched Nyquist raised cosine channel, whereby the link half amplitude bandwidth-symbol time ( $BT$ ) product was increased to optimize the error rate. Initially, only  $\text{sinc}^{-1}$  amplitude approximations were evaluated. Later, delay equalization was analyzed and found to substantially influence the results.

Active network realizations are presented to demonstrate how the approximation poles and zeros might be transformed into actual network structures. These include implementations for complex pole, complex pole-zero, and second-order group delay equalization topologies.

An added section explores the utility of square-root  $\text{sinc}^{-1}$  compensation at both ends of the link. Solutions for poles and zeros, BER, and network realizations have been included as before. The result is that about 0.1 dB in performance may be sacrificed to allow for identical filtering in both modulator and demodulator.

In summary, it was found that single pole-zero  $\text{sinc}^{-1}$  matching was not suitable for operation at the Nyquist rate. The complex pole-zero and delay-equalized complex pole solutions had virtually identical performances over the entire range of roll-off rates. Also for rates between 10

and 50 percent, these solutions were capable of performing with 0.1 dB of ideal. To achieve similar performance for roll-off rates approaching 100 percent, the delay-equalized complex pole-zero solution was required. Thus, the softer the filter, the more extensive the approximation required.

### Background

A simplified data transmission system, as depicted in Figure 1, consists of a data source, which produces information bits at a rate  $R$  in the

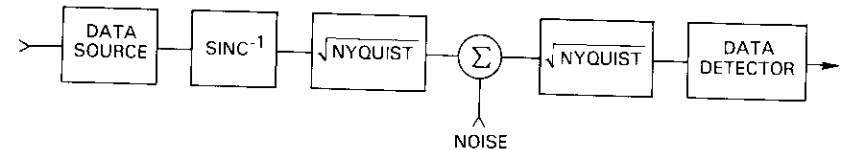


Figure 1. Data Transmission System

form of digital pulses of duration  $T = 1/R$ . Also included are transmit and receive filtering, a linear additive noise channel, and a data detector. The filter characteristics and apportionment are explained as follows. If the channel is band limited, individual pulses will smear and interfere with adjacent symbols. Nyquist, however, has set forth criteria on the channel transmittance function that permit operation without intersymbol interference [3]. These are illustrated in Figure 2. Basically, any frequency response whose magnitude has odd symmetry about the half-amplitude

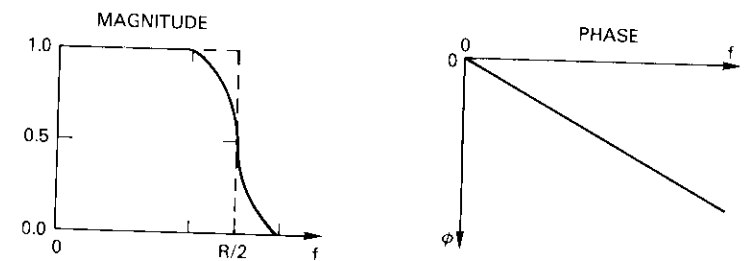


Figure 2. Nyquist Magnitude and Phase Criteria

point (where frequency equals symbol rate divided by 2), and whose phase is linear, satisfies the Nyquist criteria. In addition, from optimum detection theory it is well-known that with a linear additive white Gaussian noise channel, the receive filter should be matched to the transmit.

Since Nyquist signals exhibit even time symmetry, a delayed time-reversed version of the transmit impulse response is still the transmit impulse response. Thus, the optimal way to subdivide the Nyquist characteristic is by imparting its square root to both transmitter and receiver. Moreover, the link would be well-defined if the source delivered impulses. Instead, an incoming data pulse of width  $T$  has a spectrum given by

$$S(f) = \frac{\sin(\pi fT)}{(\pi fT)} = \text{sinc}(\pi fT) \quad (1)$$

whereas the impulse spectrum is flat. Consequently, an additional filtering operation is necessary to equalize or whiten the spectrum of the source. The characteristic which is required, the reciprocal of  $\sin(\pi fT) / (\pi fT)$ ,  $\text{sinc}^{-1}$ , is shown in Figure 3. Note that its group delay is exactly equal to zero over each lobe, and impulsive at the nodal points.

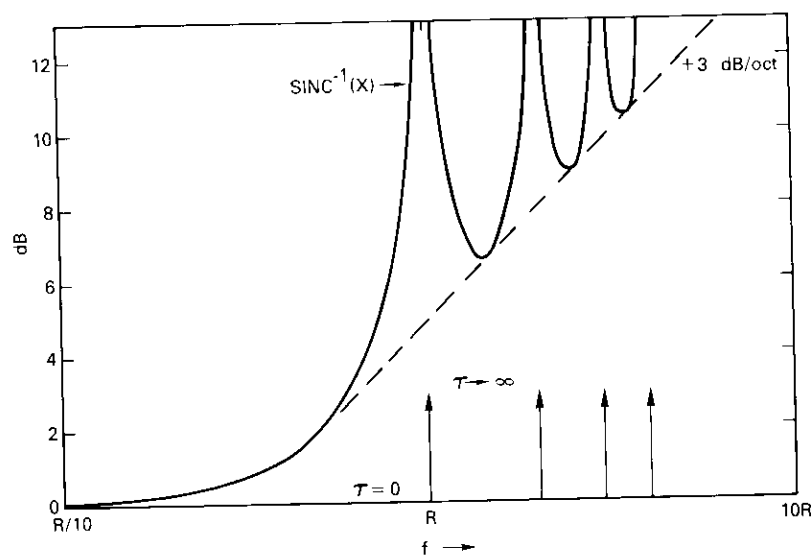


Figure 3.  $\text{Sinc}^{-1}$  Magnitude and Group Delay

This is due to abrupt  $180^\circ$  phase transitions at the zero crossings of the sinc function. Clearly, it would be impossible to realize this function exactly. A reasonable spectral approximation for the amplitude response, however, is conceivable. The group delay should automatically be com-

pensated to some extent because of its one-to-one relationship with amplitude in minimum phase networks.

### Solution method

A power series approximation technique was selected because of the relative ease with which the trigonometric sinc function may be characterized. Likewise, a candidate network transfer function will be expanded as a power series in frequency. In this manner, like coefficients can be equated, and the poles and zeros of the approximation may be determined. Inherent to this particular approach is that, for a monotonic function with restricted complexity, the matching will be virtually perfect at low frequencies and gradually diverge as the range is increased. This is in contrast to a minimum mean square error technique which generally has a uniform equiripple error over the limits of interest.

How far along the frequency axis must the sinc function be approximated? The tendency is to assume that just beyond the Nyquist bandwidth,  $B = R/2$  might be sufficient. However, the ultimate system performance indicator, BER, will subsequently be used to make this determination.

### Power series expansion

For convenience, the solution will be carried out for the original function  $\text{sinc}(\pi fT)$ . Since the magnitude squared characteristic is more conducive to power series manipulation, the expansion yields

$$|G(\omega)|^2 = 1 - \frac{2}{4!}(\omega/R)^2 + \frac{2}{6!}(\omega/R)^4 - \frac{2}{8!}(\omega/R)^6 + \dots \quad (2)$$

The next step is to choose a network whose transfer function will approximate the power series. Clearly, the higher the order the better the match will be. As the order increases, however, so does the complexity of the solution. A reasonable place to begin is with a generalized second-order transfer function in numerator and denominator. In this manner, the first five coefficients in equation (2) may be equated. Lower order degenerate cases can then easily be formed by setting appropriate terms to zero.

### Generalized second-order network solution

In terms of time constants and damping ratios, the transfer function in Laplace notation is

$$H(s) = \frac{1 + s(2Z_p\tau_z) + s^2(\tau_z^2)}{1 + s(2Z_p\tau_p) + s^2(\tau_p^2)} \quad (3)$$

Substituting variables ( $s = j\omega$ ) and taking the magnitude squared of the reciprocal gives

$$|G(\omega)|^2 = \frac{1 + a_1\omega^2 + a_2^2\omega^4}{1 + b_1\omega^2 + b_2^2\omega^4}$$

where

$$\begin{aligned} a_1 &= (2Z_p\tau_p)^2 - 2\tau_p^2 \\ a_2^2 &= \tau_p^4 \\ b_1 &= (2Z_z\tau_z)^2 - 2\tau_z^2 \\ b_2^2 &= \tau_z^4 \end{aligned} \quad (4)$$

A power series is obtained by dividing out equation (4). Equating these coefficients with those from expression (2) yields four independent equations:

$$a_1 - b_1 = \frac{-2}{4!R^2} \Delta K_1 \quad (5a)$$

$$(a_2^2 - b_2^2) - b_1K_1 = \frac{-2}{6!R^4} \Delta K_2 \quad (5b)$$

$$-b_2^2K_1 - b_1K_2 = \frac{-2}{8!R^6} \Delta K_3 \quad (5c)$$

$$-b_2^2K_2 - b_1K_3 = \frac{2}{10!R^8} \Delta K_4 \quad (5d)$$

Since each succeeding expression is a linear combination of its previous counterparts, the solutions are as follows:

$$b_1 = \frac{K_2K_3 - K_1K_4}{K_1K_3 - K_2^2} = \frac{2.5641 \times 10^{-2}}{R^2} \quad (6a)$$

$$a_1 = K_1 + b_1 = \frac{-5.7692 \times 10^{-2}}{R^2} \quad (6b)$$

$$b_2^2 = \frac{b_1K_2 + K_3}{K_1} = \frac{2.5946 \times 10^{-4}}{R^4} \quad (6c)$$

$$a_2^2 = b_2^2 + K_2 + b_1K_1 = \frac{9.0049 \times 10^{-4}}{R^4} \quad (6d)$$

These values can be converted into the second-order network parameters. It is evident that  $a_2$  and  $b_2$  must be positive, but  $a_1$  and  $b_1$  may be less than zero.

$$f_z = \frac{1}{2\pi\tau_z} = \frac{1}{2\pi} \sqrt[4]{\frac{1}{b_2^2}} = 1.25401R, \text{ Hz} \quad (7a)$$

$$f_p = \frac{1}{2\pi\tau_p} = \frac{1}{2\pi} \sqrt[4]{\frac{1}{a_2^2}} = 0.91876R, \text{ Hz} \quad (7b)$$

$$\zeta_z = \sqrt{\frac{1 + 2b_1(\pi f_z)^2}{2}} = 0.94761 \quad (7c)$$

$$\zeta_p = \sqrt{\frac{1 + 2a_1(\pi f_p)^2}{2}} = 0.13915 \quad (7d)$$

They can also be expressed in pole-zero form as

$$\begin{aligned} \text{complex zero: } &-(\zeta_p \pm j\sqrt{1 - \zeta_p^2}) \omega_z \\ &-(7.4664 \pm j2.5169) R, \text{ rad/s} \end{aligned} \quad (8a)$$

$$\begin{aligned} \text{complex pole: } &-(\zeta_z \pm j\sqrt{1 - \zeta_z^2}) \omega_p \\ &-(0.80326 \pm j5.7166) R, \text{ rad/s} \end{aligned} \quad (8b)$$

The magnitude response of this network is plotted in Figure 4a. It is interesting to note that the mathematical solution does not coincide with that anticipated by circuit designers. It is expected that the zero break frequency should precede that of the pole to yield an overall upward swing. However, the mathematics has accounted for the peaking by means of a dominant underdamped complex-pole pair.

From Figure 4a, it is evident that the approximation is virtually exact out to  $0.75R$ . This amply exceeds the Nyquist half-amplitude point of  $0.5R$ , which was the tentative goal. The corresponding group delay response is shown in the lower portion of Figure 4b. The upper curve is group-delay equalized and will be discussed later. Note that the lower curve has negative delay at the lower frequencies. This corresponds to increasing phase shift, which is characteristic of networks whose phase shift from zeros exceeds that from the poles. It can easily be visualized that in the vicinity of  $R$  the curve is approaching the impulse produced at the first node of the sinc function. In addition, the group delay is nearly

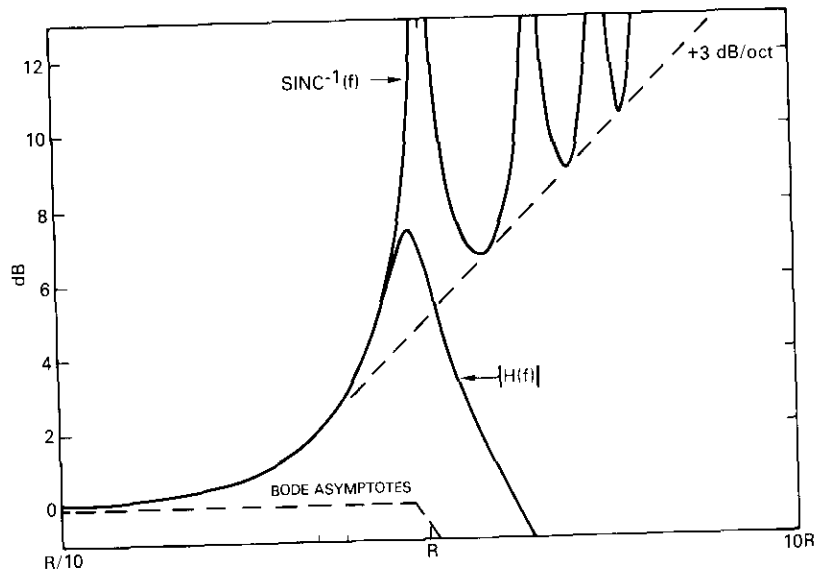


Figure 4a. Complex Pole-Zero Magnitude Approximation

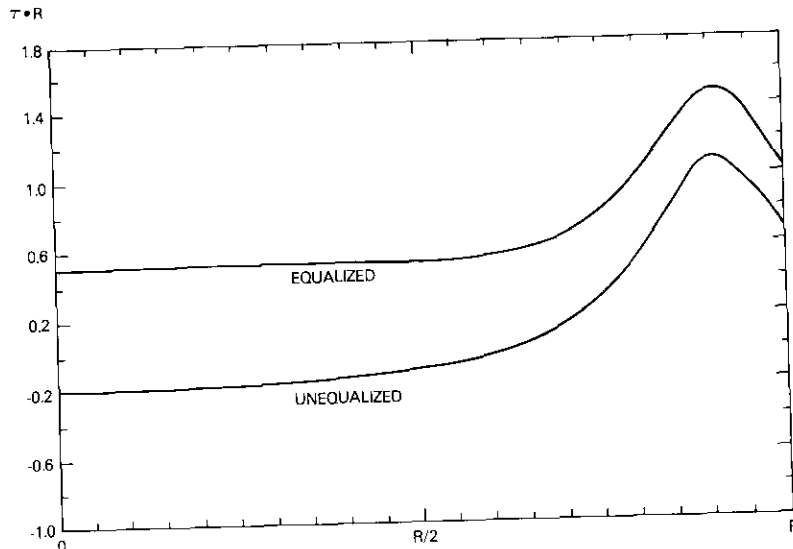


Figure 4b. Complex Pole-Zero Group Delay

flat over the Nyquist band. Thus, most of the energy within the main lobe has been appropriately weighted. However, this energy argument also

implies that the sharpness of the data filtering affects the range of compensation necessary; as with softer roll-off rates, the high frequency error divergence will be more pronounced. This will be evaluated quantitatively by BER comparisons in subsequent sections.

**Complex pole solution**

With the generalized second-order solution, it was evident that the underdamped pole pair did most of the work. Thus, it would appear worthwhile to develop the approximation for a single complex-pole pair. This can be accommodated simply by setting  $b_1$  and  $b_2^2$  to zero in equations (4), (5a), and (5b). The solution then degenerates to

$$a_1 = \frac{-2}{4!R^2} = \frac{-8.3333 \times 10^{-2}}{R^2} \tag{9a}$$

$$a_2^2 = \frac{2}{6!R^4} = \frac{2.7778 \times 10^{-3}}{R^4} \tag{9b}$$

$$f_p = \frac{1}{2\pi} \sqrt[4]{\frac{1}{a_2^2}} = 0.69326R, \text{ Hz} \tag{9c}$$

$$\zeta_p = \sqrt{\frac{1 + 2a_1(\pi f_p)^2}{2}} = 0.32360 \tag{9d}$$

$$\begin{aligned} \text{complex pole: } & -(\zeta_p \pm \sqrt{1 - \zeta_p^2}) \omega_p \\ & -(1.4096 \pm j4.1215) R, \text{ rad/s} \end{aligned} \tag{9e}$$

The magnitude and group delay responses for this case have been plotted in Figure 5a and the lower part of Figure 5b, respectively.

**Single pole-zero solution**

For completeness, it is desirable to undertake an approximation for the most degenerate form possible, a purely real zero. However, a dummy pole is required to satisfy the stability requirements of computer simulation. Thus,  $a_2^2$  and  $b_2^2$  are set to zero in equation (4) so that

$$(a_1 - b_1) = \frac{-2}{4!R^2} \tag{10a}$$

Then, with  $a_1$  arbitrarily chosen as  $b_1/120$  ( $\omega_p^2 = 120\omega_c^2$ ), the design equations are

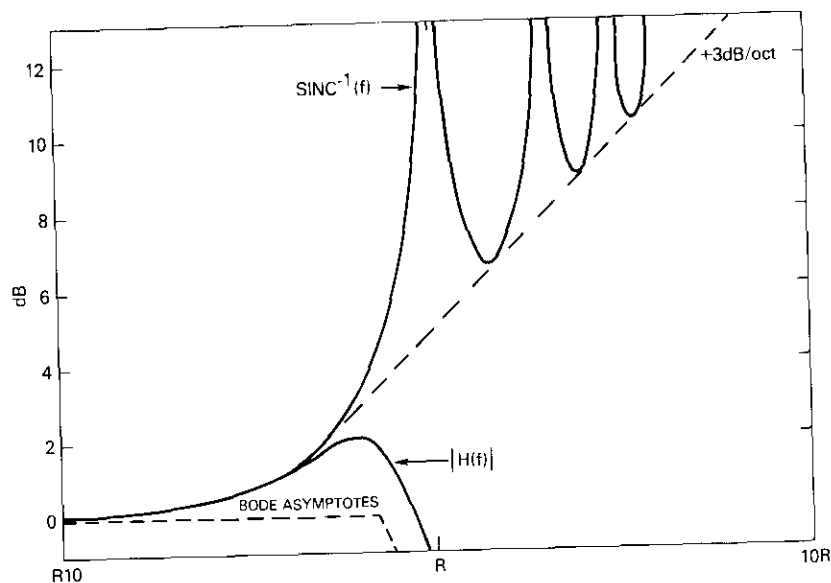


Figure 5a. Complex Pole Magnitude Approximation

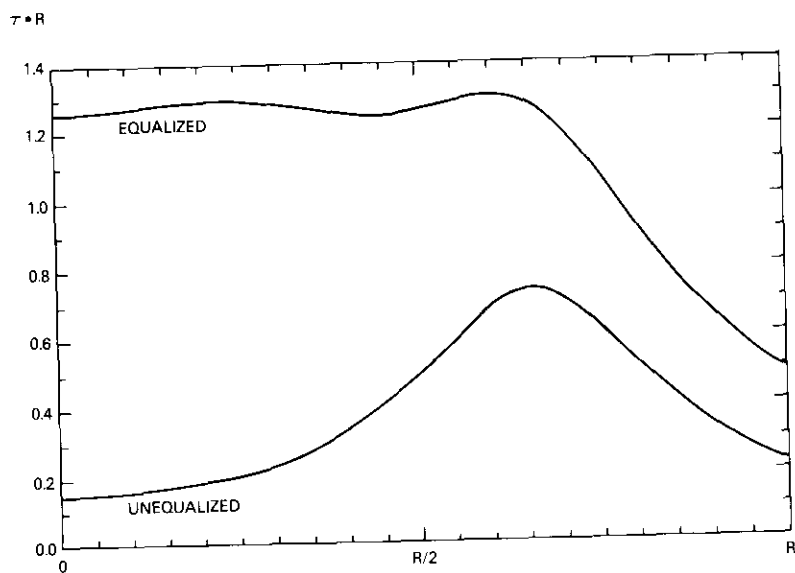


Figure 5b. Complex Pole Group Delay

$$b_1 = \frac{10}{119} \quad (10b)$$

$$f_z = \frac{1}{2\pi\tau_z} = \frac{1}{2\pi} \sqrt{\frac{1}{b_1}} = 0.54903R, \text{ Hz} \quad (10c)$$

$$f_p = \frac{1}{2\pi\tau_p} = \frac{1}{2\pi} \sqrt{\frac{1}{a_1}} = 6.0143R, \text{ Hz} \quad (10d)$$

$$\begin{aligned} \text{real zero: } -\omega_z \\ -3.4497R, \text{ rad/s} \end{aligned} \quad (10e)$$

$$\begin{aligned} \text{real pole: } -\omega_p \\ -37.789R, \text{ rad/s} \end{aligned} \quad (10f)$$

Again, curves for the magnitude and group delay responses are shown in Figures 6a and 6b.

### Performance comparison

At this juncture, it is appropriate to determine the relative merits of the hierarchy of reciprocal sinc compensation networks that were developed in the previous sections. This will be done by means of a BER comparison from computer simulations of the overall channel [4]. To isolate the degradation attributed to the sinc approximation, ideal Nyquist shapes have been selected for data filtering with equal apportionment to transmitter and receiver. Also, since earlier it had been stated that the approximation would be sensitive to roll-off rate, 10-, 50-, and 100-percent raised cosine responses have been chosen to illustrate the trends that ensue with progressively sharper filtering.

### Uncompensated Nyquist channel

Before the error rate of the sinc approximation networks is explored, it will be informative to see what might be attainable without any such aperture equalization. To do this, the  $BT$  product was expanded ( $BT \geq 0.5$ ) until the best error rate was obtained. Curiously enough, this occurred when  $BT = (1 + 0.29r)/2$  for all three cases ( $r = 0.1, 0.5, 1.0$ ). Figure 7 depicts the results. It is evident that little improvement is achievable in the 50- to 100-percent roll-off range of the cosine filters, as they merely suffer 0.2- to 0.3-dB degradation in the absence of compensation. In contrast, the 10-percent case is considerably

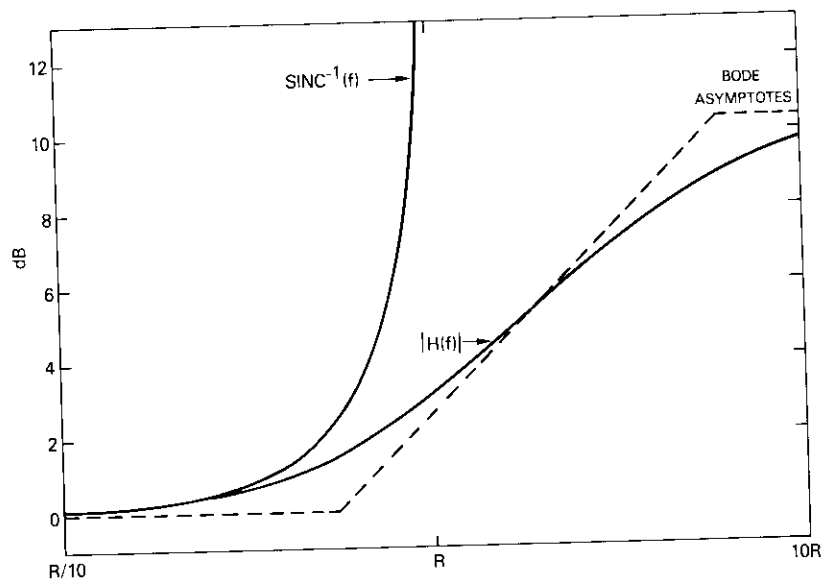


Figure 6a. Single Pole-Zero Magnitude Approximation

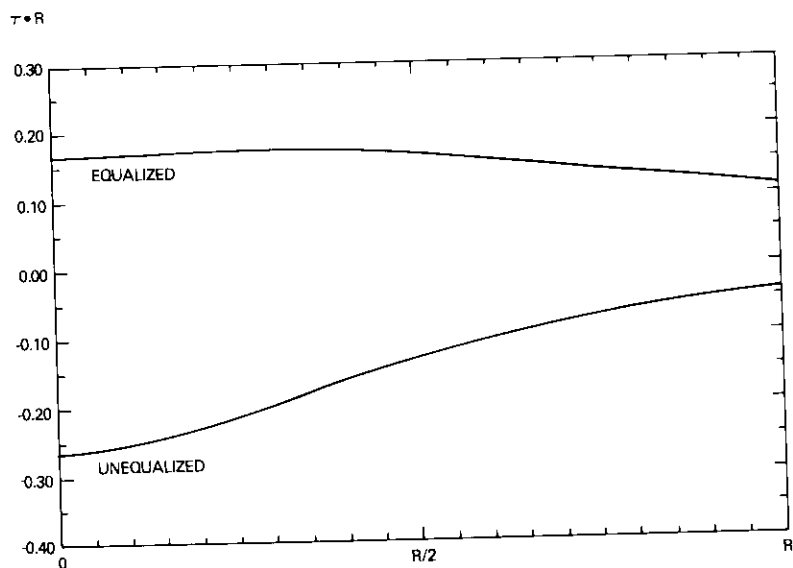


Figure 6b. Single Pole-Zero Group Delay

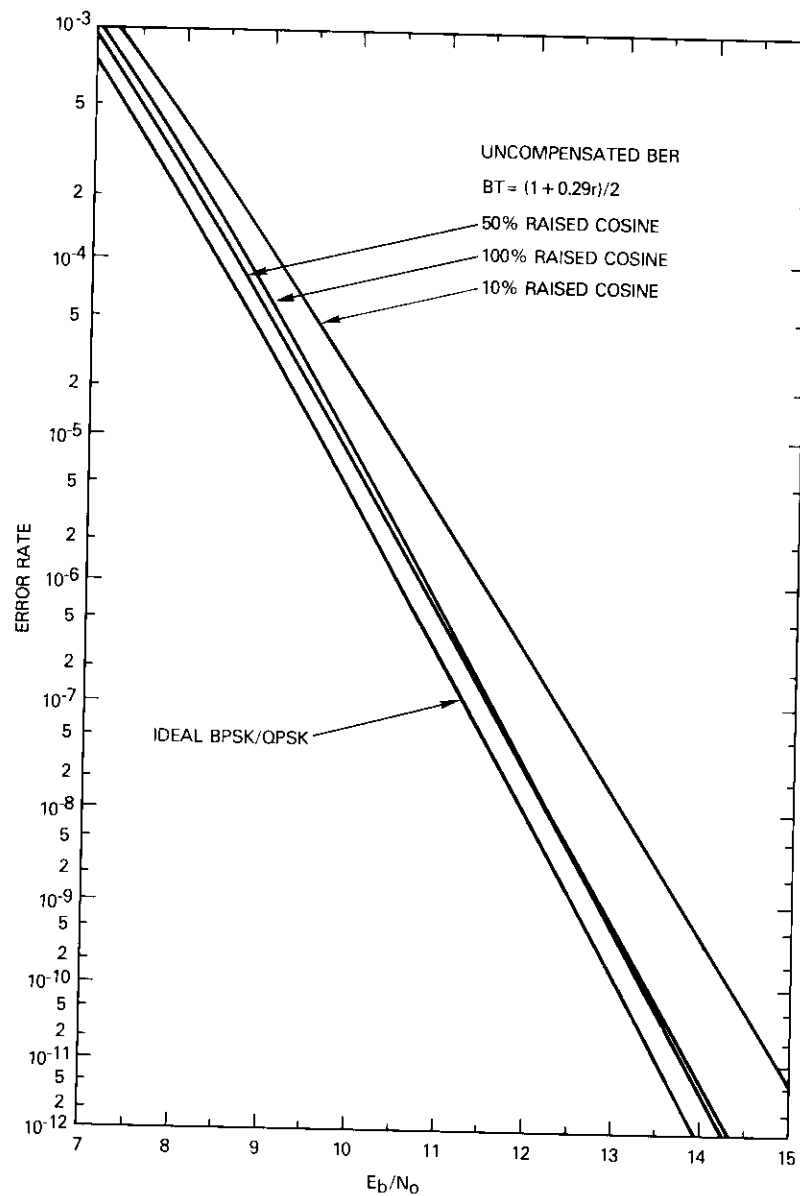


Figure 7. Uncompensated BER

worse. Moreover, the approximation circuitry must enhance these characteristics to the extent that their accompanying increase in complexity is warranted. The particular application will generally reconcile this question. In many instances, however, the aperture equalization may be aggregated into the data filtering with no additional circuitry requirements. Eye patterns for the 50- and 100-percent responses have been included in Figures 8a, 8b, and 8c, respectively.

#### Reciprocal sine amplitude compensation

Comparisons pertaining to the approximation networks will be made with operation at the Nyquist rate only,  $BT = 0.5$ . This will avoid undue complications that would ensue if the  $BT$  product were optimized for each possible solution. It is also in keeping with the ultimate goal of not having to search for an optimum  $BT$  product if sinc compensation is utilized.

Figures 9a, 9b, and 9c illustrate BER performance for the 10-, 50-, and 100-percent raised cosine roll-off filters, respectively. Each plot displays a family of curves with progressively improving error rate, corresponding to the single pole-zero, complex pole, complex pole-zero, and ideal solutions. For roll-off rates of 10 through 50 percent, complex pole-zero equalization demonstrates nearly ideal performance, whereas when the roll-off approaches 100 percent, it yields  $< 0.1$ -dB improvement. These trends appear realistic since the energy distribution of the signal is more spread out with softer filtering, which consequently should entail more elaborate compensation with a power series approximation technique. The eye diagrams corresponding to the acceptable solutions are given in Figures 10a, 10b, and 10c.

#### Reciprocal sine amplitude and group delay compensation

With the relatively simple amplitude equalization solutions developed thus far, the group delay response is not as representative of the Nyquist criterion as it might be. Therefore, the next logical step is to provide delay compensation, and determine whether further enhancement is realizable. This was accomplished by means of a computer program that perturbs all-pass root locations to smooth the delay variation over some prescribed frequency interval. The limits were arbitrarily selected to extend from DC to the Nyquist bandwidth  $R/2$ . The composite group delay responses are given in the upper portions of Figures 4b, 5b, and 6b. Root locations for the delay compensation are listed in Table 1. BER curves for the 10-, 50-, and 100-percent cases are depicted in Figures 11a, 11b, and 11c, respectively.

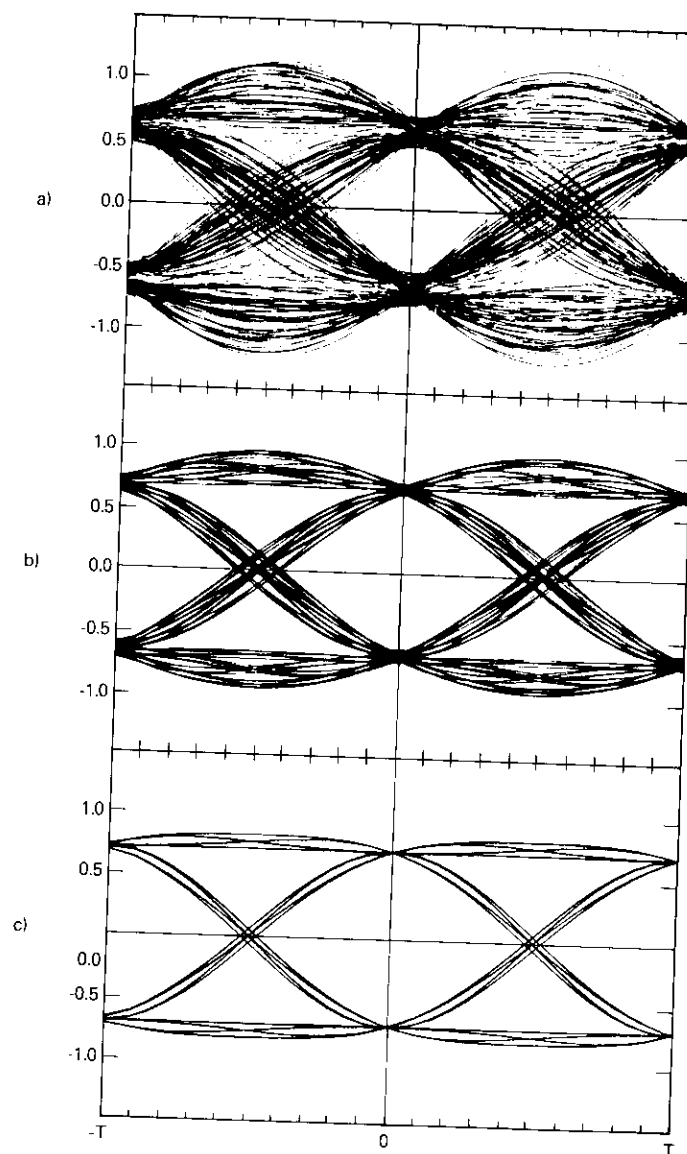


Figure 8. Uncompensated Eye Patterns

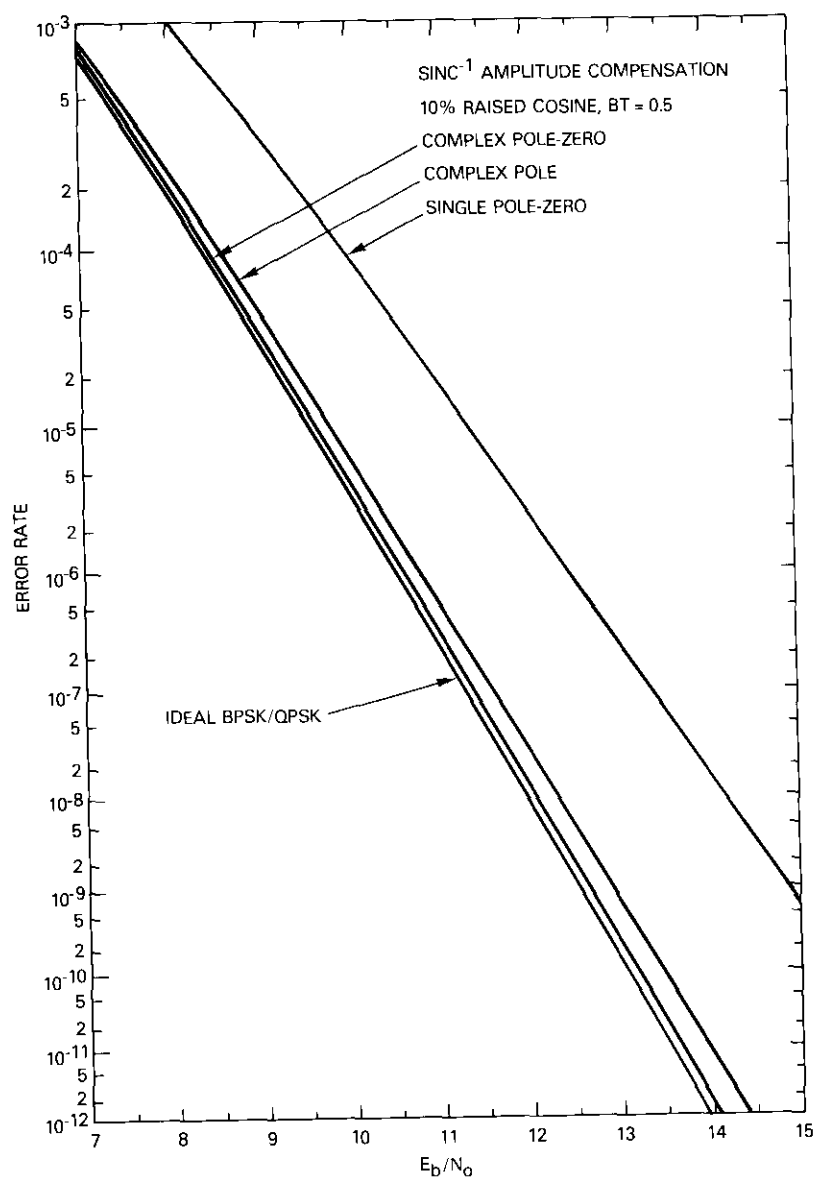


Figure 9a. BER,  $Sinc^{-1}$  Amplitude Compensation 10% Raised Cosine,  $BT = 0.5$

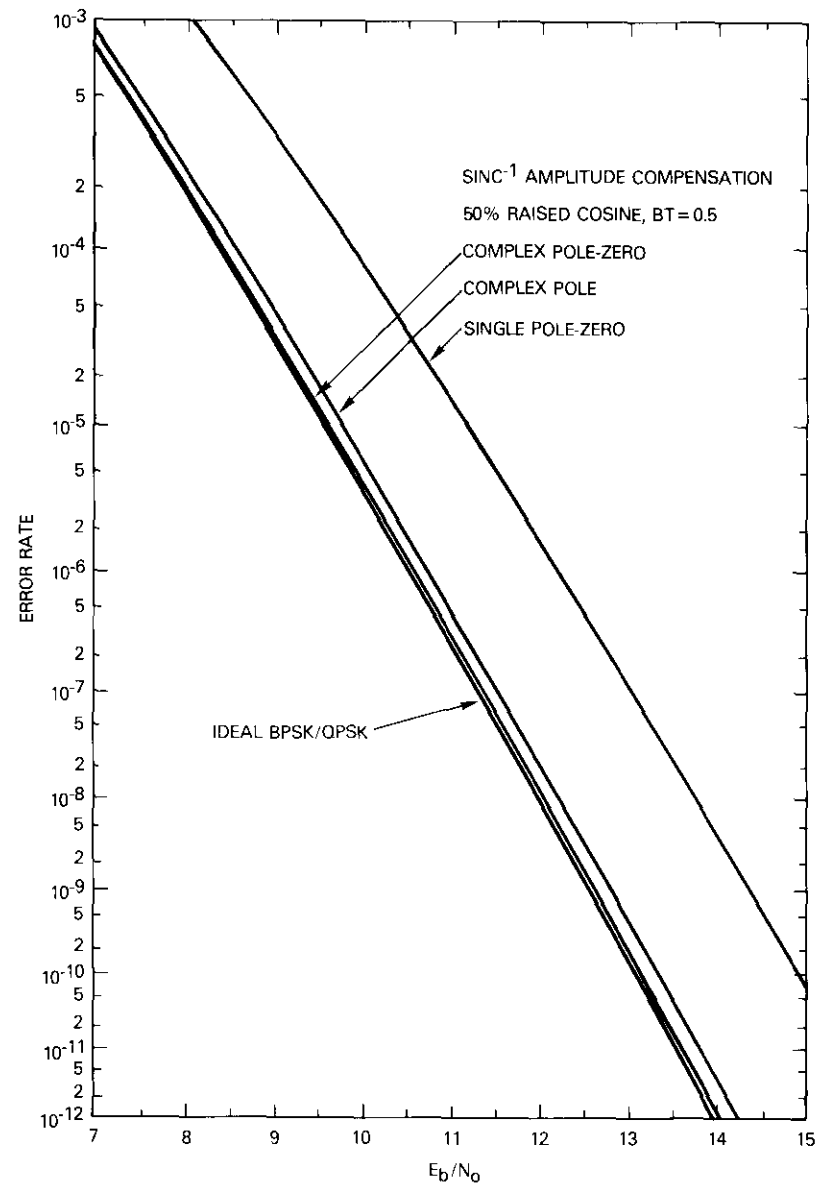


Figure 9b. BER,  $Sinc^{-1}$  Amplitude Compensation 50% Raised Cosine,  $BT = 0.5$

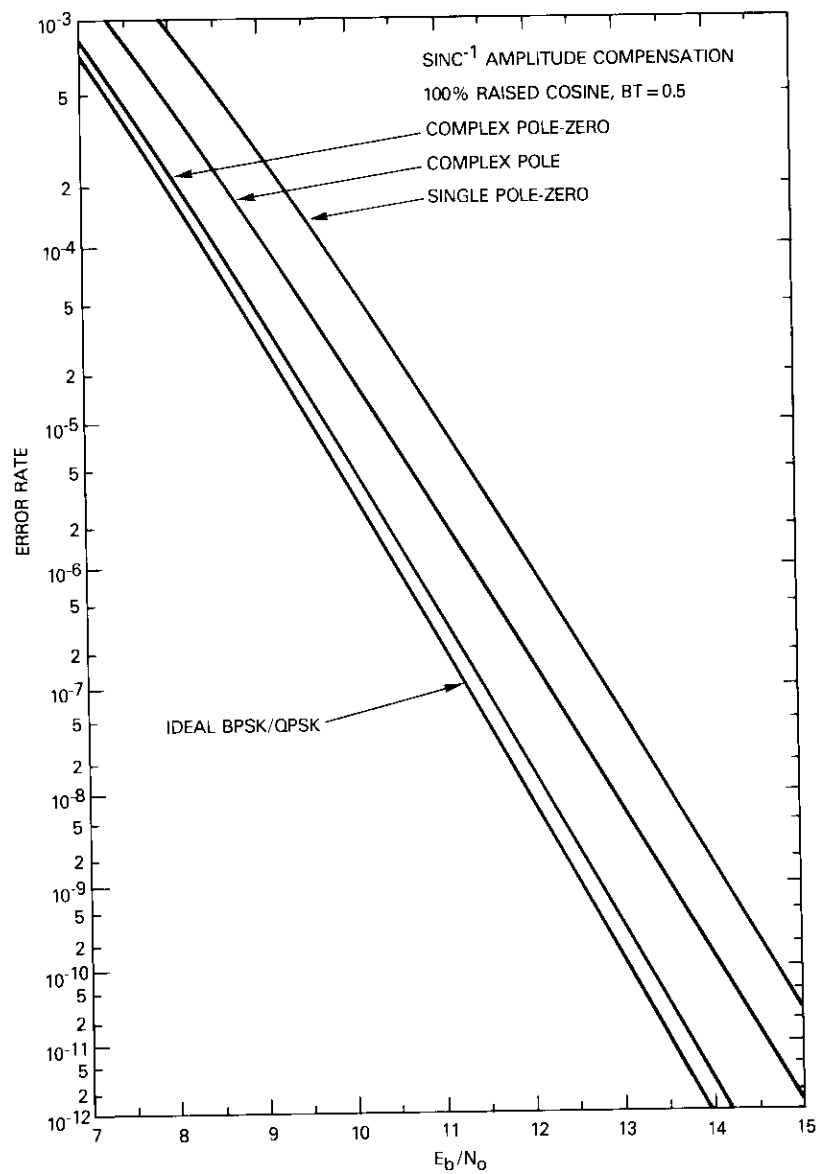


Figure 9c. BER,  $Sinc^{-1}$  Amplitude Compensation 100% Raised Cosine,  $BT = 0.5$

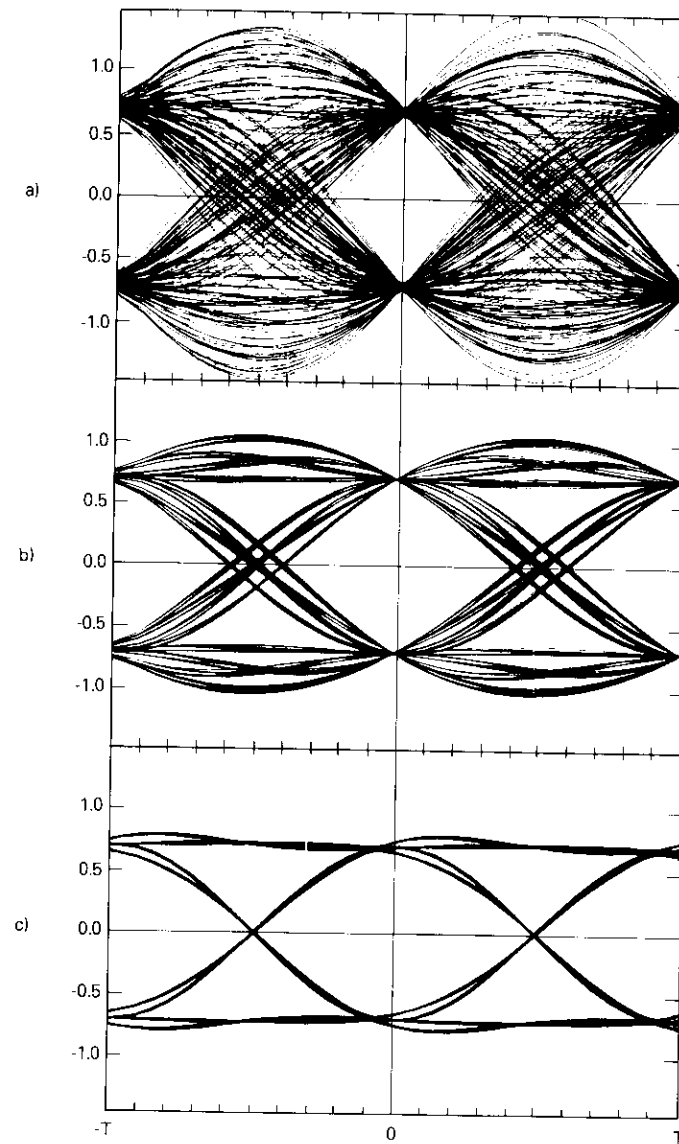


Figure 10.  $Sinc^{-1}$  Amplitude Compensated Eye Patterns

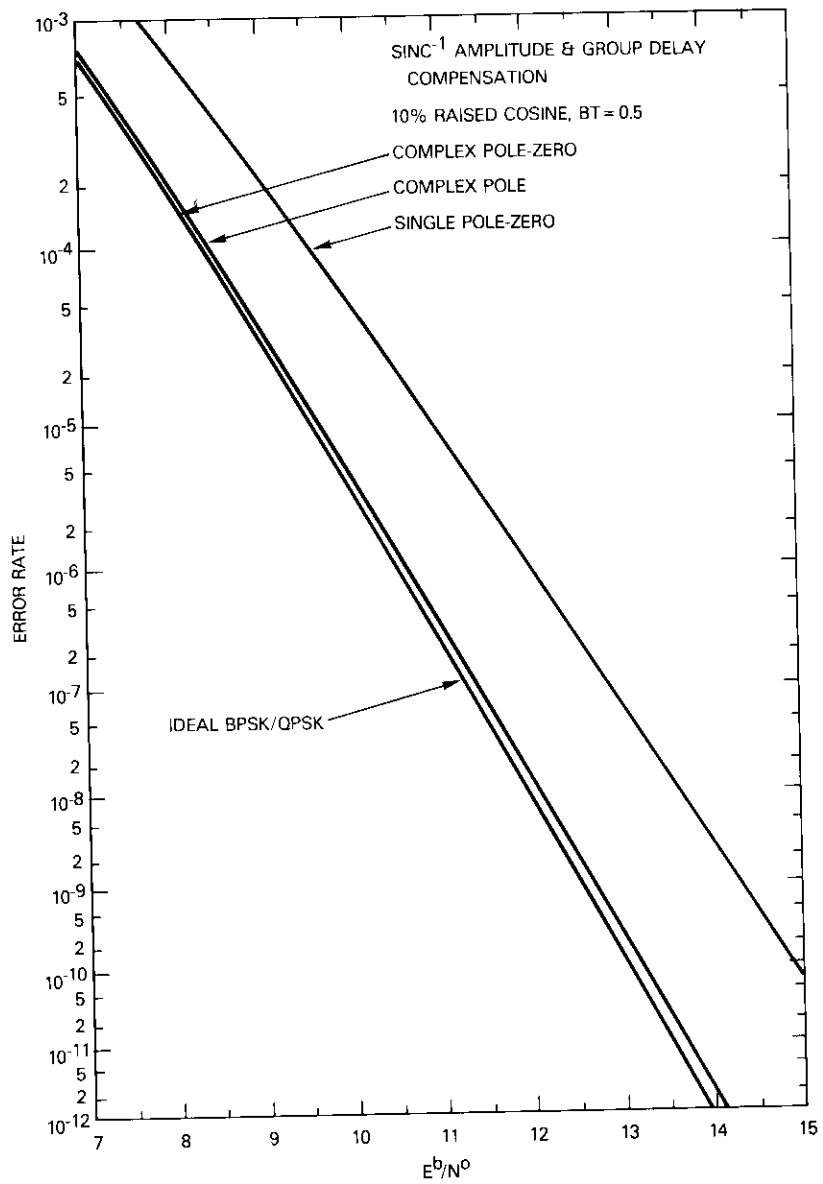


Figure 11a. BER,  $Sinc^{-1}$  Amplitude and Group Delay Compensation, 10% Raised Cosine,  $BT = 0.5$

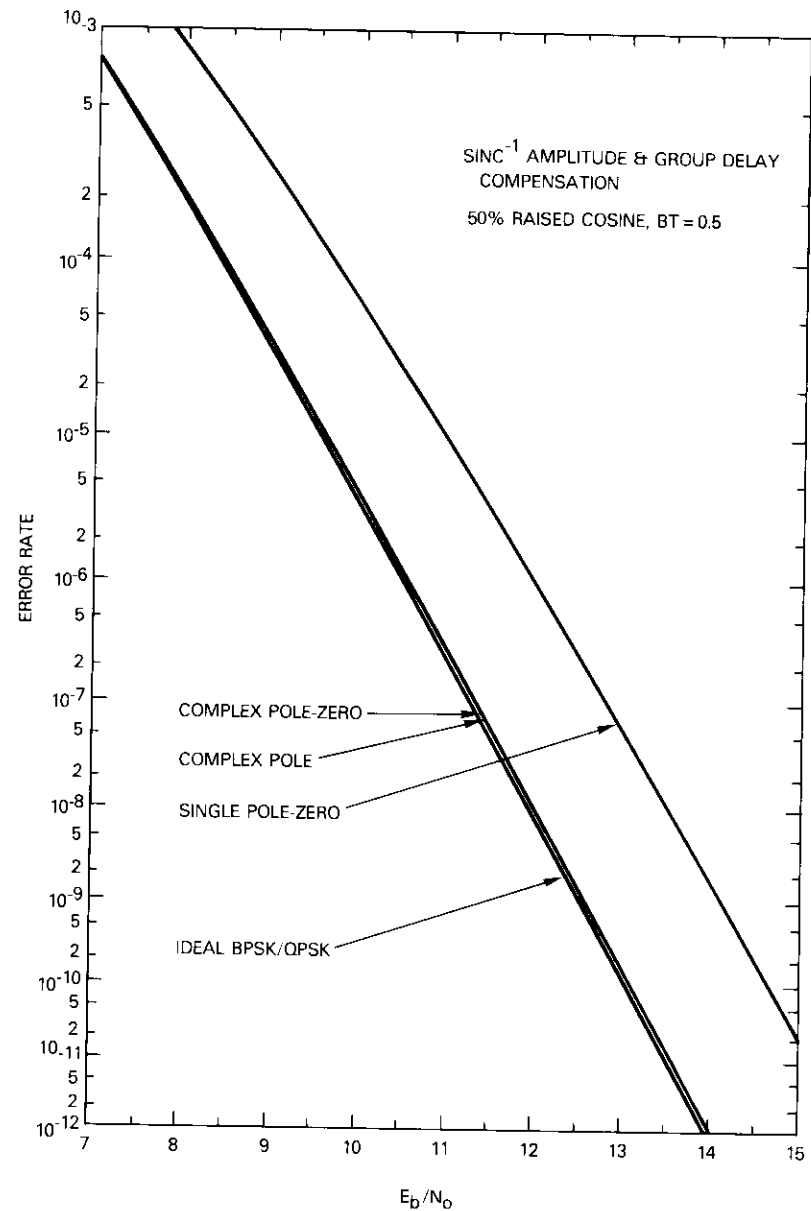


Figure 11b. BER,  $Sinc^{-1}$  Amplitude and Group Delay Compensation, 50% Raised Cosine,  $BT = 0.5$

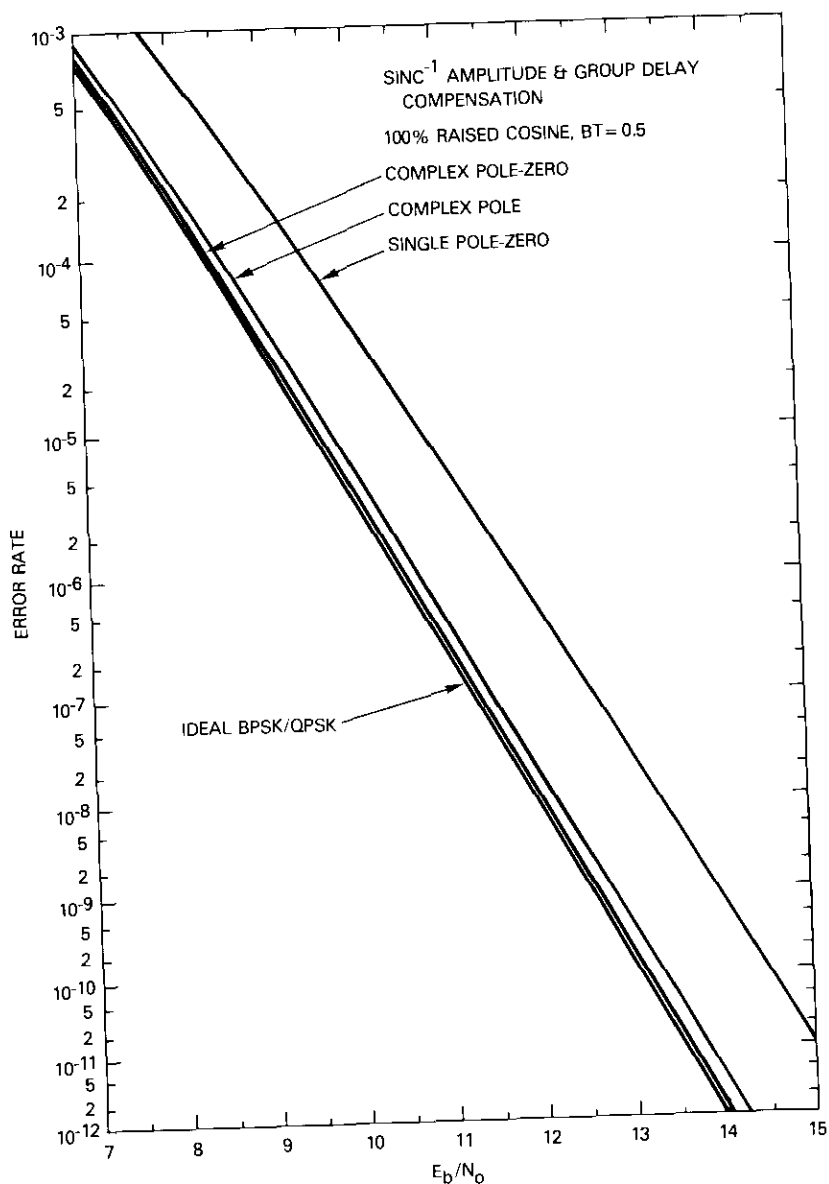


Figure 11c. BER,  $Sinc^{-1}$  Amplitude and Group Delay Compensation, 100% Raised Cosine,  $BT = 0.5$

TABLE 1. ALL-PASS GROUP DELAY EQUALIZER ROOTS

SINC APPROXIMATION	LEFT HALF-PLANE POLE LOCATIONS
Real Zero	$-(4.6631 \pm j0.0) R$ , rad/s
Complex Pole	$-(2.5731 \pm j1.6396) R$ , rad/s
Complex Pole-Zero	$-(4.4937 \pm j2.3200) R$ , rad/s

For 10- through 50-percent roll-off rates, the complex pole and complex pole-zero solutions yielded virtually identical error rate performances ( $\Delta E_b / N_o < 0.03$  dB). This, coupled with the solution's proximity to the ideal BER curve ( $< 0.1$  dB), indicates that the complex pole with delay equalization is adequate. For 100-percent roll-off, however, the complex pole-zero network affords the best results. Again, eye patterns for the acceptable solutions are given in Figures 12a, 12b, and 12c.

In summary, delay compensation has resulted in significant improvement over the entire range of roll-off rates. Also, in many situations the accompanying increase in network complexity may be eliminated if the delay equalization is combined with the circuitry already required for the data filters.

### Active network realizations

#### Complex pole

The lowest order transfer function of interest for amplitude compensation is that of the complex pole. It may be realized with a basic Sallen and Key structure as depicted in Figure 13a [5]. Its transfer function in terms of the  $R$  and  $C$  elements is

$$H(s) = \frac{1}{1 + s(R_1 + R_2)C_2 + s^2R_1C_1R_2C_2} \quad (11)$$

When equation (11) is compared with equation (3) it is clear that two of the values may be solved for as follows:

$$(R_1 + R_2) C_2 = 2Z_p\tau_p \doteq \frac{0.14858}{R} \quad (12a)$$

$$R_1C_1R_2C_2 = \tau_p^2 \doteq \frac{0.052705}{R^2} \quad (12b)$$

The other two are determined by selecting a normalizing impedance, and either a resistance or capacitance ratio ( $R_2/R_1$ ,  $C_2/C_1$ ).

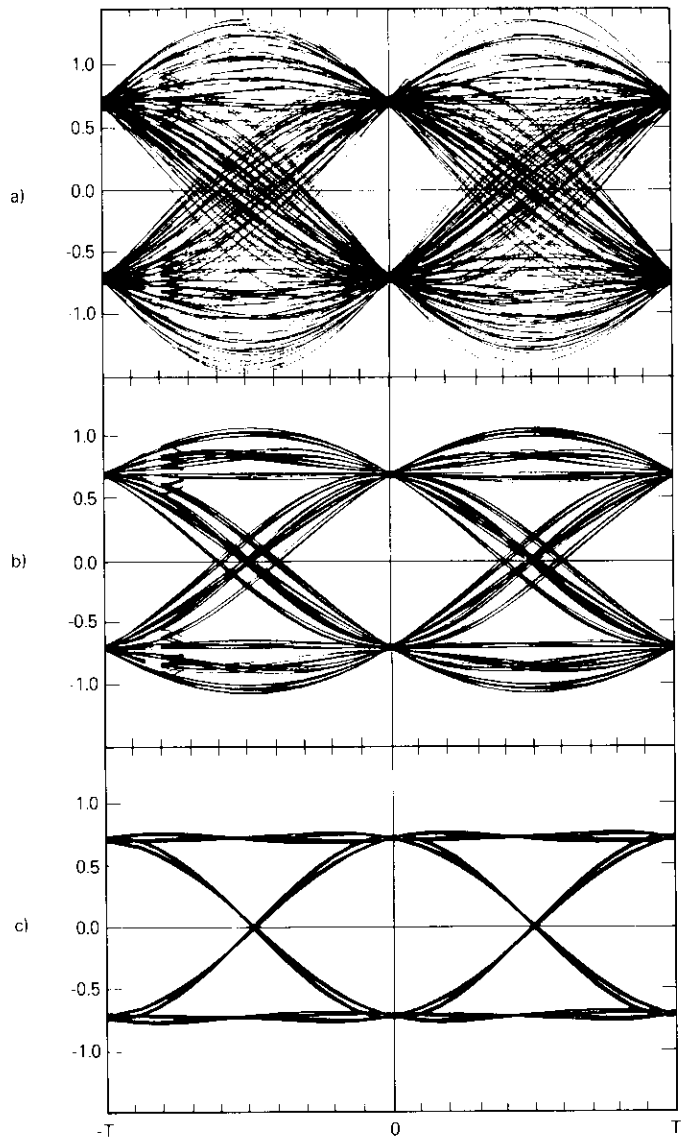


Figure 12.  $Sinc^{-1}$  Amplitude and Group Delay Compensated Eye Patterns

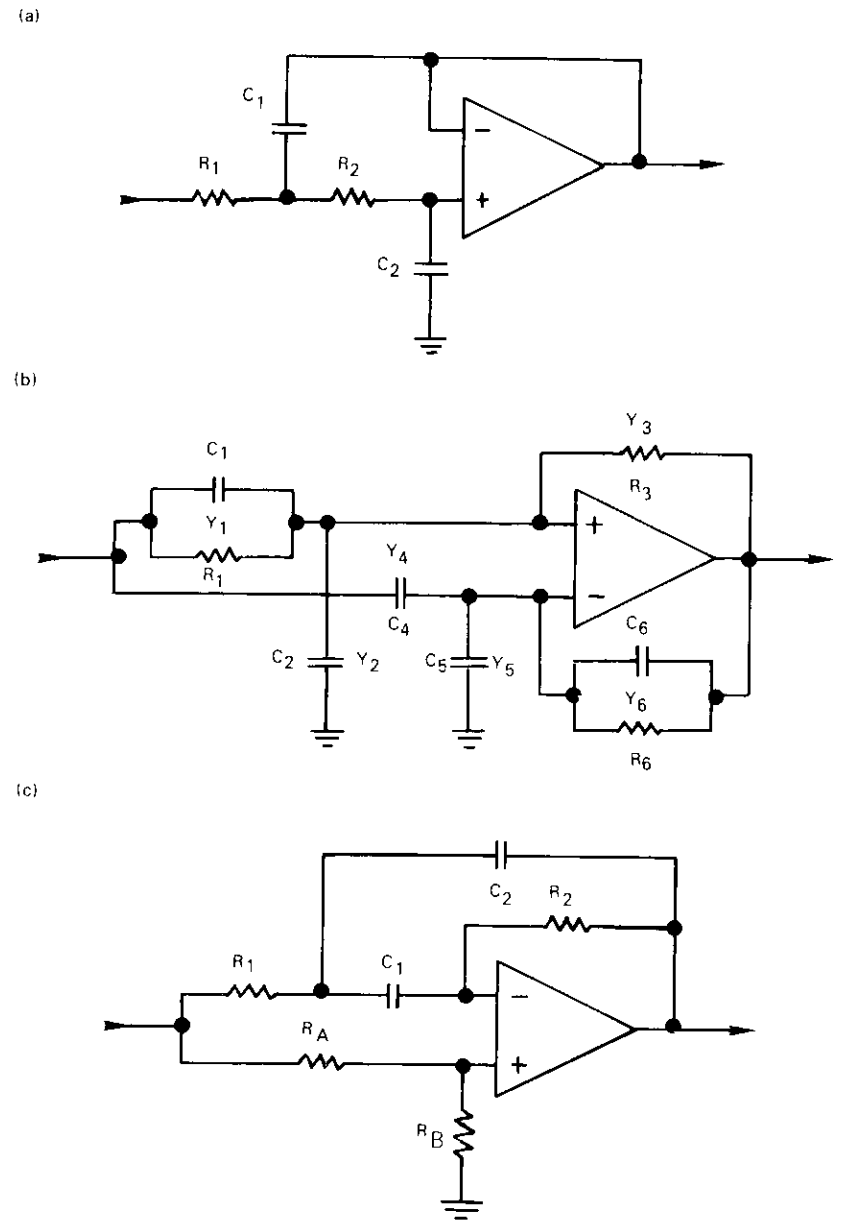


Figure 13. Active Network Realizations

**Complex pole-zero**

The complex pole-zero solution is considerably more complicated. A network realization consisting of only one active device is shown in Figure 13. Its generalized transfer function in terms of the admittances taken from Huelsman [6] is

$$H(s) = \frac{Y_1(Y_4 + Y_5 + Y_6) - Y_4(Y_1 + Y_2 + Y_3)}{Y_6(Y_1 + Y_2 + Y_3) - Y_3(Y_4 + Y_5 + Y_6)} \quad (13)$$

To assimilate the desired response, the admittances were chosen as

$$\begin{aligned} Y_1 &= G_1 + sC_1, & Y_2 &= sC_2 \\ Y_3 &= G_3, & Y_4 &= sC_4 \\ Y_5 &= sC_5, & Y_6 &= G_6 + sC_6 \end{aligned} \quad (14)$$

The resultant transfer function in terms of  $R$ 's and  $C$ 's is

$$\begin{aligned} H(s) &= [1 + s[R_1C_1 + R_6(C_5 + C_6) - G_3R_1R_6C_4] \\ &\quad + s^2\{R_1R_6[C_1(C_5 + C_6) - C_2C_4]\}] / \\ &\quad [1 + s[R_1(C_1 + C_2) + R_6C_6 \\ &\quad - G_3R_1R_6(C_4 + C_5)] \\ &\quad + s^2[R_1R_6(C_1 + C_2)C_6]] \end{aligned} \quad (15)$$

Equating this with the values from equations (3) through (5) provides four simultaneous expressions for determining the frequency response:

$$\begin{aligned} R_1C_1 + R_6(C_5 + C_6) - G_3R_1R_6C_4 \\ = 2\zeta_z\tau_z \doteq \frac{0.24054}{R} \end{aligned} \quad (16a)$$

$$\begin{aligned} R_1R_6[C_1(C_5 + C_6) - C_2C_4] \\ = \tau_z^2 \doteq \frac{0.016108}{R^2} \end{aligned} \quad (16b)$$

$$\begin{aligned} R_1(C_1 + C_2) + R_6C_6 - G_3R_1R_6(C_4 + C_5) \\ = 2\zeta_p\tau_p \doteq \frac{0.048209}{R} \end{aligned} \quad (16c)$$

$$\begin{aligned} R_1R_6[(C_1 + C_2)C_6] \\ = \tau_p^2 \doteq \frac{0.030008}{R^2} \end{aligned} \quad (16d)$$

Since there are eight unknowns and only four equations, four values must be assigned. However, arbitrary selections may result in impractical component values. Consequently, the solution procedure is as follows. Assume that  $R_1$ ,  $R_6$ ,  $C_1$ , and  $C_6$  are known, and solve for  $R_3$ ,  $C_2$ ,  $C_4$ , and  $C_5$ . The resulting expressions are

$$aC_4^2 + bC_4 + c = 0 \quad (17a)$$

where

$$a = R_6^2 \left[ \left( \frac{\tau_p^2}{\tau_1\tau_6} \right) \left( \frac{\tau_z^2}{\tau_1\tau_6} - 1 \right) \right]$$

$$\begin{aligned} b = R_6 \left[ \left( \tau_1 + \frac{\tau_z^2}{\tau_1} \right) \left( \frac{\tau_p^2}{\tau_1\tau_6} \right) + \left( \frac{\tau_p^2}{\tau_1\tau_6} - 1 \right) \left( \frac{\tau_z^2}{\tau_1} - \tau_6 \right) \right. \\ \left. - \left( \frac{\tau_p^2}{\tau_6} + \tau_6 - 2\zeta_p\tau_p \right) - 2\zeta_z\tau_z \left( \frac{\tau_p^2}{\tau_1\tau_6} \right) \right] \end{aligned}$$

$$c = \left[ \left( \frac{\tau_z^2}{\tau_1} - \tau_6 \right) \left( \tau_1 + \frac{\tau_z^2}{\tau_1} - 2\zeta_z\tau_z \right) \right]$$

with  $\tau_1 = R_1C_1$ ,  $\tau_6 = R_6C_6$ .

The unknowns are then solved for as

$$G_3 = \frac{1}{R_1} \frac{\tau_p^2/\tau_6 + \tau_6 - 2\zeta_p\tau_p}{\tau_z^2/\tau_1 + (R_6C_4/\tau_1) (\tau_p^2/\tau_6) - \tau_6} \quad (17b)$$

$$C_2 = \frac{\tau_p^2}{R_1\tau_6} - C_1 \quad (17c)$$

$$C_5 = \frac{\tau_z^2}{R_6\tau_1} + \frac{C_2C_4}{C_1} - C_6 \quad (17d)$$

To have maximum flexibility for scaling the element values, it is best to manipulate the coefficients in equation (17a) to give two real roots for  $C_4$ . Thus, the parameters of 17a were chosen to force  $a, c > 0$  and  $b < 0$ , with the time constants selected as  $\tau_1 = 1/2\pi R$  and  $\tau_6 = 1/4\pi R$ . These parameters result in the following values for the unknowns,

$$C_4 = \frac{0.10097/R}{R_6} \quad (18a)$$

$$G_3 = \frac{1.5658}{R_1} \quad (18b)$$

$$C_2 = \frac{0.21794/R}{R_1} \quad (18c)$$

$$C_5 = \frac{0.15990/R}{R_6} \quad (18d)$$

$$R_1 = 2R_6, \quad C_1 = C_6 \quad (18e)$$

which may be frequency and impedance scaled as desired. It should be mentioned that this is only one of a variety of possible solutions for arbitrary choices of  $R_1, R_6, C_1$ , and  $C_6$ .

#### Group delay equalization

Delay compensation may be accommodated with the structure of Figure 13c [7]. Its transfer function in terms of the  $R$ 's and  $C$ 's is

$$H(s) = \alpha \left\{ \frac{1 + s[R_1(C_1 + C_2) - R_2C_1(R_a/R_b)]}{1 + s[R_1(C_1 + C_2)] + s^2[(R_1C_1)(R_2C_2)]} + \frac{s^2[(R_1C_1)(R_2C_2)]}{1 + s[R_1(C_1 + C_2)] + s^2[(R_1C_1)(R_2C_2)]} \right\} \quad (19)$$

where

$$\alpha = \frac{R_b}{R_a + R_b}$$

For the magnitude response to be all-pass it is necessary that

$$R_2C_1 \frac{(1 - \alpha)}{\alpha} = 2R_1(C_1 + C_2) \quad (20)$$

With the root locations from Table 1 defined by  $-(\sigma_c \pm j\omega_c)$ , the design equations are

$$R_1(C_1 + C_2) = \frac{2\sigma_c}{\sigma_c^2 + \omega_c^2} \quad (21a)$$

$$(R_1C_1)(R_2C_2) = (\sigma_c^2 + \omega_c^2)^{-1} \quad (21b)$$

Thus, upon selection of an attenuation factor,  $a$ , and a normalizing impedance, equations (20), (21a), and (21b) may be employed to find the particular  $R$ 's and  $C$ 's required for delay equalization.

#### Square root reciprocal sinc compensation

Although not optimum, it is sometimes practical to impart half of the sinc equalization to both transmitter and receiver, which has the advantage of allowing for identical filtering at both ends of the data link. This technique may be desirable for nonlinear channel applications, where amplitude peaking can result in severe distortion. In lieu of the results in the previous sections, the analysis for square root compensation will focus on only one type of realization, the complex pole with group delay equalization.

#### Power series expansion

With square-root inverse sinc compensation, the magnitude squared of the filter response must be equated to the first power of the sinc function rather than to its square.

$$|G(\omega)|^2 = 1 - \frac{1}{3!} \left( \frac{\omega}{2R} \right)^2 + \frac{1}{5!} \left( \frac{\omega}{2R} \right)^4 - \frac{1}{7!} \left( \frac{\omega}{2R} \right)^6 + \dots \quad (22)$$

The candidate complex pole transfer function is

$$H(s) = \frac{1}{1 + s(2\zeta_p\tau_p) + s^2(\tau_p^2)} \quad (23)$$

The reciprocal of its magnitude squared is written as

$$|G(\omega)|^2 = \frac{1}{|H(\omega)|^2} = 1 + \omega^2[2\tau_p^2(2Z_p^2 - 1)] + \omega^4(\tau_p^4) \quad (24)$$

Equating coefficients yields

$$2\tau_p^2(2Z_p^2 - 1) = \frac{-1}{4 \cdot 3!R^2} \quad (25a)$$

$$\tau_p^4 = \frac{1}{16 \cdot 5!R^4} \quad (25b)$$

Solving for the second-order network parameters gives

$$f_p = \frac{1}{2\pi\tau_p} = \frac{R}{2\pi} \sqrt[4]{16 \cdot 5!} = 1.0535R, \text{ rad/s} \quad (26a)$$

$$Z_p = \sqrt{\frac{1}{2} - \frac{1}{16 \cdot 3! \tau_p^2 R^2}} = 0.20872 \quad (26b)$$

The complex pole locations for the sinc approximation are

$$-(Z_p \pm j\sqrt{1 - Z_p^2}) \omega_p = -(1.3816 \pm j6.4737) R, \text{ rad/s} \quad (27)$$

Lastly, the poles of the delay equalizer computed from the aforementioned group delay compensation program are

$$-(5.3027 \pm j2.6643) R, \text{ rad/s} \quad (28)$$

Their magnitude and group delay responses have been plotted in Figures 14a and 14b.

**Performance comparison**

BER curves for the 10-, 50-, and 100-percent roll-off cosine filters with square root compensation on both ends of the link are illustrated in Figure 15. Eye diagrams have also been included in Figure 16. As before, this compensation demonstrates very good performance in the 10- to 50-percent range; whereas toward 100 percent, a more elaborate approximation is necessary. However, it is interesting to note that although this technique is suboptimum from a transmit/receive allocation point of view, very little degradation in error rate is experienced.

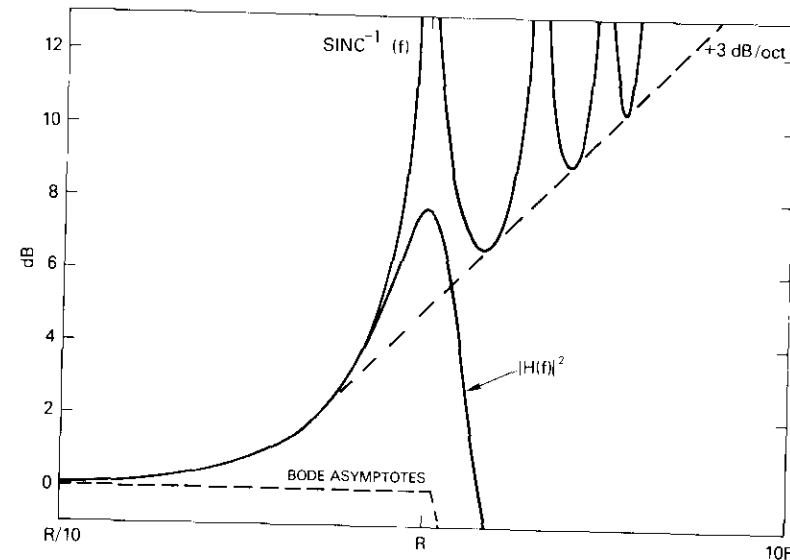


Figure 14a. Complex Pole Square Root Magnitude Approximation

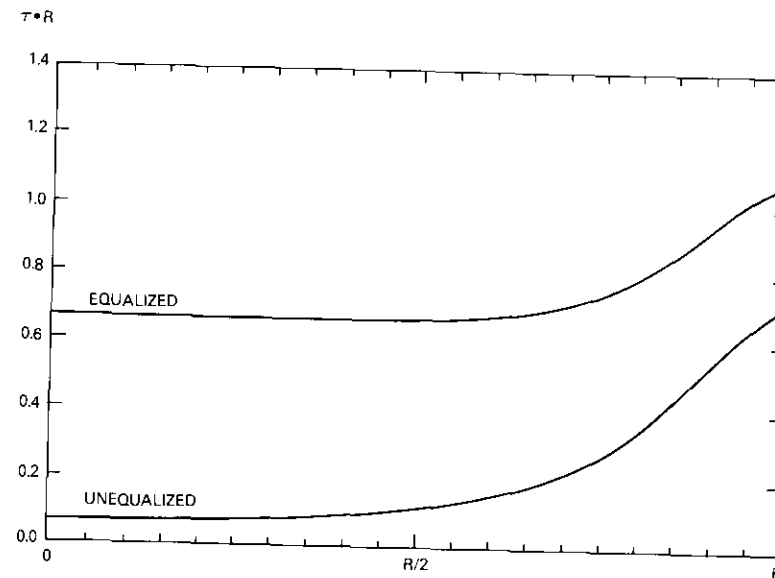


Figure 14b. Complex Pole Group Delay ( $Sinc^{-1/2}$ )

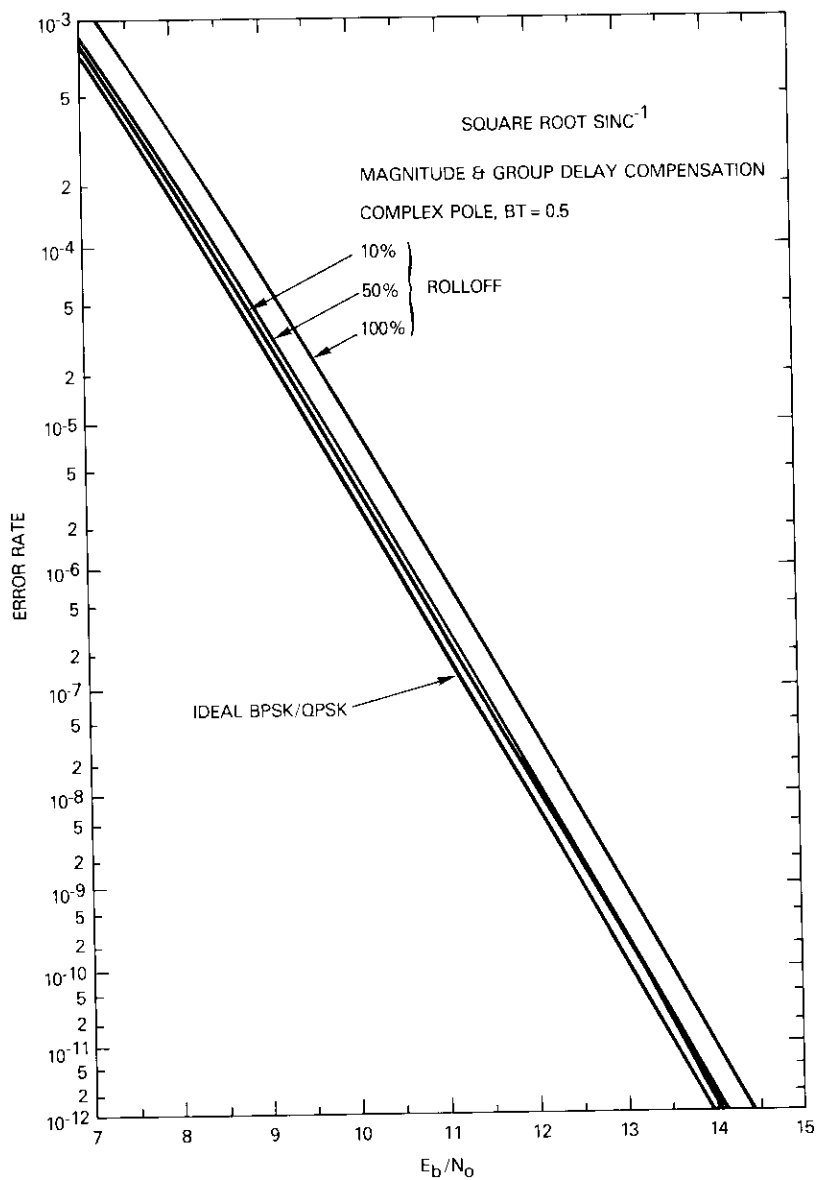


Figure 15. BER, Square Root Sinc<sup>-1</sup> Amplitude and Group Delay Compensation

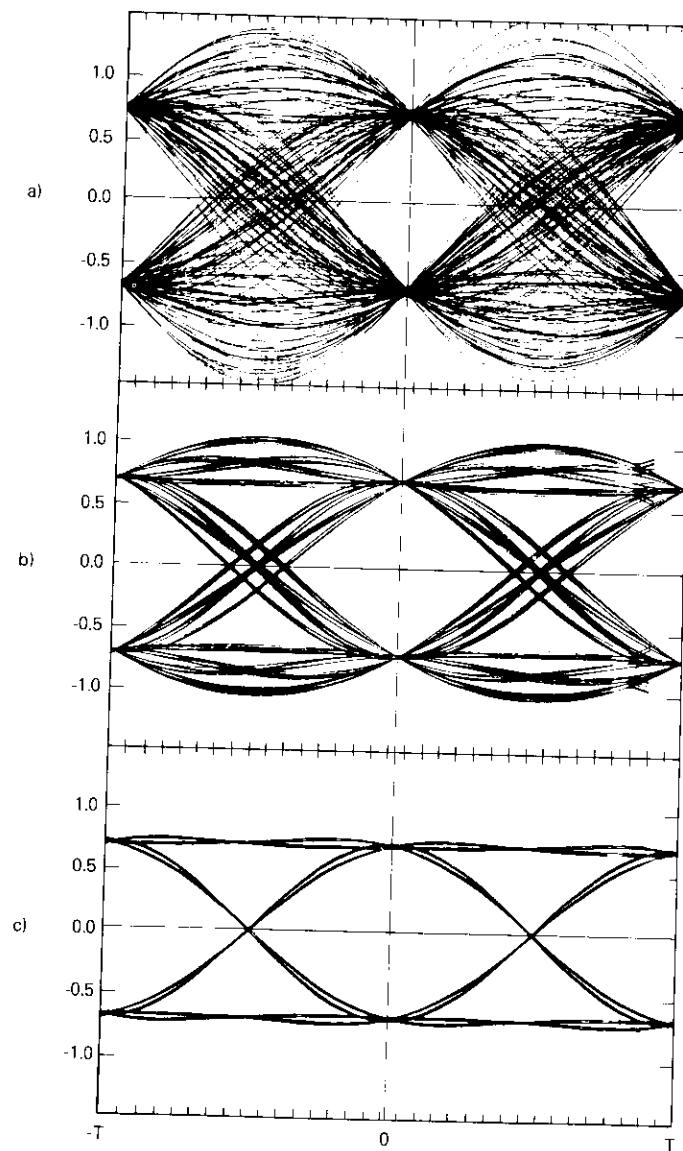


Figure 16. Square Root Sinc<sup>-1</sup> Eye Patterns

### Network realization

This type of compensation may be accommodated with the network topologies from Figures 13a and 13c. The design equations for the amplitude shaping are

$$(R_1 + R_2) C_2 = 2\zeta_p \tau_p = \frac{0.063062}{R} \quad (29a)$$

$$R_1 C_1 R_2 C_2 = \tau_p^2 = \frac{0.022822}{R^2} \quad (29b)$$

Similarly, element values for group delay equalization are found by solving

$$R_2 C_1 \frac{(1 - \alpha)}{\alpha} = 2R_1(C_1 + C_2) \quad (30a)$$

$$R_1(C_1 + C_2) = \frac{2\sigma_c}{\sigma_c^2 + \omega_c^2} = \frac{0.30114}{R} \quad (30b)$$

$$(R_1 C_1) (R_2 C_2) = (\sigma_c^2 + \omega_c^2)^{-1} = \frac{0.028395}{R^2} \quad (30c)$$

### Conclusions

With the reciprocal sinc compensation networks developed in this study, it is possible to operate at the Nyquist rate ( $B/R = 0.5$ ) and obtain nearly ideal error rate performance (degradation  $< 0.1$  dB). The transfer functions utilized are fairly simple, typically second order, and can often be incorporated into the data filtering without any increase in complexity. In particular, there were two implementations that rendered superior error rate over a broad roll-off range (10 to 50 percent): the complex pole-zero and the group delay equalized complex pole solutions. The single pole-zero case proved inadequate in the absence of  $BT$  product manipulation.

The largest improvement in BER was attained with the sharper data filtering. For example, 10-percent cosine roll-off initially had considerably worse error rate than the others, yet it was relatively easy to compensate; the 100 percent cosine had reasonable error rate to begin with but required more elaborate equalization. This was reconciled because

softer data filtering disperses the energy further out in frequency, and consequently the inverse sinc amplitude and delay characteristics must be emulated over a broader range. Moreover, the approximation networks appeared most useful over the roll-off range of 10 through 50 percent.

It was also found that imparting the square root of the reciprocal sinc approximation to both transmitter and receiver resulted in less than 0.1 dB degradation of optimum apportionment. Thus, a small penalty in error rate can allow for identical filtering at both ends of the link. From a practical standpoint, this could be a very attractive feature. In addition, it may provide better error rate performance for some nonlinear channel applications.

For the future, it appears that performance comparisons of inverse sinc compensation imbedded in data filtering would be worthwhile. The techniques developed here represent quantitative guidelines on amplitude and delay compensation and help determine their impact on system error rate performance.

### Acknowledgments

The author would like to thank W. Cook, S. Lebowitz, and S. Baker of COMSAT Laboratories who developed and perfected the communications channel analysis program (CHAMP).

### References

- [1] F. T. Assal, "Optimum Bandpass Network Designs for Coherent 4 PSK-PCM Digital Communications," Second International Conference on Digital Satellite Communications, November 1972, *Proceedings*, pp. 164-174.
- [2] P. N. Sargeant, "A 120 Mbit/s QPSK Modem for TDMA Applications," International Conference on Communications, 1977, *Conference Record*, Vol. III, pp. 184-187.
- [3] W. Bennett and J. Davey, "Effects of Restricted Bandwidth," *Data Transmission*, New York: McGraw-Hill, 1965, pp. 49-82.
- [4] W. Cook and S. Lebowitz, Private Communication.
- [5] Sallen and Key, "A Practical Method of Designing RC Active Filters," *IRE Transactions on Circuit Theory*, March 1955, pp. 74-85.
- [6] L. Huelsman, "Infinite Gain Realizations," *Theory and Design of Active RC Circuits*, New York: McGraw-Hill, 1968, pp. 202-204.
- [7] A. Budak and P. Aronhime, "Frequency Limitation on an Operational Amplifier Realization of All-Pass Transfer Functions with Complex Poles," *Proceedings of the IEEE*, July 1970, pp. 1127-1138.



*John J. Poklemba received a B.S.E.E. from Drexel University in 1972, and an M.S. and E.E., concurrently, from M.I.T. in 1974. Prior to joining COMSAT Laboratories, he spent two years working with HF receivers and high-resolution video signal processing. For the past five years, Mr. Poklemba has been a Member of the Technical Staff in the Modulation Techniques Department. His principal interests are the application of detection and estimation theory to practical receiver structures, and the development of various types of filtering relevant to information transmission.*

**Index:** networks, small terminals, synchronization, TDMA, transmission systems

## ***A demand-assigned mixed TDMA and FDMA/TDMA system\****

R. J. F. FANG

(Manuscript received November 6, 1981)

### ***Abstract***

The concept of an effective demand-assigned satellite communications system is presented. High- and low-data rate TDMA terminals and large and small G/T earth stations can be employed at network nodes having a wide range of traffic requirements. With proper time-sharing of the satellite transponder, a mixed TDMA and FDMA/TDMA transmission mode can minimize terminal costs at nodes with low traffic requirements and maximizes the transponder throughput. Burst-rate reduction, centralized control for each subnetwork, and simple open-loop synchronization methods are employed at nodes with low traffic requirements to achieve cost reduction. It is shown that networks with nonhomogeneous traffic requirements can be cost-effectively served with such a system.

### ***Introduction***

TDMA digital transmission techniques, which were developed and demonstrated more than a decade ago [1]-[3], have not yet been widely implemented mainly because of equipment complexity and high cost.

\* Portions of this paper were presented at the 1979 National Telecommunications Conference in Washington, D.C.

The rapid advances in large-scale integration (LSI) technology during the past decade, however, have significantly reduced hardware costs. On the other hand, microwave technology has also advanced, leading to significant reductions in the cost of antennas, high-power amplifiers, low-noise receivers, and converters. Consequently, networking via satellite with small earth stations located at the customer's premises has become more cost-effective and attractive, particularly for data communications.

To efficiently use the power and bandwidth of the satellite transponders, TDMA terminals have traditionally been designed to transmit and receive bursts at data rates of the order of tens of megabits per second, or at a symbol rate comparable to the transponder bandwidth. High data rates require large power amplifiers, large antennas, low-noise amplifiers, high bit rate burst modems, high-speed compression/expansion buffers, and high-speed TDMA controllers. All these items are costly.

Since nodal traffic in a network is often nonhomogeneous, earth stations designed for heavy traffic are too costly to serve nodes with light traffic. Because the number of light traffic nodes is usually greater than that of major traffic nodes, use of identical large earth stations for all nodes in the network may not be very cost-effective. Although the most cost-effective approach might require the use of different G/T earth stations and TDMA bit rates for each node, it is more convenient to limit the choice of G/T ratios and TDMA terminal characteristics to a few carefully selected values.

This paper considers two sets of values of the G/T ratio and two TDMA bit rates. In order to avoid duplicate equipment at large traffic nodes, which must communicate with large as well as small traffic nodes, it may be desirable to allow mixed bit rate TDMA transmissions over a given transponder. Traffic between large nodes is carried by high bit rate TDMA bursts that occupy the entire transponder bandwidth. Traffic between small nodes, or between small and large nodes, is carried by low bit rate TDMA bursts which require only a fraction of the transponder bandwidth.

This paper proposes an effective method to provide mixed bit rate TDMA and FDMA/TDMA transmissions over a given transponder. The bit-error rate (BER) performance of both the high data rate TDMA transmission and the low data rate FDMA/TDMA transmission is evaluated for a real satellite transponder configuration including the effects of adjacent transponder interference. When the high and low data rate time slots are apportioned according to demand, the proposed system would lead to high transponder efficiency while it would drastically reduce the cost of the earth segment equipment. An example is provided to illustrate the usefulness of this concept.

### System description

It is postulated that a number of subnetworks can access a given satellite transponder at two bit rates, one high and one low. In Figure 1, which depicts a general network configuration over a satellite transponder, capital letters indicate earth stations with large G/T values capable of handling the higher bit rate, and lower case letters indicate earth stations with small G/T values capable of handling the lower bit rate.  $R1$  and  $R2$  represent reference stations that generate frame and subframe reference bursts at high and low bit rates and broadcast to all (large and small) earth stations. The two reference stations provide backup for each other, but only one is the master station at any instant.

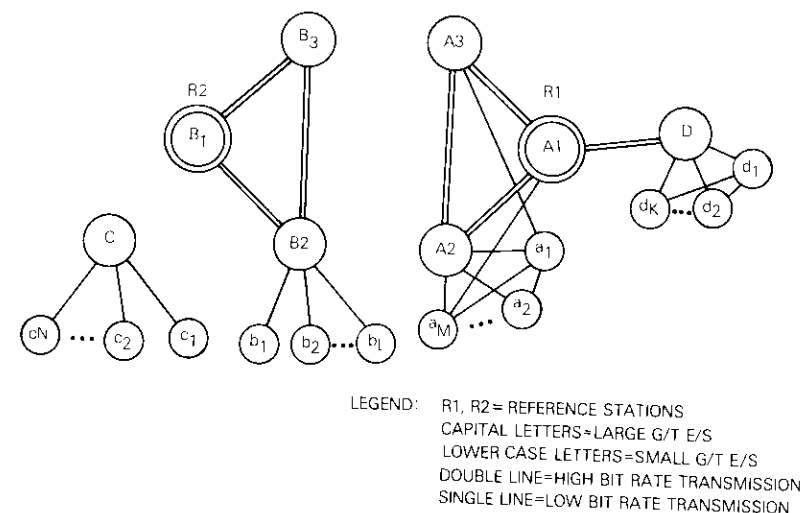


Figure 1. Network Configurations

Nodes  $A_1$  and  $B_1$  are the central controlling nodes for the high bit rate subnetworks ( $A_1, A_2, A_3, D$ ) and ( $B_1, B_2, B_3$ ), respectively. In the lower data rate subnetworks ( $D, d_1, d_2, \dots, d_k$ ), ( $A_2, A_3, a_1, \dots, a_m$ ), ( $B_2, b_1, b_2, \dots, b_l$ ), and ( $C, c_1, c_2, \dots, c_n$ ), the nodes  $D, A_2, B_2$ , and  $C$ , respectively, will control each subnetwork. At the subnetwork control nodes  $D, A_2$ , and  $B_2$ , both high and low bit rate transmit and receive equipment must be provided in addition to the network control apparatus. At node  $C$ , however, only low bit rate (transmit and receive) equipment is needed. In either case, each

subnetwork controller must generate all necessary control information for that subnetwork and broadcast this information in the subframe to all nodes under its control.

Figure 2 illustrates a conceptual burst scheduling and transponder loading plan. For the first time interval,  $T_e$ , of frame duration  $T$ , the transponder is accessed in the TDMA mode by high bit rate bursts that occupy the entire transponder bandwidth. For the remaining time interval,  $T_s = T - T_e$ , multiple carriers access the transponder in an FDMA/TDMA

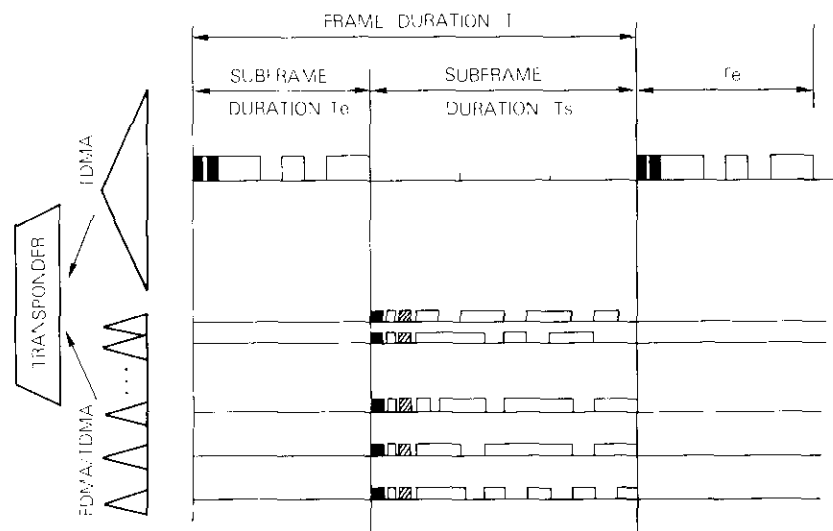


Figure 2. Transponder and Frame Loading

mode. Thus, the transponder is frequency-division multiple-accessed; however, each carrier slot is accessed by multiple lower bit rate TDMA bursts. Figure 3 shows the frame and burst format. For subnetworks with moderate traffic, multiple carrier frequency slots may be required, in which case the central controller of this subnetwork must transmit a control burst in each subframe in each carrier frequency slot. For simplicity of controller and modem implementation, it is assumed that each FDMA/TDMA carrier frequency slot serves no more than one subnetwork. Although this assumption is obviously not necessary, it may be desirable from a practical standpoint.

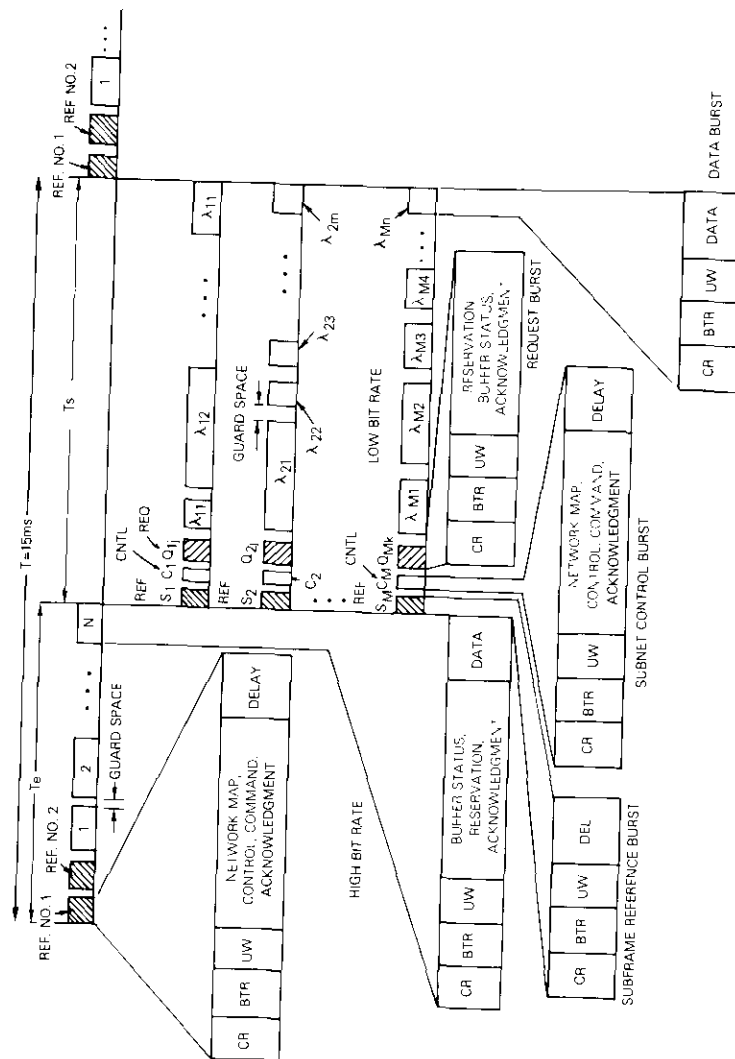


Figure 3. Frame and Burst Format

Figures 4 and 5 are block diagrams of the small and large earth stations, respectively. For illustrative purposes, G/T values of 25.8 and 30.2 dB/K have been selected which correspond to antenna diameters of 3.6 and 5.5 m, respectively, at 12 GHz, assuming a noise temperature of 215 K for the LNA subsystem using field-effect transistor amplifiers.

The low bit rate small G/T earth station requires an 11-W power amplifier (HPA). The TDMA terminal consists of a QPSK modem, a rate one-half forward error correction (FEC) codec, a network and satellite access controller, a compression buffer, an expansion buffer, and a terrestrial port interface unit which performs the necessary time-division and/or statistical multiplexing and protocol conversion. In order to minimize the cost of the terrestrial interface unit, it is assumed that the port speeds at the input would not exceed 56 kbit/s. Ports with speeds higher than 56 kbit/s, but not exceeding 1.544 Mbit/s, could be made available. In this case, however, no protocol conversion would be required for these ports. Their outputs are fed directly into the compression buffer. It is assumed that the user equipment can handle the necessary protocol control and has the required buffer storage for data rates higher than 56 kbit/s, but not exceeding 1.544 Mbit/s, including video conferencing capability.

An FEC code is employed to trade off bandwidth for power. With a rate  $\rho$  FEC code, the operating bit rate of the burst modem must be increased from  $R$  to  $R/\rho$  bit/s to achieve the same information bit rate of  $R$  bit/s. In Figure 4, it is assumed that  $\rho = 1/2$ , for illustrative purposes. Thus, at an information rate  $R = 1.544$  Mbit/s, the rate  $1/2$  FEC codec output bit rate as well as the burst modem bit rate must be 3.088 Mbit/s, which is well within the capability of medium-scale integration (MSI) transistor-transistor logic (TTL) technology.

The network and access controller of the subnetwork TDMA terminal contains a small amount of microprocessor-based digital hardware plus memory storage. An open-loop burst synchronization technique and a centralized network control method are employed, as shown in Figure 6. Initially, all low bit rate terminals in the subnetwork are prohibited from transmitting. The central controller must obtain the subframe reference from the main reference station  $R1$  or  $R2$ . The relative time delays between the subframe reference burst and the central controller's burst, as well as between the bursts from other terminals in the subnetwork, are precomputed at the main reference station,  $R1$  (or  $R2$ ), with updated satellite parameters. The controller then sends a control burst for the subnetwork under its control. This control burst contains the relative delay parameters and an initial network map generated by the controller.

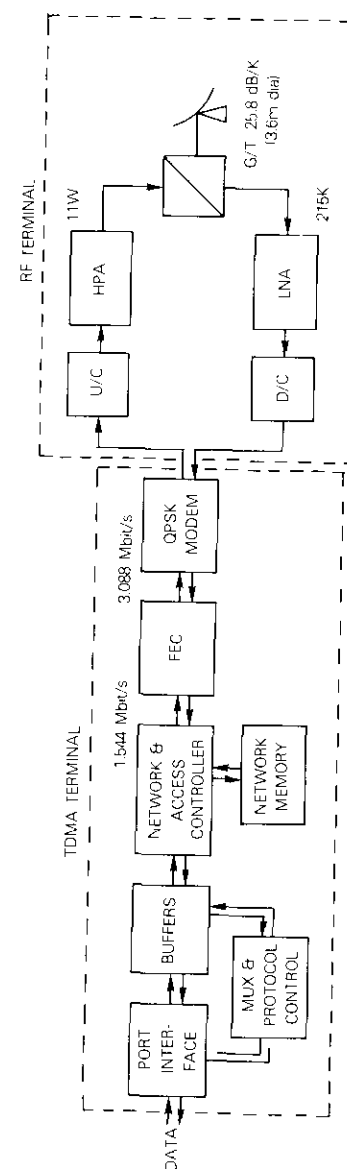


Figure 4. Block Diagram of a Small G/T Earth Station

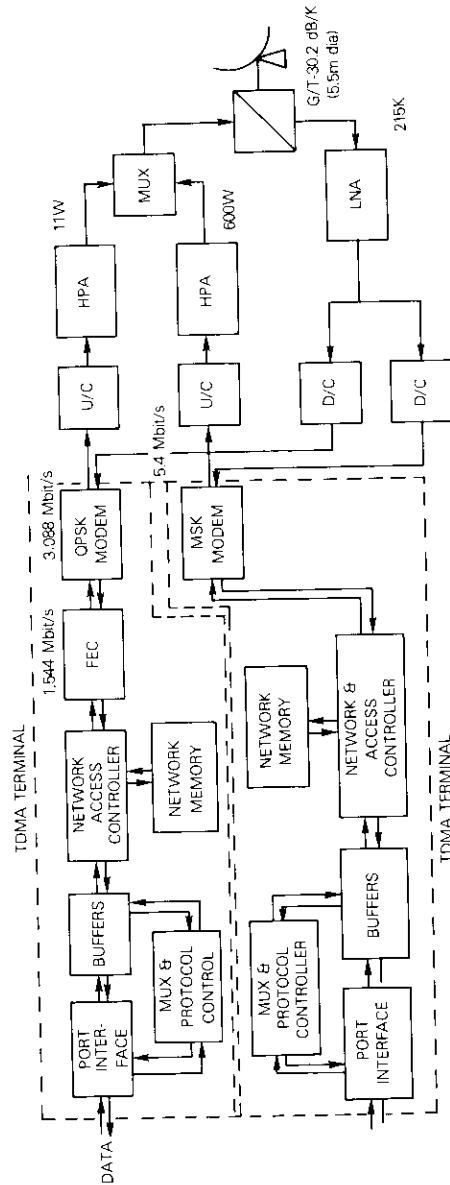


Figure 5. Block Diagram for a Large G/T Earth Station Equipped with a Centralized Controller for a Low Data Rate Subnetwork

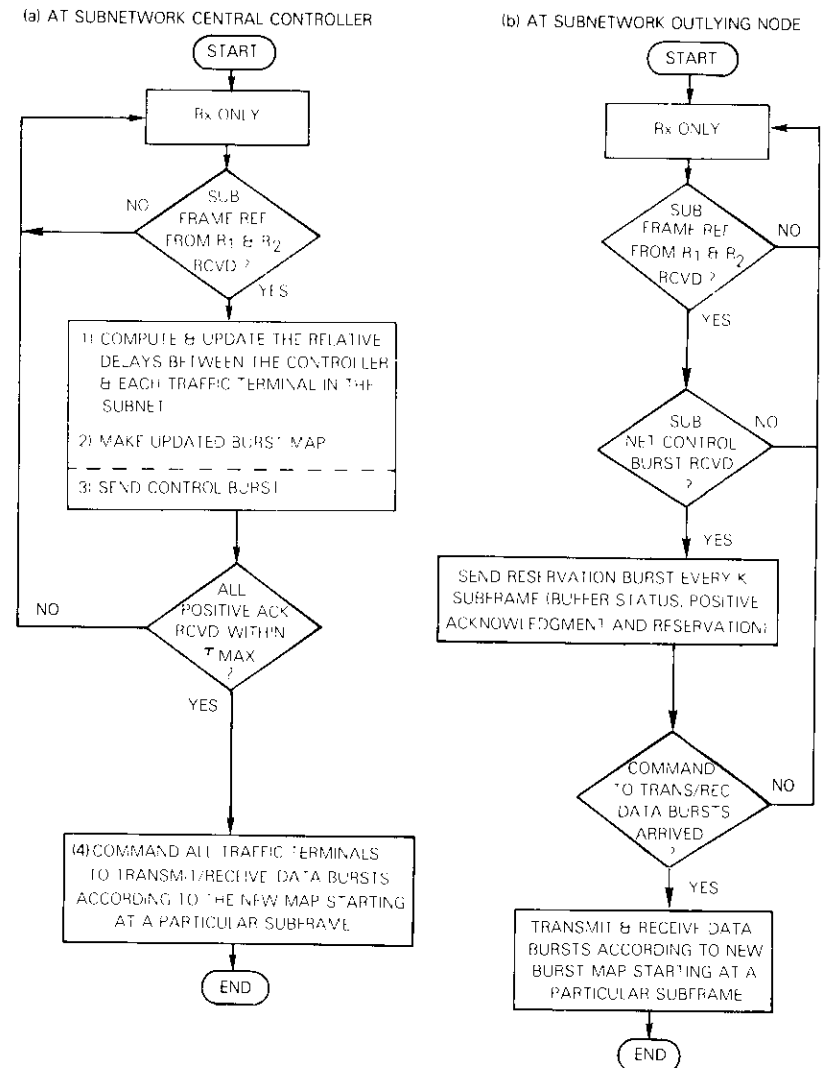


Figure 6. Network Control Algorithm for Low Bit Rate Subnetworks

Each low bit rate TDMA terminal in the subnetwork uses an open-loop method for acquiring burst synchronization. A burst is sent to the proper time window according to the initial network map obtained from the subnetwork central controller via the control burst. A TDMA terminal in the subnetwork, which might fail to acquire burst synchronization within

a prespecified time, would be inhibited from transmitting into that time slot under the command from the subnetwork central controller until a later time and within a time slot determined by the subnetwork central controller.

The status of the buffers at each TDMA terminal is periodically reported to the subnetwork central controller for every  $K$  subframe. This controller generates and transmits a new network map to all TDMA terminals in the subnetwork for every  $L$  subframe with proper error protection. Positive acknowledgment information is transmitted back to the controller from each TDMA terminal. The controller retransmits the new network map within a prespecified maximum time to the TDMA terminal from which no positive acknowledgment has been received until all positive acknowledgments are received. Therefore, upon command from the subnetwork central controller, all TDMA terminals can be switched over to the new network map at a time determined by the controller.

A particular time slot in the subframe is reserved for sending a reservation request and the buffer status to the central controller. In each subframe, however, only one TDMA terminal can access this time slot. The order is cyclic or can be preassigned by the central controller, in which case it must be broadcast to all TDMA terminals in the subnetwork. With  $K$  active terminals in the subnetwork, it will take  $K$  subframes for any terminal to access this time slot again. Since each frame is numbered (periodically) and since the subnetwork central controller knows exactly which burst to anticipate, the burst length for a reservation request and the buffer status can be made reasonably short without losing frame efficiency.

If an inactive TDMA terminal desires to send a reservation request, it must first acquire the control burst from the subnetwork central controller and then use the open-loop method for burst acquisition by sending the request burst, which includes the buffer status, in the designated time slot of the predetermined frame. When the central controller receives the request, a new network map will be generated and broadcast to all terminals. Upon command from the central controller, all terminals in the subnetwork will be switched to accommodate the new network map at the time determined by the central controller. Fully mesh-like networking can thus be realized, even though the control is accomplished in a centralized (tree network) fashion.

For high bit rate TDMA subnetworks such as  $A_1$ ,  $A_2$ , and  $A_3$  in Figure 1, larger G/T earth stations and high bit rate TDMA terminals are employed. For a 14/12-GHz satellite with transponder spacing of about 50 MHz, the antenna diameter and HPA power level are about 5.5 m and 600 W, respec-

tively, to achieve a 54-Mbit/s transmission rate. It is assumed that the TDMA burst modem at each earth station uses minimum-shift-keying (MSK) modulation with proper pulse shaping and adequate circuits for carrier and bit timing synchronization. To minimize earth station costs, no up-link power control is employed. The network and satellite access controller must operate at a bit rate as high as 54 Mbit/s.

The terrestrial interface must have significantly more buffer storage to accommodate higher traffic requirements. High-speed ports ranging from 224 kbit/s to 6.3 Mbit/s can be provided for high-speed computer data transfer. Their outputs are fed directly into the compression buffer without link control protocol. It is assumed that necessary buffer and link control will be performed at the user equipment. Therefore, the equipment and associated software can be significantly more complex than that used in the low bit rate subnetworks. Minicomputer-based or multiple-microprocessor-based implementations may be necessary; however, the same centralized network control principle is used as in the low bit rate subnetworks.

### ***Compatibility with multibeam satellites***

The system described thus far assumes that the up- and down-beam coverage of the transponder can "see" all earth stations. Therefore, every station can see its own burst. In multibeam satellite systems, however, it is sometimes impossible for a station to see its own transmissions. Hence, the network control problem can be more complicated. (For instance, the network control problem of the multibeam INTELSAT V TDMA system is much more complex than many of the single-beam coverage domestic TDMA systems.) Two network control issues are of particular importance: the spot-beam network synchronization and the demand assignment method.

TDMA network synchronization in the multibeam system must be achieved with the aid of stations in other beams. It is assumed that the high bit rate main reference stations,  $R_1$  and  $R_2$ , will have the necessary means to perform satellite ranging, initial acquisition, and steady-state synchronization with the cooperation of reference stations in other beams similar to the method employed in the INTELSAT V TDMA system. It is desirable, however, that the reference stations in each beam or the reference station in one beam and the cooperating relay station in the other beam coordinate the reference burst transmission to ensure that bursts originating from the two up-beams arrive at the satellite simultaneously with respect to the frame reference. Therefore, all frames on the satellite will be synchronized.

This can be achieved as follows: the primary reference station transmits a reference burst which establishes the start of frame at the satellite. The secondary station in the other beam, either a reference station itself or a relay station, receives the reference burst of the primary reference station at a time  $t$  and calculates the necessary delay  $d$  so that a reference burst transmitted by the secondary station at time  $t + d$  would arrive at the satellite in synchronization with the start of a frame. When this is accomplished, stations in each beam can align their bursts with the start of a frame by simply listening to the corresponding reference burst transmission in the individual beam.

For the FDMA/TDMA earth stations, the subframe reference bursts in the transponder are again generated by the main reference station  $R1$  (or  $R2$ ) in each beam, which also computes and updates the relative delays between the reference station and the other stations in the low bit rate subnetworks and broadcasts them in the subframe reference bursts. Each earth station, including the central controller of the subnetworks, performs the functions described in the previous sections except that the transmitting and receiving bursts are dedicated to, and come from, a separate transponder. Thus, the system should be compatible with multi-beam satellites.

### **Compatibility with satellite-switched TDMA**

Satellite-switched (SS) TDMA systems have been planned for future multiple-beam satellites to improve network connectivity and satellite throughput capacity. Since SS-TDMA systems are regarded as the natural successors of TDMA systems, it is of interest to determine whether the mixed TDMA and FDMA/TDMA system proposed in this paper is compatible with SS-TDMA system concepts.

From Figure 2, it is obvious that during the portion of the frame when simple TDMA is employed, the proposed system is compatible with SS-TDMA operation. During subframe  $T_s$ , if all bursts from the FDMA/TDMA carriers in a specific time period are destined for the same beam, they can all be time-switched into that beam. If in a specific frequency slot there is no traffic destined for that beam for a specific time duration, no burst will be transmitted to that beam in this particular frequency slot, but there may be traffic bursts to that same beam from other carrier frequency slots. Thus, the whole transponder must still be switched to that beam to accommodate the traffic requirements in the other carrier frequency slots. Clearly, with some potential loss in transponder loading efficiency, the FDMA/TDMA mode of transmission in subframe  $T_s$  can be made

compatible with the SS-TDMA operation by proper burst scheduling. Therefore, the proposed mixed TDMA and FDMA/TDMA system appears compatible with SS-TDMA operation. To maximize transponder efficiency, however, and to ease control of SS/TDMA switch time, it is necessary to allow the reference station to know the complete burst map of both TDMA and FDMA/TDMA systems.

### **Transmission system performance**

Figure 7 shows the transmission system block diagram for performance evaluation over a hypothetical satellite. At a high data rate (54 Mbit/s), it is assumed that the earth station HPA operates at saturation, and that the corresponding satellite power amplifier is overdriven by about 4 dB to reduce the down-link power losses induced by up-link fades. Since no up-link power control is employed, the desired high bit rate signal may experience significant losses when subjected to severe up-link fades, due to interference from high bit rate TDMA carriers in adjacent transponders. Proper pulse shaping and use of the "more constant" envelope MSK modulation technique can minimize the impairments caused by adjacent transponder interference [4].

Figure 8 shows the power spectral density at the output of the earth station HPA for this shaped MSK signal by using the filter characteristics shown in Figure 9 on an ideal MSK signal before HPA amplification. (The amplitude and phase characteristics of the HPA are shown in Figure 10.) Even with sidelobe minimization, adjacent transponder interference can still be a major cause of system performance degradation, especially under severe up-link fades. The required  $E_b/N_o$  for achieving a given BER performance for the high rate TDMA/MSK system, as determined by computer simulation, is shown in Figure 11 with various levels of up-link fade as parameters. (The satellite receive and transmit filters are assumed to be 6- and 4-pole elliptic filters with group delay equalization, respectively. The TWTA amplitude and phase characteristics are shown in Figure 10.)

For the 1.544-Mbit/s low-information bit rate FDMA/TDMA/QPSK transmission, it is assumed that the earth station HPA operates at 4-dB input backoff from saturation. Because of the FDMA/TDMA mode of access, the satellite power amplifier must be backed off considerably into the quasi-linear region. Since no up-link control is employed, the desired signal must have adequate margin to compensate for the losses caused by adjacent carrier interference, intermodulation noise, and loss of down-link power. Carrier frequency assignments must be carefully planned to minimize the degradation caused by intermodulation and adjacent carrier

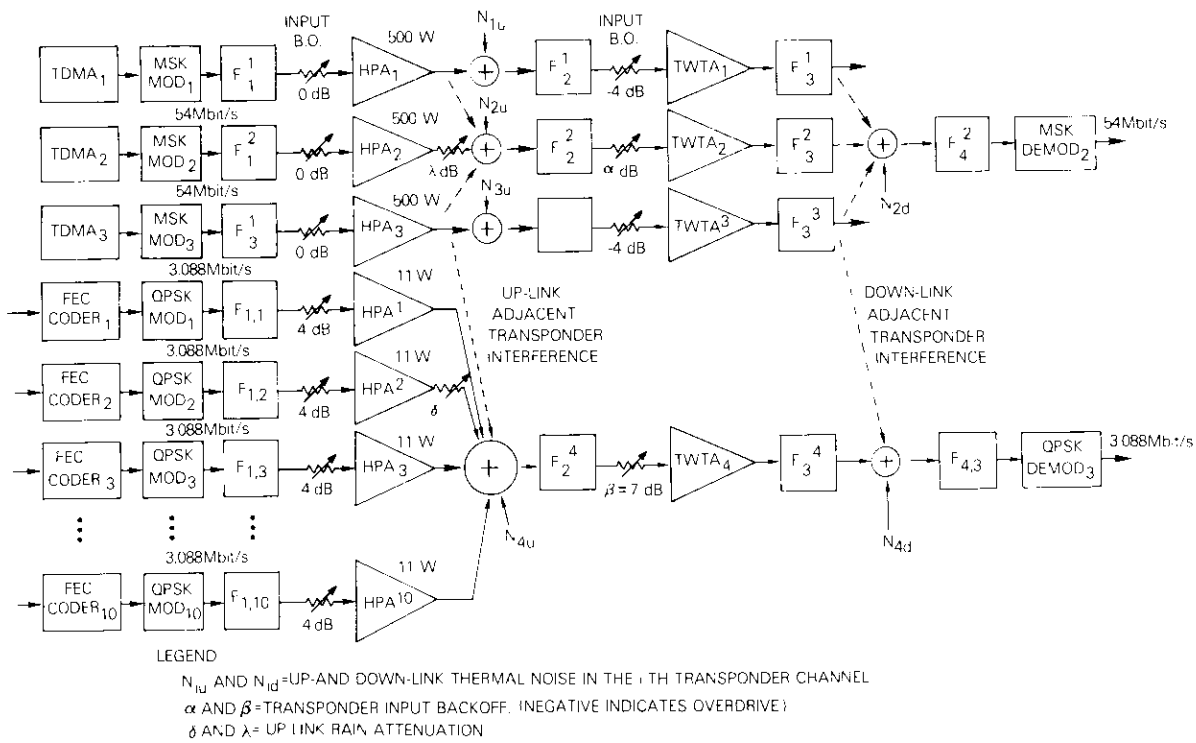


Figure 7. General Transmission System Block Diagram for Performance Evaluation

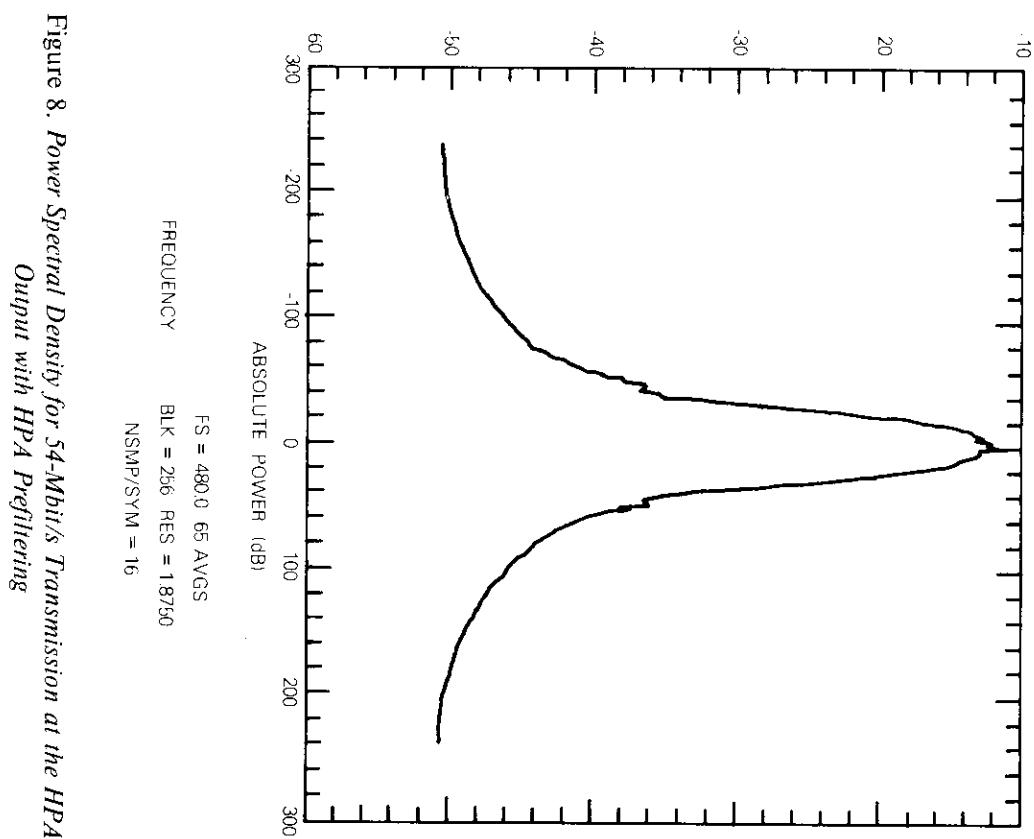


Figure 8. Power Spectral Density for 54-Mbit/s Transmission at the HPA Output with HPA Prefiltering

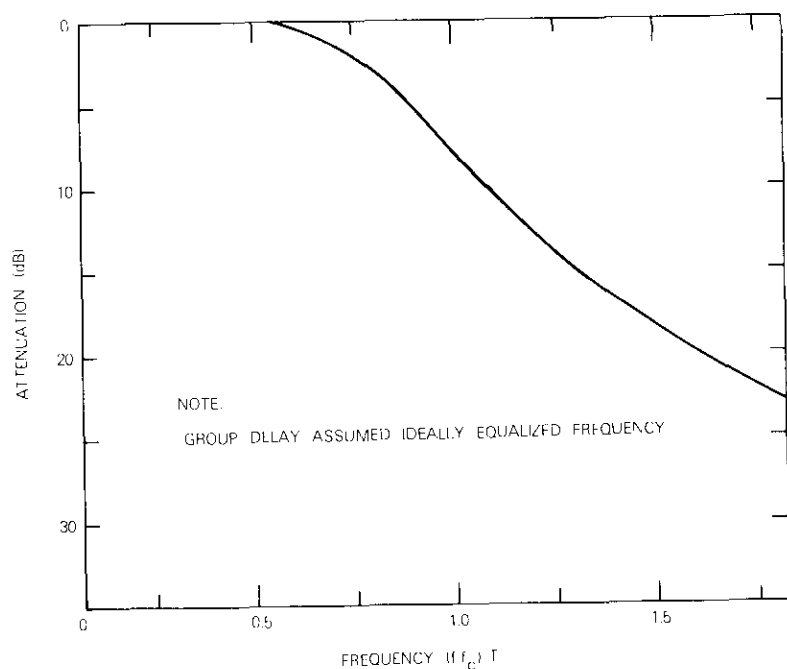


Figure 9. Filter Characteristics for Ideal MSK Signal Before HPA Amplification

interference. Figure 12 illustrates the intermodulation power spectral density for a rate 1/2 FEC coded 10-carrier assignment plan which minimizes the effect of intermodulation and adjacent interference on the assigned carriers. This plan was generated by using the difference-set concept for channel frequency assignment developed in Reference 5. The intermodulation power spectral density was computed by the PRIME software developed in Reference 6. The QPSK modem transmit and receive filters were assumed to be of the 4-pole Butterworth type with BT products of 1.5 and 1.1, respectively.

Figure 13 shows the BER versus the required down-link  $E_b/N_o$  performance of the QPSK system for the worst carrier in the 10-carrier plan for the cases of no up-link fade and 3-dB up-link fade, respectively. The rate one-half FEC was assumed to be an extended Golay (24, 12) code with 2-bit weighted erasure decoding [7], which is relatively inexpensive and simple to implement. Should additional power margin be required, the

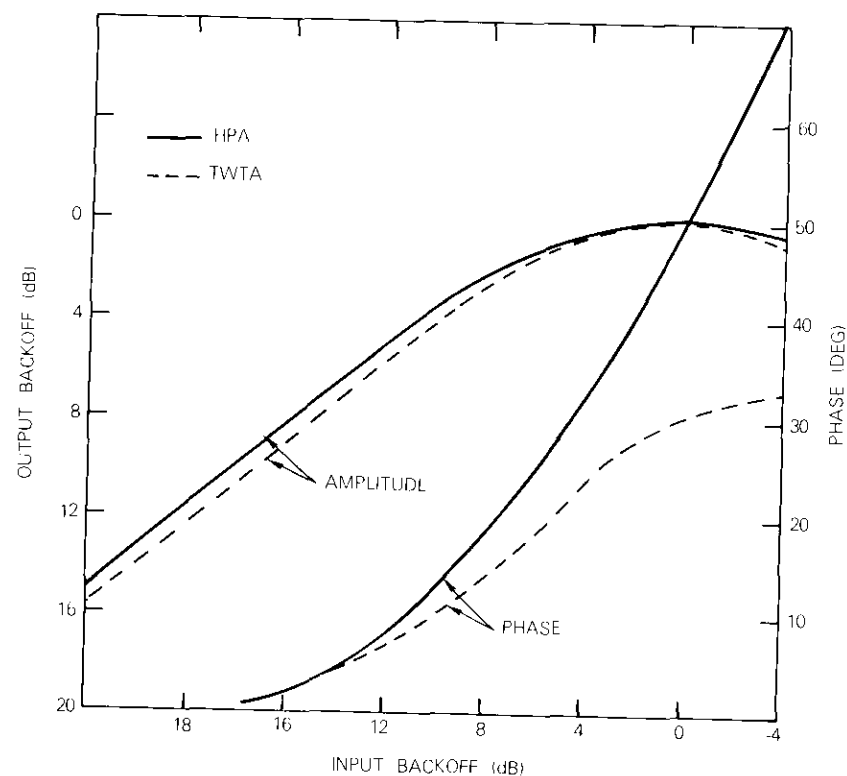


Figure 10. Amplitude and Phase Characteristics of HPA and TWTA

rate 1/2, constraint length 7, convolutional code with Viterbi decoding could be used to yield an additional 3-dB coding improvement in  $E_b/N_o$  at a BER of  $10^{-5}$ .

### Example network

To illustrate the usefulness of the proposed system concept, the hypothetical network shown in Figure 14, which includes 10 national data processing centers (DPCs) with large traffic requirements, will be considered. Traffic between these national DPCs can vary between 224 kbit/s and 1.544 Mbit/s. A total capacity of 15.44 Mbit/s, therefore, is needed to handle the peak traffic condition for the high data rate subnetwork between the 10 national DPCs.

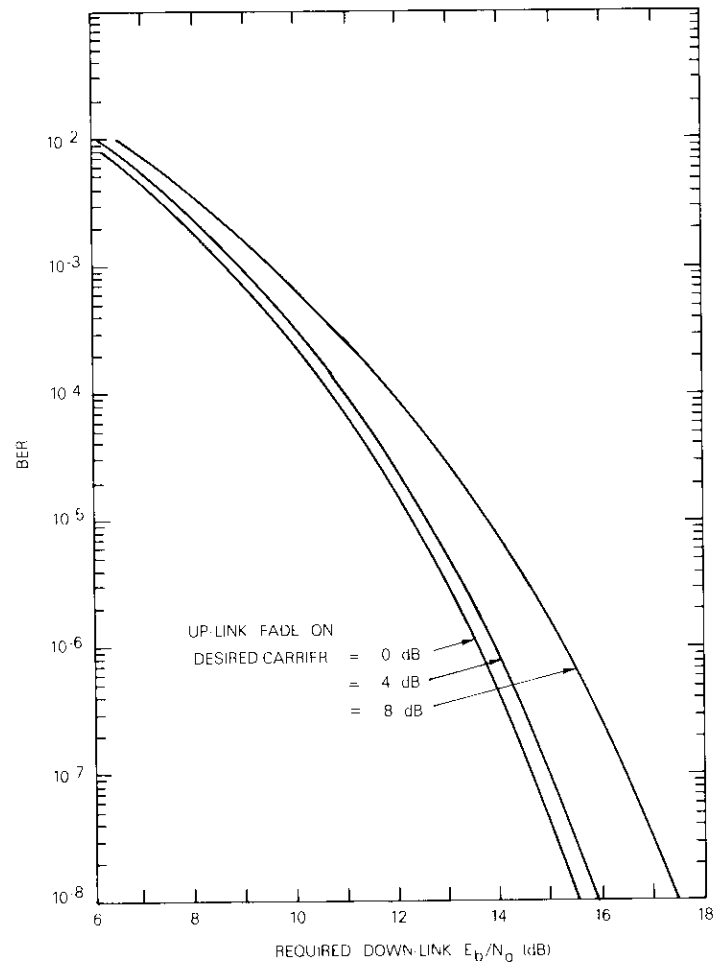


Figure 11. BER vs Required Down-Link  $E_b/N_0$  for 54-Mbit/s Pulse-Shaped MSK Transmission (earth station HPAs at saturation; satellite TWTA's nominally overdriven by 4 dB at input)

Each of the national DP centers is also connected by a full-duplex 50-kbit/s link to eight regional DP centers, and serves as a hub to these centers. Occasionally, some of the regional DP centers may require a full-duplex 50-kbit/s link to exchange data, in which case the link capacity from the hub to these nodes will be assigned to other links. Thus, each

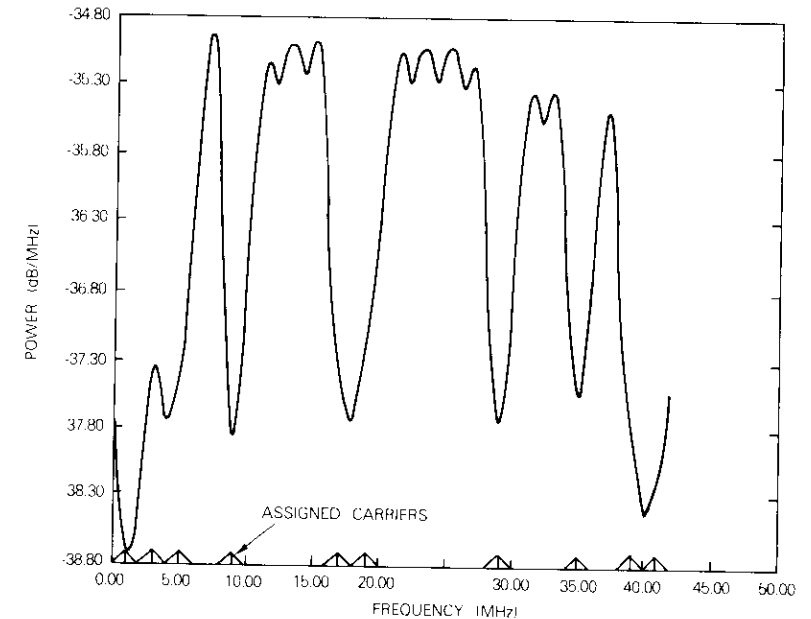


Figure 12. Intermodulation Power Spectral Density for the Rate 1/2 FEC Coded 10-Carrier Plan at 7-dB TWTA Input Backoff

regional subnetwork requires  $8 \times 2 \times 50$  kbit/s = 0.8-Mbit/s capacity.

Two network design options are available for this example network. One employs a large earth station operating at 54 Mbit/s at each national and regional node. A total of  $(10 + 8 \times 10) = 90$  large earth stations is required. With about 200 symbols per burst for preamble and guard time, this homogeneous high bit rate solution using large earth stations will consume about 45 percent of the 54-Mbit/s transponder resources.

The second design option employs large earth stations only at the national DP centers; small earth stations are used for all regional nodes. A total of 10 large and 80 small earth stations is required. The national subnetwork with a total capacity of 15.44 Mbit/s requires about one-third of the transponder resources or a subframe of about 5 ms of the 15-ms frame at 54 Mbit/s. Each regional subnetwork can be carried by one FDMA/TDMA carrier at a 1.544-Mbit/s information rate with a subframe

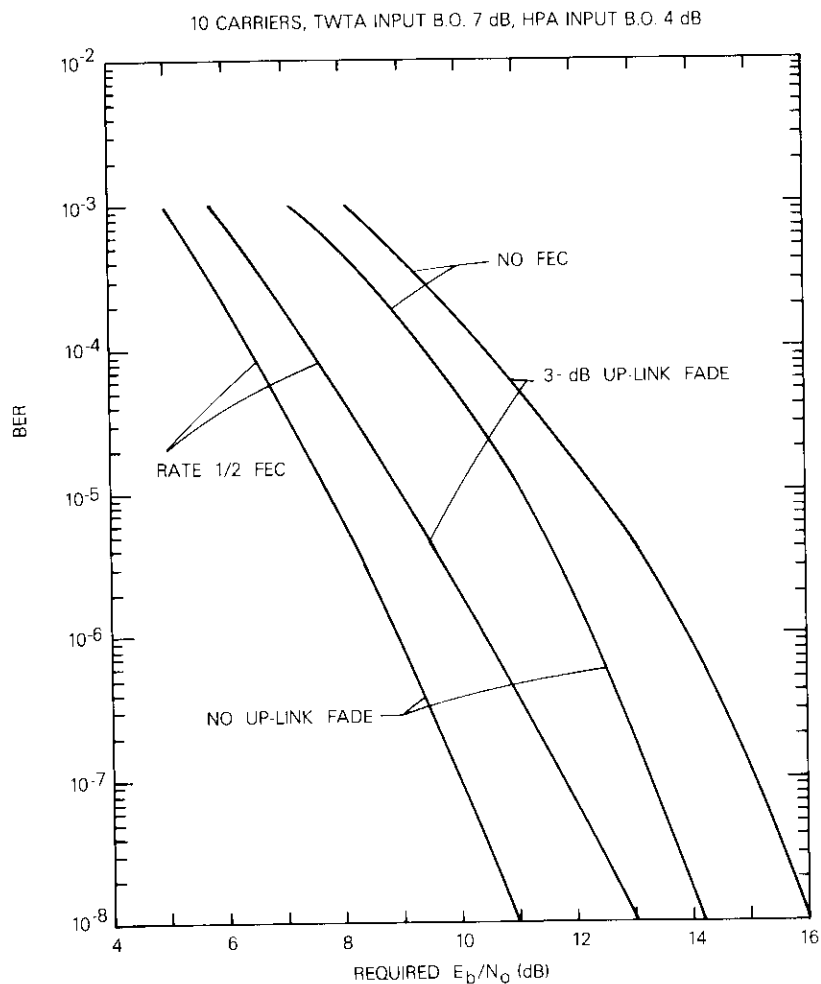


Figure 13. BER vs Required Down-Link  $E_b/N_0$  Performance for the 10-Carrier Plan

duration of approximately 10 ms. With about 240 symbols per burst at a 1.544-Mbaud rate for preamble and guard time, each regional subnetwork uses nearly a complete subframe. The 10 regional subnetworks occupy all 10 FDMA/TDMA subframes of 10 ms each in the 10 channel frequency slots. Therefore, with this mixed G/T and mixed burst rate approach, the complete transponder (100 percent) is occupied.

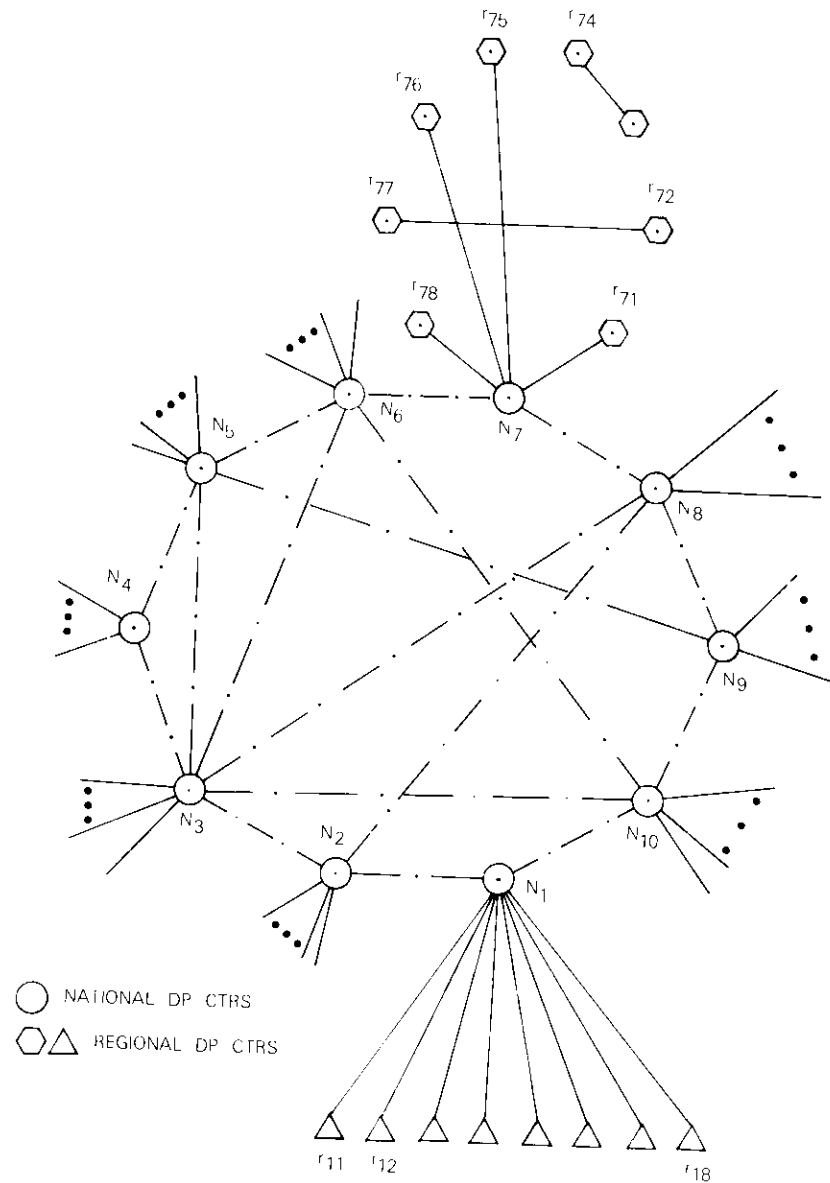


Figure 14. Example Network

If it is assumed that a large earth station costs  $t$  times (e.g.,  $t = 5$ ) more than a small one, and that the cost of a small earth station is 1 unit, then the homogeneous approach (large earth stations at all nodes) would lead to a cost of about  $90 \times 5 = 450$  units, while the nonhomogeneous approach would lead to a cost of about  $10 \times 5 + 80 = 130$  units. Thus, a cost reduction factor of about 3.5 to 1 can be achieved at the expense of about a 2-to-1 reduction in total transponder throughput (45 percent vs 100 percent). These factors represent only an illustrative example; detailed trade-off studies will be required for specific situations.

The frame duration for high and low data rate transmissions should be apportioned by the overall satellite system manager (controller). The subframe boundaries should be optimized to maximize the overall satellite transponder throughput according to demand, which could be adjusted not on a call-by-call basis, but on some periodic basis, e.g., hourly, daily, weekly, or monthly. The central controller of each subnetwork, however, should perform the burst scheduling within the assigned subframe boundaries.

### Conclusions

The proposed demand-assigned satellite communications system could provide a cost-effective solution for networks having a wide range of traffic requirements. Mixed G/T and data rate earth stations are employed to minimize the earth segment costs at nodes with low traffic requirements. The mixture of high data rate TDMA and low data rate FDMA/TDMA nonhomogeneous mode of transmission could significantly reduce earth segment costs at the expense of only a slight reduction in space segment utilization. The proposed system appears promising as a cost-effective means for allowing both large and small networks to share given transponder resources while employing both large and small earth stations. The system could be useful for interconnecting low data rate subnetworks into a larger network. The proposed system is compatible with satellite-switched TDMA operation in future multi-beam satellite systems.

### Acknowledgment

The author would like to thank S. Lebowitz for his help in generating some of the computer simulation results.

### References

- [1] T. Sekimoto and J. G. Puente, "A Satellite Time-Division Multiple-Access Experiment," *IEEE Transactions on Communication Technology*, COM-16, No. 4, August 1968, pp. 581-588.
- [2] O. G. Gabbard, "Design of a Satellite Time-Division Multiple-Access Burst Synchronizer," *IEEE Transactions on Communication Technology*, COM-16, No. 4, August 1968, pp. 589-596.
- [3] W. G. Schmidt, "An Efficient TDMA System for Use by Emerging Nations with the INTELSAT IV Satellite," *EASCON '68*, Washington, D.C., September 1968, pp. 21-27.
- [4] R. J. F. Fang, "Quaternary Transmission Over Satellite Channels with Cascaded Nonlinear Elements and Adjacent Channel Interference," *IEEE Transactions on Communications*, COM-29, No. 5, May 1981, pp. 567-581.
- [5] R. J. F. Fang and W. A. Sandrin, "Carrier Frequency Assignment for Nonlinear Repeaters," *COMSAT Technical Review*, Vol. 7, No. 1, Spring 1977, pp. 227-246.
- [6] P. Y. K. Chang and R. J. F. Fang, "Intermodulation in Memoryless Nonlinear Amplifiers Accessed by FM and/or PSK Signals," *COMSAT Technical Review*, Vol. 8, No. 1, Spring 1978, pp. 89-140.
- [7] M. I. Weng and L. N. Lee, "Weighted Erasure Decoding for Binary Block Codes With Two-Bit Soft-Decision Demodulation," *COMSAT Technical Review*, Vol. 10, No. 2, Fall 1980, pp. 397-415.



*Russell J. F. Fang received a B.S.E.E. in 1962 from National Taiwan University, Taipei, China, and an M.S.E.E. and Ph.D. from Stanford University in 1964 and 1968. From 1964 to 1966 he was a research engineer at Stanford Research Institute, engaged in fading channel characterization and communications systems analysis while he worked on his doctoral degree under the Stanford honors cooperative program. Since joining COMSAT Laboratories in 1968, Dr. Fang has been a Member of the Technical Staff, Staff Scientist, and Department Manager, and is currently Director of the*

*Transmission Systems Laboratory. He is responsible for research and development of multiple small user satellite communications systems concepts and techniques, including mobile and data collection applications; R&D of advanced transmission system technologies; analysis, simulation, and modeling of transmission systems; and theoretical computer simulation and hardware simulation support in the areas of modulation/access techniques, forward error correction coding, encryption, and network control. Dr. Fang has authored or co-authored more than 20 papers in professional journals. He is a senior member of IEEE.*

Index: modulation, demodulation, modems, networks, small terminals, systems monitoring

## **SATNET packet data transmission\***

L. PALMER, J. KAISER, S. ROTHSCHILD, AND D. MILLS

(Manuscript received December 18, 1981)

### **Abstract**

The Atlantic Packet Satellite Network (SATNET) has operated experimentally via the INTELSAT IV-A Atlantic primary satellite since 1975. The system allows packet data transmission between three INTELSAT standard A earth stations at Etam, West Virginia; Goonhilly, United Kingdom; and Tanum, Sweden. Packet transmissions are time shared on a single carrier in the SPADE transponder of the satellite in a format designated as multidestination half duplex (MDHD).

During the final phase of the experimental period (mid-1979 through early 1981), new packet satellite program (PSP) terminals were installed at the three INTELSAT standard A earth stations, and at a fourth smaller earth station at Clarksburg, Maryland. These terminals provided expanded capability through several additional transmission modes that allow the smaller earth station to participate in the distributed control of the demand-assigned network. New test and monitoring (T&M) features were also included in the PSP terminals to assist in the monitoring and maintenance of the transmission links.

In the second quarter of 1981, SATNET was converted from experimental to operational status. This paper describes the SATNET system and summarizes the performance of the RF transmission links. Future plans are discussed, including the utilization of the new T&M features.

\*The work reported in this paper was sponsored by the Defense Advanced Research Projects Agency (DARPA).

### **Introduction/background**

This paper reviews COMSAT's recent experience with SATNET, which connects ARPANET [1]-[10] to similar networks in Europe via the INTELSAT Atlantic primary satellite. SATNET has operated on an experimental basis since 1975 and utilizes a single 64-kbit/s channel in the SPADE transponder to interconnect three large 30-m (INTELSAT standard A) earth stations in the United States, the United Kingdom, and Sweden. These stations time share this channel and transmit packets of digital data which are received by all three stations in the network. The interconnection to the terrestrial network is provided by a satellite interface message processor (satellite IMP or SIMP) located at each earth station.

The mode of transmission used in SATNET is designated as multidirectional half duplex, which is distinctly different from that used in other international satellite data communications. Conventionally, digital data are sent at rates from 300 to 4,800 bit/s (sometimes as high as 9,600 bit/s) over 4-kHz analog voice channels. These channels are provided by common carriers and are routed to an international gateway earth station from remote telephone exchanges. The channels are multiplexed with other voice-band channels in an FDM baseband. Generally, the multiplexed baseband signals are transmitted intact to a particular country from the gateway earth station so that the receiving earth station is unaware that a particular channel carries data rather than analog speech. The global satellite system also provides primarily two-way (duplex) voice circuit capabilities, *i.e.*, a channel in each direction. (Data transmission may or may not require simultaneous two-way channels.) Connecting  $N$  nodes (countries) using conventional voice-band data circuits would therefore require  $N(N - 1)$  channels in the spacecraft, and equipment at each earth station to handle the transmissions to and from  $N - 1$  other nodes.

SATNET departs significantly from this conventional mode of international data transmission. SATNET utilizes only a single channel in the satellite (half-duplex operation), and all earth stations transmit on the 6-GHz up-link frequency corresponding to this channel. Simultaneously, all stations receive the 4-GHz down-link carrier corresponding to the down-link transmissions. Thus, all transmissions are multidirectional or broadcast, since all stations in the network receive all transmissions on the single channel. Bursts of data are "addressed" so that a specific receiving station retains only those bursts intended for that station.

This mode of operation is made possible by subdividing time into slots approximately 10 ms long and assigning these time slots to the different earth stations for data transmission. (A 10-ms interval corresponds to 640 bits at 64 kbit/s.) A collection of 128 slots (approximately 1.3 s in dura-

tion) constitutes a frame. A few slots are reserved for control (*i.e.*, for requesting future information slots), and most of the remainder are reserved for the actual transmission of information. Four slots transmit "hello" bursts to allow earth stations in the network to remain synchronized, and hence to share the frame, even during periods of the day when none of the stations has data to transmit.

Synchronization and channel scheduling are performed in the SIMP, which is operated by a minicomputer located at each earth station. The SIMP, which also serves as an interface to the terrestrial network, is connected via high-speed (~50-kbit/s) data transmission lines to nodes in the terrestrial network. These nodes are generally located several hundred miles from the large standard A earth stations that serve as international gateways.

In the direction of the satellite channel, the SIMP is connected to interfaces and burst modems that convert the packet data into a form that is suitable for transmission over the satellite channel. For early SATNET experiments, these interfaces and modems were implemented partly by modified SPADE channel units. Currently, all of these functions have been integrated into a permanent PSP terminal that is installed at each earth station along with the SIMP.

Packet switching experiments between the United States and Europe began in the fall of 1975, when the first SIMP-SPADE interface (SSI) modules were installed at the Etam and Goonhilly earth stations. This initial two-station "network" was used to determine the performance of a communications satellite system in which two earth stations, or nodes, share a single 64-kbit/s channel. At each earth station, the SIMP initiated burst transmissions. The SIMP was implemented by a Honeywell 316 computer, which was modified by Bolt, Beranek, and Newman, Inc. (BBN), of Cambridge, Massachusetts, for operation in SATNET. New SSIs were installed at Etam and Goonhilly in 1977, and later in the same year, at Tanum, resulting in the present network of three standard A earth stations.

In addition to these three large earth stations, an unattended earth terminal (UET) at COMSAT Laboratories has occasionally been used as a fourth node in SATNET. Forward error correction coding of the data is necessary when the UET participates in the network, since the UET operates at a  $G/T$  of 28.5 dB/K, as compared to a  $G/T$  of 40.7 dB/K for INTELSAT standard A stations. Because of its lower  $G/T$ , the UET cannot receive the normal 64-kbit/s QPSK transmission mode, so that bursts intended for the small station must be sent as rate 1/2 coded BPSK (16-kbit/s information bit rate).

**Network configuration**

Figure 1 shows the network configuration of SATNET, with nodes at Etam, Clarksburg, Goonhilly, and Tanum. Each node has a PSP terminal, built by COMSAT laboratories, which contains advanced design burst modems and codecs built by the Linkabit Corporation; and the SIMP, a 32k-word Honeywell 316 minicomputer with special interfaces and software supplied by Bolt, Beranek, and Newman Corporation. Traffic between SATNET and the terrestrial networks flows through gateways, which are in most cases separate devices created from DEC PDP/LSI-11 machines connected to both networks.

The gateways shown in Figure 1 are as follows: BBN gateway, connecting an ARPANET IMP to Etam via a 50-kbit/s line; UCL gateway connecting University College, London, to Goonhilly via a 48-kbit/s line; and the NDRE (Norwegian Defense Research Establishment) gateway connecting NORSAR (Norwegian Seismic Array) to Tanum via a 9.6-kbit/s line.

Figure 2 shows the system configuration inside the earth stations. Data packets are received at the terrestrial interface of the SIMP where the data are stored briefly. These packets, or bursts, of digital data are processed in the SIMP, buffered as necessary, and scheduled for transmission over the satellite channel according to priority and/or allowable message delay. The SIMP also synchronizes time slots within a 1.3-s time-division multiple-access (TDMA) frame, and initiates time slot requests in a control subframe to effect distributed control and demand assignment of segments of the channel, in cooperation with the SIMPs located at the overseas terminals. Several channel-scheduling protocols are available in SATNET; contention-based priority-oriented demand assignment [11] is generally used by the large stations.

At the proper time within the TDMA frame, the SIMP forms a packet containing header and data portions and sends this burst to the PSP terminal, where it is processed for transmission over the satellite channel. In addition to prefixing acquisition preambles on the front of each packet, the interfaces in the PSP terminal can apply error-control coding to all, or only a part, of the packet. These optional modes of transmission are selected by the SIMP and passed to the PSP terminal as information in the first two header words; the optional modes include uncoded QPSK (channel rate of 64 kbit/s); rate 1/2 coded QPSK (information bit rate of 32 kbit/s); and rate 1/2 coded BPSK (information bit rate of 16 kbit/s). The mode of transmission selected by the SIMP depends on the receiving potential of the least capable earth station in the network that must receive that particular packet. With only large earth stations (*i.e.*,

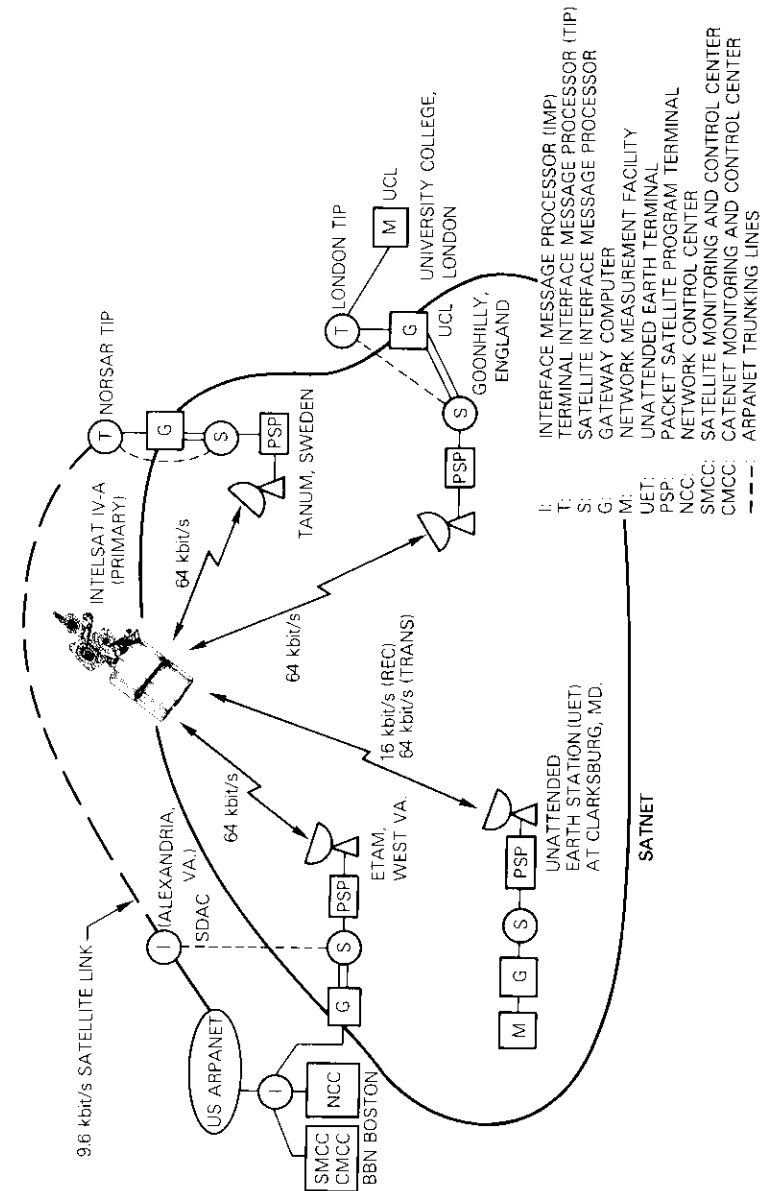


Figure 1. Network Configuration of SATNET

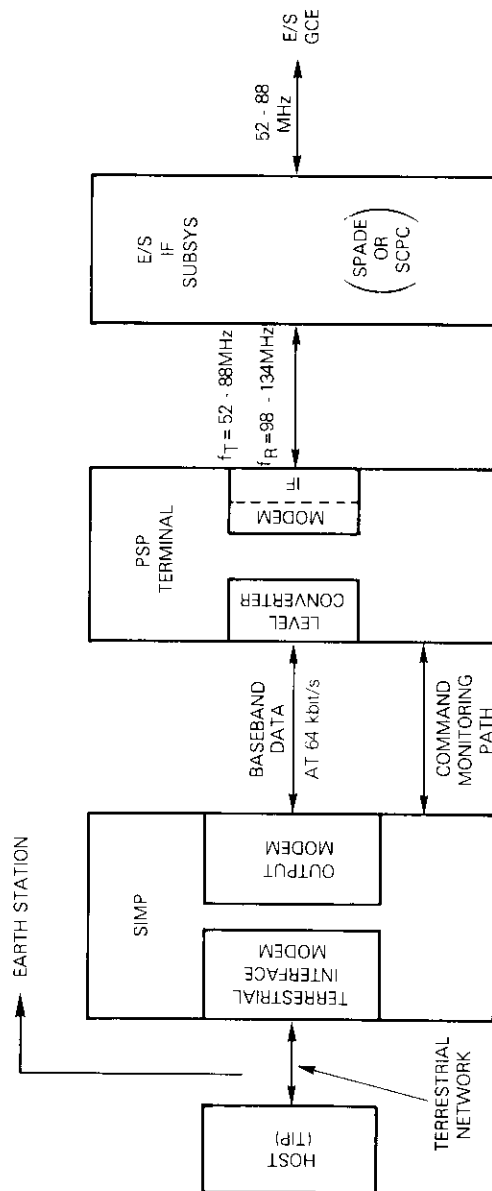


Figure 2. Earth Station Equipment

INTELSAT standard A) in the network, uncoded QPSK transmission is used; the PSP terminal contains redundant interface units and modems for this transmission mode.

The modulated carrier from the PSP terminal is combined with all SCPC carriers at Etam, or with all SPADE carriers at Goonhilly or Tanum in their respective IF subsystems, and then transmitted to the earth station ground control equipment (GCE). The PSP terminal thus interfaces the IF subsystem of the earth station and generates bursts of QPSK (or BPSK) modulated signals for up-conversion, amplification, and transmission to the satellite.

In addition to the data transfer paths between the SIMP and the PSP terminal, a command and monitoring path is available through which the SIMP can automatically reconfigure the PSP terminal and extract monitoring data from the interfaces and modems. These functions are utilized for status monitoring, link quality monitoring, and for reconfiguration and troubleshooting.

Upon signal reception, the down-link channel from the satellite is down-converted to an intermediate frequency and applied to the receive side of the modem in the PSP terminal. The modem detects the presence of a burst, synchronizes to the incoming signal, and performs coherent demodulation of the binary data. For coded packets, error-correcting decoding is performed in the receive interfaces. The received data, less the acquisition preambles, are then passed to the SIMP as serial binary data. The SIMP, in turn, processes the received data, stores them briefly, and then retransmits them over the terrestrial channel to a gateway or host computer. By making use of redundant data within each packet, the SIMPs, utilizing both hardware and software checksums, check for any bit errors in the received packet and thus determine if data are to be passed to their host computer or discarded. If a packet is discarded because of detected errors, the host-resident protocols will initiate selective retransmission of that packet.

### Transmission characteristics

SATNET is assigned to one of the 800 available channels in the SPADE transponder of the Atlantic primary path INTELSAT satellite. These channels have 45-kHz center-to-center spacing. Most carriers in the SPADE transponder carry 56-kbit/s speech using 7-bit PCM with voice activation. The SATNET carrier has a different transmission format, as discussed later in this section.

The link budget for 64-kbit/s transmission in the SPADE transponder gives  $(C/N_o)_{up}$  of 69 dB-Hz and  $(C/N_o)_{down}$  into a standard A terminal of 64.7 dB-Hz. When combined with a worst-case intermodulation noise density of 69 dB-Hz, these up- and down-link carrier power-to-noise-density ratios  $(C/N_o)$  give an overall  $(C/N_o)_T$  value of approximately 62 dB-Hz. This results in a nominal  $E_b/N_o$  of 14 dB for 64-kbit/s transmission. In a 38-kHz noise bandwidth, this gives a  $C/N$  of 16.2 dB as the nominal operating condition of the links into the large earth stations. For packets received at the small earth station at Clarksburg,  $(C/N_o)_{DN}$  is reduced by the difference between the G/T values of the standard A earth station ( $G/T = 40.7$  dB/K), and the UET ( $G/T = 28.5$ ), resulting in overall transmission that is almost completely down-link limited with  $(C/N_o)_T = 52.5$  dB-Hz. The small terminal thus operates at  $C/N = 6.7$  dB in a 38-kHz bandwidth, and  $E_b/N_o = 10.5$  dB for 16-kbit/s transmission.

Measured modem back-to-back error-rate performance is plotted in Figure 3 for both uncoded QPSK (64-kbit/s) and rate 1/2 coded BPSK (16-kbit/s) operation.

### Transmission format

The frame structure used in SATNET is controlled by the SIMP. The 10- $\mu$ s clock in the Honeywell 316 SIMP is divided by 1024 to produce the epochs of the virtual slots (vs), each having a duration of 10.24 ms. The frame consists of 128 vs and has a duration of 1.31072 s. The current frame format reserves four vs/frame for hello bursts, one transmitted by each of the three standard A stations, and one reserved for the small station at Clarksburg. During a 24-hour period, each station transmits 65,918 hello bursts which are received by all active stations.

The rest of the frame is divided into control and information subframes as shown in Figure 4. The control subframe can utilize one of several access protocols. In the first, fixed priority-oriented demand assignment (FPODA), each station is assigned a time slot in which to request assignments in the information subframe. In the second, contention-based priority-oriented demand assignment (CPODA) [11], the control subframe is utilized in a slotted Aloha mode. For this mode to operate properly, reliable detection of colliding control bursts (contentions) must occur at all receiving stations.

The format of the bursts transmitted in SATNET is shown in Figure 4. Each burst is preceded by a preamble of 64 alternating symbols to allow modem acquisition. For operation into small earth stations, this preamble

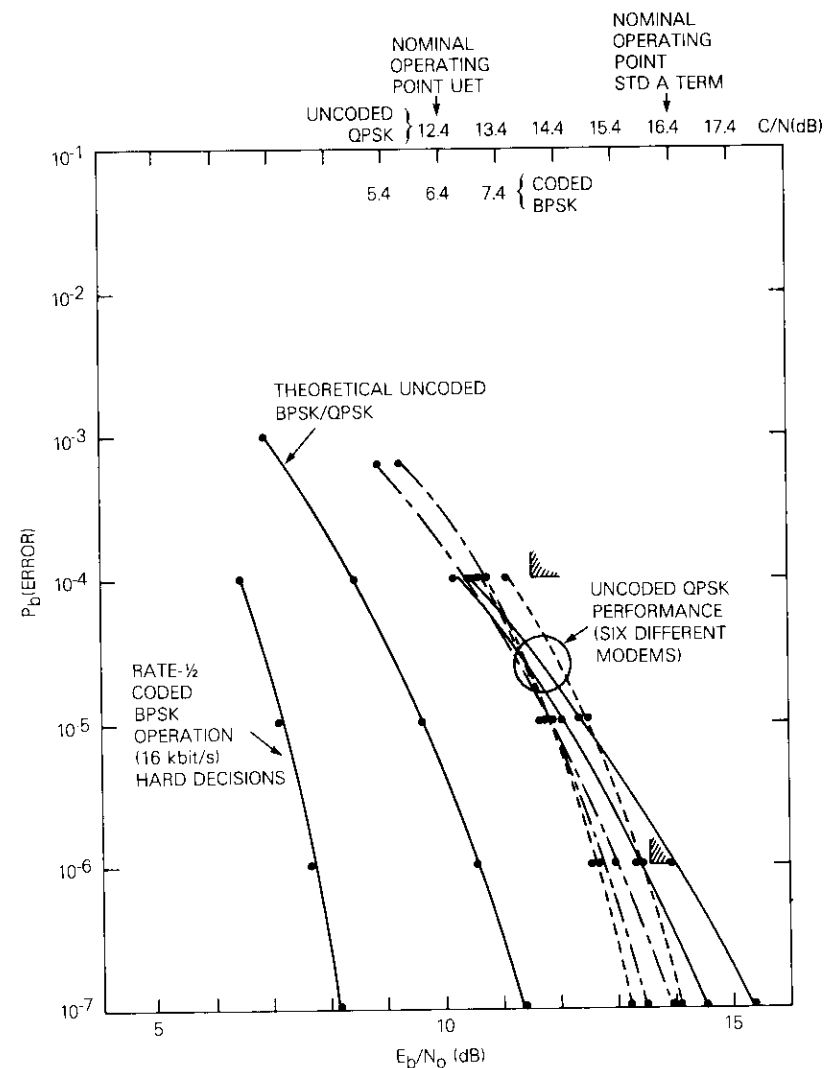


Figure 3. Measured Error-Rate Performance

must be lengthened to 96 symbols. Following the preamble is a 16-symbol unique word, divided into two 16-bit quadrature sequences, which provides word synchronization for the data and allows for phase ambiguity resolution of the modem output. After the unique word, four



station. As noted earlier, each station transmits about 66,000 hello packets per day and receives its own packets and those of each of the other stations. There are, therefore, nine links among the three large earth stations. Each SIMP in the network is programmed to count the hello packets received from each station during an interval of 64 frames (1.4 minutes). During this interval, 64 hello packets are expected from each station and the actual numbers received with and without a good check-sum are counted.

Figure 5 shows the events that contribute to this counting process. Hello packets can be missed completely due to failure of the modem to acquire the preamble or of the interface to detect the unique word. This can occur if the burst from a station is low in power level or out of frequency tolerance. Power levels for all stations are adjusted, if necessary, via Etam. Figure 6 shows envelope levels of a typical set of three hello bursts received at Etam. For this example, the hello burst received from Tanum is 2 dB low, requiring adjustment of Tanum's transmission. Frequency tolerance is kept within  $\pm 2.0$  kHz, which is a fairly large fraction (six percent) of the symbol rate. Achieving rapid, reliable acquisition despite such a frequency uncertainty of  $\pm 2.0$  kHz was one of the more difficult tasks in development of the microprocessor-based PSP modem.

The packet acquisition process involves several steps. First, the presence of a packet must be detected. The microprocessor is thus constantly processing the samples taken from the in-phase and quadrature (I&Q) channels of the receiver and applying these to a matched filter (inverting the sign of alternate pairs of samples), looking for the alternating BPSK preamble at the beginning of the packet. This process is essentially one of energy detection, although the quadriphase signal must contain an alternating preamble. (The modem will not detect a burst with an unmodulated carrier preamble, for example.) Parallel matched filters are used so that a measure of coarse symbol timing is achieved when packet presence is detected in one of the filters [12].

When packet presence is detected, a sequence of the most recent samples is processed again to estimate the frequency offset between the incoming packet and the local reference. The final local oscillator in the modem heterodynes incoming signals to zero frequency  $\pm 2.0$  kHz (the maximum initial frequency uncertainty in the system). With this maximum initial uncertainty, the incoming phasor can rotate  $22.5^\circ$  during one symbol time or a full cycle over 16 symbols. The frequency estimator basically makes an estimate of  $\dot{\theta}$  (phase derivative) over a span of 32 symbols in the preamble. This technique yields a frequency estimate with an accuracy of approximately 30 Hz. The initial frequency estimate is

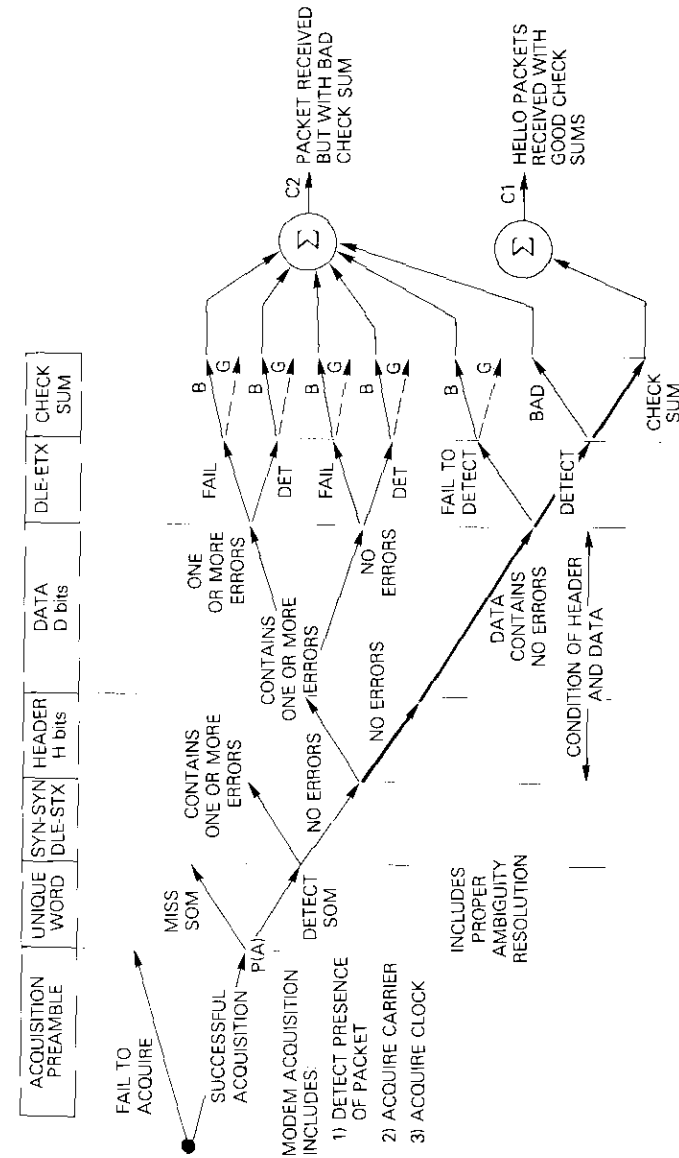


Figure 5. Missed Hello Packet Counting Procedure

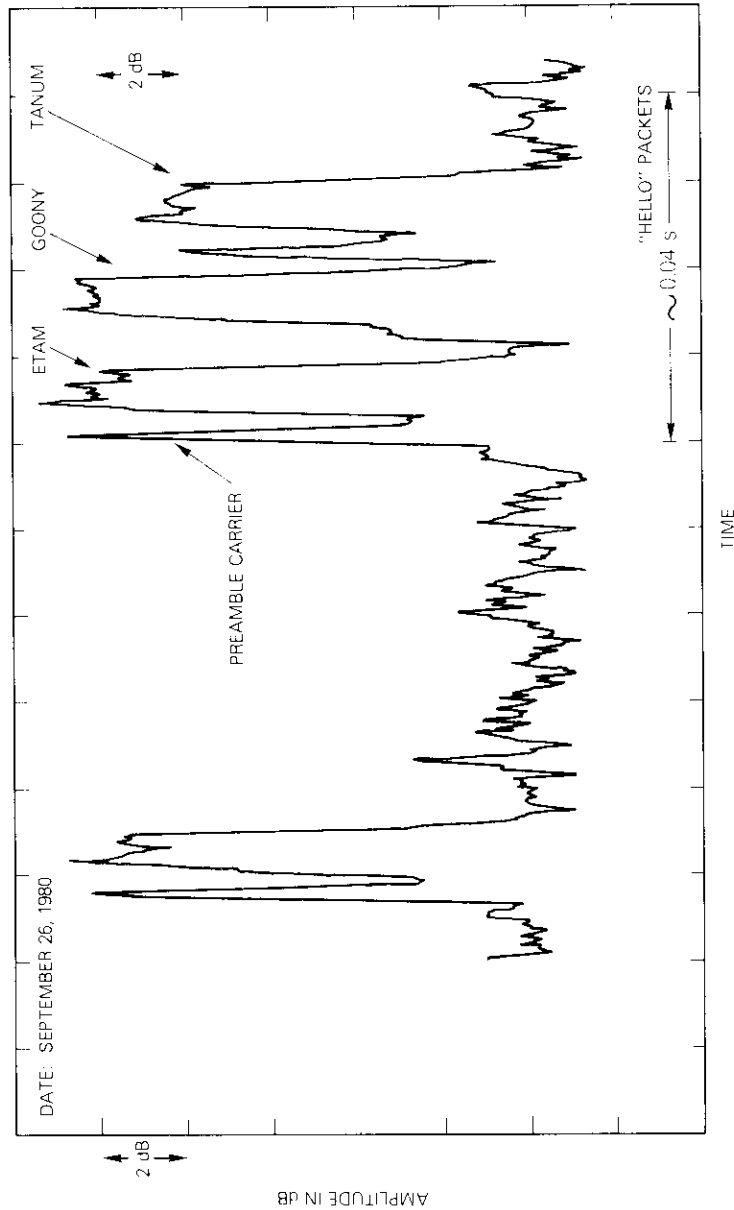


Figure 6. Envelope of SATNET Packets

applied to initialize a digital second-order phase-locked loop that tracks the signal phase over the remainder of the packet. This final "local oscillator" rotates the complex sample pairs, thus accomplishing a final heterodyning very close to zero frequency.

The modems in the PSP terminals yield acquisition probabilities higher than 0.9999 with 64-symbol preambles when operating into large earth stations with  $C/N$  of 16–17 dB. For coded operation into small terminals, a 96-symbol preamble is necessary to maintain the detection probability at 0.999 or slightly better when operating under normal conditions ( $C/N \cong 6$  dB). With the large stations, therefore, the failure to acquire a packet should have only a small effect on the missed-packet performance goal of 0.1 percent.

Following acquisition, the modem outputs two channels of binary data to a receive interface which contains matched filters that are searching for the unique words. These filters must search for the  $I$  and  $Q$  patterns or their inverse on each channel and detect a match with no more than two errors in either comparison. At normal binary error probabilities ( $10^{-4}$  to  $10^{-6}$ ), this process is highly reliable and contributes very little to missed packet performance.

All of the data following the unique words are protected by a 24-bit cyclic redundancy check (CRC) checksum which fails, with high probability, if one or more bit errors occur in the header, the data, the checksum itself, or in the 48 bits of SIMP control characters. The missed packet percentage should, therefore, correspond roughly to the bit-error rate on the channel,  $p$ , times the number of bits included in the packet.

Prior to April 1979, long hello packets were used in SATNET and the fraction of packets missed would be expected to be  $1,400p$ , *i.e.*, 1.4 percent missed if  $p = 10^{-5}$ . After this time, the hello packets were shortened and the fraction missed would be expected to decrease to approximately  $250p$  (0.25 percent missed for  $p = 10^{-5}$ ). This approximate relationship for packet miss rate allows the comparison in Table 1 between the bit-error rate standards for the speech users of the SPADE transponder and the missed hello packet behavior in SATNET. The packet transmission network begins to experience problems at a miss rate of 1 percent and these problems become serious at 10 percent. The latter miss rate corresponds to bit-error rates in the region  $10^{-4}$ , which are barely perceptible to speech users. SATNET is thus much more sensitive to impairments in the SPADE transponder and the SATNET reporting serves as a sensitive indicator of these impairments.

Figure 7 shows long-term missed-packet behavior on SATNET. Over the long term, about 0.1 percent of the hello packets are missed and it is in-

TABLE 1. EXPECTED MISSED PACKET BEHAVIOR VERSUS CHANNEL,  $p$

CHANNEL BIT ERROR PROBABILITY, $p$	QUALITY STANDARD (ACTUALLY APPLIES TO AN 8-BIT PCM VOICE CHANNEL)	QUALITY OF PCM SPEECH	% MISSED HELLO PACKETS IN SATNET	
			LONG (1,400-BIT) HELLO PACKETS	SHORT (250-BIT) HELLO PACKETS
$10^{-6}$	Will be achieved 80% of time	Excellent	0.16	0.05
$10^{-5}$	Allowed 0.3% of worst month	Very good	1.2	0.3
$10^{-4}$		Noise barely perceptible	12.0	3.0
$2 \times 10^{-4}$		Noise definitely noticeable	25.0	5.0
$5 \times 10^{-4}$	Allowed 0.01% of year	Noise bad but tolerable to some users	50.0	12.0
$10^{-3}$		PCM speech severely degraded	76	20

ferred that this miss rate applies to control and information packets as well. Such performance is perfectly acceptable in terms of throughput experienced by the users and corresponds approximately to an error rate of  $10^{-6}$ . An increase in error rate to  $10^{-5}$ , resulting from a reduction in  $E_b/N_o$  of only 1 dB at an earth station, can result in a miss rate of 1 percent; this causes noticeable degradation in throughput. An increase in power level is not permitted by INTELSAT operating procedures. Thus, the power balancing on the SATNET links to better than  $\pm 0.5$  dB has been a critical operational problem.

**Test and monitoring parameters**

An important feature of the modems in the new PSP terminals is the provision of test and monitoring (T&M) parameters on each packet received by that modem. These measurements, in the form of six 8-bit words, are combined with 16 bits generated in the receive interface so that a total of four 16-bit words are transmitted to the SIMP at the end of each packet. The format of the data transmitted to the SIMP with and without

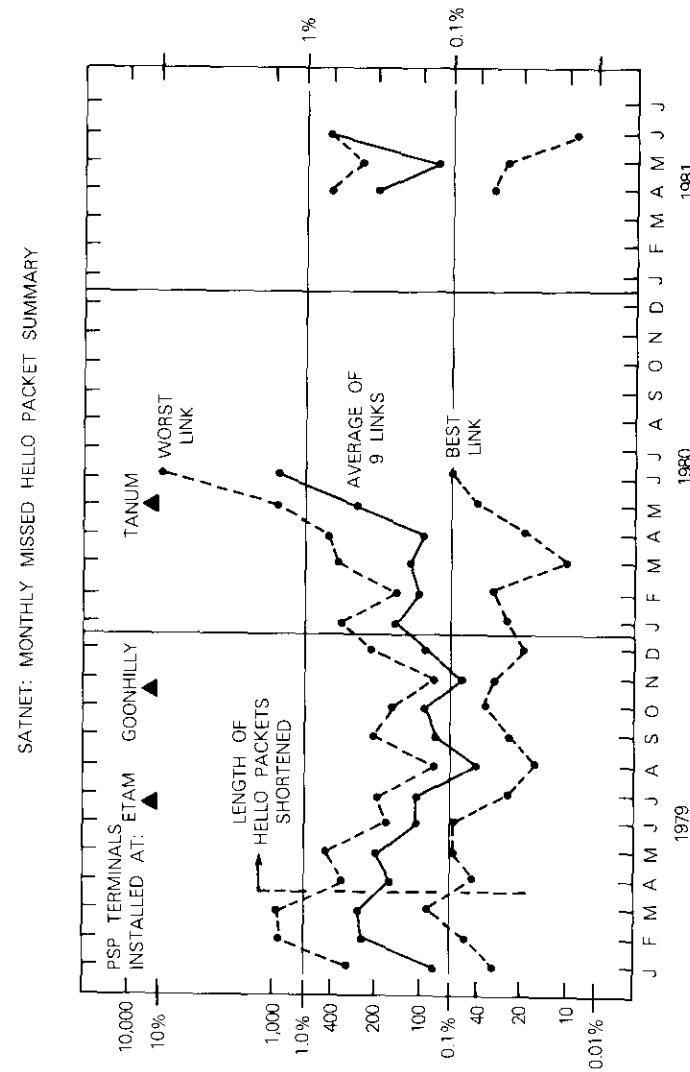


Figure 7. Monthly Missed Hello Packets

the T&M words is shown at the top of Figure 8. Note that when T&M words are appended to the packet by the modem, these extra words are added immediately after the information bits, but they are not protected by the CRC checksum that was calculated before transmission. Consequently, error detection must now be done in the receive interface, with the result (good or bad) inserted as a single bit in the fourth T&M word. The SIMP must then ignore the result of its own hardware checksum calculation when the T&M words are enabled.

The three modem-generated T&M words (16 bits each) are each made up of two 8-bit words representing measurements made in the micro-processor (*i.e.*, the digital) portion of the modem. These words represent the following measurements:

*a. Word #1.* This word is made up of two bytes, the first a quiescent AGC level with no signal present, and the second representing the packet AGC level. The AGC operation in this particular modem is accomplished by feeding back an 8-bit word from the processor which is D/A converted to provide a control current to a diode which serves as a variable attenuator in the analog portion of the modem. An error signal is derived by attempting to maintain gain such that the combination of  $S + N$  into the quadrature pair of A/D converters is slightly below the clipping level. Typical measured values of packet AGC are shown in Figure 9. These data indicate T&M byte value, on a scale of 0-255, versus power into the modem,  $P_{in}$ .

*b. Word #2.* The two 8-bit bytes in the second T&M word give initial and final values of the frequency offset between the carrier frequency of the incoming packet and an internal reference oscillator within the modem. The initial frequency estimate (output as the first byte) is made during the acquisition preamble, which consists of 64 symbols of an alternating BPSK sequence. At the end of this preamble, the initial frequency estimate is supplied as an initial condition to a second-order phase-locked loop that continues to track phase (and refine the frequency estimate) during the remainder of the received packet. The second byte of the word represents the final frequency estimate. Both bytes use seven active bits, thus dividing the possible  $\pm 2$ -kHz input frequency difference into  $4,000/128 \approx 31.25$ -Hz "cells."

*c. Word #3.* The third T&M word contains two 8-bit bytes, the first giving a measure of  $E_b$  (energy per bit) and the second a measure of  $N_b$  (input noise density in W/Hz). If the samples from the two channels of the QPSK modem are collected in pairs and plotted as a

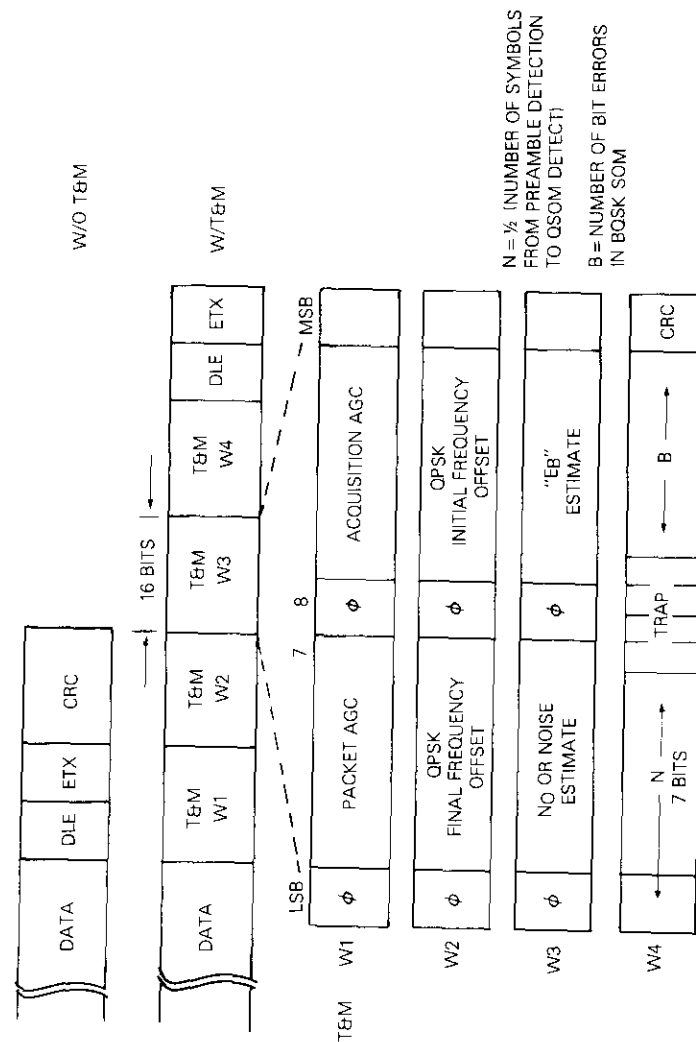


Figure 8. Format of T&M Words

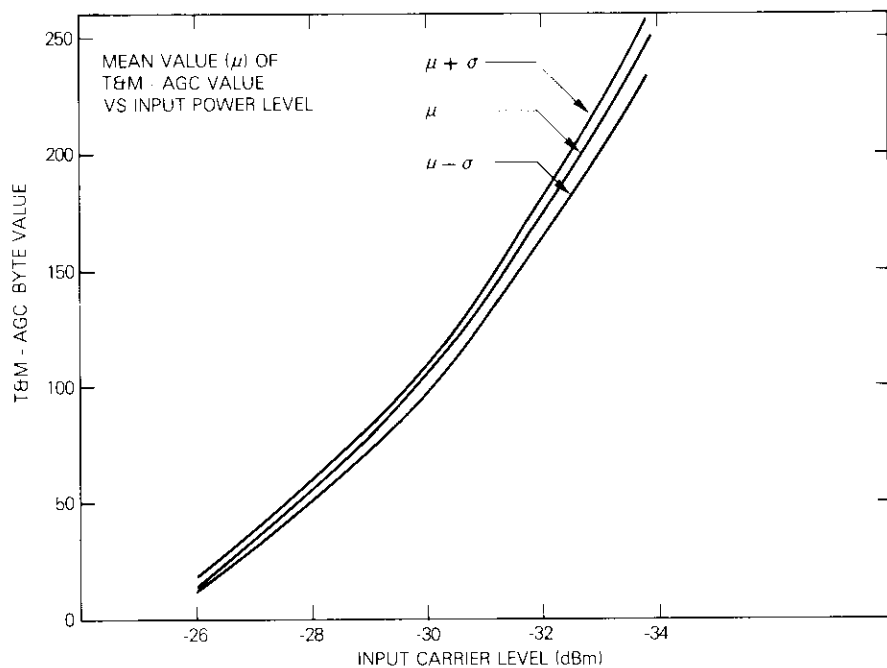


Figure 9. Packet AGC and T&M Byte Value vs  $P_{in}$  for Modems #2 and #3

scatter diagram as shown in Figure 10, the mean vector length is proportional to  $\sqrt{E_b}$  and the variance of the scatter about this mean is proportional to  $\sqrt{N_o/2}$ . This scatter would be caused by the combination of all sources of noise in the system (thermal noise, intersymbol interference, quantizing noise, etc.), but this equivalent " $N_o/2$ " should be representative of the C/N ratio into the modem. Figure 11 shows typical measured values of the ratio of the  $E_b$  and  $N_o$  byte values ( $E_b/N_o$ ). The measurement of  $E_b$  tends to be constant because of the AGC action and exhibits very little statistical fluctuation; the  $N_o$  estimate, on the other hand, tends to be much noisier. In practice, additional processing is needed on these two T&M words to form the ratio  $E_b/N_o$ . This ratio exhibits an accuracy of about  $\pm 1.0$  dB on individual packets.

Each of the three types of parameters measured in the modem is potentially useful in monitoring link performance and pointing out areas of misalignment and imbalance between transmitting stations. The measure-

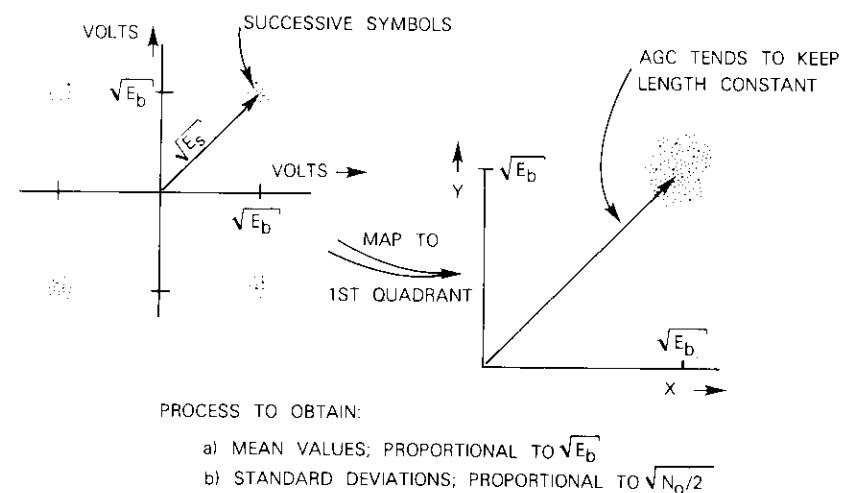


Figure 10. Scatter Diagram of  $E_b$  and  $N_o$  Measurements

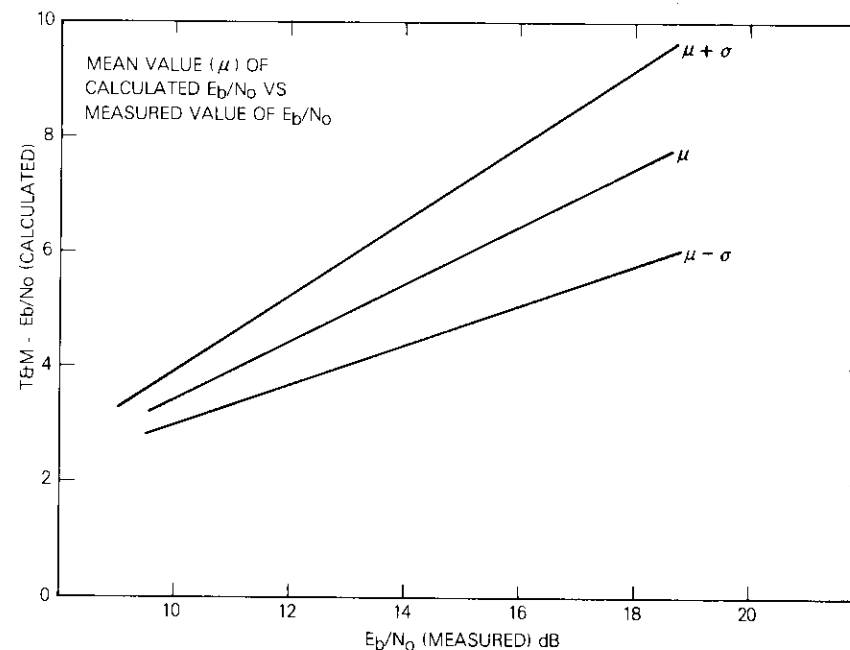


Figure 11. Variation in  $E_b$  and  $N_o$  Bytes with Packet Length

ment of frequency offset on incoming packets has turned out to be an accurate and stable measurement. Observing these measurements at a single receiving station (Etam, for example) makes it possible to measure the relative frequency offsets between packets received from the three stations (including Etam's own transmissions). The resolution of the measurements ( $\sim 30$  Hz) is more than adequate to maintain alignment between stations.

The measurement of packet AGC level at a single receiving site is also potentially very useful in resolving one of the more troublesome problems in SATNET, namely, the maintenance of power balance between the transmissions from the three different earth stations.

The measurement of  $E_b$  and  $N_o$ , or the ratio  $E_b/N_o$ , is potentially the most useful T&M word, since this variable should be a direct indicator of bit-error rate on the links and, hence, of link quality. The AGC operation on each packet tends to normalize the  $E_b$  measurement on each received packet. Thus, this parameter tends to be a constant and exhibits very little statistical fluctuation. The noise measurement, however, shows much more statistical fluctuation even for long packets in which many symbols are averaged to give the single T&M byte. Thus, the single-packet  $E_b/N_o$  measurement accuracy is limited by the noisy  $N_o$  estimate and accuracy is approximately  $\pm 1$  dB for long (1,000-bit) packets. This accuracy can be improved by averaging over all packets received on a particular link over an observation interval of 5 to 10 minutes.

### **PSP terminal**

The PSP terminal is a self-contained baseband-to-IF unit which interfaces with the SIMP at baseband and the earth station IF subsystem at 70 MHz. Included in the terminal are two channel units, each capable of supporting a burst mode data transmission rate of 64 kbit/s. One of the channel units is also capable of supporting burst-mode transmission rates of 16 and 32 kbit/s.

The subassemblies in the terminal include the following:

- a. command and monitor module (CMM);
- b. burst mode data test set (DTS);
- c. the two channel units;
- d. self-contained power supplies;
- e. timing and frequency unit (TFU).

Figure 12 shows the locations of subassemblies *a* through *d*. Figure 13 is a view of the modules that are included in the redundant channel unit configuration.

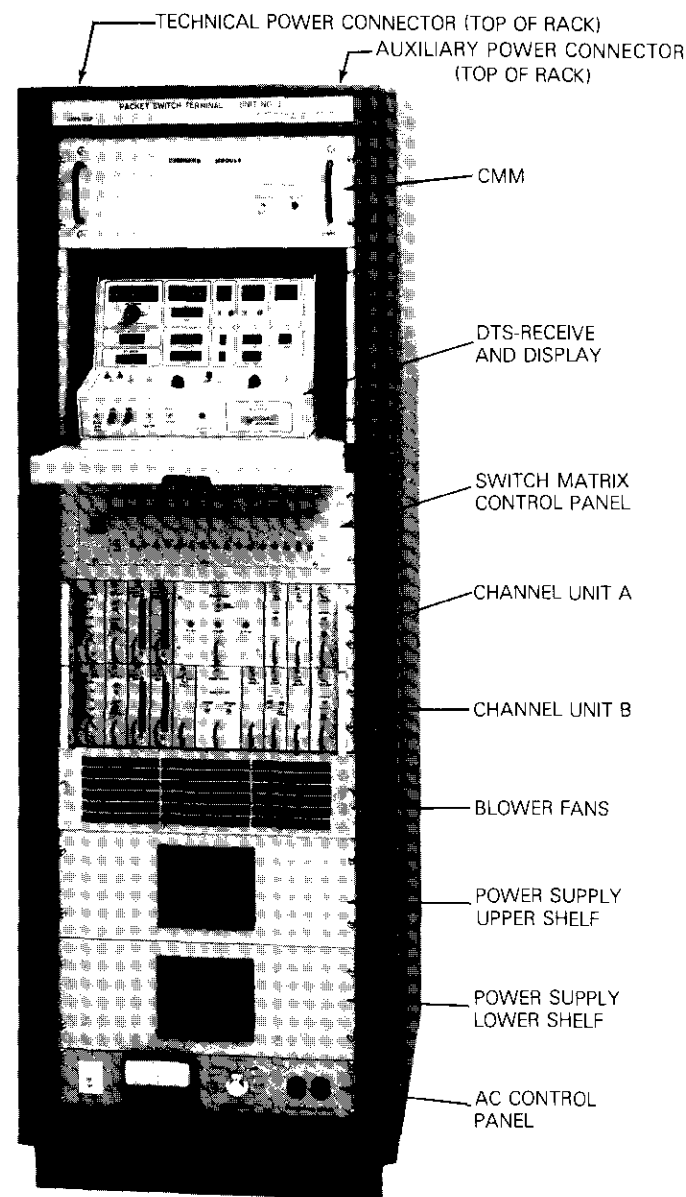


Figure 12. PSP Terminal

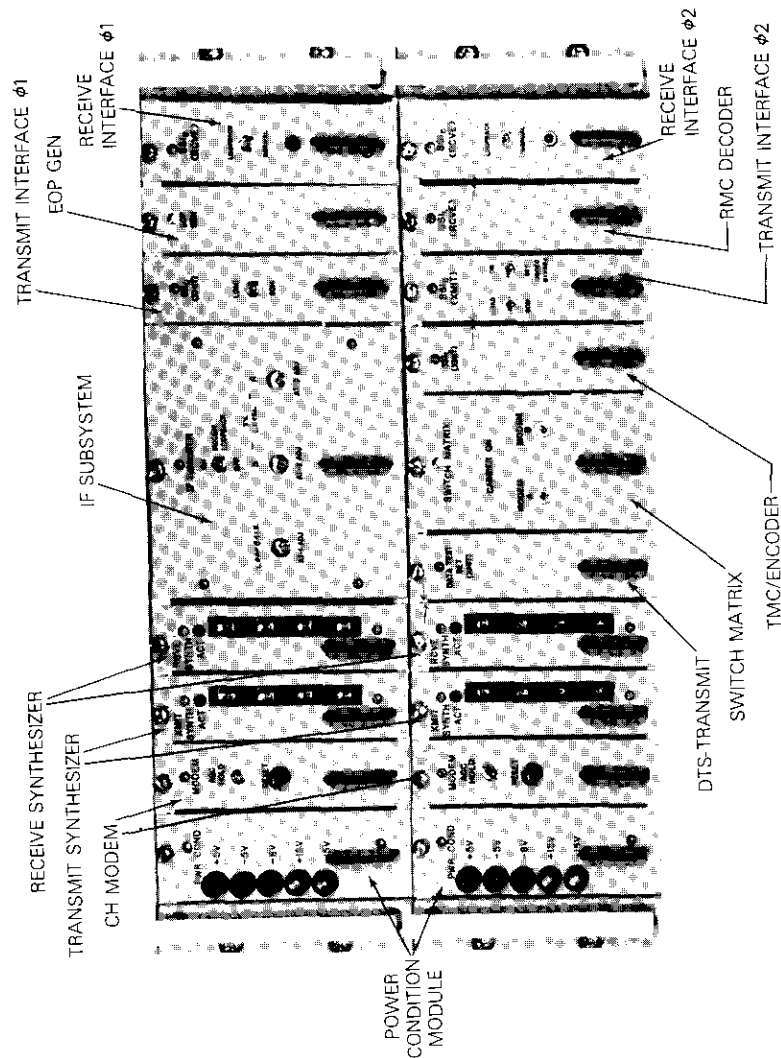


Figure 13. Channel Unit Modules

Figure 14 is a functional block diagram of the PSP terminal showing its relationship with the SIMP and the earth station IF subsystem. The channel units contain the interface modules between the SIMP and burst modem. In Figure 13, the upper channel unit, IFACE-A, is capable of transmission at the 64-kbit/s uncoded QPSK rate only, while the lower channel unit, IFACE-B, is capable of transmitting the coded and uncoded data using either QPSK or BPSK.

Packet transmission is initiated by a signal (designated GOSIG) from the SIMP. Reception of GOSIG causes the interface unit to generate a preamble consisting of an alternating 1-0 pattern for bit timing recovery and a start of message (SOM) sequence, each of a specified length. The SOM sequence consists of a particular pattern, determined by whether transmission is to a standard A or B station.

A second signal from the SIMP initializes the interface unit prior to occurrence of the next GOSIG, so that the proper preamble and SOM are generated for each packet to be transmitted. After completion of the preamble and SOM, the interface unit supplies a clock to the SIMP, which causes data to be passed to the interface unit from the SIMP. The SIMP data are converted from serial to parallel and the two resulting data streams are passed to the modem at a 32-ksymbol/s rate. For QPSK modulation, the two data streams will be different, depending upon the particular data pattern, whereas for BPSK modulation, both data streams are identical. Coding of the data, if required, is performed on the transmit side in the transmit mode controller/encoder, and upon reception, decoding of the data, if required, is performed by the reception mode controller/decoder.

Figure 15 shows typical formats for the three packet types: uncoded QPSK, rate 1/2 coded BPSK, and a mixed format consisting of rate 1/2 coded BPSK and uncoded QPSK modes.

Note that in Figure 15c, a second SOM is inserted in the data to separate QPSK from BPSK data. This SOM is required on the receive side to resolve the phase ambiguities of the demodulated QPSK data. The BPSK SOM resolves the phase ambiguities in the BPSK data.

A burst-mode data test set (DTS) has been implemented and included in the terminal to provide a realistic simulation of the SIMP as a packet source and receiver, and to assist earth station personnel in maintaining the terminal. The DTS packet format is similar to that generated by SIMP. The transmission parameters such as packet length, coded length, mode of transmission, and interpacket interval, as well as the data pattern (all zeros, all ones, or pseudorandom), can be set manually. The receive side of the DTS provides displays for indicating the number of packets received, the number of packets received with bit errors, and the total number of bit

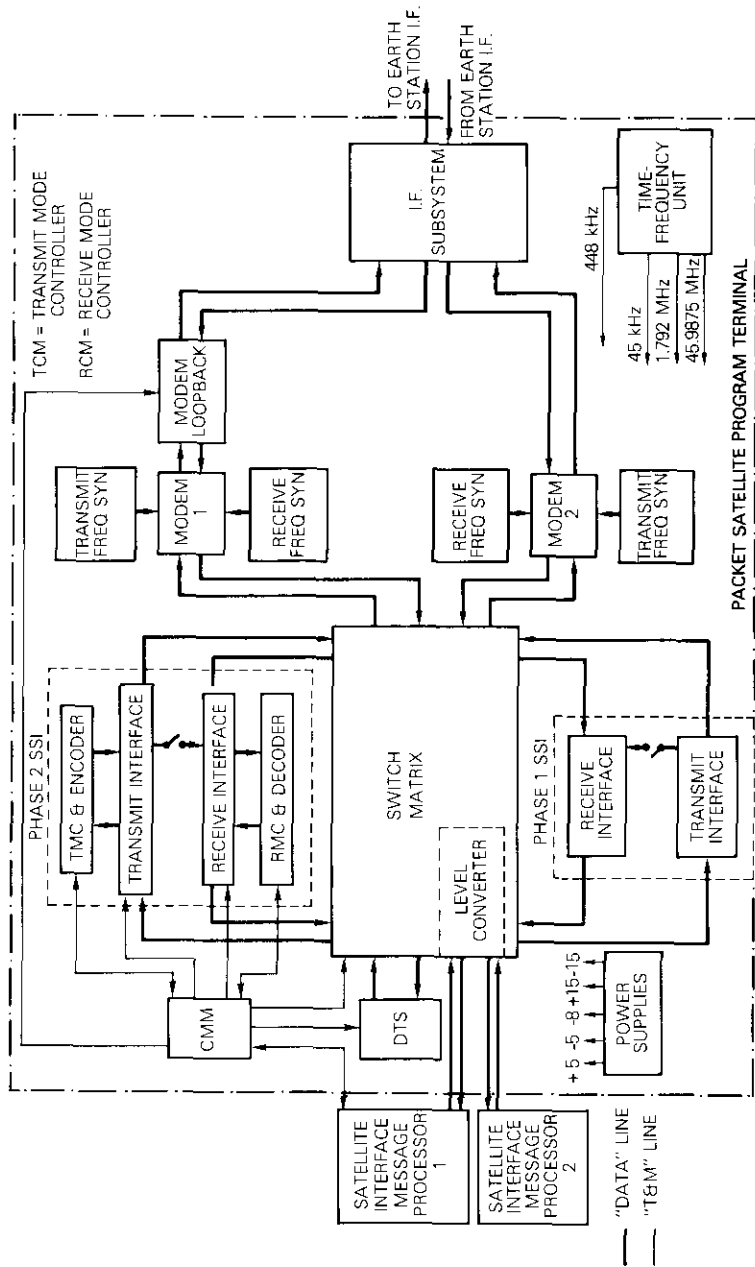


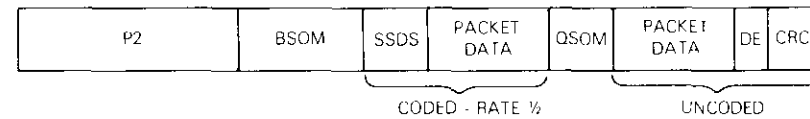
Figure 14. Functional Block Diagram of the PSP Terminal



(a) PACKET FORMAT QPSK UNCODED



(b) PACKET FORMAT BPSK CODED RATE 1/2



(c) PACKET FORMAT MIXED MODE

LEGEND

- P1: 64 SYMBOLS OF ALTERNATING 1 0
- P2: 96 SYMBOLS OF ALTERNATING 1-0
- QSOM: QPSK START OF MESSAGE
- BSOM: BPSK START OF MESSAGE
- SSSD: FOUR ASCII WORDS, SYN SYN DLE STX, USED AS CONTROL (i.e., START OF MESSAGE) CHARACTERS BY THE SIMP
- DE: TWO ASCII WORDS, DLE ETX, USED AS CONTROL (i.e., END OF MESSAGE) CHARACTERS BY THE SIMP
- CRC: 24 BITS OF CYCLIC RECURSIVE CHECKSUM

Figure 15. Formats of Different Packet Modes

errors in all received packets. From this information, the satellite channel bit-error rate can be calculated. Since the stations have identical test sets, it is possible to perform transmission tests among the three stations to determine their performance characteristics.

Another major subsystem of the terminal is the command and monitor module (CMM), a microprocessor-based unit that can receive commands from the SIMP and issue commands to various modules in the terminal.

The CMM can carry out several SIMP-initiated commands, which can be initiated either by earth station personnel or by remote command from the SATNET control center at BBN in Cambridge, Massachusetts. In addition to being able to reset all internal registers in the PSP terminal, it is also possible to set certain other parameters within the terminal, e.g., the length of the preamble for transmission to either standard A or B stations, the pattern and/or length of the SOMs, and the allowable SOM correlation error threshold from 2 to 5. The CMM can also request that the T&M data generated in the modem and RMC/decoder be passed from the terminal to the SIMP.

### **Conclusions and future plans**

Some valuable lessons have been learned during the 5-year experimental period regarding operation of future systems such as SATNET.

Currently, SATNET operates with a goal of  $\leq 0.1$ -percent missed packets. Missed packets are primarily those which contain one or more bit errors. Thus, operation of SATNET links is sensitive to the bit-error rate of the links. The range of bit-error rate objectives for speech,  $\leq 10^{-6}$  usually (80 percent of the time),  $\geq 10^{-4}$  occasionally, and  $\geq 10^{-3}$  rarely, are perfectly acceptable to the speech users of the SPADE transponder, but cause wide variations in SATNET operation. Variations in link  $C/N$ 's of 1 dB generally cause the bit-error rate to vary by a factor of 10, which changes the missed packet rate by a like amount.

An important feature of SATNET is the real-time monitoring provided by the network control center. Each link is monitored minute-by-minute, 24 hours a day, 365 days per year. Since even brief transitory disruptions are logged and reported, SATNET is a much more critical user of the satellite link than a PCM speech user.

Mixed operation of standard A and standard B stations was shown to be feasible in SATNET. Coding and information bit rate reduction are necessary for the standard B station to receive packets from the satellite intended for the small station; this situation leads to a moderate increase in equipment complexity. The small station must also be able to participate in the distributed control concept.

Although small station operation was shown to be feasible, problems were encountered during mixed-mode operation of large and small stations (with coded and uncoded packets) when the CPODA control algorithm was used. Then, certain coded control packets were detected, demodulated, and decoded correctly even though a contention occurred in the Aloha control subframe. Although problems of this kind were rare

and occurred at only one station, they resulted in serious disruption of the scheduling algorithm. This problem was accentuated by power imbalance between the bursts received at the satellite. Reliable contention detection remains a problem that must be solved before CPODA can be used in a network with mixed station sizes. CPODA offers little advantage in a 3- or 4-station network; as the network expands, however, it becomes more and more desirable, because it would tend to minimize control overhead.

Future plans involve the addition of one or two more stations to the network. To accommodate these new stations and the increasing traffic among existing stations, the SIMPs and PSP terminals will be modified to allow 128-kbit/s operation. This will be done by utilizing two SCPC channels and channeling traffic to either. (Bursts would be sent on frequency  $f_1$  or  $f_2$ , or both, with two receivers monitoring both channels.) This approach will allow increased capacity, with minimum impact on the frequency planning in the SPADE transponder and on individual hardware modules.

Also in the future, procedures will be developed to allow routine use of the T&M parameters that are available on each packet. Experience has shown that the SATNET channel is highly reliable except for rare events in which power-level misadjustments or frequency drifts cause large missed-packet rates. Use of the T&M parameters to warn of the onset of these events is very valuable in the operational system [13].

### **Acknowledgment**

*The authors would like to thank the individuals who have been involved in the SATNET program. At DARPA, Robert Kahn and Vinton Cerf were constant in their support and encouragement. Many individuals at BBN and the Linkabit Corporation contributed significantly to the success of the program. Special thanks are due to Jim Thomas at COMSAT Laboratories, who was active in all phases of PSP terminal development, delivery, and installation.*

### **References**

- [1] L. G. Roberts, "Computer Network Development to Achieve Resource Sharing," Spring Joint Computer Conference, *AFIPS Proceedings*, Vol. 36, 1970, pp. 543-549.
- [2] R. E. Kahn, "Resource Sharing Computer Networks," *Proc. IEEE*, Vol. 60, No. 11, November 1972, pp. 1397-1407.

- [3] S. M. Ornstein et al., "The Terminal IMP for the ARPA Computer Network," Spring Joint Computer Conference, *AFIPS Proceedings*, Vol. 40, 1972, pp. 243-254.
- [4] H. Frank et al., "Computer Communications Network Design-Experience with Theory and Practice," Spring Joint Computer Conference, *AFIPS Proceedings*, Vol. 40, 1972, pp. 255-270.
- [5] L. Kleinrock and S. S. Lam, "Packet Switching in a Slotted Satellite Channel," *1972 National Computer Conference Proceedings*, pp. 703-710.
- [6] N. Abramson, "Packet Switching with Satellites," *1973 National Computer Conference Proceedings*, pp. 695-700.
- [7] F. E. Heart et al., "The Interface Message Processor of the ARPA Computer Network," Spring Joint Computer Conference, *AFIPS Proceedings*, 1970, pp. 551-567.
- [8] L. G. Roberts, "Dynamic Allocation of Satellite Capacity through Packet Reservation," *1973 National Computer Conference Proceedings*, pp. 711-716.
- [9] D. A. McNeill et al., "SATNET Monitoring and Control," 1979 National Telecommunications Conference, *Proceedings*, Vol. 3, pp. 45.3.1-45.3.4.
- [10] I. Jacobs et al., "General Purpose Satellite Networks," *Proc. IEEE*, Vol. 66, No. 11, November 1978, pp. 1448-1467.
- [11] I. Jacobs et al., "CPODA—A Demand Assignment Protocol for SATNET," *Proceedings DCM/IEEE Fifth Data Communications Symposium*, September 1977, pp. 2.5-2.9.
- [12] C. Heegaard, J. Heller, and A. Viterbi, "A Microprocessor-Based PSK Modem for Packet Transmission over Satellite Channels," *IEEE Transactions on Communications*, COM-26, No. 5, May 1978, pp. 552-564.
- [13] P. Cudhea et al., "SATNET Operations," 1982 AIAA 9th Communications Satellite Systems Conference, *Collection of Technical Papers*, pp. 100-105.

*Larry C. Palmer received a B.S. from Washington and Lee University, a B.E.E. from Rensselaer Polytechnic Institute and an M.S. and Ph.D. from the University of Maryland. Before joining COMSAT, he was employed by Computer Sciences Corporation, where he participated in systems engineering studies related to digital communications systems, satellite communications and navigation systems, and digital signal processing systems. He also supervised time-domain simulation programs to investigate impairments in digital data transmission by satellite. Prior to this, he participated in a study of advanced trilateration tracking techniques for the U.S. Army ECOM.*



*Dr. Palmer joined COMSAT in October 1974, and has participated and directed research in digital transmission for future global satellite systems. From January 1980 to July 1981 he was COMSAT's Program Manager in the ARPA SATNET Program. He is presently Senior Scientist in the Systems Technology Division, responsible for computer simulation and system studies related to digital transmission via satellite. He is a member of Tau Beta Pi, Eta Kappa Nu, and IEEE.*



*Joachim Kaiser received a B.A. and an M.A. in mathematics in 1943 and 1948, respectively, and completed additional graduate work in communications theory at the University of Michigan in 1967 and 1968. He joined COMSAT Laboratories in 1968 and is Manager of Special Projects. He has performed numerous experiments in satellite communications using small earth terminals, and was the principal investigator for COMSAT's experiment on the Communications Technology Satellite. He is a senior member of the IEEE.*



*Stanley Rothschild received a B.S.E.E. from Ohio University, Athens, in 1958, and an M.S.E.E. from Case Institute of Technology, Cleveland, in 1962. He joined COMSAT in 1970, and since 1973 has been principally involved with the DARPA SATNET program, with responsibility for the design and installation of the earth station equipment. Mr. Rothschild is a member of the IEEE Communications Society.*

*David L. Mills received a Ph.D. from the University of Michigan in 1971. Before joining COMSAT, Dr. Mills held faculty positions at the University of Maryland, the University of Edinburgh (Scotland), and the University of Michigan in computer science and electrical engineering. Since joining COMSAT in 1977, where he is now a Senior Research Scientist with the Computer Sciences Laboratory, he has worked on research projects in computer networks and protocols. During the period 1977-1979, he designed the DARPA Atlantic SATNET, assessed its performance, and refined the design. Since 1979, he has directed and participated in internetworking research projects that have focused on multimedia mail, communications protocols, and performance evaluation. He has also contributed to the design and implementation of INTELPOST, and supervised implementation of the communications software for that system. Dr. Mills has published over three dozen technical articles and reports, and has directed a number of research projects sponsored by various agencies, including DARPA.*



Index: platform despin, nutation, mass properties

## **Digital simulations of SBS spacecraft despin operation**

J. C. HSING

(Manuscript received November 4, 1981)

### **Abstract**

The despin maneuver of a Satellite Business Systems (SBS) spacecraft is unique because the effective spin-to-transverse inertia ratio is greater than unity in the all-spinning configuration and less than unity in the despun configuration. Thus, the vehicle changes from a passively stable to a passively unstable configuration. For a brief period during this transition, the effective spin inertia ratio is intermediate and the nutation angle diverges exponentially. A successful despin maneuver depends on certain spacecraft mass properties. Digital simulations have been used to determine the sufficient constraints on spacecraft mass properties for acceptable despin operations. The performance and characteristics of platform despin can also be investigated based on the simulation results. Several runs using the expected worst-case mass properties of the SBS F-3 spacecraft were also conducted. The results can be used to predict the spacecraft despin maneuver.

### **Introduction**

During the despin operation of an SBS spacecraft, the spin-to-transverse inertia ratio changes from an all-spun value greater than unity ( $\sim 1.1$ ) to a despun value less than unity ( $\sim 0.82$ ). This number is defined as the ratio of the spin-axis moment of inertia and the vehicle transverse moment of inertia. Before the despin operation, the platform spin-axis inertia is in-

cluded in the ratio; afterwards, only the rotor inertia is included. Hence, the vehicle changes from a passively stable to a passively unstable configuration as described in Reference 1.

For a short period, the effective spin inertia is intermediate and the nutation angle diverges exponentially. Successful platform despin depends on the amount of rotor transverse inertia asymmetry, dynamic imbalance of both the rotor and the platform, and the torquing capability of the despin motor(s). References 2 through 4 discuss the dynamics of dual-spin spacecraft with this type of asymmetry and dynamic imbalances. Constraints on mass properties for successful despin have been established by the spacecraft manufacturer, Hughes Aircraft Corporation, primarily by digital simulation. Independent simulation runs have been performed at COMSAT Laboratories to investigate the characteristics of the despin operation for SBS spacecraft.

This paper reports on these digital simulation results, including those of four runs using the expected worst-case mass properties of the SBS F-3 spacecraft. The results can be used to predict the spacecraft despin maneuver.

**System characteristics**

The spacecraft rotor and platform are locked together throughout the transfer orbit and apogee kick motor firing. In drift orbit, after the correction of apogee injection errors, the platform launch locks are released with pyrotechnic bolt cutters in preparation for initial platform despin. The despin operation produces a transition of spin-to-transverse inertia ratio  $\sigma$  from an all-spun value greater than unity ( $\sim 1.1$ ) to a despun value less than unity ( $\sim 0.82$ ). Hence, the vehicle changes from a passively stable to a passively unstable configuration. During the transition period, vehicle transverse rates diverge exponentially. If the transition is not rapid enough, the platform cannot be despun successfully.

While the platform spins about the intermediate axis, the nutation angle diverges. The degree of divergence depends on the initial rate at entry into the intermediate axis spin phase, the divergence rate, and the dwell time in this state. These divergency factors are functions of rotor transverse inertia asymmetry and dynamic imbalances for both the rotor and platform. Constraints on mass properties for successful despin can be established by digital simulations.

Figure 1 defines the coordinate axes to which the following parameters apply:

- $m_s, m_p$  = rotor and platform mass
- $(x_1, x_2, x_3)^T$  = position coordinates of platform CM (center of mass) with respect to vehicle CM
- $I_{33}^r$  = moment of rotor inertia about the 3-axis with respect to the rotor CM
- $I_{11}^r, I_{22}^r$  = transverse moments of rotor inertia with respect to the rotor CM
- $I_{13}^r, I_{23}^r$  = dynamic imbalance products of rotor inertia with respect to the rotor CM
- $I_{33}^p$  = moment of platform inertia about the 3-axis with respect to the platform CM
- $I_{11}^p, I_{22}^p$  = transverse moments of platform inertia with respect to the platform CM
- $\bar{I}_{13}^p, \bar{I}_{23}^p$  = dynamic imbalance products of platform inertia with respect to the platform CM
- $I_{13}^p = \bar{I}_{13}^p + m_p \left( 1 + \frac{m_p}{m_s} \right) x_1 x_3$
- $I_{23}^p = \bar{I}_{23}^p + m_p \left( 1 + \frac{m_p}{m_s} \right) x_2 x_3$
- $(y_1, y_2, y_3)^T$  = position coordinate of the rotor CM with respect to the vehicle CM.

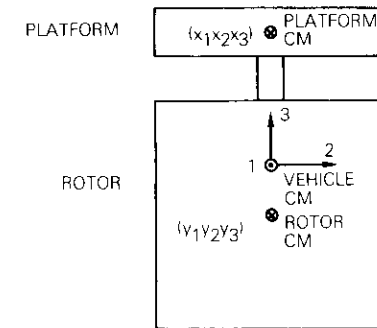


Figure 1. Spacecraft Coordinate Axes

The sign convention for the product of inertia is defined as follows:

$$I = \begin{bmatrix} iiI_{11} & -ijI_{12} & -ikI_{13} \\ \text{etc.} & & \end{bmatrix}$$

$$I_{12} = \int xy \, dm, \text{ etc.}$$

A linear accelerometer in the rotor measures the nutation angle. Its sensitive axis, parallel to the 3-axis, has position coordinates  $(a_1, a_2, a_3)^T$  with respect to the vehicle CM.

The rate servo which controls platform despin is characterized by the block diagram in Figure 2. One or two motors can be used in the despin maneuver. Table 1 lists the assumed parameter values, except for perturbations to rotor asymmetry and dynamic imbalances for the rotor and platform.

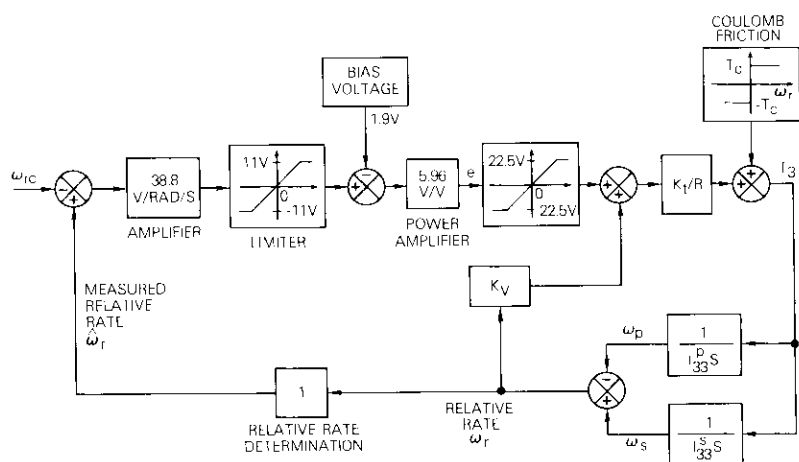


Figure 2. Simplified Block Diagram of Despin Rate Control System

Numerous parametric simulations have been conducted at COMSAT to determine sufficient constraints on mass properties, thus assuring an acceptable despin operation. Figure 3 shows some of the simulation results. The next section briefly describes the dual-spin simulation program used by COMSAT.

**Digital simulation program**

A computer program, HDCPG1, was used to perform the digital simulations of SBS spacecraft despin operation. This program simulates the full

TABLE 1. ASSUMED PARAMETER VALUES IN METRIC UNITS

PARAMETER	VALUE FOR INVESTIGATION RUNS	VALUE FOR PREDICTION RUNS	UNIT
$m_S$	388.09	401.23	kg
$m_p$	175.08	175.08	kg
$x_1, x_2$	0.00	0.00	m
$x_3$	0.47	0.47	m
$I_{11}^r$	204.2	213.41	kg-m <sup>2</sup>
$I_{22}^r$	$I_{11}^r + (I_{22}^p - I_{11}^p)$	$I_{11}^r + (I_{22}^p - I_{11}^p)$	kg-m <sup>2</sup>
$I_{33}^r$	284.69	294.98	kg-m <sup>2</sup>
$I_{12}^r$	0.00	0.68	kg-m <sup>2</sup>
$I_{11}^p$	98.37	100.68	kg-m <sup>2</sup>
$I_{22}^p$	74.8	77.24	kg-m <sup>2</sup>
$I_{33}^p$	99.19	99.73	kg-m <sup>2</sup>
$I_{12}^p$	0.68	-0.41	kg-m <sup>2</sup>
$y_1, y_2$	0.00	0.00	m
$y_3$	-0.21	-0.203	m
$a_1$	-0.43	-0.43	m
$a_2$	0.85	0.85	m
$a_3$	-0.196	-0.196	m
$K_t^*$	1.15	1.15	Nm/A
$K_v^*$	1.15	1.15	V/rad/s
$R^*$	16.20	16.20	ohm
$T_s^*, †$	1.599	1.599	Nm
$T_c^*, ‡$	0.149	0.312	Nm

\* Motor parameters.  
 † Motor stall torque.  
 ‡ Coulomb friction torque.

nonlinear dynamics for a rigid dual-spin spacecraft composed of two main bodies, connected by a bearing assembly and containing several damping mechanisms. Each main body has an arbitrary inertia tensor and arbitrary body rates.

The complete source program consists of 21 original and 9 modified IBM FORTRAN programs. It also uses subroutines from the IBM Scientific Subroutine Package, FORTRAN functions, and CALCOMP plot programs. The load module accommodates approximately 130 Kbytes, which, together with plot tape output buffers and other dynamic storage requirements, result in a required partition size of about 140-145 Kbytes. Reference 5 provides a detailed discussion, and Reference 6 describes the deviation of dynamic equations for the simulation programs.

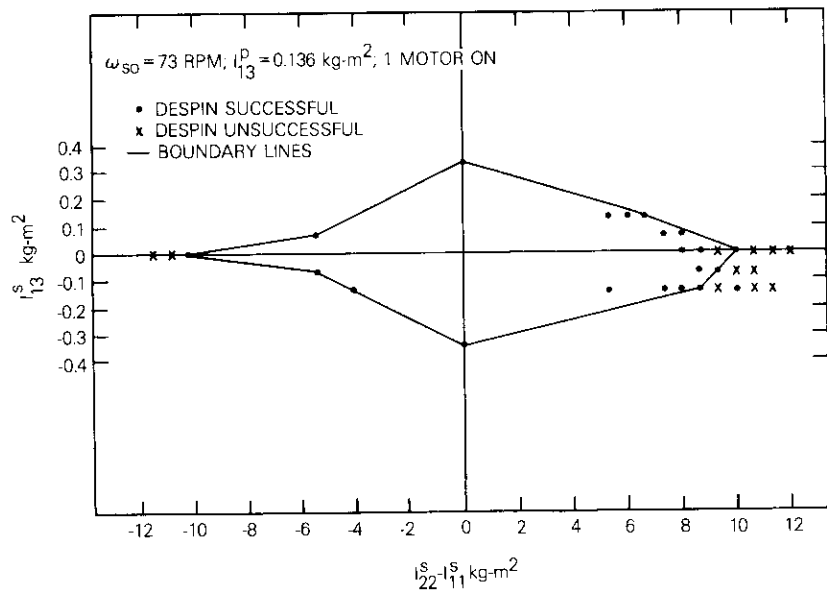


Figure 3. Despin Simulation Results

**Simulation results and discussions**

The HDCPG1 program simulates the 3-axis nonlinear dynamics of a rigid dual spinner. The rotor asymmetry and dynamic imbalances of the rotor and the platform can be specified through input data. It has been assumed that both the rotor and platform are statically balanced. The BAPTA torque motor, which has a maximum torque of 1.599 Nm, is modeled in Figure 2. The emf and Coulomb friction are included in the model, but viscous friction and friction due to BAPTA bending moment are not.

Thirty-six parametric simulations were performed. Some of these results were recorded in Figure 3. All runs used only one motor, assuming a failure of the redundant motor. Active Nutation Controllers (ANCs) were not used for each despin operation because with certain mass properties, both ANCs can be ineffective in controlling nutation during the intermediate axis spin phase. For all successful despin simulations, the resulting constant nutation angle can be nulled by turning on an ANC at the proper time. In the successful despin operations, the nutation angle stabilizes to a constant value; it does not decrease, because the nutation

damping was not simulated. Four cases have been identified for detailed investigation and are defined in Table 2, accompanied by COMSAT's simulation results.

TABLE 2. INVESTIGATION RUNS\*

RUN No.	No. OF MOTORS	$W_{so} \dagger$ (rpm)	$I_{22}^s - I_{11}^s$ (kg-m <sup>2</sup> )	$I_{13}^p$ (kg-m <sup>2</sup> )	$I_{13}^s$ (kg-m <sup>2</sup> )	COMSAT RESULTS ‡
1	1	67	2.71	0.271	0.068	S
2	2	89	2.71	0.271	0.068	S
3	1	73	11.518	0.136	-0.136	U
4	1	73	10.84	0.136	-0.068	U

\*  $I_{23}^s = I_{23}^p = 0$  in all cases, and initial platform rate = initial rotor rate.

†  $W_{so}$  = spin rate of rotor when platform is finally despun (assuming that the maneuver is successful).

‡ S means a successful despin, and U an unsuccessful despin.

Table 3 defines the plotted variables for the investigation runs. Run 1 corresponds to platform despin with a failed redundant motor. Figures 4a through 4d describe the events in the despin run. At  $t = 10$  seconds, the despin started; full despin motor torque was applied (first curve, Figure 4d); and small transverse rates exist due to the total dynamic im-

TABLE 3. PLOTTED VARIABLES FOR THE INVESTIGATION RUNS

VARIABLE	UNIT	DESCRIPTION
WP1	rad/s	Platform inertial rates in a platform basis
WP2	rad/s	
WP3	rpm	
Nutation Angle ( $\theta_n$ )	deg	Angle between 3-axis and total angular momentum vector
WS	rpm	Rotor inertial rate about 3-axis
WR	rpm	Rate of rotor relative to platform
T3	N-m	Net 3-axis torque on platform due to motor(s) and friction (see Figure 2)
ACC	g	Envelope of the accelerometer output
Sigma1 ( $\sigma_1$ )	----	Effective spin-to-transverse inertia ratios*
Sigma2 ( $\sigma_2$ )	----	

$$* \sigma_1 = (I_{33}^s + I_{33}^p \omega_p / \omega_s) / \max I_T ; \quad \sigma_2 = (I_{33}^s + I_{33}^p \omega_p / \omega_s) / \min I_T$$

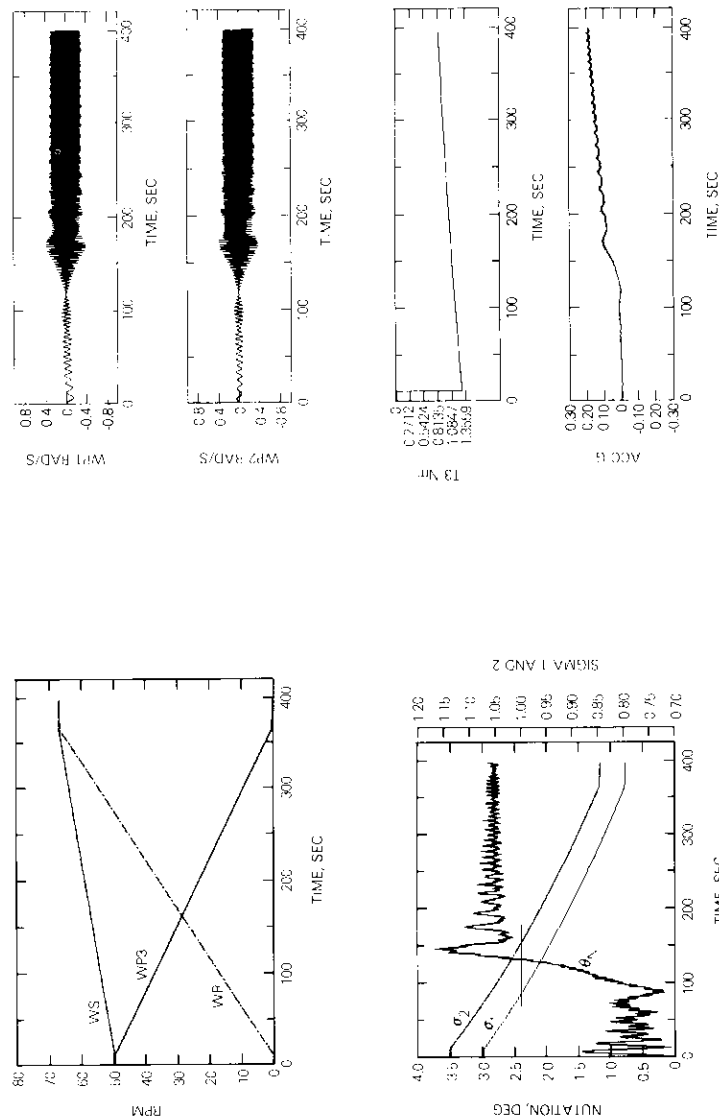


Figure 4. Despin Simulation Run 1

balance of the all-spun vehicle. Effective inertia ratios  $\sigma_1$  and  $\sigma_2$ , accompanied by the nutation angle, are plotted in Figure 4b, which also shows the unit inertia ratio line. During the intermediate axis spin phase, the nutation angle diverged and reached approximately  $3^\circ$ . Platform inertia rates along the transverse axes are shown in Figure 4c. These rates diverged during the intermediate spin phase and stabilized after the inertia ratio,  $\sigma_2$ , across the unit line. During the despin maneuver, the rotor inertia rate about the 3-axis and the rate of rotor relative to the platform, increased monotonically and converged to the same value. This despin phenomenon is recorded in Figure 4a.

Run 2 simulated platform despin from a high all-spun spin rate. This upper limit resulted in failure of the spin-down radial thruster. Two motors were used, and results are shown in Figures 5a through 5d. At initiation, full motor torques were commanded; and at the end, a steady-state nutation angle of  $1.3^\circ$  was observed.

Simulation run 3 assumed large rotor asymmetry and was unsuccessful in platform despin. Interesting variables are plotted in Figures 6a and 6b. Starting from the intermediate axis spin phase, all variables changed drastically and the platform could not be despun successfully. The parameters for this run are located in the lower right of Figure 3. According to Hughes, this run was a successful despin. Since the boundaries in Figure 3 are vaguely defined, it is not surprising that the results are inconsistent.

Run 4 was unsuccessful. Because of the excessive asymmetry, the rotor spin-up stalled during the intermediate axis spin phase. Figures 7a and 7b reveal that this stall occurred at about 100 seconds. Between the stall and 140 seconds, the spin motor transferred momentum to coning with a rapid buildup to about  $45^\circ$ , and a strong dynamic torque despun the rotor by about 20 rpm. Violent dynamics were observed during the 140- to 200-second period, and simulation results could be subject to modeling errors.

Four additional runs, A1, A2, A3, and A4, predict the despin maneuver of the SBS F-3 spacecraft. The parameters used in the simulations are the expected worst-case mass properties of the F-3 spacecraft listed in Table 1. The rotor asymmetry and spacecraft dynamic imbalances are specified in Table 4.

Run A1 used the expected worst-case mass properties of the SBS F-3 spacecraft. Initially, the spacecraft had an all-spun rate of 38 rpm. At  $t = 10$  seconds, the despin started by using only one motor. Figures 8a through 8d give the results of the despin operation. The despin maneuver was finished in 390 seconds, and the final nutation angle was about  $2.8^\circ$ . Figure 8c shows the spacecraft transverse angular rates, and Figure 8d

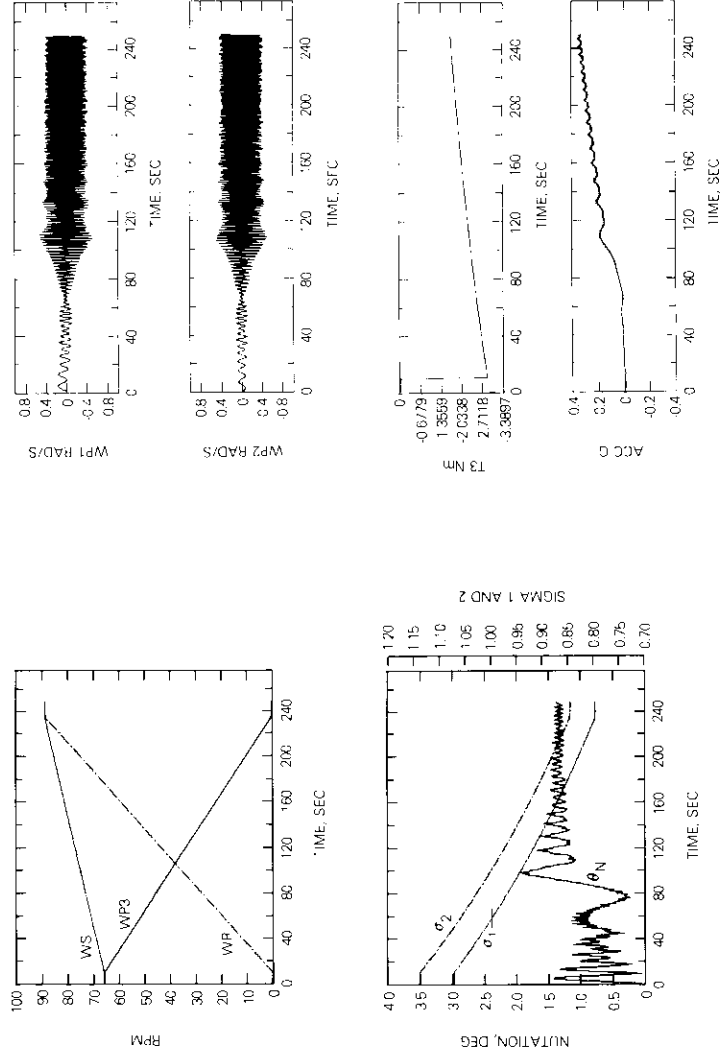


Figure 5. Despin Simulation Run 2

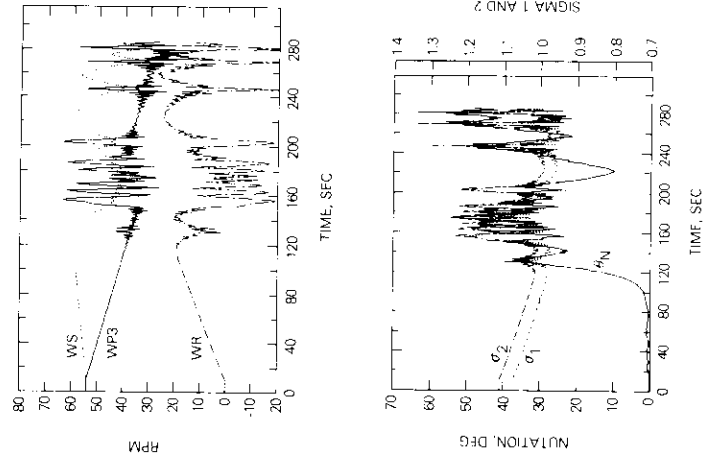


Figure 6. Despin Simulation Run 3

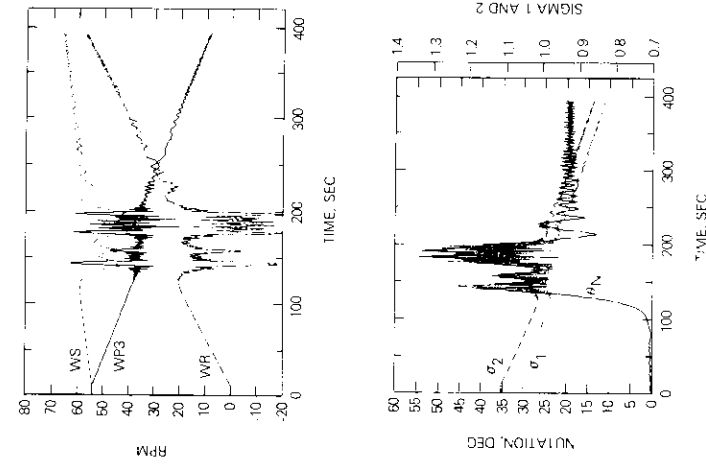


Figure 7. Despin Simulation Run 4

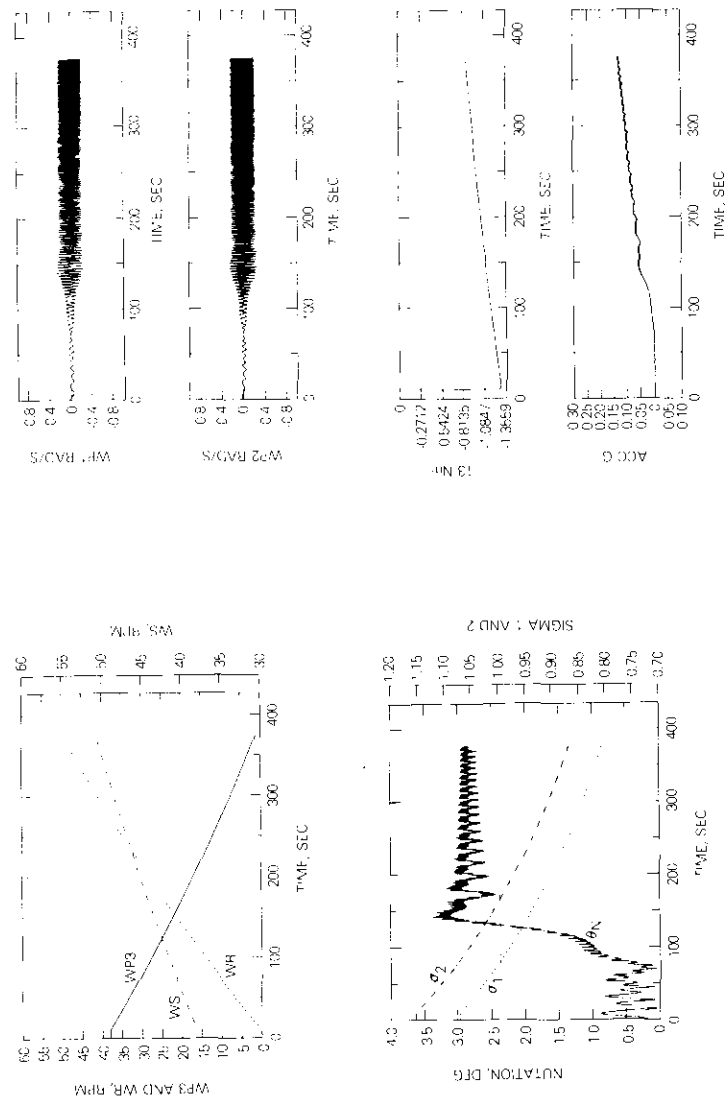


Figure 8. Despin Simulation Run A1

TABLE 4. PREDICTION RUNS\*

RUN No.	No. OF MOTORS	$W_{s0}$ (rpm)	$I_{22}^0 - I_{11}^0$ (kg-m <sup>2</sup> )	$I_{33}^0$ (kg-m <sup>2</sup> )	$I_{13}^0$ (kg-m <sup>2</sup> )	RATIONALF
A1	1	51	-2.71	0.271	-0.068	Expected worst case
A2	1	51	-5.42	0.136	-0.203	Margin of A1 and A3
A3	2	51	-2.71	0.271	-0.068	Two motor despin
A4	0	†	-5.42	0.271	-0.203	Friction spin-up

\*  $I_{23}^0 = I_{32}^0 = 0$  in all runs.

† WP3(0) = 18 rpm; WS(0) = 44.9 rpm.

records the platform despin control torque and the envelope of the accelerometer output. Run A3 is shown in Figures 9a and 9b with the platform despin using two motors. The operation required less than 3 minutes and the steady-state nutation angle was approximately 1.5°.

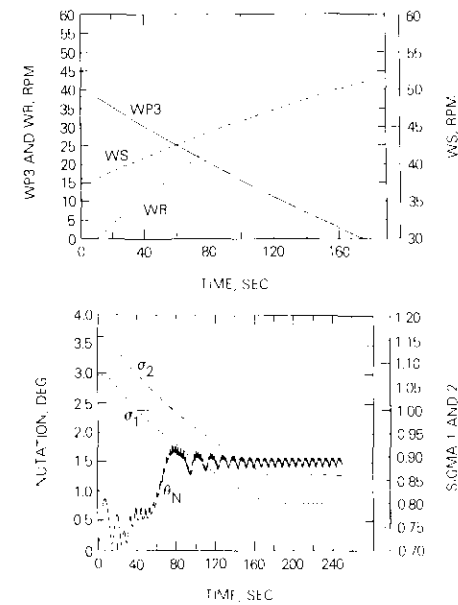


Figure 9. Despin Simulation Run A3

Run A2 used larger rotor asymmetry and dynamic imbalance. The platform was successfully despun, and the final nutation angle was quite large, as expected. Figures 10a and 10b provide the results of this run. Run A4 was a simulation of friction spin-up. Initial angular rates for the platform and the rotor were selected to highlight the intermediate inertia axis spin and to preserve the spacecraft initial angular momentum. From  $t = 75$  to 386 seconds, the spacecraft was spinning along the intermediate inertia axis, and the vehicle transverse rates diverged. Finally, the nutation angle settled down to around  $16^\circ$  and the spacecraft spun along its major axis. Figures 11a through 11d report the results of run A4.

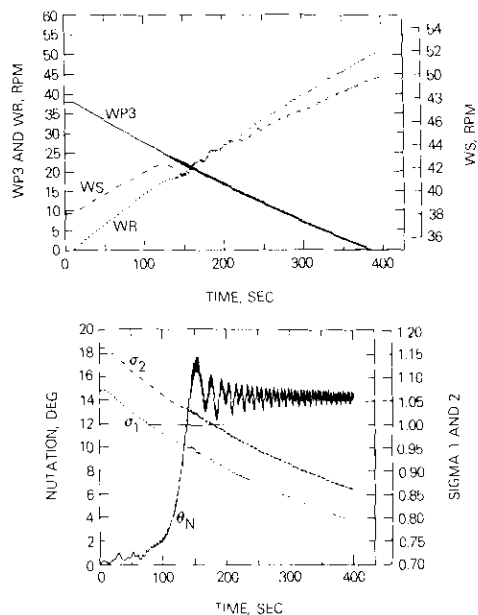


Figure 10. Despin Simulation Run A2

**Conclusion**

Digital computer simulations have been performed at COMSAT Labs to investigate the characteristics of the despin operation for SBS spacecraft. Numerous parametric simulations have been conducted to determine

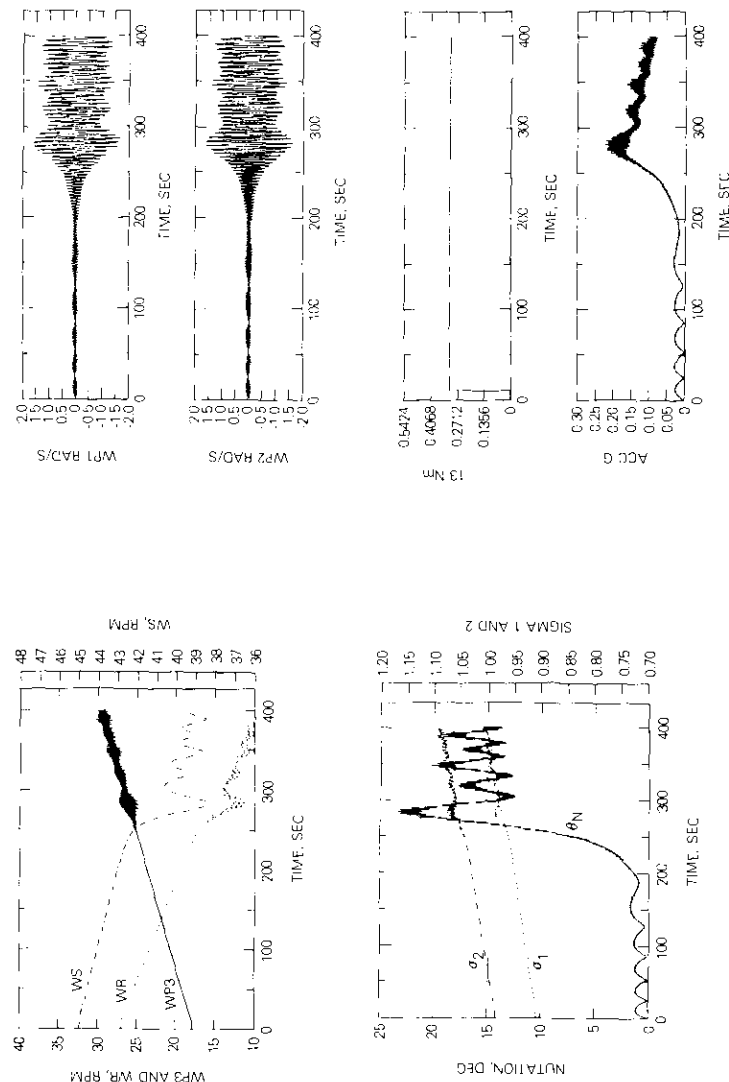


Figure 11. Despin Simulation Run A4

constraints on spacecraft mass properties for acceptable despin operations. Several cases have been identified for detailed investigation on the characteristics of platform despin operations. The results of these simulations have been described. Four additional simulations using the expected worst-case mass properties of the SBS F-3 spacecraft were also included. The results can predict the despin maneuver of the F-3 spacecraft.

### **Acknowledgment**

The author would like to thank Mr. A. Ramos for supplying the model of the despin control loop and for many helpful discussions and suggestions; Mr. T. Patterson for comments on the HDC programs; and Dr. G. D. Gordon for reviewing the original manuscript.

### **References**

- [1] P. W. Likins, "Attitude Stability Criteria for Dual-Spin Spacecraft," *Journal of Spacecraft and Rockets*, Vol. 4, No. 12, December 1967, pp. 1632-1643.
- [2] M. P. Scher and R. L. Farrenkopf, "Dynamic Trap States of Dual-Spin Spacecraft," AIAA Guidance and Control Conference, Key Biscayne, Florida, August 20-22, 1973, AIAA paper 73-908.
- [3] G. J. Adams, "Dual-Spin Spacecraft Dynamics Under Conditions of a Rotating Unbalanced Platform and Rotor Asymmetry," International Astronautical Federation Conference, Anaheim, California, October 1976.
- [4] G. J. Adams, "Dual-Spin Spacecraft Dynamics During Platform Spinup," *Journal of Guidance and Control*, Vol. 3, No. 1, January-February 1980, pp. 29-36.
- [5] E. F. Lyon, R. Kramer, and G. Blustein, "Report to COMSAT on the Program Set 'HDCPG1' for the Simulation of the Dynamic Equations of Motion of a Many-Body Spacecraft," HD&C, Inc. TR-70-2, March 1970.
- [6] E. F. Lyon and R. Kramer, "Deviation of Equations of Motion of a Many-Body Spacecraft," HD&C, Inc. TR-70-4, May 1970.

John C. Hsing received a B.S.E.E. from National Taiwan University in 1967, and an M.S. and a Ph.D. in electrical engineering from the University of Massachusetts in 1970 and 1974. His research was in the field of Adaptive Control Systems. In 1974, he joined COMSAT Laboratories, and is currently a Member of the Technical Staff in the Stabilization, Telemetry, and Command Department of the Spacecraft Laboratory. He has worked on the preliminary design of attitude control systems for communications satellites, and is currently involved in studies of advanced stabilization and large spacecraft control. Since 1980, he has been teaching control systems courses at The George Washington University. He is a member of IEEE, AIAA, Sigma Xi, and Eta Kappa Nu.



## ***Translations of Abstracts in this issue***

### ***Statistiques d'affaiblissement par les précipitations des signaux de balise des satellites COMSTAR à 19/29 GHz et mesures radiométriques à 12 GHz***

PRABHA N. KUMAR

#### **Sommaire**

La littérature scientifique actuelle comporte peu de mesures de propagation à long terme aux fréquences supérieures à 10 GHz, et cette lacune est particulièrement marquée en ce qui concerne la paire de bandes 19/29 GHz. L'article porte sur des études des effets de la pluie sur les signaux de balise des satellites COMSTAR à 19 et à 29 GHz, et sur la température de bruit atmosphérique mesurée au radiomètre dans la bande des 12 GHz. On y présente des données recueillies sur une période de quatre années de mesures ininterrompues, lesquelles comportaient des mesures de signaux de balise émanant de trois satellites COMSTAR (COMSTAR D-1, D-2 et D-3), la température de bruit atmosphérique mesurée au radiomètre à 11,6 GHz, et l'indice pluviométrique en un point de la surface. L'analyse de ces données comporte des distributions d'affaiblissement cumulé à 19,04 et 28,56 GHz ; des distributions d'affaiblissement diurnes et des histogrammes de durée d'affaiblissement à 19,04 et 28,56 GHz ; des distributions cumulées de l'indice pluviométrique mesuré en un point de la surface ; l'affaiblissement excessif dû à la pluie obtenu de la température de bruit atmosphérique mesurée au radiomètre ; et des histogrammes diurnes et de durée dans le cas de ces affaiblissements à 11,6 GHz. L'article s'attarde brièvement sur la question de l'affaiblissement en fonction de l'angle de site.

### ***Centre de commutation de bord pour les télécommunications en AMRT-CS***

F. ASSAL, R. GUPTA, J. APPLE ET A. LOPATIN

#### **Sommaire**

Cet article porte sur la conception et la mise au point d'un centre de commutation de bord  $8 \times 8$  (SSC) pour l'exploitation en mode d'accès multiple par répartition dans le temps avec commutation de bord (AMRT-CS) à 6 GHz (trajet montant) et/ou 4 GHz (trajet descendant). L'organe SSC se compose d'une matrice légère de commutation hyperfréquence (MSM) crossbar à large bande et d'un organe d'aiguillage (DCU). Grâce aux diviseurs/combineurs de puissance Wilkinson à large bande et aux commutateurs à diodes PIN à résistance équilibrée et à faible con-

## ***Author Index, CTR 1981***

Code numbers listed below are to be used for ordering reprints from Lab Records, COMSAT Laboratories, 22300 COMSAT Drive, Clarksburg, Maryland 20871

- ATIA, A. E. & Bonetti, R. R.,\* "Generalized Dielectric Resonator Filters," Fall, pp. 321-344 [CTR81/216].
- BONETTI, R. R., see Atia, A. E. [CTR81/216].
- CAMPANELLA, S. J., see Inukai, T. [CTR81/203].
- CARLTON, P. A., see Childs, W. H. [CTR81/204].
- CHILDS, W. H., Carlton, P. A., Egri, R. G., Mahle, C. E. & Williams, A. E., "A 120-Mbit/s 14-GHz Regenerative Receiver for Spacecraft Applications," Spring, pp. 103-130 [CTR81/204].
- CHITRE, D. M., "Analysis of Throughput Efficiency and Delay in ARQ Systems," Fall, pp. 345-368 [CTR81/217].
- CHOU, S. M., "19- and 28-GHz High Power/Efficiency IMPATT Amplifiers," Fall, pp. 441-458 [CTR81/222].
- CHURAN, G. G. & Leavitt, W. E., "Summary of the SBS Satellite Communications Performance Specification," Fall, pp. 421-432 [CTR81/220].
- CURRY, Jr., W. H., "SBS System Evolution," Fall, pp. 267-292 [CTR81/214].
- DIFONZO, D. F., see Krichevsky, V. N. [CTR81/205].
- DURAND, D. L., "Home Equipment Terminal Characteristics, Fall," pp. 241-247 [CTR81/211].
- DURAND, D L., "Up-Link and Ground Control Facilities," Fall, pp. 248-254 [CTR81/212].
- EGRI, R. G., see Childs, W. H. [CTR81/204].
- FANG, D. J. & Pontes, M. S.,\* "4/6-GHz Ionospheric Scintillation Measurements During the Peak of Sunspot Cycle 21," Fall, pp. 293-320 [CTR81/215].
- GERSON, H. I., "Fabrication Techniques of Lightweight INVAR Microwave Filters," Fall, pp. 403-420 [CTR81/219].
- HYMAN, N. L., "Solar Absorptance Degradation of the COMSTAR Satellite Centimeter Wave Beacon Thermal Radiators," Spring, pp. 159-178 [CTR81/206].
- HYMAN, N. L., "Solar Absorptance Degradation of an Uncleaned Radiator," Fall, pp. 433-440 [CTR81/221].
- INUKAI, T. & Campanella, S. J., "Onboard Clock Correction for SS/TDMA and Baseband Processing Satellites," Spring, pp. 77-102 [CTR81/203].

---

\*Non-COMSAT author.

- KAISER, J., see Veenstra, L. [CTR81/218].
- KEANE, L. M., ed., "A Direct Broadcast Satellite System for the United States," Fall, pp. 195-201 [CTR81/207].
- KRICHEVSKY, V. N. & DiFonzo, D. F., "Optimum Feed Locus for Beam Scanning in the Symmetry Plane of Offset Cassegrain Antennas: Two-Dimensional Case," Spring, pp. 131-158 [CTR81/205].
- LEAVITT, W. E., see Churan, G. G. [CTR81/220].
- LEI, T. R., "Synchronization Accuracy and Error Analysis of Open-Loop TDMA Systems," Spring, pp. 59-76 [CTR81/202].
- MAHLE, C. E., see Childs, W. H. [CTR81/204].
- MARTIN, E. R., "Satellite Characteristics," Fall, pp. 227-240 [CTR81/210].
- MARTIN, E. R., "System Characteristics," Fall, pp. 215-226 [CTR81/209].
- REINHART, E. E., "Regulatory Considerations," Fall, pp. 202-214 [CTR81/208].
- SUYDERHOUD, H. G., see Szarvas, G. G. [CTR81/201].
- SZARVAS, G. G. & Suyderhoud, H. G., "Enhancement of FDM-FM Satellite Capacity by Use of Compandors," Spring, pp. 1-58 [CTR81/201].
- VEENSTRA, L., Kaiser J., Costain, C.\* Klepczynski, W.\* & Allan, D.,\* "Frequency and Time Coordination via Satellite," Fall, pp. 369-402 [CTR81/218].
- WHITWORTH, J. E., "DBS/FS Frequency Sharing," Fall, pp. 255-266 [CTR81/213].
- WILLIAMS, A. E., see Childs, W. H. [CTR81/204].

\*Non-COMSAT author.

## Comsat Authors' Presentations and Publications—1981

The following is a cross-referenced index of technical publications and presentations by COMSAT authors outside of *COMSAT Technical Review*. The code number at the end of an entry is the reprint number by which copies may be ordered from Lab Records at COMSAT Laboratories, 22300 COMSAT Drive, Clarksburg, Maryland 20871.

- AGRAWAL, B. N.\* & James, P. K., "Energy Dissipation Due to Liquid Slosh in Spinning Spacecraft," *Proc. of the Symp. on Dynamics & Control of Large Flexible Space Structures*, June 1981, *PROC.*, pp. 439-452 [81CLR70].
- ALLISON, J. F., see Arndt, R. A. [81CLR22]; Rittner, E. S. [81CLR04].
- APPLE, J. H., "An Onboard Baseband Switch Matrix for SS-TDMA," 5th Int. Conf. on Digital Satellite Comm., March 81, *PROC.*, pp. 429-434 [81CLR44].
- ARNDT, R. A., see Meulenberg, Jr., A. [81CLR34].
- ARNDT, R. A., Meulenberg, A., Allison, J. F. & Weizer, V. G.,\* "Advances in High Output Voltage Silicon Solar Cells," 15th IEEE Photovoltaic Specialists Conf., May 81, *PROC.*, pp. 92-96 [81CLR22].
- ASSAL, F. T., see Gupta, R. K. [81CLR24].
- ASSAL, F., Berman, A. & Gupta, R., "Satellite Switching Center for SS-TDMA Systems," *IEEE ICC June 81 CONF REC*, Vol. 1, pp. 5.1.1-5.1.8 [81CLR26].
- ASSAL, F. T., Betaharon, K.,\* Zaghoul, A. I. & Gupta, R., "Wideband Microwave Switch Matrix for SS-TDMA Systems," 5th Int. Conf. on Digital Satellite Comm., March 81, pp. 421-428 [81CLR43].
- ATIA, A. E., see Bonetti, R. R.,\* [81CLR16], [81CLR17], [81CLR32].
- BARGELLINI, P. L., "Satelliti Commerciali degli Stati Uniti," *L'Elettrotecnica*, Vol. LXVII, No. 4, Apr. 80, pp. 351-359 [80CLR63].
- BARGELLINI, P. L., "SIRIO-Propagation and Communications Satellite (Italy)," *Compendium of Communications and Broadcast Satellites 1958 to 1980*, ed., M. P. Brown, Jr., New York: IEEE Press, 1981, Part B, pp. 283-286 [81CLR76].
- BARGELLINI, P. L. & Campanella, S. J., "An Overview of Satellite Transmission Techniques," Int. Symp. on Innovations in Telecommunications, Kuwait, Apr. 81, *Innovations in Telecommunications*, Part B, ed., J. T. Manassah, New York: Academic Press, 1982, pp. 565-602 [81CLR68].
- BERMAN, A., see Assal, F. [81CLR26].
- BLAKER, H. T.,\* Dorian, C., Plamer, L. M.,\* & Walsh, T. M.,\* "Mobile Services and the ITU—Mobile WARC's 1983 and 1988," *NTC Dec. 81 CONF REC*, Vol. 2, pp. C5.4.1-C5.4.4 [81CLR58].
- BLEIWEIS, J., see Gordon, M.D. [81CLR71].

\*Non-COMSAT author.

- BONETTI, R. R.\* & Atia, A. E., "Analysis of Microstrip Circuits Coupled to Dielectric Resonators," *IEEE MTT-29*, Dec. 81, pp. 1333-1337 [81CLR17].
- BONETTI, R. R.\* & Atia, A., "Coupling of Cylindrical Dielectric Resonators to Microstrip Lines," *IEEE MTT-S Int. Microwave Symp.*, June 81, *DIGEST*, pp. 167-169 [81CLR32].
- BONETTI, R. R.\* & Atia, A. E., "Design of Cylindrical Dielectric Resonators in Inhomogeneous Media," *IEEE MTT-29*, Apr. 81, pp. 323-326 [81CLR01].
- BRISKMAN, R. D., see Edelson, B. I. [81CLR16].
- BRISKMAN, R. D., "Domestic Communications Satellites: System Considerations for Rural Areas," *IEEE COM-19*, Nov. 81, pp. 26-33 [81CLR15].
- BRISKMAN, R. D., "Future Commercial Satellite Possibilities," *Signal*, Feb. 81, pp. 23-26 [81CLR05].
- BRISKMAN, R. D., "The Sky's Not the Limit," *Microwave J.*, Aug. 81, pp. 18-20 [81CLR69].
- CAMPANELLA, S. J., see Bargellini, P. L. [81CLR68]; Chakraborty, D. [81CLR39].
- CAMPANELLA, S. J., "Voice Processing Techniques," *Int. Symp. on Innovations in Telecommunications, Kuwait*, Apr. 81, *Innovations in Telecommunications*, Part A, ed., J. T. Manassah, New York: Academic Press, 1982, pp. 59-95 [81CLR67].
- CAMPANELLA, S. J. & Colby, R. J.,\* "Network Control for TDMA and SS-TDMA in Multiple-Beam Satellite Systems," 5th Int. Conf. on Digital Satellite Comm., March 81, *PROC.*, pp. 335-343 [81CLR45].
- CAMPANELLA, S. J. & Inukai, T., "SS/TDMA Frame Synchronization," *IEEE ICC June 81 CONF REC*, pp. 5.5.1-5.5.7 [81CLR23].
- CARLTON, P. A., see Childs, W. H. [81CLR36].
- CHAKRABORTY, D., "Maximum Likelihood Sequence Detection in Nonlinear Satellite Channels," *IEEE COM-19*, Nov. 81, pp. 47-53 [81CLR10].
- CHAKRABORTY, D. & Jones, M. E., "Laboratory Simulation Results of 120 Mbit/s QPSK Nonlinear Channel Modems," 5th Int. Conf. on Digital Satellite Comm., March 81, *PROC.*, pp. 55-62 [81CLR37].
- CHAKRABORTY, D., Wolejsza, C., Campanella, S. J. & Noguchi, T.,\* "Application of Maximum Likelihood Sequence Detection in Nonlinear Satellite Channels," 5th Int. Conf. on Digital Satellite Comm., March 81, *PROC.*, pp. 285-294 [81CLR39].
- CHANG, P., Fang, R. J. & Jones, M. E., "Performance Over Cascaded and Band-limited Nonlinear Satellite Channels in the Presence of Interference," *IEEE ICC June 81 CONF REC*, pp. 47.3.1-47.3.10 [81CLR18].
- CHILDS, W. H., Carlton, P. A., Egri, R., Mahle, C. E. & Williams, A. E., "A 14-GHz Regenerative Receiver for Spacecraft Application," 5th Int. Conf. on Digital Satellite Comm., March 81, *PROC.*, pp. 453-460 [81CLR36].

\*Non-COMSAT author.

- DEVIEUX, C. & Jones, M. E., "A Practical Optimization Approach for QPSK/TDMA Satellite Channel Filtering," *IEEE Com-29*, May 81, pp. 556-566 [81CLR07].
- DIFONZO, D. F., see Yatsuzuka, Y.\* [81CLR53].
- DOBYNS, T., Gupta, S., Ridings, R., Lindstrom, R. & Hoover, P., "Simplified TDMA Terminal," 5th Int. Conf. on Digital Satellite Comm., March 81, *PROC.*, pp. 369-375 [81CLR40].
- DORIAN, C., see Blaker, H. T. [81CLR58].
- EDELMAN, R. B., "Rate Base Evaluation and Its Effect on the Rate-of-Return," Pacific Telecomm. Conf., Honolulu, Jan. 81, *PTC'81 PROC*, pp. C5-22-C5-28 [81CLR64].
- EDELSON, B. I. & Briskman, R. D., "Space Applications: The Communications Outlook," Pres. at AIAA 1981 Annual Meeting and Technical Display, May 81, AIAA Preprint 81-0888 [81CLR16].
- EGRI, R., see Childs, W. H. [81CLR36].
- ESCH, F. H., see Pentlicki, C. J. [81CLR72].
- FANG, D. J., "C-band Ionospheric Scintillation Measurements at Hong Kong Earth Station During the Peak of Solar Activities in Sunspot Cycle 21," *Symp. on the Effect of the Ionosphere on Radiowave Syst.*, Apr. 81, Paper 3A-2, *PROC.*, pp. 1-12 [81CLR52].
- FANG, R. J. F., see Chang, P. [81CLR18]; Hui, J. [81CLR20].
- FANG, R. J. F., "A Bandwidth and Power Efficient Modulation System," *Int. Symp. on Innovations in Telecommunications, Kuwait*, Apr. 81, *Innovations in Telecommunications*, Part A, ed., J. T. Manassah, New York: Academic Press, 1982, pp. 29-57 [81CLR66].
- FANG, R. J. F., "Applications of Cryptographic Techniques to Commercial Digital Satellite Communications," *NATO Adv. Study Inst. on New Concepts in Multi-user Communication*, Norwich, UK, Aug. 80, *PROC.*, pp. 677-696 [81CLR64].
- FANG, R. J. F., "Quaternary Transmission Over Satellite Channels with Cascaded Nonlinear Elements and Adjacent Channel Interference," *IEEE COM-29*, May 81, pp. 567-581 [81CLR09].
- FORCINA, G.,\* Pontano, B.,\* Colby, R. J.\* & Lei, R., "Acquisition, Synchronization and System Management for the INTELSAT TDMA System," 5th Int. Conf. on Digital Satellite Comm., March 81, *PROC.*, pp. 377-386 [81CLR41].
- GATFIELD, A. G., "Satellite Links in the Integrated Services Digital Network," 5th Int. Conf. on Digital Satellite Comm., March 81, *PROC.*, pp. 235-239 [81CLR38].
- GHAIS, A. F., Kolsrud, J.,\* Skjei, S. M.\* & Suyderhoud, H. G., "U. S. Results of TDMA Field Trials," 5th Int. Conf. on Digital Satellite Comm., March 81, *PROC.*, pp. 133-139 [81CLR46].

\*Non-COMSAT author.

- GORDON, M. D. & Bleiweis, J., "The SBS TT&C System," Int. Telemetry Conf., Oct. 81, *ITC/USA/81*, Vol. XVII, pp. 23-36 [81CLR71].
- GOVER, S., see Rieger, F. [81CLR49].
- GUPTA, R., see Assal, F. [81CLR26], [81CLR43].
- GUPTA, R. K. & Assal, F. T., "Integration, Environmental, and Radiation Testing of a Microwave Switch Matrix System," *IEEE ICC June 81 CONF REC*, pp. 5.4.1-5.4.6 [81CLR24].
- GUPTA, S., see Dobyns, T. [81CLR40].
- HANNSEN, J. C., see Kirkendall, T. D. [81CLR31].
- HARRINGTON, J. V., "Trends in Electronics Information Transfer," Int. Symp. on Innovations in Telecommunications, Kuwait, Apr. 81, *Innovations in Telecommunications*, Part A, ed., J. T. Manassah, New York: Academic Press, 1982, pp. 3-26 [81CLR65].
- HOOVER, P., see Dobyns, T. [81CLR40].
- HORNA, O. A., "Correction Algorithms for Extended Range Echo Cancellers," Int. Conf. on Acoustics, Speech, & Signal Processing, March and Apr. 81, *PROC.*, pp. 560-563 [81CLR03].
- HORNA, O. A., "Extended Range Echo Cancellers," SOUTHEASTCON '81, Apr. 81, *CONF PROC.*, pp. 846-853 [81CLR02].
- HUI, J. & Fang, R. J. F., "Convolutional Code and Signal Waveform Design for Band-limited Satellite Channels," *IEEE ICC June 81 CONF REC*, pp. 47.5.1-47.5.10 [81CLR20].
- HUNG, H. L., see Hyman, N. [81CLR50].
- HYMAN, N. L., "Solar Absorbance Degradation of OSR Radiators on the COMSTAR Satellites," 16th Thermophysics Conf., June 81, AIAA Preprint 81-1185 [81CLR51].
- HYMAN, N. & Hung, H. L., "Thermal Design of a Thermoelectrically Cooled Low Noise Amplifier," 16th Thermophysics Conf., June 81, AIAA Preprint 81-1077 [81CLR50].
- INUKAI, T., see Campanella, S. J. [81CLR23].
- INUKAI, T., "SS-TDMA Networking Via ISL," *IEEE ICC June 81 CONF REC*, pp. 70.6.1-70.6.5 [81CLR27].
- INUKAI, T. & Weinberg, L.,\* "Whitney Connectivity of Mastroids," *Siam J. on Algebraic and Discrete Methods*, June 1981, pp. 108-120 [81CLR74].
- JAMES, P. K., see Agrawal, B. N. [81CLR70].
- JONES, M. E., see Chakraborty, D. [81CLR37]; Chang, P. [81CLR18]; Devieux, C. [81CLR07].
- KELLY, W. H. & Reisenweber, Jr., J. H., "Optimization of a Heat Pipe Radiator for Spacecraft High-Power TWTAs," 14th Int. Heat Pipe Conf., London, Sept. 81, *Advances in Heat Pipe Tech.*, ed., D. A. Reay, pp. 505-516 [81CLR75].

\*Non-COMSAT author.

- KINAL, G. V. & Toal, B.,\* "Preoperational Tests of High-speed (56 Kbps) Transmission over MARISAT," *NTC Dec. 81 CONF REC*, Vol. 1, pp. B9.2.1-B9.2.5 [81CLR57].
- KIRKENDALL, T. D. & Hannsen, J. C., "Electron Probe Study of Electrochemical Corrosion of Ti/Pd/Ag Contacts on Si," 16th Annual Conf. of the Microbeam Analysis Soc., *Microbeam Analysis 1981*, pp. 269-272 [81CLR31].
- LEBOWITZ, S. H.\* & Rhodes, S. A., "Performance of Coded 8PSK Signaling for Satellite Communications," *IEEE ICC June 81 CONF REC*, pp. 47.4.1-47.4.8 [81CLR19].
- LEE, D. J., "In-Orbit Performance of COMSTAR TWTAs," *IEEE ICC June 81 CONF REC*, pp. 54.4.1-54.4.5 [81CLR29].
- LEE, L.-N., "Error-correction Coding for Commercial Satellite Channels," *IEEE ICC June 81 CONF REC*, pp. 2.5.1-2.5.4 [81CLR25].
- LEE, Y. S., "Technology Assessment for Implementation of Optical Intersatellite Link," *IEEE ICC June 81 CONF REC*, pp. 15.4.1-15.4.4 [81CLR06].
- LEE, Y. S. & Moltz, J. L., "Fiber Optic Analog Transmitter and Receiver Systems," Electro-Optics/Laser 81 Conf. & Expo, Nov. 81, *PROC.*, pp. 289-296 [81CLR77].
- LEI, R., see Forcina, G. [81CLR41].
- LINSTROM, R., see Dobyns, T. [81CLR40].
- LIPKE, D. W., "Maritime Satellite Systems," Int. Symp. on Innovations in Telecommunications, Kuwait, Apr. 81, *Innovations in Telecommunications*, Part B, ed., J. T. Manassah, New York: Academic Press, 1982, pp. 689-723 [81CLR78].
- LYONS, J. W. & Meulenberg, A., "Radiation Testing of Spectrally Selective Reflectors for Solar Array Concentrators," 16th Intersoc. Energy Conv. Eng. Conf., *PROC.*, pp. 393-396 [81CLR33].
- MACKENTHUN, K. M., "Noiseless Coding of Error Detection Information," *IEEE IT-27*, March 81, pp. 227-230 [81CLR08].
- MAHLE, C. E., see Childs, W. H. [81CLR36].
- MEULENBERG, A., see Arndt, R. A. [81CLR22]; Lyons, J. W. [81CLR33]; Rittner, E. S. [81CLR04].
- MEULENBERG, Jr., & Arndt, R. A., "High- and Low-Resistivity Silicon Solar Cells," 16th Intersoc. Energy Conv. Eng. Conf., Aug. 81, *PROC.*, Vol. 1, pp. 397-399 [81CLR34].
- MOLTZ, J. L., see Lee, Y. S. [81CLR77].
- ONUFY, M., see Suyderhoud, H. G. [81CLR42].
- PENTLICKI, C. J. & Esch, F. H., "Communications Satellite Configurations for the 1990's," Int. Telemetry Conf., Oct. 81, *ITC/USA/81*, Vol. XVII, pp. 461-474 [81CLR72].
- PERSINGER, R. R., see Yatsuzuka, Y.\* [81CLR53].

\*Non-COMSAT author.

- RAAG, H., "International Electronic Mail," Pres. at Frost and Sullivan Symp. of Electronic Mail, Apr. 81.
- RAAG, H., "International Electronic Mail," *NTC Dec. 81 CONFREC* [81CLR55].
- RAAG, H., "The Intelpost System, A Progress Report," Int. Symp. on Graphics and Text Communications, Paris, Nov. 81 [81CLR63].
- REINHART, E. E., "Progress Report on CCIR Studies for Guaranteeing Access to the Geostationary Satellite Orbit," *IEEE ICC June 81 CONFREC*, pp. 43.1.1-43.1.3 [81CLR28].
- REISENWEBER, Jr., J. H., see Kelly, W. H. [81CLR75].
- REVESZ, A. G., "On the Structure of Noncrystalline Si and  $\text{Si}_{2-x}\text{H}_x$  Films," *Physica Status Solidi (A)*, 1980, pp. 619-629 [80CLR62].
- REVESZ, A. G., "Structural Changes in  $\text{SiO}_2$  Films and at the Si/ $\text{SiO}_2$  Interface During Thermal Growth," IEEE Semiconductor Interface Specialists Conf., Dec. 81 [UP088CL].
- REVESZ, A. G., "Structural Changes in  $\text{SiO}_2$  Films During Thermal Growth," Electrochem. Soc. Meeting, May 81, Extended Abstracts No. 281 [UP100CL81].
- REVESZ, A. G., "The Not-Quite-Random Network Structure of Vitreous  $\text{SiO}_2$ ," American Ceramic Soc. Meeting, May 81, *American Ceramic Soc. Bulletin*, 1981, p. 410, abstract only [UP100CL81].
- REVESZ, A. G. & Fehlner, F. P.,\* "The Role of Noncrystalline Films in the Oxidation and Corrosion of Metals," *Oxidation of Metals*, 1981, pp. 297-321 [81CLR14].
- REVESZ, A. G. & Walrafen, G.,\* "On Raman Scattering in Vitreous Silica," American Ceramic Soc. Meeting, May 81, *American Ceramic Soc. Bulletin*, 1981, p. 408, abstract only.
- REVESZ, A. G., Wemple, S. H.\* & Gibbs, G. V.,\* "Structural Ordering Related to Chemical Bonds in Random Networks," 9th Int. Conf. on Amorphous & Liquid Semiconductors, Grenoble, France, July 1981, *J. Phys.*, Oct. 81, C4-217-C4-219.
- RHODES, S. A., see Lebowitz, S. H. [81CLR19].
- RHODES, S. A. & Lebowitz, S. H.,\* "Performance of Coded OPSK for TDMA Satellite Communications," 5th Int. Conf. on Digital Satellite Comm., March 81, *PROC.*, pp. 79-87 [81CLR35].
- RIDINGS, R., see Dobyns, T. [81CLR40].
- RIEGER, F. & Gover, S., "Predict C/I Performance with Simple Measurements," *Microwaves*, Aug. 81, 107-110 [81CLR49].
- RIESER, J. H., Suyderhoud, H. G. & Yatsuzuka, Y.,\* "Design Considerations for Digital Speech Interpolation," *IEEE ICC June 81 CONFREC*, pp. 49.4.1-49.4.7 [81CLR21].

\*Non-COMSAT author.

- RITTNER, E. S., Meulenberg, A. & Allison, J. F., "Dependence of Efficiency of Shallow Junction Silicon Solar Cells on Substrate Doping," *J. Energy*, Jan.-Feb. 81, pp. 9-14 [81CLR04].
- ROGERS, D. V., "Diversity- and Single-Site Radiometric Measurements of 12-GHz Rain Attenuation in Different Climates," 2nd Int. Conf. on Antennas and Propagation, Apr. 81, *Part 2: Propagation*, pp. 118-123 [81CLR47].
- SINHA, A. K., "The Potential Role of Intersatellite Links in Future Satellite Communications," *NTC Dec. 81 CONF REC*, Vol. 1, pp. B5.3.1-B5.3.5 [81CLR56].
- SLABINSKI, V. J., "A Dynamical Objection to the Inversion of the Earth on Its Spin Axis," *J. of Physics, A: Math. and General*, 1981, pp. 2503-2507 [81CLR13].
- SLABINSKI, V. J., "Continental Drift and the Rotation of the Earth—A New and Critical Evaluation," *Celestial Mechanics*, 1981, pp. 89-91 [81CLR12].
- STOCKEL, J., "The NTS-2  $\text{NiH}_2$  Battery—an Update," 16th Intersoc. Energy Conv. Eng. Conf., Aug. 81, *PROC.*, Vol. 1, pp. 212-215 [81CLR73].
- STRAUSS, R. & Owens, J. R.,\* "Past and Present INTELSAT TWTA Life Performance," *J. Spacecraft and Rockets*, Nov.-Dec. 81, pp. 491-498 [81CLR48].
- SUYDERHOUD, H. G., Onufry, M., Yatsuzuka, Y.\* & Virupaksha, K., "Digital Speech Interpolation with Nearly Instantaneous Companding or ADPCM," 5th Int. Conf. on Digital Satellite Comm., March 81, *PROC.*, pp. 273-281 [81CLR42].
- SUYDERHOUD, H. G., see Ghais, A. F. [81CLR46]; Reiser, J. H. [81CLR21]; Yatsuzuka, Y.\* [81CLR59].
- VIRUPAKSHA, K., see Suyderhoud, H. G. [81CLR42].
- WEISS, H. J., "Conservation of the Geostationary Spectrum," *NTC Dec. 81 CONF REC*, Vol. 3, pp. E7.2.1-E7.2.5 [81CLR60].
- WEISS, H. J., "Considerations Relating to Geostationary Intersatellite Links," *IEEE ICC June 81 CONF REC*, pp. 43.2.1-43.2.5 [81CLR30].
- WILLIAMS, A. E., see Childs, W. H. [81CLR36].
- WOLEJSZA, C., see Devieux, C. [81CLR39].
- YAM, E. S., "Line-rate Energy Dispersal Waveforms for FM TV," *NTC Dec. 81 CONF REC*, Vol. 3, pp. E7.5.1-E7.5.5 [81CLR62].
- YATSUZUKA, Y.,\* Persinger, R. R. & DiFonzo, D. F., "Design Procedures for Multi-feed Satellite Shaped-Beam Antennas," 11th European Microwave Conf., Sept. 81, *CONFERENCE PROC.*, pp. 540-545 [81CLR53].
- YATSUZUKA, Y.\* & Suyderhoud, H. G., "Discrimination of Speech and High-Speed Data Using an Adaptive Predictor for DSI Application," *NTC Dec. 81 CONF REC*, Vol. 3, pp. E5.2.1-E5.2.6 [81CLR59].
- ZAGHLOUL, A. I., see Assal, F. T. [81CLR43].

\*Non-COMSAT author.